

ADVANCES IN MODELING HIGH TEMPERATURE PARTICLE FLOWS IN
THE FIELD OF CONCENTRATING SOLAR POWER

A THESIS SUBMITTED TO
THE GRADUATE SCHOOL OF NATURAL AND APPLIED SCIENCES
OF
MIDDLE EAST TECHNICAL UNIVERSITY

BY

EVAN F JOHNSON

IN PARTIAL FULFILLMENT OF THE REQUIREMENTS
FOR
THE DEGREE OF DOCTOR OF PHILOSOPHY
IN
MECHANICAL ENGINEERING

FEBRUARY 2021

Approval of the thesis:

**ADVANCES IN MODELING HIGH TEMPERATURE PARTICLE FLOWS
IN THE FIELD OF CONCENTRATING SOLAR POWER**

submitted by **EVAN FAIR JOHNSON** in partial fulfillment of the requirements
for the degree of **Doctor of Philosophy in Mechanical Engineering, Middle East
Technical University** by,

Prof. Dr. Halil Kalıpçılar
Dean, Graduate School of **Natural and Applied Sciences**

Prof. Dr. M. A. Sahir Arıkan
Head of the Department, **Mechanical Engineering**

Prof. Dr. İlker Tari
Supervisor, **Mechanical Engineering, METU**

Prof. Dr. Derek Baker
Co-Supervisor, **Mechanical Engineering, METU**

Examining Committee Members:

Prof. Dr. M. Metin Yavuz
Mechanical Engineering, METU

Prof. Dr. İlker Tari
Mechanical Engineering, METU

Prof. Dr. Murat Köksal
Mechanical Engineering, Hacettepe University

Asst. Prof. Dr. Mehdi Mehrtash
Energy Systems Engineering, Atilim University

Asst. Prof. Dr. Çağla Meral Akgül
Civil Engineering, METU

Date: 08.02.2021

I hereby declare that all information in this document has been obtained and presented in accordance with academic rules and ethical conduct. I also declare that, as required by these rules and conduct, I have fully cited and referenced all material and results that are not original to this work.

Name, Last name : Evan F Johnson

Signature :

ABSTRACT

ADVANCES IN MODELING HIGH TEMPERATURE PARTICLE FLOWS IN THE FIELD OF CONCENTRATING SOLAR POWER

Johnson, Evan F
Doctor of Philosophy, Mechanical Engineering
Supervisor : Prof. Dr. İlker Tari
Co-Supervisor: Prof. Dr. Derek Baker

February 2021, 224 pages

Within the field of concentrating solar power (CSP), central receiver (“tower”) type systems are capable of achieving temperatures reaching or exceeding 1000 °C. To utilize this heat efficiently, a growing body of research points to the benefits of using solid, sand-like particles as a heat storage medium in CSP plants. Modeling capabilities for flowing groups of particles at high temperatures are lacking in several aspects, and thermal radiation in particle groups has received relatively little attention in research. This thesis focuses on developing the modeling capabilities needed to simulate heat transfer in solid particle solar receivers and heat exchangers using the Discrete Element Method (DEM), where particle mechanics and heat transfer are modeled at the particle scale. Several original contributions are made in this thesis: A) a 3D Monte Carlo Ray Tracing code is developed for modeling radiation for gray, uniformly sized particles, B) an expression for the effective thermal conductivity due to radiation is derived from Monte Carlo simulations, C) the “Distance Based Approximation” (DBA) model for radiative heat transfer in particle groups is developed, which can be implemented directly into DEM codes, D) an open source heat transfer code is developed for dense granular flows, named Dense Particle Heat Transfer (DPHT),

which uses the DBA radiation model and several previously proposed heat conduction models to form a code which is readily usable for particle-based heat exchange devices, and E) the DPHT code is used to model a solar receiver for preheating of lime particles for calcination. In addition to modeling, experimental work on dense granular flows is carried out under a high-flux solar simulator, with particle temperatures reaching 750 °C. Results show a relatively close match between experimental results and the newly developed DPHT heat transfer code.

Keywords: Particle radiation, Discrete Element Method heat transfer, Monte Carlo radiation, Concentrating Solar Power, Dense granular flow heat transfer

ÖZ

KONSANTRE GÜNEŞ ENERJİSİ ALANINDA YÜKSEK SICAKLIKLI PARTİKÜL AKIŞLARINI MODELLEMEDEKİ GELİŞMELER

Johnson, Evan F
Doktora, Makina Mühendisliği
Tez Yöneticisi: Prof. Dr. İlker Tarı
Ortak Tez Yöneticisi: Doç. Dr. Derek Baker

Şubat 2021, 224 sayfa

Konsantre güneş enerjisi (CSP) alanında, merkezi alıcı ("kule") tipi sistemler 1000 °C'ye ulaşan veya bu sıcaklığı aşan sıcaklıklara ulaşabilir. Bu ısıyı verimli bir şekilde kullanmak için, büyüyen bir araştırma grubu, CSP tesislerinde ısı depolama ortamı olarak katı, kum benzeri partiküllerin kullanılmasının faydalarına işaret ediyor. Yüksek sıcaklıkta akan partikül grupları için modelleme yetenekleri, çeşitli yönlerden eksiktir ve partikül gruplarındaki termal radyasyon, araştırmada nispeten az ilgi görmüştür. Bu tez, parçacık mekaniğinin ve ısı transferinin parçacık ölçeğinde modellendiği Ayrık Eleman Yöntemi (DEM) kullanılarak katı parçacık güneş alıcılarında ve ısı değiştiricilerinde ısı transferini simüle etmek için gereken modelleme yeteneklerini geliştirmeye odaklanmaktadır. Bu tezde birkaç orijinal katkı yapılmıştır: A) gri, tek tip boyutlu parçacıklar için radyasyonu modellemek için bir 3D Monte Carlo Işın İzleme kodu geliştirilmiştir, B) Radyasyona bağlı etkili termal iletkenlik için bir ifade, Monte Carlo simülasyonlarından türetilmiştir, C) Parçacık gruplarında ışınlama ısı transferi için doğrudan DEM kodlarına uygulanabilen "Mesafe Tabanlı Yaklaşım" (DBA) modeli geliştirildi, D) DBA radyasyonunu kullanan yoğun taneli akışlar için açık kaynaklı bir ısı aktarım kodu geliştirildi model ve daha önce önerilen birkaç ısı iletim modeli, partikül bazlı ısı

değişim cihazları için kolaylıkla kullanılabilen bir kod oluşturmak için ve E) geliştirilen ısı transfer kodu kireçleme için kireç partiküllerinin ön ısıtması için bir güneş alıcısı modellemek için kullanılır. Modellemeye ek olarak, partikül sıcaklıkları 750 °C'ye ulaşan yüksek akıllı güneş simülatörü altında yoğun granül akışlar üzerinde deneysel çalışma yürütülmektedir.

Anahtar Kelimeler: Parçacık radyasyonu, Ayrık Eleman Yöntemi ısı transferi, Monte Carlo radyasyonu, Konsantre Güneş Enerjisi, Yoğun granüler akışlı ısı transferi

ACKNOWLEDGMENTS

I would like to express my deepest gratitude to my advisors İlker Tarı and Derek Baker for their help, guidance, and encouragement. In the laboratory, Mustafa Yalçın was a constant source of ideas and knowledge, and I appreciate all the hard work he undertook to ensure a positive outcome of the experiments.

Throughout this work, I have had an ongoing collaboration with Serdar Hiçdurmaz, who has been working on the centrifugal solar receiver at the German Aerospace Center. This collaboration led to many important developments and a joint conference paper at SolarPaces conference, 2020. The heat conduction sub-models in Chapter 5 were explored and implemented in collaboration with Serdar. The collaboration has been both fruitful and enjoyable, and Serdar has my gratitude for all of the ideas and input he has given over the span of this thesis.

TABLE OF CONTENTS

ABSTRACT	v
ÖZ.....	vii
ACKNOWLEDGMENTS	ix
TABLE OF CONTENTS	x
LIST OF TABLES	xvii
LIST OF FIGURES	xix
LIST OF ABBREVIATIONS	xxvii
CHAPTERS	
1 INTRODUCTION	1
1.1 Background.....	2
1.2 Preview of Research Contributions	4
1.3 CSP with Solid Particles.....	6
1.4 Effective Thermal Conductivity in Particle Beds.....	9
1.5 Modeling Heat Transfer in Particle Flows	13
1.6 Experimental Studies of Dense Particle Flows	17
2 AN OPEN SOURCE MONTE CARLO CODE FOR THERMAL RADIATION IN GROUPS OF PARTICLES	19
2.1 Model Details	20
2.2 Validation	23
2.2.1 Two Touching Spheres	23
2.2.2 Two Separated Spheres.....	24
2.2.3 Randomly Packed 50-Sphere Domain.....	25

2.2.4	Particle-Wall Validation.....	27
2.3	File Structure.....	28
2.4	Particle-Particle RDF Example.....	29
2.5	Particle-Wall RDF Example	32
2.6	MCRT Conclusion	34
3	EFFECTIVE THERMAL CONDUCTIVITY DUE TO RADIATION	35
3.1	Method for finding k_{rad}	36
3.1.1	Generating the Particle Domain with DEM	38
3.1.2	Simulating Photons with Monte Carlo Ray Tracing	40
3.1.3	Particle-Particle Heat Exchange Simulation	40
3.1.4	Calculating k_{rad} from the Temperature Profile	43
3.1.5	Finding the Exchange Factor.....	45
3.2	Validation.....	45
3.3	Results and Discussion	47
3.3.1	Near-Edge Effects	47
3.3.2	Number of Photons.....	48
3.3.3	Thickness of the Particle Wall	49
3.3.4	Independence of F_E with Respect to Temperature	50
3.3.5	Reproducibility with Different Particle Positions	51
3.3.6	Exchange Factor Results	51
3.3.7	Comparisons with Previous Research	53
3.3.8	Total Effective Thermal Conductivity	56
3.4	Conclusions for k_{rad}	57

4	PARTICLE-SCALE RADIATION: THE DISTANCE BASED APPROXIMATION MODEL.....	59
4.1	Introduction of the Distance Based Approximation Model	59
4.2	Methods	61
4.2.1	PP Radiation: Generation of Particle Domains.....	61
4.2.2	PP Radiation: Monte Carlo Ray Tracing	63
4.2.3	PP Radiation: RDF Tables	64
4.2.4	PP Radiation: Calculating Heat Exchange in DEM.....	65
4.2.5	PW Radiation: Generation of Particle-Wall Domains	66
4.2.6	PW Radiation: Monte Carlo Ray Tracing.....	68
4.2.7	PW Radiation: RDF Tables	68
4.2.8	PW Radiation: Calculating Heat Exchange in DEM	69
4.3	Model Validation.....	69
4.3.1	Validation of Particle-Particle DBA Model.....	69
4.3.2	Validation of Particle-Wall DBA Model	73
4.4	Results and Discussion	74
4.4.1	Particle-Particle Results and Discussion.....	74
4.4.2	Particle-Wall Results and Discussion	78
4.5	Modeling Radiation in a Dense Granular Flow	80
4.6	Conclusions and Future Work for DBA Model	87
5	AN OPEN SOURCE CODE FOR DENSE PARTICLE HEAT TRANSFER	89
5.1	Motivation	90
5.2	Applications and Assumptions	91
5.3	Software Notes	92

5.4	Heat Transfer Models.....	93
5.4.1	Particle-Particle Conduction	94
5.4.2	Particle-Wall Conduction	96
5.4.3	Particle-Fluid-Particle Conduction.....	97
5.4.4	Particle-Fluid-Wall Conduction	105
5.4.5	Particle-Particle and Particle-Wall Radiation.....	107
5.5	Boundary Conditions	108
5.6	File Structure.....	109
5.6.1	DPHT_code	110
5.6.2	Mesh.....	115
5.6.3	PPF_PFW_conduction	115
5.6.4	Post.....	115
5.6.5	PP_RDF_tables	115
5.6.6	PW_RDF_tables.....	116
5.6.7	Results_to_save	116
5.7	Example Simulation with DPHT: Flow Through a Heated Tube.....	116
5.7.1	Geometry Creation	117
5.7.2	Mesh Generation	117
5.7.3	Mesh Extraction	118
5.7.4	DEM Modeling	119
5.7.5	DPHT Modeling.....	120
5.7.6	Post-Processing	121
5.8	Comparison with ZBS Model	123
5.9	Solving Conjugate Heat Transfer Problems	126

5.9.1	Matching the Interface of the Two Domains	127
5.9.2	Overall Heat Transfer Coefficient	127
5.10	Conclusions for DPHT	129
6	EXPERIMENTAL INVESTIGATION OF A DENSE GRANULAR FLOW AT HIGH TEMPERATURES	131
6.1	Experiment Design	132
6.1.1	Overall Setup	132
6.1.2	Hopper	135
6.1.3	Shutoff Valve	137
6.1.4	Test Section.....	137
6.1.5	Inlet and Outlet Measurement Blocks	139
6.1.6	Orifice Plates, Overflow Channels, Mixing Devices.....	140
6.1.7	Data Acquisition	142
6.2	Testing and Results.....	142
6.2.1	Particle Materials Tested	142
6.2.2	Procedure	143
6.2.3	Results.....	144
6.2.4	Summary and Discussion.....	150
6.3	Discussion of Practical Lessons Learned	152
6.3.1	Particle Filtration	152
6.3.2	Minimizing Heat Loss	153
6.3.3	Heated Hopper Design.....	155
6.3.4	Mixing the Particle Stream	157
6.4	Conclusions for Experimental Investigation	161

7	COMPARISON OF EXPERIMENTAL AND DPHT MODEL RESULTS ...	163
7.1	DEM Simulation	163
7.2	DPHT Simulation.....	166
7.2.1	Modified PFP Heat Transfer Model.....	166
7.2.2	Thermal Properties	168
7.2.3	Thermal Boundary Conditions	169
7.3	Results and Discussion	173
7.3.1	Test 2 Results	173
7.3.2	Test 3 Results	176
7.3.3	Uncertainty and Repeatability	177
7.4	Conclusions for Comparison of Experimental and DPHT Model Results ...	179
8	A SOLAR RECEIVER FOR PREHEATING LIME PARTICLES	181
8.1	Receiver Design	182
8.2	Modeling Methods	183
8.2.1	Ray Tracing of the CSP System.....	183
8.2.2	Particle-Scale Heat Transfer Modeling with DPHT	185
8.2.3	Overall Receiver Heat Transfer Model	190
8.3	Conclusions for Solar Receiver Model	195
9	CONCLUSIONS AND RECOMMENDED FUTURE WORK.....	197
	REFERENCES	201
	APPENDICES	
A.	Particle-Particle RDF Tables	215
B.	Particle-Wall RDF Tables.....	217
	CURRICULUM VITAE.....	223

LIST OF TABLES

TABLES

Table 2.1. View factor validation between two spheres separated by various distances.....	24
Table 2.2 Input parameters for PW validation of MCRT code.....	27
Table 2.3. Total heat transfer calculated with Fluent and MCRT code.....	28
Table 2.4 Data in the <i>all_RDF</i> output file, showing the RDF from each particle to each other particle.....	32
Table 2.5 The <i>dist_vs_RDF</i> output file, with table truncated to 12 rows.....	32
Table 2.6 Data output in the <i>PW_RDF</i> file.....	34
Table 3.1. Exchange Factor calculated at various temperatures for a solid fraction of 0.45 and an emissivity of 0.7.....	51
Table 3.2 Exchange Factor results for various solid fractions and emissivity (ϵ) values.....	52
Table 4.1. Mean of the total PP RDF over 100 particles, for the ten PP RDF cases studied.....	70
Table 4.2. Total heat transfer from the hot core, comparing results from the DBA model with a full Monte Carlo ray tracing simulation.....	72
Table 4.3. Total heat transfer rate (W) from the wall to the red particles in the hemispherical volume, comparing Monte Carlo and DBA results for each PW RDF curve presented in Appendix B.....	74
Table 4.4. PP center-to-center cutoff distance based on 99.9% of photons absorbed.....	77
Table 4.5. PW cutoff distance based on 99.9% of photons absorbed.....	79
Table 4.6. Properties and boundary conditions used in the DEM and heat transfer simulations.....	82
Table 6.1 Steady state temperature conditions from each test.....	150
Table 7.1. DEM parameters used in simulation of experimental setup.....	164

Table 7.2. Thermal parameters used in simulation of experimental setup.....	168
Table 7.3. Measured temperatures in center of wall, and calculated temperatures at interior surface.....	171
Table 7.4. Steady state heat transfer rate from wall to particles, Test 2.....	174
Table 7.5. Steady state heat transfer rate from wall to particles, Test 3.....	176
Table 8.1 Properties used in DEM and DPHT modeling.....	186

LIST OF FIGURES

FIGURES

Figure 1.1. Main components of a concentrating solar power plant for electricity generation.....	7
Figure 1.2. Heat transfer modes in a particle-fluid-wall domain.	14
Figure 2.1. (a) Sphere with random photon emission location, (b) random emission direction in temporary axes, and (c) emission direction vector passing through several neighboring spheres, in XYZ axes.	22
Figure 2.2. View factors calculated with various numbers of photons emitted per particle, for two touching spheres.	24
Figure 2.3. (a) The 50-sphere domain and surrounding sphere used for Fluent validation, (b) view factors between the central sphere and all neighboring spheres.	26
Figure 2.4. The 3-sphere domain and walls used for PW validation against a Fluent Surface-to-Surface radiation simulation.	27
Figure 2.5. File structure of the MCRT code.....	28
Figure 2.6. Eight-particle simulation domain.	30
Figure 2.7. Parameters input to initiate MRCT code.	31
Figure 2.8. Particle and wall positions used in the example simulation.	33
Figure 2.9. Parameters for the particle-wall simulation.....	33
Figure 3.1. Close-up view of a domain with a solid fraction of (a) 0.64, and (b) 0.25.....	39
Figure 3.2. (a) Initial cubic shaped domain, (b) the final spherical shaped domain after removing the necessary spheres, and (c) a cut-away view to show the central sphere.	40
Figure 3.3. Particle temperatures over time, with initial temperatures shown in red and steady state temperatures shown in purple, and (b) steady state particle temperatures of a slice of the domain.	42
Figure 3.4. Steady state particle temperatures and curve fit equation of form $T=C_1/r + C_2$ for a solid fraction of 0.45 and emissivity 0.5.	44

Figure 3.5. Steady state temperatures of spheres of particle domain shown in Figure 2.3, with results from both Fluent and the MCRT plus particle-particle heat exchange simulation.	47
Figure 3.6. Exchange Factor found at various radial positions throughout the particle wall, for a solid fraction of 0.64 and an emissivity of 1.	48
Figure 3.7. Exchange Factor at various radial positions for a solid fraction of 0.45 and an emissivity of 0.7, with 10^2 , 10^3 , 10^4 , and 10^5 photons used in the Monte Carlo simulation.	49
Figure 3.8. Exchange Factor measured at various radial positions, showing simulations with different numbers of particles.	50
Figure 3.9. Exchange Factor results, with points representing data from Table 3.2, and lines representing the surface fit of Eq. (3.11).	53
Figure 3.10. Exchange Factor comparison to previous models and experimental work, for a solid fraction of 0.60 [37][29][28][42].	54
Figure 3.11. Comparison of Exchange Factors between present study and models by Zehner, Bauer, and Schlünder (ZBS), and Breitbach and Barthels (BB).	55
Figure 4.1. Group of 50,000 particles with a solid fraction of 0.45.	62
Figure 4.2. Particle-particle RDF at various distances between particles, for $\epsilon_p = 0.86$ and $SF = 0.55$, showing individual data points and a smoothing spline fit.	64
Figure 4.3. (a) Particle-wall domain with a $SF_{bulk} = 0.64$, (b) domain with $SF_{bulk} = 0.25$, and (c) local solid fraction at various distances from the wall, showing various bulk solid fractions.	67
Figure 4.4. Particle-wall RDF at various distances, for a $\epsilon_p = 0.86$, $\epsilon_w = 0.80$, and $SF_{bulk} = 0.45$	68
Figure 4.5. Mean cumulative RDF (fraction of photos absorbed) at various distances from the emitting particle, calculated with Monte Carlo and the DBA models, for $\epsilon_p = 0.65$ and various solid fractions.	71
Figure 4.6. Cross section of the spherical domain used for validating the DBA model, with 10,000 particles and a solid fraction of 0.45.	72

Figure 4.7. Particle-wall domain with a SF_{bulk} of 0.45. Half of the domain is semi-transparent to show the red particles included in the PW heat transfer calculation. 73

Figure 4.8. PP RDF as a function of distance for (a) $\epsilon_p = 0.65$, (b) $\epsilon_p = 0.86$, and (c) the extreme values of SF and ϵ_p 76

Figure 4.9. (a) Particle-particle RDF data and three proposed curves for SF = 0.64 and $\epsilon_p = 0.65$, and (b) Cumulative PP RDF at various distances from the emitting particle..... 77

Figure 4.10. Particle-wall RDF for (a) $\epsilon_p = 0.65$, $\epsilon_w = 0.8$, and various bulk solid fractions, and (b) $\epsilon_p = 0.86$, $SF_{\text{bulk}} = 0.45$, and various wall emissivities. 78

Figure 4.11. Simulation domain of a heated channel in dense granular flow..... 81

Figure 4.12. (a) Total PW heat transfer over time, (b) steady state particle temperatures, and (c) steady state PW heat transfer per particle. 85

Figure 4.13. Steady state heat transfer rate from the wall, comparing results with various radiation time step sizes. 86

Figure 4.14. (a) Mean PP heat transfer per particle, and (b) mean PW heat transfer per particle, both as a function of distance from the wall. 87

Figure 5.1. The six heat transfer modes included in DPHT..... 93

Figure 5.2. (a) The three particle-particle heat transfer modes, and (b) the three particle-wall heat transfer modes (blue = fluid, red = wall). 94

Figure 5.3. Geometry of two contacting spheres used to calculate PP conduction.. 95

Figure 5.4. Dimensions relevant to Eq. (5.9) for calculating PFP conduction, showing (a) non-contacting and (b) contacting spheres. Outline of the double cone volume is shown in orange. 98

Figure 5.5. PFP conduction as a function of distance, for $k_{s_i}=k_{s_j}=2.0$, $k_f=0.0702$, $\alpha_s = 0.60$, and $R=0.0005$ m, showing (a) heat flux as a function of radial position, for various particle distances, and (b) heat transfer coefficient as a functions of particle distance (d_{ij}). 102

Figure 5.6. PFP heat transfer coefficient solved for various particle distances and temperatures (same parameters as Figure 5.5). 103

Figure 5.7. Particle-fluid-wall geometry.	105
Figure 5.8. Particle-wall HTC values found for $k_{sf}=2.0$, $\alpha_s = 0.60$, $R=0.0005$	107
Figure 5.9. Particle and wall element geometry used for applying boundary conditions.	109
Figure 5.10. DPHT file structure.	110
Figure 5.11. (a) Surface of tube with nozzle, drawn with Onshape, and (b) meshed surface using Gmsh.	117
Figure 5.12. ParaView settings for exporting the vertices.	118
Figure 5.13. ParaView settings for exporting the relations between cell IDs and vertices.	118
Figure 5.14. ParaView settings for exporting the cell centers.	119
Figure 5.15. Commands to run the DPHT code from the Julia terminal.	121
Figure 5.16. Particle temperatures at the outlet, showing (a) view from the outside, and (b) cross section view.	122
Figure 5.17. Total PW heat transfer over time, separated by heat transfer mode.	123
Figure 5.18. Simulation domain for finding k_{eff} from a DPHT simulation.	124
Figure 5.19. Results for k_{eff} calculated using the DPHT simulation, also showing the values predicted using the ZBS model for solid-fluid conduction [29] plus the radiative portion calculated with ZBS, Breitbach and Barthels [28], and the k_{rad} model from Chapter 3.	125
Figure 5.20. k_{eff} with radiation eliminated, comparing ZS and DPHT simulation results.	126
Figure 6.1. (a) Experimental setup in front of high flux solar simulator, and (b) front view of lamps.	133
Figure 6.2. Main components of the experimental setup.	133
Figure 6.3. Close-up of measurement test section.	134
Figure 6.4. Diagram of the components and flow regimes in the setup.	135
Figure 6.5. Hopper, with insulation removed to expose ends of the heating tubes.	136
Figure 6.6. Shutoff valve used to stop the particle flow.	137

Figure 6.7. (a) Hopper and test section, with holes for thermocouple probes visible, circled in red, (b) front view of test section with thermocouples installed at locations circled in red, and (c) extra insulation installed in front test section.....	138
Figure 6.8. Inlet temperature measurement block with grooves cut for thermocouples wires.	139
Figure 6.9. Paddle wheel mixing device showing (a) paddle wheel installed inside the insulation block, and (b) 9V DC motor mounted on the exterior, connected to stainless steel shaft.....	140
Figure 6.10. Top overflow channel shown (a) on full setup, and (b) close-up where it attaches to the insulation blocks.	142
Figure 6.11. Temperature data from Test 1.	145
Figure 6.12. Mass of particles accumulated over time during Test 1.....	145
Figure 6.13. Sintered bauxite particles can be seen glowing at the exit, where (a) a gradient can be seen before while mixer is off, and (b) the gradient is eliminated once mixer is turned on.....	146
Figure 6.14. Stream of sintered bauxite radiating visible red light at ~750 °C.....	147
Figure 6.15. Temperature data from Test 2.	148
Figure 6.16. Mass of particles accumulated over time during Test 2.....	148
Figure 6.17. Temperature data from Test 3.	149
Figure 6.18. Mass of particles accumulated over time during Test 3.....	150
Figure 6.19. Test section, well-insulated on three sides with ceramic insulation.	154
Figure 6.20. Top view of the hopper, where U-shaped steel rods are placed over the heating tubes to promote conduction inside the hopper and reduce temperature gradients.....	157
Figure 6.21. Three prototype passive mixing devices, none of which were found to completely mix the particle stream.	158
Figure 6.22. Paddle wheel mixing device used to achieve a uniform stream temperature.	160
Figure 6.23. Three frames of video showing the high-speed and chaotic particle flow imparted by the paddle wheel, leading to a high degree of mixing.	160

Figure 7.1. Square tube test section and orifice plate used in modeling the experimental setup.....	164
Figure 7.2. Mass accumulation over time, and equation for mass flow rate.	165
Figure 7.3. Particle group used for evaluation of k_{eff} , leading to a correction factor value of 1.28 in Eq. (7.2).....	167
Figure 7.4. K_{eff} at several temperatures, showing the ZS model, the original PFP model, and the PFP model modified with a correction factor of 1.28 in Eq. (7.2).	168
Figure 7.5. Specific heat as a function of temperature.	169
Figure 7.6. Temperature locations shown in red (a) on the front of the square tube, and (b) on all surfaces of the unfolded surface, subdivided into 16 panels.....	170
Figure 7.7. Temperature map of right half of square tube test section, found from polynomial surface fitting of eight known temperature locations.	172
Figure 7.8. Temperature boundary condition applied to inner surface of square tube.	173
Figure 7.10. Steady state particle temperatures, showing (a) entire particle stream, and (b) section view to show interior particles, and (c) close-up section view to show particles near the outlet.	175
Figure 7.11. Heat flux of test section at steady state.	176
Figure 8.1. Receiver design and 1-mm diameter particles descending between parallel plates.....	182
Figure 8.2. Secondary reflector used to further concentrate rays onto the receiver surface (image of secondary reflector supplied by Canavarro [107]).	184
Figure 8.3. Configuration of heliostat field and solar receiver (supplied by Canavarro [107]).	184
Figure 8.4. Incident radiative flux on the receiver surface.....	185
Figure 8.5. (a) Parallel plates with diamond-shaped obstruction, and (b) particles in between the 8-mm by 8-mm parallel plate strip studied.	186
Figure 8.6. Overall heat transfer from wall to particles, separated by heat transfer mode.	187

Figure 8.7. Particles at the outlet, colored by temperature.	188
Figure 8.8. Outputs from DPHT simulation analyzed to show (a) bulk temperature, and (b) overall heat transfer coefficient, both as a function of distance from the inlet.	189
Figure 8.9. One element of the metal receiver surface and the adjoining cell containing the particle-air mixture.	191
Figure 8.10. Receiver surface showing (a) external surface temperature, and (b) absorbed heat flux.	194

LIST OF ABBREVIATIONS

BB	Breitbach and Barthels model for radiative effective thermal conductivity
CentRec	Centrifugal Receiver, a solar receiver design pursued by the German Aerospace Center (DLR)
CFD	Computational Fluid Dynamics
CSP	Concentrating Solar Power
DBA	Distance Based Approximation radiation model developed in this thesis
DEM	Discrete Element Method
DLR	German Aerospace Center
DPHT	Dense Particle Heat Transfer, a DEM-based heat transfer code developed in this thesis
LRM	Long Range Model, a particle-scale radiation model
MCRT	Monte Carlo Ray Tracing
MPI	Message Passing Interface
NREL	National Renewable Energy Laboratory
PFM	Particle-Fluid-Particle, a heat conduction model
PFW	Particle-Fluid-Wall, a heat conduction model
PP	Particle-Particle
PV	Photovoltaic solar panels
PW	Particle-Wall
RDF	Radiation Distribution Factor
SF	Solid Fraction, or particle volume fraction
SLE	Special Limit of Error, a high accuracy thermocouple
SRM	Short Range Model, a particle-scale radiation model
TRL	Technology Readiness Level
ZBS	The Zehner, Bauer, and Schlünder model for effective thermal conductivity, which builds upon the original ZS model to include numerous parameters, including radiation
ZS	The continuum model for effective thermal conductivity by Zehner and Schlünder, which accounts for heat transfer in packed particle beds

CHAPTER 1

INTRODUCTION

Within the field of concentrating solar power (CSP), central receiver (“power tower”) type systems are capable of achieving high solar concentration ratios and therefore very high temperatures. A growing body of research points to the efficiency and cost benefits of switching from a liquid heat transfer fluid to using solid sand-like particles as a heat transfer medium in CSP plants [1]. Unfortunately, our understanding of the mechanics and heat transfer of granular materials lags far behind that of the closely related field of fluid mechanics. According to the authors of *Granular Materials; Fundamentals and Applications*:

Despite wide interest and more than five decades of experimental and theoretical investigations many aspects of the behavior of flowing granular materials are not well understood. At this stage, there is still no complete understanding of the constitutive relations that govern the flow of granular materials. The general field is very much in a stage of development comparable to that of fluid mechanics before the advent of the Navier-Stokes relations. [2]

The Navier-Stokes (fluid momentum) equations are fundamental to solving fluid mechanics problems both analytically and with Computational Fluid Dynamics (CFD), so this passage clearly states that there is still much to learn in this field. To help address the challenges facing CSP with solid particles, the overarching goal of this thesis is to improve the modeling capabilities regarding heat transfer in flowing groups of particles, with special focus on thermal radiation.

1.1 Background

In the past decades, CSP systems have been installed for electricity generation, where the heat collected is used to run a steam Rankine cycle. In addition to electricity generation, research and demonstration projects are currently underway for supplying heat directly to industrial processes (without converting to electricity), such as cement, metallurgy, melting of aluminum for recycling, waste treatment, and formation of liquid fuels [3].

When used for electricity production, the key advantage of CSP over other renewable energies is the low cost of integrating energy storage. By storing heated materials in large, insulated tanks, the heat can be converted to electricity as needed, providing a predictable electricity output to the power grid all 24 hours per day, or as required by the grid operator. Electricity from photovoltaic (PV) panels has become the least expensive power available in some electricity markets in recent years, but it is rarely coupled with energy storage, resulting in large amounts of curtailed electricity and even negative wholesale energy prices due to overproduction in areas of high PV deployment [4]. Thus, instead of competing with other inexpensive renewables, CSP with storage actually enables using more of them by providing the reliability and flexibility needed to smoothly operate an electricity grid with a high proportion of renewable energy. Specifically, CSP plants can store all the collected energy during the daytime when inexpensive PV electricity is available, and then thermal storage can be dispatched during the nighttime when PV electricity is not available. Electric battery storage technology has made great advances in recent years, but installations have remained small compared to CSP systems such as the NOOR III in Morocco, in operation since 2018, with ~ 1 GWh_e of storage capacity [5].

Decarbonizing the electricity sector is well under way, largely due to falling costs of solar and wind power in recent years. However, industrial processes, such as cement production, steel production, and manufacturing, are responsible for $\sim 24\%$ of the overall carbon dioxide emissions worldwide [6]. Much of the emissions from

these processes come not from electricity use, but instead come from burning fossil fuels to bring raw materials to high temperatures. Unfortunately, there are very few current solutions available to stop the use of fossil fuels in these processes. CSP can supply very high temperatures and heat fluxes, so coupling CSP with high temperature industrial processes could provide a pathway to decarbonize these industries, which is a growing area of research [3][6]. Like CSP for electricity, CSP plants which supply heat to industrial processes likely also need thermal storage, enabling them to supply a steady stream of heat at all hours of the day.

State-of-the-art central receiver systems for electricity production use molten salt as the heat transfer and storage medium, which is a mixture of sodium nitrate and potassium nitrate and is a liquid above ~ 200 °C. Numerous researchers in recent years have studied the benefits of switching from a molten salt (liquid) heat transfer and storage medium to using solid particles, such as sand or sintered bauxite, for the same role [1]. One benefit is the improvement in cycle efficiency. Molten salt chemically breaks down above ~ 600 °C, imposing a temperature limit on the entire system, whereas solid particles can work even above 1000 °C, with no chemical or phase changes. Increasing the working temperature would increase the Carnot efficiency and the actual thermal efficiency of the steam Rankine cycle typically used in these power plants. Furthermore, the power cycle could be changed to a higher temperature cycle such as supercritical CO₂ or air Brayton, which both promise a large increase in efficiency [1][7]. Another benefit is the low cost of these materials as a heat storage medium, which is important because many tons are required for a large system. Sand is widely available and very inexpensive, and sintered bauxite is produced in large quantities for the hydraulic fracturing industry, making it slightly more expensive, but still much cheaper than using molten salt to store the same quantity of heat. Lastly, molten salt changes to a solid if it drops below 200 °C, so steps must be taken to avoid this, adding to the cost and complexity of a molten salt power plant. Each of these benefits of a particle-based system decreases the price of the overall plant and therefore the energy output.

Switching from a liquid to a solid particle based CSP plant requires reengineering several components, with the heat exchange devices being the chief components under research. However, solving for heat transfer in flowing groups of solid particles can be quite complex. Unlike fluids, particles do not form a continuum, and the Eulerian or continuum equations of motion are not generally applicable. Heat transfer mechanisms in particle flows are also completely different from those of fluids, as particles transfer heat through direct contact, through the fluid gap in between particles, and through radiation. Because the field is much less developed than fluid mechanics, there are far fewer modeling capabilities available, making it more difficult to design heat exchange devices in the proposed particle-based CSP systems.

The overall goal of this thesis is to improve the modeling capabilities for heat transfer in flowing groups of particles, especially heat transfer through thermal radiation, which has been omitted from many analyses due to its complexity and its negligible effect at temperatures below ~ 400 °C. However, at the high temperatures of CSP, radiation is an important heat transfer mechanism and must be modeled to accurately predict the performance of a heat exchange device.

1.2 Preview of Research Contributions

Each chapter builds on the previous chapters, with Chapter 1 serving as the introduction. Specific contributions of this thesis beyond the current state of research include:

- Chapter 2: A Monte Carlo Ray Tracing (MCRT) code is developed to model radiation in large groups of particles. This is a useful code for others to use in their research, and it will be posted in an online repository as an open source C++ code. This MCRT code is used as a tool throughout the thesis and is required for all of the subsequent chapters.

- Chapter 3: The MCRT code is used to solve for the effective thermal conductivity using a new method which is more fundamental and physically realistic than previous methods. It also covers a wider range than the current models and is likely more accurate.
- Chapter 4: A model for calculating radiative heat transfer at the particle level is developed for use in Discrete Element Method (DEM) simulations. In this method the distance between two particles is used to estimate radiative transfer, which is shown to have a high accuracy but a very low computational cost compared to other particle-scale radiation models. This is termed the Distance Based Approximation (DBA) model in this thesis.
- Chapter 5: The DBA radiation model is implemented, along with the relevant heat conduction modes, into a new open source code for heat transfer in dense granular flows, termed Dense Particle Heat Transfer (DPHT). An example simulation is given, along with an in-depth explanation of how the code functions, so it can be easily modified to simulate devices by other researchers. Though the focus of this thesis is on radiation, several improvements to the existing heat conduction models are implemented as well.
- Chapter 6: An experimental investigation is run to study heat transfer in a dense granular flow inside a square tube heated under highly concentrated radiation. This is used both for validation of the DPHT code and for studying dense granular flows for CSP heat exchangers.
- Chapter 8: The DPHT code (from Chapter 5) is used to study a solar receiver for heating particles to 700 °C, with final results including the overall heat gain and thermal efficiency of the solar receiver. The receiver envisioned is for preheating of sandstone particles for lime calcination in the production of cement.

Though chapters are all related and build upon each other, each chapter in this thesis forms a distinct research effort. Therefore, detailed conclusions are

included within each chapter, and only broad conclusions are presented in the final chapter.

This thesis spans several fields of research, including particle-based CSP power plants, packed particle beds, DEM modeling, and experimental studies of heat transfer in particle flows. Therefore, the literature review spans several diverse fields as well, so it is divided into these sub-topics in the following sections.

1.3 CSP with Solid Particles

The main components of a CSP plant for electricity generation are shown in Figure 1.1. The sun's rays strike the heliostats (individually actuated, highly reflective mirrors) which reflect sunlight toward the top of the tower, where the solar receiver is positioned. The solar receiver receives radiation which has been concentrated several hundred times, and it transfers the energy to the heat transfer medium (solid particles in this case) which can reach temperatures of 700 to 1000 °C. The particles then descend to the well-insulated hot particle storage tank. When they are needed for electricity production, the particles are passed through the particle-fluid heat exchanger to deliver their heat to the working fluid of the power cycle, such as a steam Rankine cycle, a Brayton cycle, or a supercritical CO₂ cycle [7]. Alternatively, heat from particles can be transferred to a fluid stream such as air to be used directly in an industrial process. Particles are then stored in a "cold" particle storage tank with a temperature in the range of 400 to 600 °C until sunlight is available, when they are transported to the top of the tower to be reheated in the solar receiver. At the time of publication, there is only one fully functional power plant utilizing solid particles, a research plant at King Saud University where heat from stored particles is used to preheat the air stream in a 100 kW_e gas turbine system, to reduce fuel consumption [8].

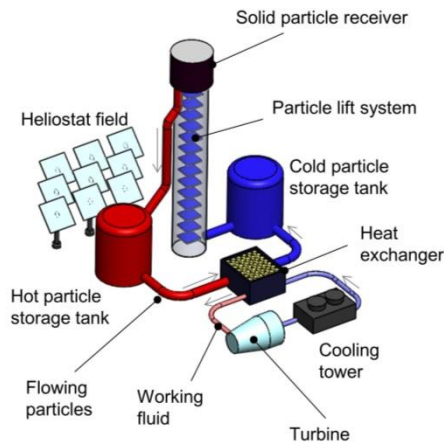


Figure 1.1. Main components of a concentrating solar power plant for electricity generation.

CSP using solid particles as a heat transfer and storage medium was first proposed in the late 1970s [9][10], but research in this field has grown in the last decade to include many national laboratories and universities worldwide. In order to switch from a liquid (molten salt) based system to a solid particle based system, the chief problems to solve are the two heat exchange devices: the solar receiver and the particle-fluid heat exchanger.

Many solar receiver designs have been proposed, with summaries of the pros and cons reviewed in literature [11], but the leading designs will be outlined here. Researchers at Sandia National Laboratory in the USA, CSIRO in Australia, and King Saud University [12][13] have focused on falling particle solar receivers, where a curtain of particles is dropped from the top of the receiver, and particles are directly irradiated through the open receiver aperture as they fall. This design has the benefit that particles are *directly* irradiated, meaning there is no receiver surface or tube wall in between the incident radiation and the particles being heated. In contrast, *indirect* designs have particles flowing through tubes or behind a wall, which may melt if the incident radiation is too strong. The falling particle receiver design is promising, though it does not offer control over the particle residence time within the receiver, so there is little control over the output temperature [14]. The original design was simply a curtain of falling particles, but due to the acceleration of particles with gravity, the curtain stops being fully

opaque after several meters of drop distance, which led researchers at CSIRO and Sandia National Laboratory to re-drop the particle curtain in multiple stages, while researchers at King Saud University introduced many small obstructions to slow the fall of the particles [13].

The centrifugal receiver (CentRec) [15][16] is developed by the German Aerospace Center (DLR). The receiver consists of a spinning drum which is open on the bottom end and tilted at 45 °C relative to vertical. Particles are inserted at the top end of the spinning drum, and they cling to the walls due to centrifugal effects, forming a particle layer ~4 diameters thick, as they descend slowly down the length of the drum in the axial direction. Concentrated sunlight enters the open bottom of the drum and strikes the particle film clinging to the walls. This design has the benefit of directly irradiating particles, like a falling particle receiver, but it also offers control over the flow rate and residence time, as increasing the rotational speed increases the particle-wall friction and therefore slows down the axial speed of the particle film.

An *indirect* approach was proposed by the National Renewable Energy Laboratory (NREL) in the USA, where radiation enters an array of hexagonal tubes, and particles filter down between them. By spreading out the absorption surface with the hexagonal tubes, it may offer an increased efficiency and reduced risk of melting the metal receiver surface [17].

In another leading solar receiver, studied by the French National Centre for Scientific Research, particles are fluidized with air and driven upward through a set of tubes [18]. Concentrated radiation strikes the outside of the tubes, and heat is transferred to the fluidized particles and air mixture on the interior, making this an indirect receiver. Research has shown high heat transfer coefficients due to the turbulence and particle velocities inside the tubes.

Another indirect design uses particles in tubes, descending with gravity in a dense granular flow, which has been studied by the author in previous work [19][20] and by others [21]. Due to relatively little mixing, the particle-wall heat transfer

coefficient in such a system is low compared to a fluidized flow. However, the benefits are that it is very simple, and the flow rate is adjustable with a valve, so the particle residence time and output temperature can be easily controlled over a wide range. This design is revisited in this thesis, in Chapter 8.

Particle-fluid heat exchangers have also been studied by numerous researchers. A “moving bed heat exchanger” has been studied by DLR, which consists of a bank of horizontal tubes, through which runs the working fluid of the power plant (such as steam), and particles flow vertically downward through the tube bank [22]. Researchers at METU have also worked on particle-fluid heat exchange, where a concept was developed to transfer heat from particles to air directly, by using the air to fluidize stored particles [23]. Flat plate heat exchanger designs have been recently tested by Sandia National Laboratory, consisting of a gravity-driven dense granular flow in between parallel plates, with supercritical CO₂ as the working fluid [24].

This is a thriving area of research where numerous devices have been proposed for both solar receivers and particle-fluid heat exchangers, and though several prominent designs exist, there is not yet a single clear design that is best for all applications. After examining the research on these devices, it is clear that some designs use diffuse or dispersed flows (such as falling or fluidized particles), while others use dense granular flows, and some exhibit both types of flow in one device.

1.4 Effective Thermal Conductivity in Particle Beds

The effective thermal conductivity (k_{eff}) of a group of particles is the thermal conductivity of the bulk material taken as if it were a continuous medium instead of a collection of individual particles. It is an important parameter for thermal design in many industries, including packed bed nuclear reactors [25], drying processes [26], and particle-based CSP [24]. Using k_{eff} is a convenient way to combine the various modes of heat transfer in the particle-fluid domain into a single thermal

conductivity value which is representative of the bulk. In the center of the domain, far from walls, heat is transferred through A) the solid contact where two particles touch, B) the fluid gap between particles, and C) radiation between particles [26], assuming a transparent fluid which does not participate in radiation. The effective thermal conductivity of each heat transfer mode can be found independently, denoted as k_{solid} , k_{fluid} , and k_{rad} respectively, and later they can be summed to find the total effective thermal conductivity, k_{eff} [27]. This thesis focuses only on the radiative portion, k_{rad} , which is the least studied component. It also focuses on randomly distributed particle groups typical of most natural and industrial systems, as opposed to an ordered packing structure studied by some previous researchers. At low temperatures, radiation has a small effect and k_{rad} is neglected in many applications, but for high temperature industries (above ~ 400 °C) k_{rad} can play an important or even dominant role in the overall heat transfer.

A variety of correlations have been proposed to express k_{rad} as a function of the particle emissivity and the solid fraction, which is the proportion of solid particle volume to the whole volume. The solid fraction is known by other names, including volume fraction, solid volume fraction, particle fraction, particle volume fraction, and packing fraction, and it sums to one with the porosity or void fraction. One method to determine k_{rad} is to adopt and analyze a representative unit cell which is assumed to be repeated throughout the domain [28]. Among the k_{eff} models, the Zehner, Bauer, and Schlünder unit cell model (commonly referred to as the “ZBS” model) [29][30][31] is perhaps the most commonly used, which is derived based on two opposing non-spherical particles with heat flux contours assumed to be parallel across the unit cell. (Note: the so-called ZBS model consists of the original model by Zehner and Schlünder from 1970 [30], which only accounts for heat transfer through the fluid gap between spheres, plus improvements by the same authors in 1972 [29] and by Bauer and Schlünder in 1978 [31]. The later studies add effects such as radiation, gas pressure, and non-spherical particles. Because the original papers are written in German, English speakers are directed to [32][33].) Although the radiative portion of the ZBS model

could be considered rudimentary compared to more recent research methods, the ZBS model has become widely used, as the portion regarding heat conduction through the fluid and solid has been extensively studied.

Another method to find k_{rad} is to first find the absorption and scattering coefficients corresponding to the Radiative Transfer Equation, and then k_{rad} can be calculated with one of several proposed equations [34]. Chen and Churchill [35] found the scattering and absorption coefficients experimentally, while others [36][37] have found these numerically. Singh and Kaviany [38] used a Monte Carlo approach but only studied simple cubic packed particle beds.

Experimental validation of k_{rad} over a wide range of parameters is challenging, and experiments have only been attempted by few researchers. To isolate k_{rad} , heat transfer experiments must be performed under vacuum conditions to eliminate any heat transfer through the fluid, and conduction through the particle-particle contacts must also be either eliminated or quantified. De Beer et al. [39] were able to separate the radiative portion of k_{eff} by using experimental data along with a calibrated numerical model for packed beds of 6-cm diameter graphite spheres. Similar experiments for packed beds with graphite spheres have been performed by Breitbach and Barthels [28], Rousseau et al. [40], and Robold [41]. Kasperek and Vortmeyer [42] eliminated particle-particle conduction by mechanically separating rows of steel spheres in place, with tests also run under vacuum conditions. Slavin et al. [43] also ran experiments with 1-mm diameter alumina spheres.

Because many industries use static, packed beds, the majority of research has been focused on this condition. When the particle bed is less than fully packed, as found in fluidized beds or some particle-fluid heat exchangers [17], static experiments would be exceptionally difficult, as particles would have to be suspended in place while experiments are run. Furthermore, only certain emissivity values have been tested due to the limited number of particle materials available for high temperature experiments, and in addition the emissivity of each material is often a function of

temperature. All of these difficulties explain why very few experimental results have been reported, covering only a limited set of parameters.

In both experimental and computational research, k_{rad} has received relatively little focus in situations where the solid fraction is less than packed. With the advancement of computational modeling techniques of multi-phase heat transfer, the less than packed condition can be studied using the Discrete Element Method (DEM). The k_{rad} results presented in this study may be especially useful when used in conjunction with DEM, either by incorporating the results directly into a DEM model or for validation of particle-scale radiation models such as the model developed in Chapter 4 [44], or those studied by Qi and Wright [45], Wu et al. [46], and Pitso [47].

With very little experimental data available, the current body of research has yet to prove definitively if one of the proposed k_{rad} models is accurate over a range of independent variables, most importantly the emissivity and solid fraction. In light of this lack of certainty, a fundamental approach is taken in this research to evaluate k_{rad} over a wide range of emissivity and solid fractions. In the method developed in this thesis, particle positions are generated using DEM in the shape of a thick spherical wall consisting of uniformly sized spheres, radiation is modeled with a 3D Monte Carlo ray tracing code, a particle-particle heat transfer simulation is run to find the steady state temperature profile of the particle group, and finally k_{rad} is found with a comparison to heat conduction in an isotropic solid of the same geometry.

Monte Carlo methods are well developed and documented in literature [48][49][50], but there has been no study which uses a Monte Carlo simulation to systematically find k_{rad} over a range of solid fractions and emissivity values for gray, diffuse, monodisperse particle beds. The Monte Carlo code written is described in detail in Chapter 2. The method developed to calculate k_{rad} is described in Chapter 3, and the results culminate in an equation for k_{rad} over the entire range of emissivity values from 0.3 to 1 and solid fractions from 0.25 to the

fully packed state of 0.64. This equation for k_{rad} is combined with the Zehner and Schlünder model [30] for k_{solid} and k_{fluid} to give an equation to calculate the full k_{eff} value.

1.5 Modeling Heat Transfer in Particle Flows

Modeling of particle flows can be separated broadly into Eulerian approaches, where the bulk of particles is modeled assuming the particles form a continuum as if they were a fluid, and Lagrangian approaches, where particles are modeled individually [51]. Eulerian approaches ignore frictional and collisional effects between particles and along walls, which dominate the motion in *granular* flows [52], making the overall flow patterns much different from fluids. The Discrete Element Method (DEM) is the leading Lagrangian approach, where each particle is modeled as a sphere, and each collision is modeled with solid mechanics, allowing for detailed calculations of normal and tangential frictional effects to be incorporated at the particle scale. The strength of DEM is that because particles are modeled at the individual particle level, it is in theory possible to accurately replicate all the physical phenomena of both particle mechanics and heat transfer [51]. In contrast, Eulerian approaches always strive to approximate particle flows as a fluid, though the physical mechanisms that govern the flow are fundamentally different. Until the last decade, the Lagrangian approach was not a viable option for modeling actual devices, as the chief drawback is the high computational burden. Even with the computation power currently on a PC workstation, simulations larger than a million particles may take weeks of computation time. However, with the continuous enhancement in computer processing speeds, this approach promises to become even more advantageous in the coming decades.

Most often, particles are surrounded by an “interstitial” fluid (such as air) which must be modeled as well, and together they comprise a two-phase system. In some circumstances the “Euler-Euler” model (also known as the “Two-Fluid” model) can be used, where the particle phase is modeled as a second fluid which is

intermixed with the actual interstitial fluid, and a solution is found using a modified version of the Navier-Stokes equations and CFD. Solutions using the Euler-Euler model have been applied to fluidized beds, as well as some dense flow problems [22]. With a Euler-Lagrange approach, the fluid is modeled by simulating the interstitial fluid with CFD, and a “coupled CFD-DEM” simulation is run by alternating between the DEM and CFD models and accounting for momentum and heat transfer between the two phases [53]. With a coupled model, both frictional effects of the particles as well as the hydrodynamic and thermal effects of the fluid are simulated, which is not possible with a DEM or CFD model alone. The leading software combination for coupled CFD-DEM simulations is the open source code LIGGGHTS for DEM modeling and OpenFOAM for CFD. The software CFDEM provides the coupling by passing heat transfer and momentum information back and forth between the solid and fluid phase models [53][54].

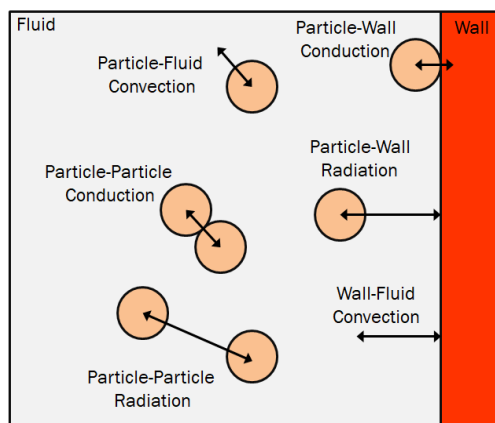


Figure 1.2. Heat transfer modes in a particle-fluid-wall domain.

Figure 1.2 shows the six relevant heat transfer modes in a generic domain consisting of particles, fluid, and a wall, where the interstitial fluid is assumed to be non-participating in radiation. The conduction and convection heat transfer modes have been studied previously, with models available in LIGGGHTS/OpenFOAM/CFDEM. However, there are currently no sub-models for particle-particle or particle-wall radiation in LIGGGHTS or commercial DEM codes, and there is relatively little analysis in literature. This is likely because it is

often neglected at the moderate temperatures of many industrial processes. In high temperature particle systems (above ~ 400 °C [55]) such as those found in CSP [56], nuclear pebble bed reactors [57], lime calcination [58][59], and biomass pyrolysis [45], particle-particle and particle-wall radiation cannot be neglected without a substantial under-prediction of heat transfer. Several previous attempts to include PP and PW radiation have been described in literature, as detailed below.

In an approach studied by Cheng and Yu [60], Wu et al. [61], and others [57][45][62][46], a “Voronoi” polyhedron is created around each particle, and the polyhedral face geometry is used to approximate radiation using what is referred to as the Short Range Model (SRM) or the Long Range Model (LRM). The SRM accounts for heat transfer only between directly contacting polyhedra, whereas the LRM accounts for heat transfer to all neighboring polyhedra [57][46]. The authors note that because the SRM neglects any radiation to polyhedra which are not in direct contact, it substantially underestimates radiative transfer, with the total view factor from one particle adding up to only 0.83 in a packed bed [46], substantially less than the theoretical value of 1. When the particle thermal conductivity is low, neglecting the conduction resistance within particles can cause an overestimation in heat transfer, and according to the authors, the SRM is accurate because these two errors may compensate for each other [57][46][63]. While this may happen to be true in some cases it is certainly not a rigorous method in all circumstances. These approaches have focused on the conditions in a packed bed where the solid fraction is ~ 0.61 , and they are generally not applicable for lower solid fractions.

In addition to the SRM and LRM, Wu et al. [46] outline several other models for consideration. The Black Model is only valid for an emissivity of 1, limiting its utility. The Uniform Radiation Model, according to the authors, is also not appropriate for modeling gray particles because it is built upon an assumption of uniform radiosity on the particle surface, which eliminates the effect of the emissivity and is therefore not physically realistic. The authors also describe a Local Radiation Model, where each particle surface is divided into many surface elements, and the radiative transfer is calculated between each element

combination. This improves upon the Uniform Radiation Model because radiosity is allowed to vary over the particle surface, but the high computational cost of calculating radiation element-by-element makes this unsuitable for simulations with thousands of particles. Finally, Wu et al. [46] derive a Particle Scale Radiation Model which uses several functions to approximate the effects of particle and wall emissivities as well as the solid fraction, though it includes many approximations and has not been validated to a great extent.

Several approaches have been described where the surrounding particles are lumped together or averaged. A model based on the “local environment temperature” of each particle has been described by Yang et al. [64] and Krause et al. [58], though this only accounts for neighboring particles within a distance of 1.5 particle diameters and suffers similar limitations to the SRM. Another approach is the Spherical Unit Nodalization model described by Pitso [47] where view factors are lumped into several concentric shells surrounding each particle. Work by Pitso also forms the basis for the Multi-sphere Unit Cell model described by Van Antwerpen et al. [25], where long range radiation (radiation between non-contacting particles) is estimated by averaging the view factors of all nearby spheres using a pre-computed distribution curve of view factors in a packed bed. These approaches offer a simple estimation of radiation, but they are tailored to packed beds and have not been developed for lower solid fractions where long range radiation becomes very important.

Several Monte Carlo approaches have also been studied. Amberger et al. [65] implemented a Monte Carlo ray tracing code directly into the DEM code LIGGGHTS [51], which could be very accurate if enough rays are traced, but the Monte Carlo method carries a very high computational cost making it unsuitable for large simulations. Liu et al. [66] used a Monte Carlo approach to solve for radiation distribution factors in randomly and regularly packed domains, but only PP radiation was studied at very low solid fractions, and results were not applied in the DEM context. Radiation in beds of packed, black particles have been studied in

previous work by the current author [67], and similar conditions have been studied by Malinouski and Rabinovich [68].

Given the shortcomings of the previously proposed models, a method to solve for radiation in large particle systems with acceptable accuracy and low computational cost is still sought [63]. For situations with static beds, low computation time is desired but not critical because the necessary view factors must only be calculated once. In contrast, for dynamic simulations such as particles flowing through concentrating solar power receivers or lime kilns, radiation must be recalculated continuously throughout a simulation, making a computationally efficient model for radiation an absolute requirement. In Chapter 4, a radiation model that can be implemented in DEM or CFD-DEM codes is developed to address these shortcomings. The central challenge is to calculate radiation at the particle scale in systems containing hundreds of thousands of particles, while adding a minimal amount of computational time to the already high computational burden of DEM and CFD-DEM.

1.6 Experimental Studies of Dense Particle Flows

Very few experimental studies exist for heated dense granular flows, especially at the high temperatures relevant to CSP devices where radiation plays a prominent role in the overall heat transfer. Natarajan and Hunt [69] studied heat transfer to glass spheres between heated, vertically-oriented parallel plates. Their experiments showed the heat transfer coefficient increases significantly with flow rate until a peak is reached around 12 cm s^{-1} and then falls off slightly at higher flow rates. They attributed this peak to two opposing factors. Increasing the flow rate increases the particle motion and mixing and therefore heat transport, but at higher velocities the low-conductivity air gap along the wall increases in thickness, reducing heat transfer. The second important conclusion drawn by Natarajan and Hunt is that inclined chutes heated on the bottom face (as opposed to vertical chutes) have higher heat transfer, and their peak heat transfer occurs at much higher velocities.

This is attributed to gravity forcing particles towards the wall and reducing the air gap between wall and particles. Similar work was undertaken by Sullivan [70]. In both studies the heated section is short, so flows did not become thermally fully developed. Furthermore, they are not directly applicable to the radiation modeling developed because they are performed at low temperatures where heat transfer via radiation is likely negligible. Still, understanding interplay between the bulk velocity, the near-wall air gap, and inclination angle is useful for envisioning the particle receiver in Chapter 8. Watkins [21] gives perhaps the only applicable experimental results for dense granular flows of sand-like materials at high temperatures, where zirconia-silica particles flow downward with gravity through an electrically heated Inconel tube, reaching temperatures around 1000 °C.

CHAPTER 2

AN OPEN SOURCE MONTE CARLO CODE FOR THERMAL RADIATION IN GROUPS OF PARTICLES

Some of the content in this chapter has already been published by the author:

E. Johnson, İ. Tari, D. Baker, A Monte Carlo method to solve for radiative effective thermal conductivity for particle beds of various solid fractions and emissivities, *Journal of Quantitative and Spectroscopic Radiative Transfer*. 250 (2020). doi:<https://doi.org/10.1016/j.jqsrt.2020.107014>.

All of the work that follows in this thesis builds upon the Monte Carlo Ray Tracing (MCRT) code presented in this chapter. The code is used to solve for thermal radiation in beds of particles and to the walls, which is used in Chapter 3 to find the effective thermal conductivity of particle beds and again in Chapter 4 to develop a particle-scale radiation model which can be implemented into DEM. This code will be placed on the GitHub repository to make it available for others to use and modify (<https://github.com/ef-johnson/Ray-Tracing-Many-Spheres>).

A 3D MCRT code is needed to simulate the radiative transfer in beds of thousands to hundreds-of-thousands of spheres. While MCRT codes have been well-studied in general [48][49], no open source code was found for this specific application. The code developed has several notable attributes:

- A) The code works seamlessly with DEM by reading the xyz particle positions from the output files, allowing ray tracing to be done for realistic groups of particles, as opposed to ordered packing structures like Kaviany [38] or less physically realistic methods for placing particles randomly in the domain [71].

- B) It is written in C++ using parallel “message passing interface” (MPI) programming, allowing for simultaneous computations on many cores of a workstation or cluster. Speedup is nearly linear with the number of processors.
- C) The particles which emit photons (rays) are specified by the user with an input text file, allowing a user to specify a certain particle or group of particles, from which photons will be emitted.
- D) Reflections and absorptions are modeled, leading to the Radiation Distribution Factor (RDF), which allows for a simpler and more accurate calculation of heat transfer compared to approaches using the more typical radiative view factor.

The Ubuntu (Linux) operating system is recommended to run the MCRT code, as LIGGGHTS is typically run in this operating system as well. The code is written in C++. OpenMPI must be installed to enable parallel processing, which most users will already have installed as it is a prerequisite for LIGGGHTS as well. For ray tracing in systems of tens to hundreds of thousands of particles, running simulations in parallel is a necessity; for the simulations of 50,000 particles run in Chapter 4, parallel computing reduced run time from months to several days.

2.1 Model Details

The MCRT code was developed under the assumptions of monodisperse (uniform-diameter) spheres, no light transmission through spheres, and a non-participating fluid phase. All reflections and emissions are modeled as gray and diffuse, implying that emissivity and absorptivity are equal according to Kirchhoff’s law [72]. The particle absorptivity is chosen by the user at the beginning of the simulation. The goal of the MCRT code is to simulate the rays or photons emitted from each sphere by following the photon path through any reflections until it is absorbed by a neighboring sphere. Often, the goal of ray tracing is to find the radiative view factor from one surface to another, which is the fraction of photons

emitted from one surface that strike a second surface [72]. However, in this study the output of the MCRT code is the radiation distribution factor (RDF), the portion of photons emitted from one particle which are eventually *absorbed* by the second particle after any number of reflections off neighboring particles [48][50]. This has also been termed the exchange factor [49], but because that exact term is already used Chapter 3 to mean something unrelated, the term RDF will be adopted here to reduce confusion.

The Monte Carlo code is initiated by identifying the “emitting” particles (the particles from which photons will be released) from a user-input text file. These are also referred to as “home” particles in the code. For each of the emitting particles, the ray tracing is started by finding a random emission location on the surface of the emitting particle, represented by the red dot in Figure 2.1(a). This requires determining an elevation angle (ϑ) where $0 \leq \vartheta \leq \pi$, and the azimuth angle (Θ) where $0 \leq \Theta < 2\pi$. These are found by drawing random numbers (R_ϑ and R_Θ) between 0 and 1 along with the probability density functions for ϑ and Θ in Equations (2.1) and (2.2) [73], which give a uniform distribution of emission locations on the sphere surface. Next, the emission direction (Figure 2.1 (b)), with respect to the temporary $x'y'z'$ axes, is chosen using the probability density functions in Equations (2.3) and (2.4), which are applicable under the gray, diffuse emission assumption [74] and give a uniform distribution of photon directions in the outward facing hemisphere from the emission location. In this case the emission direction is defined by the elevation angle γ , where $0 \leq \gamma \leq \frac{\pi}{2}$, and the azimuth angle β , where $0 \leq \beta < 2\pi$. With the emission direction determined, an arbitrary length is assumed to form a vector within the $x'y'z'$ axes ($\overline{V_{ray}}$). In Figure 2.1(c), an Euler transformation is applied to find the vector $\overline{V_{ray}}$ with respect to the XYZ axes, which are aligned to the original xyz axes but with the origin at the emission location.

$$\vartheta = \cos^{-1}(2 R_\vartheta - 1) \quad (2.1)$$

$$\theta = 2\pi R_\theta \quad (2.2)$$

$$\gamma = \sin^{-1}\left(\sqrt{R_\gamma}\right) \quad (2.3)$$

$$\beta = 2\pi R_\beta \quad (2.4)$$

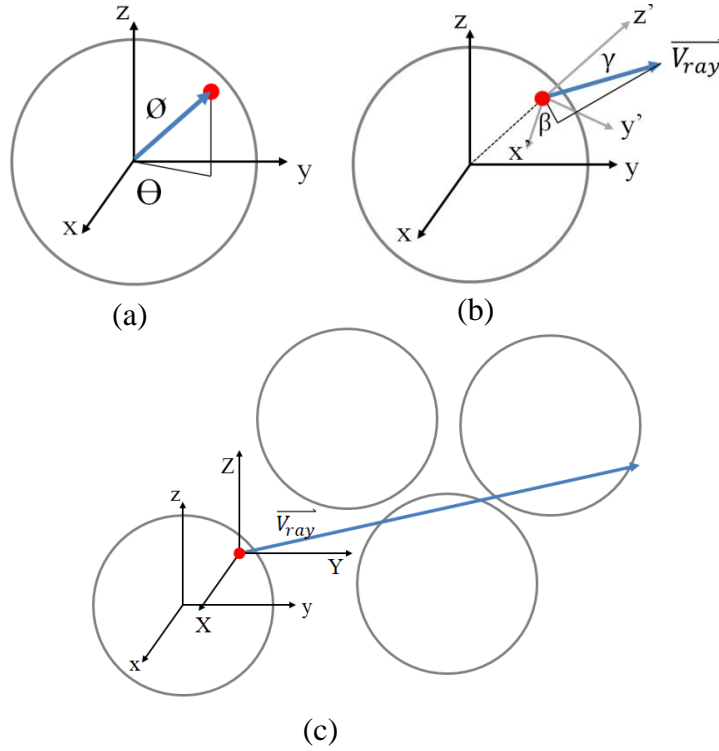


Figure 2.1. (a) Sphere with random photon emission location, (b) random emission direction in temporary axes, and (c) emission direction vector passing through several neighboring spheres, in XYZ axes.

Using vector algebra, all other spheres are checked to see if the vector \vec{V}_{ray} would pass through their surface. The closest sphere to be hit is chosen as the true incident sphere, and the actual incident location is calculated. The photon can then either be reflected or absorbed, since no transmission through the particles is assumed. Whether the photon is absorbed or reflected is determined by choosing a random number, R_α , between 0 and 1. If $R_\alpha > \alpha$, where α is the surface absorptivity, the photon is reflected and the path continues; the location of the reflection is fixed, but because reflections are assumed to be diffuse, a random reflection direction is

found by generating new γ and β angles. The definition of the photon path is continued in this way until the photon strikes a sphere and a random number $R_\alpha < \alpha$ is found, representing the photon finally being absorbed. After simulating many photons emitted from one sphere, the number of photons absorbed by each neighboring sphere is divided by the total number of photons emitted, which results in the RDF between the emitting sphere and each other sphere. Next, this process is repeated by starting with a new emitting sphere until all emitting spheres have been simulated.

If all of the spheres in the domain are specified as emitting spheres (as done in Chapter 2), the output of the MCRT simulation is a square matrix containing the RDF from each sphere to every other sphere in the domain. If the Monte Carlo simulation were perfectly accurate in predicting RDFs, the matrix would be symmetrical. The diagonals of the matrix, representing the RDF of a particle to itself, are generally *not* zero due to photons reflected back on to the original emitting particle.

2.2 Validation

Several validation steps have been performed to ensure the MCRT code produces accurate and reliable results, which are detailed in the following subsections.

2.2.1 Two Touching Spheres

For the simplest validation configuration, the MCRT code was used to calculate the view factor between two touching spheres. An analytical solution is available [75], computed by Feng and Han [76] to be 0.0755868. The MCRT simulation was run with an increasing number of photons, and as shown in Figure 2.2, the ray tracing code matches the analytical solution to a high degree when $\sim 10^5$ or more photons are used. The output of the MCRT code in general is the RDF, so in this case the

absorptivity was set to 1 to make the output the same as the more common radiative view factor.

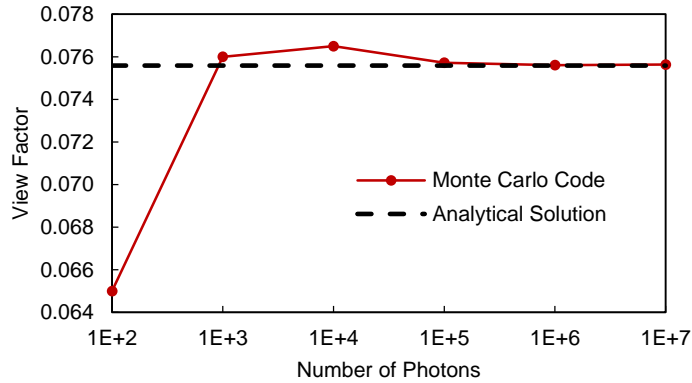


Figure 2.2. View factors calculated with various numbers of photons emitted per particle, for two touching spheres.

2.2.2 Two Separated Spheres

Next, the configuration was studied where the spheres are spaced at various distances apart. Results match closely with Feng and Han [76] as shown in Table 2.1, who found the view factors by evaluating the integral equation from Tanaka [75]. In this case, the number of photons traced by the MCRT code was very high, 10^7 , to maximize accuracy.

Table 2.1. View factor validation between two spheres separated by various distances.

Center-Center Distance (radii)	View Factor, Monte Carlo, Present Study	View Factor, Feng and Han [76]	Difference
2.00	0.07578	0.07559	0.25%
2.01	0.07450	0.07455	-0.06%
2.05	0.07073	0.07074	0.00%
2.10	0.06641	0.06650	-0.14%
2.50	0.04422	0.04412	0.23%
3.00	0.02956	0.02959	-0.09%
5.00	0.01020	0.01021	-0.10%
10.00	0.00251	0.00251	-0.04%

2.2.3 Randomly Packed 50-Sphere Domain

The CFD software package Fluent was used for validation of view factors and heat transfer in a 50-sphere domain. While this small-scale validation is possible in Fluent, both the manual effort to load spheres with specific positions as well as actual code run time make the simulation process extremely time-intensive, even for a domain of only 50 spheres. Simulating a domain of 10,000 particles in Fluent is certainly not feasible, whereas the Monte Carlo and subsequent particle-particle heat transfer simulations can be run with over 10,000 particles with minimal manual effort and manageable code execution times.

For the randomly packed 50-sphere domain, shown in Figure 2.3(a), Fluent was used to find the view factors between the central particle and all surrounding particles using the Surface-to-Surface Ray Tracing model. The particles, with radius 3 cm, were meshed and refined until decreasing the mesh size did not change the resulting view factors, and modeling proceeded with a mesh sizing parameter of 0.002 m. This is a rigorous test of the Monte Carlo code because the spheres experience a high degree of shading. A very good agreement is still shown for each sphere in Figure 2.3(b), demonstrating the high accuracy of the MCRT code developed in this research. Because Fluent only calculates view factors, not RDFs, the absorptivity was set to 1 in the MCRT code, as the RDF and view factor are identical when no photons are reflected.

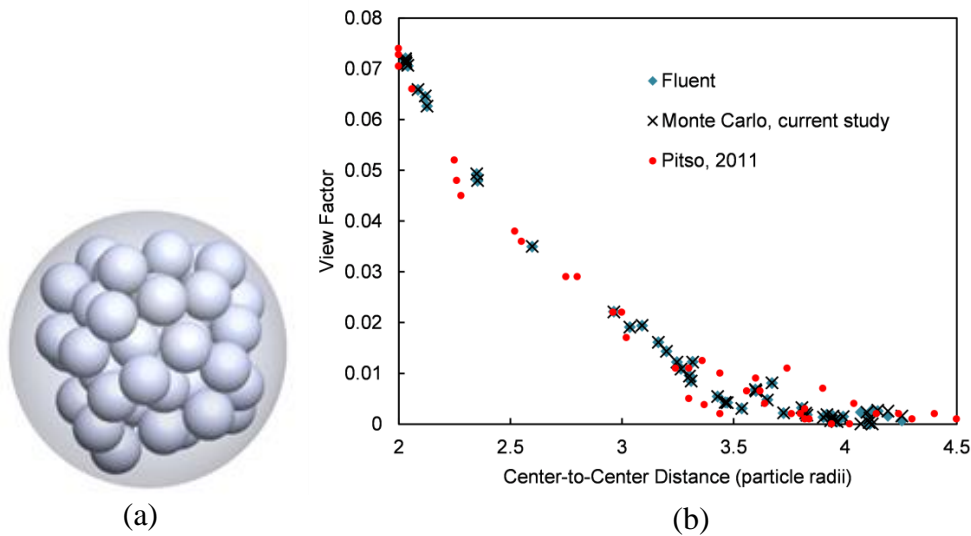


Figure 2.3. (a) The 50-sphere domain and surrounding sphere used for Fluent validation, (b) view factors between the central sphere and all neighboring spheres.

Data from Pitso [47] is overlaid in Figure 2.3(b) as well, where view factors between a central sphere and all neighboring spheres were computed using the CFD software Star-CCM+ for a packed bed. The particle positions used by Pitso are different from those generated in the current research for this verification, but because each domain is a randomly packed bed with roughly the same solid fraction, the relationship between distance and view factor shows a high level of agreement.

The abovementioned simulations prove the validity of MCRT code to find view factors, but because Fluent (as well as most other CFD codes) calculate view factors instead RDFs, a direct validation of RDFs cannot be made for the case of absorptivity less than 1. To address this, the RDFs must be combined with a heat transfer simulation, and validation can be done by comparing temperature and heat flux results. If these values match those found by Fluent, then the RDFs used must have been correct. Since this type of validation requires using both the MCRT and a particle-particle heat transfer simulation, this validation is left for Section 3.2.

2.2.4 Particle-Wall Validation

A validation for the PW calculations was performed in Fluent on the geometry shown in Figure 2.4, consisting of three 0.02 m diameter particles contained inside a bounding box, with properties listed in Table 2.2. The MCRT code is equipped to handle only a single wall, so the bottom wall is given an emissivity (and absorptivity) of 0.5, while all other walls are considered black surroundings. The random particle positions and emissivities less than 1 mean there will be a high number of photons reflected between the wall and all three particles, providing an adequately challenging test case for the MCRT code.

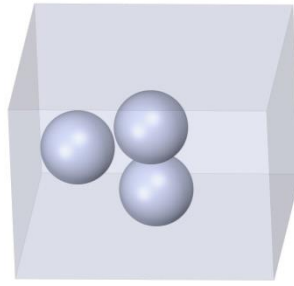


Figure 2.4. The 3-sphere domain and walls used for PW validation against a Fluent Surface-to-Surface radiation simulation.

Table 2.2 Input parameters for PW validation of MCRT code.

Surface	x	y	z	Temperature (K)	Emissivity
Sphere 1	0	0	0.011	700	0.7
Sphere 2	0	0.006	0.032	800	0.7
Sphere 3	0.019	0.015	0.030	900	0.7
Bottom wall (z=0)	-	-	-	600	0.5
Black surroundings (other walls)	-	-	-	500	1.0

After running the MCRT code, the RDF from each particle to all other surfaces is known, and the heat transfer between the particles and walls is calculated with $q_{ij} = \varepsilon_p A_p \sigma (T_i^4 - T_j^4) \times RDF$, where q_{ij} is the heat transfer, ε_p is the particle emissivity, A_p is the particle surface area, and σ is the Stefan-Boltzmann constant (more details on this equation are given in Section 3.1.3). The total heat transfer

leaving each particle is found so that the results can be compared with results from Fluent.

The exact same geometry was modeled in Fluent, with a mesh element size of 0.00001 m and radiation simulated with the Surface-to-Surface model. Heat transfer rates from the spheres are compared in Table 2.3, with nearly identical results shown between Fluent and the MCRT code. With this validation method, the RDFs (or view factors) are not compared directly, but they must be correct to arrive at the same heat transfer values as found by Fluent.

Table 2.3. Total heat transfer calculated with Fluent and MCRT code.

Surface	Heat Transfer (W) Fluent	Heat Transfer (W) MCRT	Difference
Sphere 1	6.333	6.340	0.11%
Sphere 2	14.973	15.016	0.28%
Sphere 3	27.964	28.022	0.21%

2.3 File Structure

The file structure used by the MCRT code is shown in Figure 2.5.

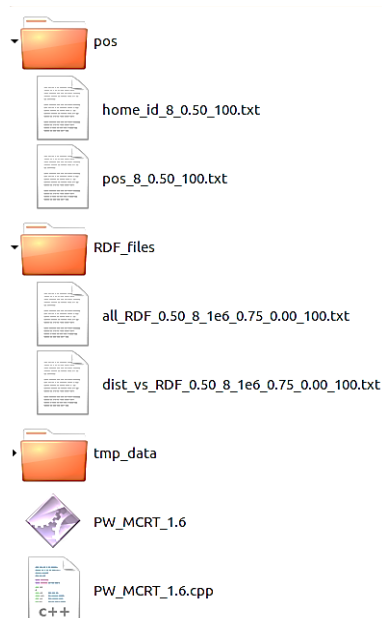


Figure 2.5. File structure of the MCRT code.

- In the *pos* folder there must be two files:
 1. *pos_[number of particles]_[solid fraction]_[LIGGGHTS time step number].txt*: this file contains the xyz position of the center of each particle, one particle per line, in a space delimited format.
 2. *home_id_[number of particles]_[solid fraction]_[LIGGGHTS time step number].txt*: this file contains a list of 0's and 1's, with one value for each particle. A 1 indicates the particle will be an “emitting” particle (“home” particle), and 0 indicates the particle will not.
- The *RDF_files* folder begins empty, and it is filled with the output files at the end of the simulation.
- The *tmp_data* folder begins empty, and it is used to temporarily store the data output from each processor, before the end of the simulation when data is gathered and consolidated into a single output file in the *RDF_files* folder. The contents can be deleted routinely.
- The text file containing the source code, such as *PW_MCRT_1.6.cpp*.
- The compiled executable, *PW_MCRT_1.6*, is present after the source code has been compiled.

2.4 Particle-Particle RDF Example

This example shows how the RDFs are calculated for the 8-particle domain shown in Figure 2.6, with the geometry defined by the particle center coordinates found in the file *pos_8_0.50_100.txt*. In the file *home_id*, there are eight rows containing a 1, so each of the particles is designated as an emitting particle (“home” particle). The *home_id* file in this case was simple to make manually, but for simulations with thousands of particles, it is recommended to create this file with Matlab or a similar program, as this gives the user full flexibility over which will be designated as home particles. For example, by reading in the particle position file, the particles in a certain region can be designated (e.g. all particles with $-0.1 < x < 0.1$), or as

done in Chapter 4, the home particles are designated as a random subset of the particles in a specified region.

From the file names, it can be seen that there are 8 particles, a solid fraction of 0.50, and a LIGGGHTS time step ID of 100. When naming the files this simple example, the solid fraction is not actually calculated, so a value of 0.50 is chosen arbitrarily. Likewise, the particle domain was created manually, so the LIGGGHTS time step is simply assigned a value of 100. These parameters are only used in the naming of the input and output files, but when working with many different LIGGGHTS time steps and solid fraction files, maintaining these naming conventions is essential to keep the inputs and outputs organized. In contrast, the number of particles in the file name *must* match the actual number of particles to be simulated.

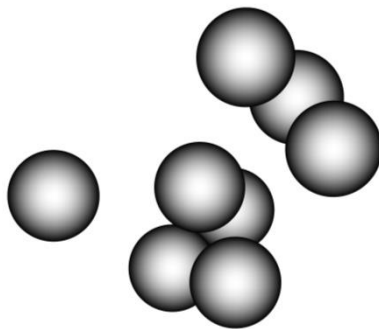


Figure 2.6. Eight-particle simulation domain.

To compile the code, a terminal window is opened in the main folder, and the command is issued: `mpicxx -std=c++11 PW_MCRT_1.6.cpp -o PW_MCRT_1.6`, which compiles the code in the text file `PW_MCRT_1.6.cpp` into the executable, called `PW_MCRT_1.6`. Next, the simulation is started either in serial with the command `./PW_MCRT_1.6`, or in parallel with `mpirun -np 4 PW_MCRT_1.6`, where 4 is the number of processors specified. As shown in Figure 2.7, the program asks for simulation parameters, including the number of photons, the volume fraction (solid fraction), the absorptivity (emissivity), the particle radius, and the

outputs desired. It then asks if the wall should be modeled, which will be covered in the next section.

```

evanj@evanj-ThinkPad-Edge-E431: ~/Documents/Particle_Modeling/MCRT/MCRT_example
evanj@evanj-ThinkPad-Edge-E431:~/Documents/Particle_Modeling/MCRT/MCRT_example$ mpicxx -std=c++11 PW_MCRT_1.6.cpp -o PW_MCRT_1.6
evanj@evanj-ThinkPad-Edge-E431:~/Documents/Particle_Modeling/MCRT/MCRT_example$ mpirun -np 4 PW_MCRT_1.6

Welcome to the Monte-Carlo code for finding Radiation Distribution Factors and Radiative Transfer within a particle bed.
Enter information - n_particles and vol_frac must match the pos file!

Enter number of photons in scientific notation (ex: 1e5): 1e6
Enter nominal volume fraction (must be in format 0.XX): 0.50
Enter number of particles: 8
Enter absorptivity of the particles (format 0.XX): 0.75
Enter LIGGGHTS timestep number (format XXXXX): 100
Enter radius of the particles (meters): .01
Do you want to export the matrix of distance vs. RDF? (Y/N): Y
Do you want to export square matrix of all RDF's? (Y/N): Y
Would you like to model the wall at Z=0? (Y/N): N
----- Processor: 1 -----
n photons: 1e6, vol_frac: 0.50, n_particles: 8, abs: 0.750000
File names:
pos/pos_8_0.50_100.txt
tmp_data/dist_vs_RDF_0.50_8_1e6_0.75_0.00_100_proc1.txt
tmp_data/all_RDF_0.50_8_1e6_0.75_0.00_100_proc1.txt
RDF_files/dist_vs_RDF_0.50_8_1e6_0.75_0.00_100.txt
RDF_files/all_RDF_0.50_8_1e6_0.75_0.00_100.txt
----- Processor: 2 -----
n photons: 1e6, vol_frac: 0.50, n_particles: 8, abs: 0.750000
File names:

```

Figure 2.7. Parameters input to initiate MRCT code.

After the run, two output files appear in folder *RDF_files*. The *all_RDF* output style is necessary when the RDF from every particle to every other particle in the domain is needed, such as when finding the effective thermal conductivity in Chapter 3. In contrast, the *dist_vs_RDF* output style is more convenient when building the distance vs. RDF curves in Chapter 4. The output files are:

- 1) *all_RDF_0.50_8_1e6_0.75_0.00_100.txt*: This file contains a square matrix of RDFs from each particle to each other particle. The naming convention is (in order) solid fraction, number of particles, number of photons, particle absorptivity, wall absorptivity, and LIGGGHTS time step number. In this case the wall emissivity is zero since the wall is not modeled. For the eight-particle system the *all_RDF* file is shown in Table 2.4, where headers are added for clarity. As expected, the matrix is symmetric, with small differences due to the inherent errors in the MCRT which diminish with increasing numbers of photons. There is one extra column for the wall, which is not modeled, so it is simply left as a column of zeros.

Table 2.4 Data in the *all_RDF* output file, showing the RDF from each particle to each other particle.

Particle i	Particle j								Wall
	1	2	3	4	5	6	7	8	
1	0.011975	0.060233	0.045472	0.021374	0.014346	0.007688	0.00539	0.008687	0
2	0.059895	0.014824	0.044933	0.045351	0.002983	0.000937	0.000166	0.018380	0
3	0.045612	0.045622	0.011462	0.036811	0.015029	0.022761	0.013724	0.020551	0
4	0.020964	0.044701	0.036431	0.006866	0.007684	0.009880	0.002730	0.007548	0
5	0.014388	0.002772	0.015116	0.008005	0.001919	0.165793	0.011853	0.002311	0
6	0.007697	0.000999	0.022712	0.009745	0.165081	0.005542	0.089800	0.004596	0
7	0.005349	0.000151	0.013608	0.002727	0.011647	0.089601	0.004403	0.006626	0
8	0.008798	0.018454	0.020660	0.007444	0.002173	0.004470	0.006838	0.001280	0

2) *dist_vs_RDF_0.50_8_1e6_0.75_0.00_100.txt*: This file contains columns for the emitting particle ID, the absorbing particle ID, the distance between the particle centers, and the RDF between the two (Table 2.5). The first line shows both emitting and receiving IDs are 0, a PP distance of 0.0000, and an RDF of 0.011975. This indicates that 1.1975% of the photons emitted from the surface of particle 0 were reflected back and absorbed by the same particle. RDFs from particle 0 to the others are shown in the next seven lines. A receiving ID of -1 indicates the wall, which in this case is not modeled so it is left as zero.

Table 2.5 The *dist_vs_RDF* output file, with table truncated to 12 rows.

Emitting ID	Absorbing ID	Distance (m)	RDF
0	0	0.000000	0.011975
0	1	0.020000	0.060233
0	2	0.0223607	0.045472
0	3	0.030000	0.021374
0	4	0.0374166	0.014346
0	5	0.0424264	0.007688
0	6	0.0512348	0.005390
0	7	0.0438748	0.008687
0	-1	0.010000	0.000000
1	0	0.020000	0.059895
1	1	0.000000	0.014824
1	2	0.0223607	0.044933

(table continues with more rows)

2.5 Particle-Wall RDF Example

The same particle positions are used, but this time a wall on the $z = 0$ plane is modeled, which extends over $-0.05 < x < 0.05$ and $-0.05 < y < 0.05$, as shown in Figure 2.8. In the MCRT code, the wall *must* be on the $z = 0$ plane. Photons are

still only released from particles, never from the wall. With the same *pos* and *home_id* files, the code is started again as shown in Figure 2.9, but this time the wall is chosen to be modeled, and the xy wall bounds and absorptivity are entered.

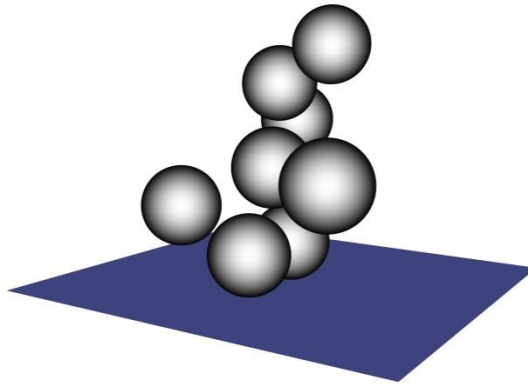


Figure 2.8. Particle and wall positions used in the example simulation.

```

evanj@evanj-ThinkPad-Edge-E431:~/Documents/Particle_Modeling/MCRT/MCRT_example
evanj@evanj-ThinkPad-Edge-E431:~/Documents/Particle_Modeling/MCRT/MCRT_example$ mpirun -np 4 PW_MCRT_1.6
Welcome to the Monte-Carlo code for finding Radiation Distribution Factors and Radiative Transfer within a particle bed.
Enter information - n_particles and vol_frac must match the pos file!

Enter number of photons in scientific notation (ex: 1e5): 1e6
Enter nominal volume fraction (must be in format 0.XX): 0.50
Enter number of particles: 8
Enter absorptivity of the particles (format 0.XX): 0.75
Enter LIGGGHTS timestep number (format XXXXXX): 100
Enter radius of the particles (meters): 0.01
Do you want to export the matrix of distance vs. RDF? (Y/N): Y
Do you want to export square matrix of all RDF's? (Y/N): Y
Would you like to model the wall at Z=0? (Y/N): Y
Enter absorptivity of the wall (format 0.XX): 0.85
Enter min x value of wall. (Photons hitting Z=0 wall outside of this will be ignored): -.05
Enter max x value of wall. (Photons hitting Z=0 wall outside of this will be ignored): .05
Enter min y value of wall. (Photons hitting Z=0 wall outside of this will be ignored): -.05
Enter max y value of wall. (Photons hitting Z=0 wall outside of this will be ignored): .05

Check that the values were read in correctly and file names are right:
----- Processor: 1 -----
n photons: 1e6, vol_frac: 0.50, n_particles: 8, abs: 0.750000

```

Figure 2.9. Parameters for the particle-wall simulation.

In addition to the *dist_vs_RDF* and *all_RDF* output files, another file is automatically generated for a PW simulation, the *PW_RDF* file (Table 2.6) with three columns: the emitting particle ID, the PW distance, and the PW RDF. This is especially useful for finding correlations for PW RDF as a function of distance, as done in Chapter 4. The same data are available in the *dist_vs_RDF* file, but it is in a much more concise form in the *PW_RDF* file.

Table 2.6 Data output in the *PW_RDF* file.

Emitting ID	PW Distance (m)	PW RDF
0	0.01	0.348029
1	0.01	0.334898
2	0.03	0.120732
3	0.02	0.216053
4	0.04	0.139871
5	0.05	0.058603
6	0.06	0.063357
7	0.03	0.150329

2.6 MCRT Conclusion

In this chapter, a MCRT code was developed which is built to be used directly after modeling the particle positions with a DEM code such as LIGGGHTS. The output files give the RDF values either as a square matrix or alongside the distance between the particle-particle or particle-wall pair. It can be used to easily find the RDF (or view factor, if absorptivity is set to 1) between spheres numbering in the hundreds of thousands. This code can be used by others to simulate radiative heat transfer in static beds of small, conductive particles (see the uniform particle temperature assumption in Section 3.1), and it can be used to develop or validate particle-scale radiation models such as those used in DEM simulations.

CHAPTER 3

EFFECTIVE THERMAL CONDUCTIVITY DUE TO RADIATION

Some of the content in this chapter has already been published by the author:

E. Johnson, Í. Tari, D. Baker, A Monte Carlo method to solve for radiative effective thermal conductivity for particle beds of various solid fractions and emissivities, *Journal of Quantitative and Spectroscopic Radiative Transfer*. 250 (2020). doi:<https://doi.org/10.1016/j.jqsrt.2020.107014>.

An accurate model to estimate the effective thermal conductivity (k_{eff}) of groups of particles is vital for simulating particle-based CSP devices, such as the parallel plate heat exchangers developed by Sandia National Laboratory [24] and the in dense flow through tubes [21]. It is also used in other industries using static beds, such as nuclear pebble bed reactors [25] and laser sintering [71]. The radiation component (k_{rad}) is the least studied component of the overall k_{eff} , but it is responsible for a significant portion of the overall heat transfer at the high temperatures of CSP. A method is developed to find k_{rad} over a wider range of parameters (solid fraction and emissivity) than previous models, and given the fundamental approach used, results should have a higher accuracy.

The resulting k_{rad} model can be combined with the other modes of heat transfer to find the total k_{eff} , or it can be used on its own to validate particle-scale radiation models, such as the Distance Based Approximation model (developed in Chapter 4) or the previously proposed models described in Section 1.5. In fact, the k_{rad} model was developed exactly for this reason; any valid particle-scale radiation model implemented in DEM must match the continuum k_{rad} model in predicting overall heat transfer through the bulk, yet there are currently no models for k_{rad} covering a wide range of solid fraction and emissivity.

Unlike most previous studies, the method does not rely on the assumption of a unit cell or absorption and scattering coefficients to derive k_{rad} . In this method, a realistic group of particles is generated by DEM modeling, and radiation between particles is modeled with the MCRT code, leading to a calculation of k_{rad} and the dimensionless Exchange Factor (F_E). The key result is a model for F_E over the entire range of emissivities from 0.3 to 1 and solid fractions from 0.25 to the fully packed state of 0.64. F_E results are compared to previous models, with agreement shown in some cases but a large disagreement found for low solid fractions. The k_{rad} results are combined with the Zehner and Schlünder model [30] for solid and fluid conduction, providing an equation for the total k_{eff} .

3.1 Method for finding k_{rad}

There are several important assumptions regarding the applicability of the following method. Particles are assumed to be uniform in temperature, which is a valid assumption under two circumstances. First, when particles are small and conductive, the resistance to heat flow due to solid conduction *within* the particle becomes negligible, so there is essentially no temperature gradient across the particle. This is the case when the dimensionless solid conductivity (Λ) is greater than 10, where $\Lambda = \frac{\lambda_s}{4d_p\sigma T^3}$, and λ_s is the thermal conductivity of the solid material in $\text{W m}^{-1} \text{K}^{-1}$, d_p is the particle diameter in meters, σ is the Stefan-Boltzmann constant of $5.67 \times 10^{-8} \text{ W m}^{-2} \text{ K}^{-4}$, and T is the absolute temperature in Kelvin or Rankine [77]. The second case where the uniform particle temperature assumption is valid is in dynamic DEM simulations where particles are continuously and quickly colliding and rotating. In this case a significant temperature gradient does not form across each particle, even if Λ is low, because the particles rotate before a significant temperature gradient can develop. Thus, the model presented is well suited for static beds of small metallic particles or for integration into dynamic DEM simulations. However, the model in its current state is not well suited for other applications such as static pebble bed reactors [40] because the relatively

large (~6 cm diameter) graphite spheres have a low thermal conductivity and are known to exhibit a temperature gradient across each particle.

Similar to previous Monte Carlo studies of particle beds [34][78][36], the modeling in this study relies on geometric optics where diffraction and near-field effects are neglected, which is a valid assumption for particles greater than 75 μm [36][79], and therefore the results are not applicable for smaller particles. Additionally, the k_{rad} correlations presented here, as with most other published correlations, are only valid for the bulk region, as the packing structure changes near the walls [26]. Finally, this study assumes gray and diffuse reflecting spheres of equal radius.

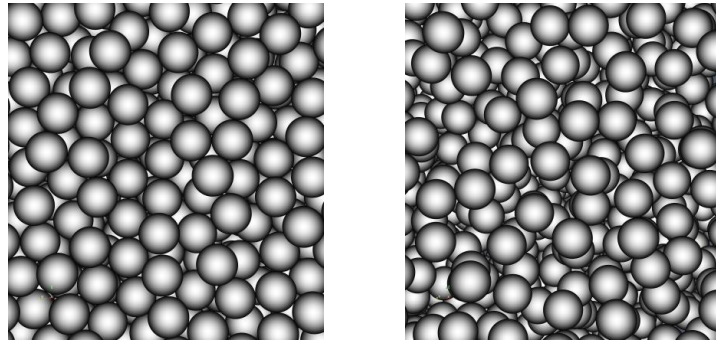
The uniform particle temperature assumption is valid for the case of sintered bauxite particles used in particle-based CSP systems: with a solid conductivity of $\sim 2 \text{ W m}^{-1} \text{ K}^{-1}$, a particle diameter of $\sim 300 \mu\text{m}$, and temperatures in the range of 500 to 1000 $^{\circ}\text{C}$, Λ is much greater than 10, and the diameter is larger than 75 μm , so it meets both criteria.

The method developed in this chapter follows the sequence detailed in the sections below. First, a domain of particles is generated using the DEM. Second, a Monte Carlo ray tracing simulation is used to solve for the Radiation Distribution Factor (RDF) between each particle and every other particle. Third, a heat transfer simulation is run where the center of a spherical group of particles is heated and the outside is cooled. Fourth, the resulting steady state temperature profile is plotted and fitted with an applicable curve, leading to a calculation of k_{rad} . Finally, k_{rad} is used to find the dimensionless Exchange Factor (F_E), which depends only on emissivity and solid fraction [26] (as opposed to k_{rad} , which also depends upon the temperature and particle radius). The key outcome is F_E , which is found for a range of emissivity and solid fractions. Using F_E , k_{rad} can be readily calculated for any desired temperature and particle radius.

3.1.1 Generating the Particle Domain with DEM

The open source DEM software LIGGGHTS [51] is used to generate the particle domain because it gives a realistic distribution of particle positions as they collide with each other. A Hertz force model is used with a Young's modulus of 10^9 Pa to simulate hard particles such as stone or metals. For the special case of a packed bed, particles are inserted into the domain and allowed to come to rest in the presence of gravity. For beds which are not fully packed (solid fraction < 0.64), a random yet realistic domain of particles is generated using the following procedure:

- A. A single spherical particle is inserted at the center of a walled, cubic domain, and it is fixed to that location throughout the DEM simulation.
- B. Around 50,000 particles are then inserted into the domain in random positions. The exact number of particles to insert depends on the desired solid fraction and domain size.
- C. Gravity is turned upside down for a short period of time to give particles some kinetic energy, and then it is turned off completely.
- D. The boundary condition is changed to periodic, allowing particles to leave one side of the domain and enter on the opposite side. The goal is to create a packing distribution representing the bulk region, without any effects from the walls, so the more common fixed wall boundary condition is avoided.
- E. The particle coefficient of restitution is set to 1, and particles continue to collide and travel around the domain indefinitely.
- F. The particle positions at a time step of choice are then analyzed, and the solid fraction of the group is determined. The solid fraction is actually calculated in numerous concentric spherical shells to ensure the solid fraction remains consistent throughout the domain. Domains with a solid fraction of 0.64 and 0.25 are shown in Figure 3.1.



(a)

(b)

Figure 3.1. Close-up view of a domain with a solid fraction of (a) 0.64, and (b) 0.25.

G. For the heat transfer simulation, a spherical wall shaped domain was chosen to ensure no heat is lost due to end effects, as opposed to a rectangular or cylindrical domain which may have this problem. As will be described in Section 2.3, the single central sphere (from step A, above) will act as a high temperature heat source, the surroundings will be kept at a cold temperature, and the spheres in between will be allowed to change temperature. A gap is created between the central sphere and the others (Figure 3.2(c)). If this gap is not created, the exact positions of the nearest several neighbors of the central sphere can have an effect on the total heat transfer from the central sphere due to its very high temperature. This can lead to a different heat transfer from the central sphere when simulating a different set of random particle positions, which is not desired for consistency, though it would also not lead to an error in k_{rad} as long as enough particles are included in the simulation. Using the gap eliminates this effect by spreading out the heat transfer from the central sphere to many particles instead of heavily weighted towards several neighbors. Various gap sizes were studied, and it was determined that eliminating 500 of the closest particles results in consistent heat transfer from the central sphere when considering various sets of random particle positions. Therefore, starting with the initial cubic shaped domain shown in Figure 3.2(a), the desired spherical wall shaped domain is created by removing 500

spheres from the interior and removing all the external spheres, leaving 10,000 spheres to make up the spherical wall. The original particle positions are shown in Figure 3.2(a), the reduced, final group is shown in Figure 3.2(b), and a cut-away view is shown in Figure 3.2(c) to show the central sphere and the gap created.

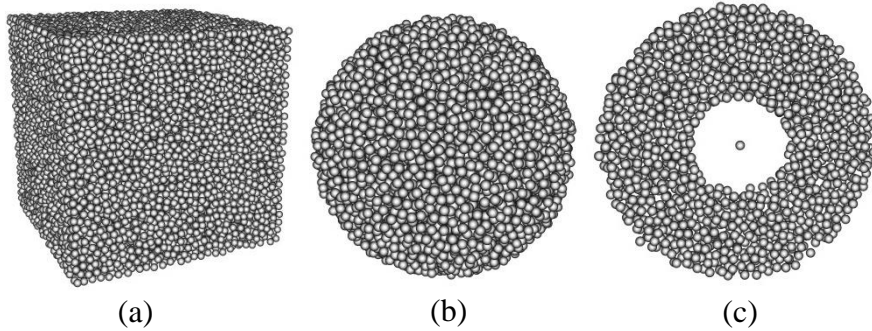


Figure 3.2. (a) Initial cubic shaped domain, (b) the final spherical shaped domain after removing the necessary spheres, and (c) a cut-away view to show the central sphere.

3.1.2 Simulating Photons with Monte Carlo Ray Tracing

The MCRT code described in Chapter 2 is used here. The output of the MCRT simulation is a square matrix containing the RDF from each sphere to every other sphere in the domain, which for the current simulation size is stored in a text file with 10,000 rows and columns. If the MCRT simulation were perfectly accurate in predicting RDFs, the matrix would be symmetrical. The diagonals of the matrix, representing the RDF of a particle to itself, are generally *not* zero due to photons reflected back on to the original emitting particle.

3.1.3 Particle-Particle Heat Exchange Simulation

The particle-particle heat exchange simulation was written in the Julia programming language [80] because it has many embedded functions, and it can manipulate large data sets such as the RDF matrix. A heat transfer code was written where the central sphere is specified with a surface temperature of T_{hot} , the surroundings are

specified with a temperature of T_{cold} , and the intermediate 9,999 particles are allowed to exchange heat until a steady state is reached. Initial temperatures are assigned to each particle, with the central particle at T_{hot} and all others at T_{cold} . The heat transfer rate (q_{ij}) between any two spheres i and j is found with Eq. (3.1) [74], where ε_p is the surface emissivity, A_p is the sphere surface area, σ is the Stefan-Boltzmann constant, T is the temperature of each sphere, and D_{ij} is the RDF between particles i and j . In Eq. (3.1), instead of using D_{ij} directly, the average of D_{ij} and D_{ji} is used, which enforces RDF reciprocity and improves accuracy by effectively doubling the number of photons used to find D_{ij} in the Monte Carlo simulation.

$$q_{ij} = \varepsilon_p A_p \sigma D_{ij} (T_i^4 - T_j^4) \quad (3.1)$$

Similarly, the heat transferred from one sphere to the surroundings (q_{i-surr}), maintained at T_{cold} is found with Eq. (3.2), and D_{i-surr} is the RDF from particle i to the surroundings.

$$q_{i-surr} = \varepsilon_p A_p \sigma D_{i-surr} (T_i^4 - T_{cold}^4) \quad (3.2)$$

D_{i-surr} is found with Eq. (3.3), where $n_particles$ is the total number of particles in the simulation domain. This is simply a statement of energy conservation; any photon not absorbed by a particle must be absorbed by the black surroundings.

$$D_{i-surr} = 1 - \sum_{j=1}^{n_particles} D_{ij} \quad (3.3)$$

With these values known, the net heat transfer rate from each i particle ($q_{net,i}$) can be found with Eq. (3.4).

$$q_{net,i} = q_{i-surr} + \sum_{j=1}^{n_particles} q_{ij} \quad (3.4)$$

After specifying the particle mass (m), specific heat (C_p), and an sufficiently small time step (Δt), the first law of thermodynamics can be written in the form of Eq. (3.5), which solves for the final temperature of each sphere, $T_{i,final}$, based on the initial temperature, $T_{i,initial}$, after a duration of one time step. The new temperature

of each sphere i is found and adjusted after each time step, except the central heated sphere which is always maintained at T_{hot} .

$$T_{i,final} = T_{i,initial} + \frac{q_{net,i} \Delta t}{m C_p} \quad (3.5)$$

The sequence is repeated for many time steps, and after an initial transient phase, a steady state is eventually reached when the total heat transfer from the central sphere equals the total heat transfer to the surroundings, and these values, as well as all particle temperatures, remain constant with successive time steps. Figure 3.3(a) shows the evolution of particle temperatures over time for a domain with a solid fraction of 0.45 and an emissivity of 0.5. Steady state particle temperatures are shown in Figure 3.3(b), where only a slice of the domain is shown so the inner particles can be seen. In both figures, the temperature scale covers the particle wall, and the central sphere at T_{hot} , 1098 K in this case, has been omitted because including it would reduce visibility of the other data points. The output from this simulation is the steady state temperature and xyz position of each particle, along with the overall heat transfer rate from the central heated sphere.

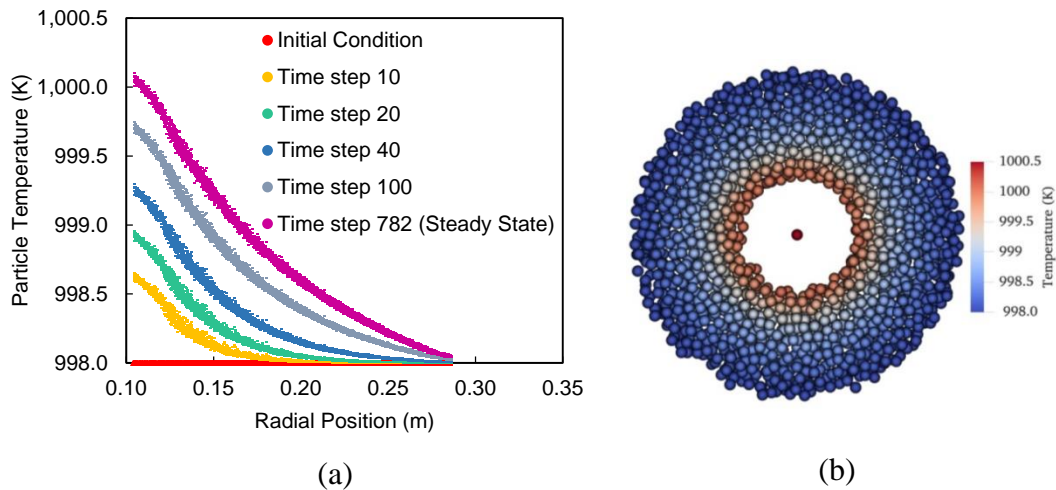


Figure 3.3. Particle temperatures over time, with initial temperatures shown in red and steady state temperatures shown in purple, and (b) steady state particle temperatures of a slice of the domain.

The small temperature difference across the spherical wall, around 2 K in Figure 3.3, is used because k_{rad} is temperature dependent; using a large temperature difference would lead to a k_{rad} that varies in the radial direction, making it difficult to determine k_{rad} at a specific temperature. In Figure 3, k_{rad} would be found for roughly 999 K, the average particle temperature of the group.

3.1.4 Calculating k_{rad} from the Temperature Profile

The xyz position of each particle is converted to a radial distance from the central heated sphere, and these are plotted against the steady state temperatures, as shown in Figure 3.4. The result is a radial temperature profile, similar to that of a spherical wall. From heat conduction theory, the temperature profile of a spherical wall of an isotropic solid has the general format of Eq. (3.6), where T is the temperature, r is the radial location, and C_1 and C_2 are constants which depend on the boundary conditions [72].

$$T = \frac{C_1}{r} + C_2 \quad (3.6)$$

From the definition of the effective thermal conductivity, the group of particles can be represented by an analogous isotropic solid with the same radial heat transfer and temperature profile. Therefore, a curve fit is found for the data, and C_1 and C_2 are determined, as shown in Figure 3.4. The change in curvature seen at the lower end of the radial position is addressed in Section 3.3.1.

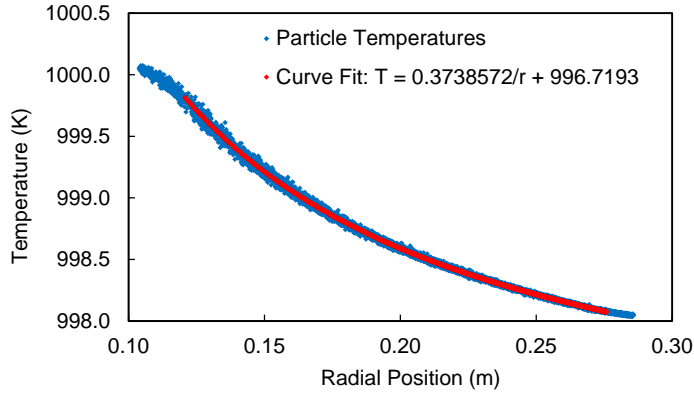


Figure 3.4. Steady state particle temperatures and curve fit equation of form $T=C_1/r + C_2$ for a solid fraction of 0.45 and emissivity 0.5.

Starting again with the general temperature profile (Eq. (3.6)) and taking a derivative with respect to the radius gives the slope in the radial direction:

$$\frac{dT}{dr} = -\frac{C_1}{r^2} \quad (3.7)$$

From Fourier's law of conduction in spherical coordinates, where q is the heat transfer rate, k is the thermal conductivity, and A is the area of heat transfer:

$$q = -kA \frac{dT}{dr} \quad (3.8)$$

Combining Equations (3.7) and (3.8) by eliminating dT/dr , using the surface area of a sphere as $A= 4 \pi r^2$, and rearranging to solve for k gives Eq. (3.9), which relates the thermal conductivity, the heat transfer rate, and constant C_1 .

$$k_{rad} = \frac{q}{4\pi C_1} \quad (3.9)$$

The total heat transfer rate (q) from the central sphere is known from the simulation, and C_1 is known from the curve fitting method above. Thus, the effective thermal conductivity of the bulk of particles, or k_{rad} , is finally found.

3.1.5 Finding the Exchange Factor

With k_{rad} determined, the dimensionless Exchange Factor (F_E) can now be calculated as described by Van Antwerpen et al. [26] using Eq. (3.10), which is valid when the temperature change across the wall-shaped domain is much less than the average temperature of the wall, or $\frac{\Delta T_{wall}}{T_{wall}} \ll 1$. The Exchange Factor is useful because it eliminates the temperature and particle radius variables. While k_{rad} is a function of solid fraction, emissivity, radius, and temperature, F_E is only a function of solid fraction and emissivity, making it much simpler to express in a table or equation.

For a particular application, k_{rad} can be found with Eq. (3.10), as long as F_E is known along with the temperature and particle radius. After running this entire modeling sequence for various solid fraction and emissivity combinations, the F_E results from this research are given in Section 3.3.6. In Eq. (3.10), σ is the Stefan-Boltzmann constant, d_p is the particle diameter, and T is the absolute temperature. In these simulations, T is taken as the mean temperature of the group of spheres.

$$F_E = \frac{k_{rad}}{4\sigma d_p T^3} \quad (3.10)$$

3.2 Validation

The MCRT code presented in Chapter 2 has been validated to accurately calculate PP and PW RDF values as long as a sufficiently high number of photons has been simulated. A second validation step is shown here to simultaneously validate the particle-particle heat exchange simulation as well as the RDF values found by the MCRT code for the case when absorptivity is less than 1. Using the same 50-particle domain used in the MCRT code validation (Section 2.2.3, Figure 2.3(a)), a heat transfer simulation was run in Fluent, and results were compared to the Monte Carlo plus particle-particle heat exchange simulation results. The surface of the

central particle was specified with a boundary condition of 1000 K, and the surroundings were comprised of the large bounding sphere encompassing all the particles with a boundary condition of 900 K and an absorptivity of 1. Spheres were modeled as a solid phase with near-infinite thermal conductivity and a surface emissivity of 0.8, and the space in between the particles was modeled as a fluid transparent to radiation and having near-zero thermal conductivity. Any conduction between spheres was eliminated by ensuring neighboring spheres were very close but not actually touching.

With the boundary conditions specified for the surface of the central sphere and the surrounding enclosure, a transient simulation was run, and the other spheres were allowed to change temperature until a steady state was reached. The steady state sphere temperatures from Fluent and from the current study are presented in Figure 3.5, showing nearly identical results. The temperature of the central particle is not included in the figure, as the y-axis would have to be extended to 1000 K, and the detail of the other particle temperatures would not be discernable. In Fluent, the steady state heat transfer from the central sphere was found to be 146.01 W, while heat transfer to the surroundings was 144.76 W, with this small discrepancy in the conservation of energy likely due to truncation errors within Fluent. In contrast, the Monte Carlo plus particle-particle heat exchange simulation method converges to a very high precision; heat transfer from the central sphere and heat transfer to the surroundings both yield a value of 145.30 W, closely aligned with results found with Fluent. Thus, the Monte Carlo plus particle-particle heat transfer simulation calculates accurate results in terms of steady state particle temperatures and heat transfer, and it is therefore validated to a high degree.

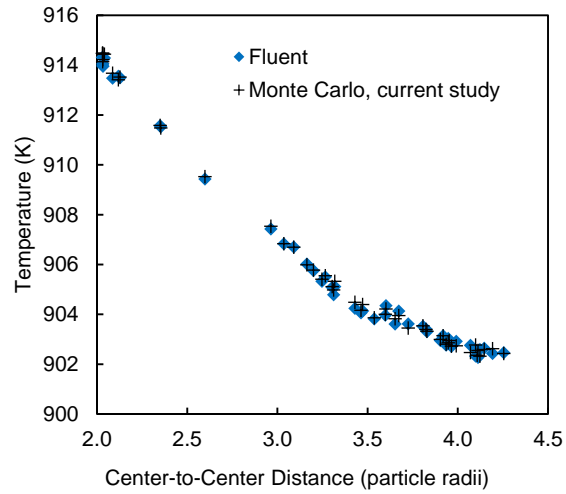


Figure 3.5. Steady state temperatures of spheres of particle domain shown in Figure 2.3, with results from both Fluent and the MCRT plus particle-particle heat exchange simulation.

3.3 Results and Discussion

Before presenting final results for F_E , several factors are examined to ensure the simulation domain and parameters chosen give accurate and reproducible k_{rad} results. These include near-edge effects, the number of photons used in the MCRT simulation, the thickness of the spherical particle wall, the independence of F_E with respect to temperature, and reproducibility with different particle positions.

3.3.1 Near-Edge Effects

As shown in Figure 3.6, the radial temperature gradient at the edges of the particle wall is less than in bulk region, and therefore a higher k_{rad} value is expected at the edge. To observe and eliminate this edge effect, the spherical particle wall is subdivided into multiple thinner spherical walls, allowing F_E to be found locally at various radial positions using Equations (3.9) and (3.10). F_E at each radial position was found by considering the particles within 0.02 m above and below each data point indicated in Figure 3.6. The plot shows F_E is higher near the edges but stable in the bulk region from radial position 0.14 to 0.22 m. Therefore to eliminate near-

edge effects, only the central portion of the wall was considered in the final F_E results presented later.

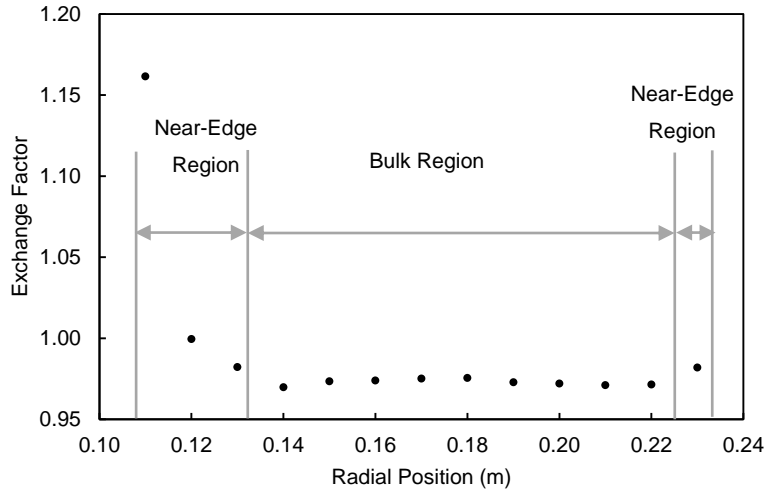


Figure 3.6. Exchange Factor found at various radial positions throughout the particle wall, for a solid fraction of 0.64 and an emissivity of 1.

3.3.2 Number of Photons

Increasing the number of photons used in the MCRT simulation increases the accuracy as well as the computation time. To find the minimum number of photons needed for accurate results, a simulation was run with 10^2 , 10^3 , 10^4 , and 10^5 photons emitted per particle, and F_E results are presented in Figure 3.7, for the case with a solid fraction of 0.45 and an emissivity of 0.7. The difference between results with 10^4 and 10^5 photons is very small, indicating that 10^5 photons is enough to obtain accurate results, and more photons would lead to unnecessary computational time. Therefore, all presented results are found using 10^5 photons emitted per particle.

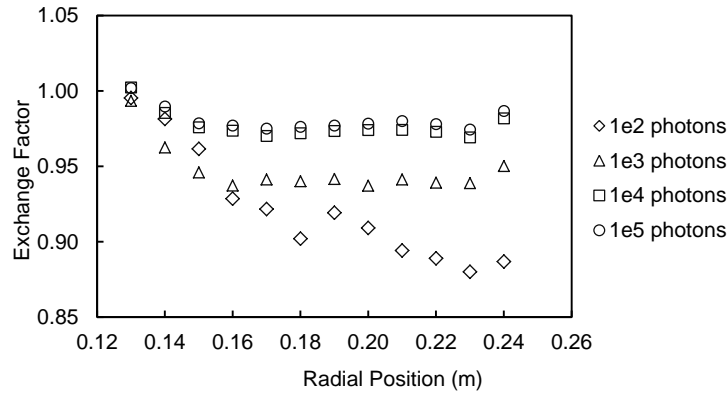


Figure 3.7. Exchange Factor at various radial positions for a solid fraction of 0.45 and an emissivity of 0.7, with 10^2 , 10^3 , 10^4 , and 10^5 photons used in the Monte Carlo simulation.

3.3.3 Thickness of the Particle Wall

The Exchange Factor should be a function of the solid fraction and emissivity, but the results should be consistent for different thicknesses of the spherical particle wall chosen for the simulation. It is important to choose a thick enough particle wall so any edge effects can be identified and eliminated. To demonstrate this, simulations were run with three different wall thicknesses, for the case with a solid fraction of 0.45, an emissivity of 0.5, and a particle radius of 0.01 m. Each of the three domains has an inner radius of 0.104 m, and they extend to an outer radius of 0.266, 0.286, and 0.307 m, with the domains containing 8,000, 10,000, and 12,500 particles respectively. As shown in Figure 3.8, the bulk region can be seen between 0.17 and 0.23 m, and consistent F_E results are shown between all of the three simulations as long as the near-edge regions can be identified and eliminated in each case. If a thinner particle wall were chosen extending up to only 0.18 m, the lower and upper near-edge regions would meet, and the bulk region would be eliminated; the domain chosen would be too small to accurately calculate F_E . A smaller domain requires less computational time, so in the case of Figure 3.8 the 10,000 and 12,500 particle simulations are unnecessarily large. However, a

simulation of 10,000 particles was chosen because it is large enough to clearly identify the bulk region and eliminate the near-edge effects in all cases run.

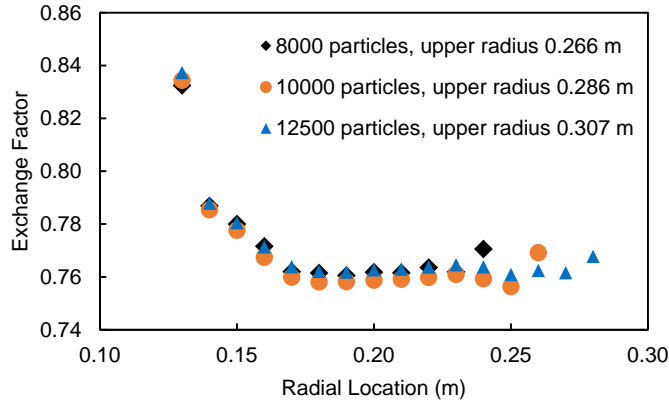


Figure 3.8. Exchange Factor measured at various radial positions, showing simulations with different numbers of particles.

3.3.4 Independence of F_E with Respect to Temperature

The Exchange Factor is a dimensionless quantity which can be used to calculate k_{rad} at any temperature using Eq. (3.10). Therefore, F_E should not depend on the temperature chosen for the simulation. To verify this independence, the particle-particle heat transfer simulation was run using a range of temperature conditions for the case of a solid fraction of 0.45 and an emissivity of 0.7. In a sequence of simulations, the temperature of the central heated particle and the surroundings were increased in increments of 100 K, while the temperature difference between the two values remained constant. As shown in Table 3.1, an increase in temperature leads to a higher k_{rad} value, but the F_E value calculated with Eq. (3.10) is nearly identical for each simulation. With a maximum deviation of 0.02% between the lowest and highest values, F_E is shown to be independent of the simulation temperature.

Table 3.1. Exchange Factor calculated at various temperatures for a solid fraction of 0.45 and an emissivity of 0.7.

Central Sphere Temperature (K)	Surroundings Temperature (K)	Average Steady State Particle Temperature in Bulk Region (K)	k_{rad} ($\text{W m}^{-1} \text{K}^{-1}$)	Exchange Factor
798	698	698.65	1.514	0.97847
898	798	798.63	2.261	0.97840
998	898	898.62	3.220	0.97835
1098	998	998.61	4.419	0.97831
1198	1098	1098.60	5.884	0.97828

3.3.5 Reproducibility with Different Particle Positions

At the beginning of this simulation sequence, a DEM simulation was run to generate a random domain of particles with the output being a static “snapshot” of the particle positions, for each solid fraction simulated. These particle positions are inputs to the Monte Carlo and particle-particle heat exchange simulation sequence. The final F_E results should be reproducible for any different set of random particle positions, so to ensure this, a second set of particle positions was generated with the DEM simulation, and all simulation cases were run to find F_E a second time. The F_E results from the two sets of simulations are very close, differing by no more than 1.1% in each case. The F_E results presented below are the average of the two sets of simulations.

3.3.6 Exchange Factor Results

The simulation sequence was run to find F_E at five values of emissivity and five values of solid fraction. All results were found using a domain of 10,000 particles with a particle radius of 0.01 m, and the Monte Carlo simulation was run with 10^5 photons emitted per particle. All particle-particle heat transfer simulations were run using a central sphere temperature of 1098 K and a surroundings temperature of 998 K, leading to a spherical particle wall with an average temperature of roughly 998.5 K, though the exact average temperature depends on the steady state particle temperatures. After eliminating the near-edge regions from the temperature profile,

k_{rad} was found for the bulk region with the curve fitting method and Eq. (3.9). F_E values were then calculated using Eq. (3.10), where the average particle temperature in the bulk region was used for T . This procedure was used to calculate F_E for each of the 25 combinations of emissivity and solid fraction. As noted in Section 3.3.5, this entire process was repeated for a second set of random particle positions, and the F_E results were averaged between the two simulations. In total, 50 simulations were run, leading to the 25 values found in Table 3.2.

Table 3.2 Exchange Factor results for various solid fractions and emissivity (ϵ) values.

Solid fraction	$\epsilon = 0.3$	$\epsilon = 0.5$	$\epsilon = 0.7$	$\epsilon = 0.9$	$\epsilon = 1$
0.25	1.5609	1.8497	2.1757	2.5572	2.7753
0.35	0.8926	1.1140	1.3675	1.6647	1.8282
0.45	0.5717	0.7602	0.9770	1.2305	1.3706
0.55	0.3897	0.5574	0.7503	0.9777	1.1060
0.64	0.2983	0.4570	0.6394	0.8527	0.9770

A polynomial surface has been fitted to these data points and the equation of the surface is presented in Eq. (3.11). With this equation, F_E can be found for any combination of solid fraction (α_s) and emissivity (ϵ) within the range of $0.3 \leq \epsilon \leq 1$ and $0.25 \leq \alpha_s \leq 0.64$. Over the 25 data points the surface fit gives an average error of 1.1%, and the highest error is 4.8% for the case where solid fraction is 0.55 and emissivity is 0.3.

$$F_E = 5.08 - 24.63\alpha_s + 2.097\epsilon + 43.54\alpha_s^2 - 5.937\alpha_s\epsilon + 0.7391\epsilon^2 - 26.9\alpha_s^3 + 5.455\alpha_s^2\epsilon - 0.6188\alpha_s\epsilon^2 \quad (3.11)$$

The F_E data points from Table 3.2 and the polynomial surface fit from Eq. (3.11) are plotted as a function of solid fraction and emissivity in Figure 3.9. It is expected that a lower solid fraction leads to higher value for F_E due to the increased distance photons can penetrate into the group of spheres, as seen in the figure. F_E increases with emissivity due to the higher radiative emission from each sphere.

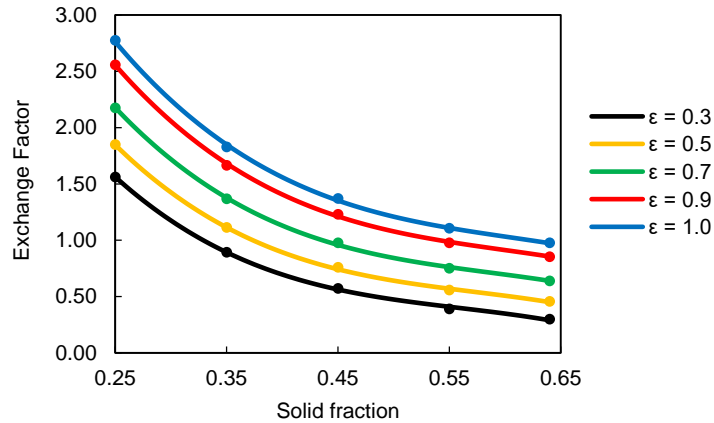


Figure 3.9. Exchange Factor results, with points representing data from Table 3.2, and lines representing the surface fit of Eq. (3.11).

3.3.7 Comparisons with Previous Research

The leading models for F_E in packed beds are compared in Figure 3.10 for a solid fraction of 0.60 and a range of emissivities, as published by Kaviany [37], ZBS [32] and Breitbach and Barthels (BB) [28], with experimental work by Kasperek and Vortmeyer [42]. Nearly all of these models are in relative agreement under these conditions, with the exception of the Kaviany Two-Flux model, which does not accurately account for the particle emissivity [37]. Results from the current study are slightly below the Kaviany Monte Carlo study and the Kasperek and Vortmeyer experimental work, which is likely because both of these studies used a simple cubic packing instead of a random packing structure. The Kasperek and Vortmeyer experiment studied a solid fraction of 0.60 using 1-cm steel spheres, with both a polished steel surface (emissivity of 0.35 and specular) and chromium oxide coated surface (emissivity of 0.85 and diffuse). In the experiment, rows of spheres were fixed in place to prevent conduction between layers, and tests were run under vacuum conditions, forcing both k_{solid} and k_{fluid} to zero. It is also important to note that due to the conductive steel particles Λ has a very high value, and therefore the uniform particle temperature assumption is valid, allowing for a useful comparison with the current work. Other experimental work has focused on

packed beds of larger graphite spheres, [28][41] but because Λ is low the results cannot be compared directly with the current study.

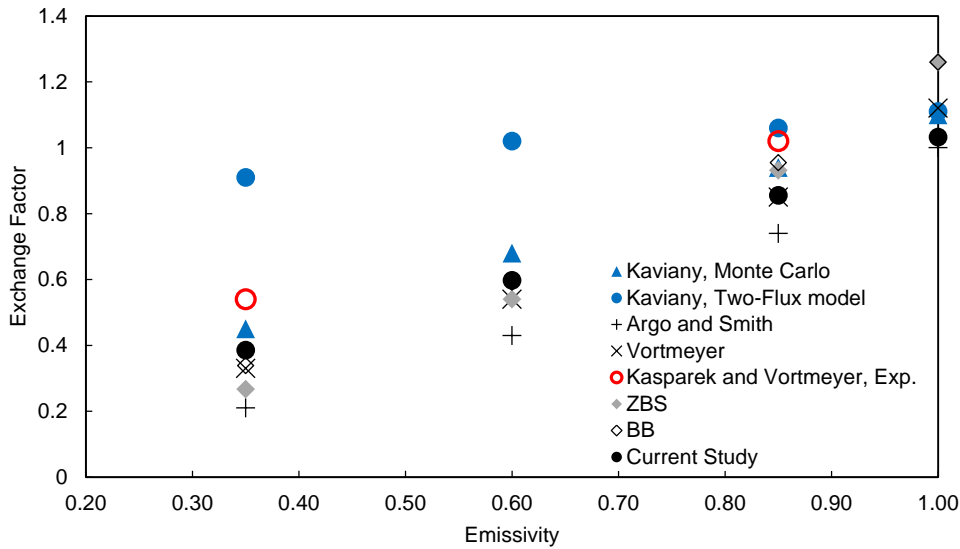


Figure 3.10. Exchange Factor comparison to previous models and experimental work, for a solid fraction of 0.60 [37][29][28][42].

There are a large number of proposed F_E models for the packed bed condition as shown in Figure 3.10, but with the exception of the ZBS and BB models, the other models shown do not account for various solid fractions. While the ZBS and BB models do include a term to account for a lower solid fraction, they are derived assuming a unit cell consisting of two touching particles. In particle beds where the solid fraction is less than ~ 0.52 very few particles are touching, so the applicability of the resulting ZBS and BB models is questionable in this range. Still, to see the difference in predicted values, the F_E results from the current study are compared to the values predicted by the radiation models of ZBS and BB in Figure 3.11, where $\Lambda > 10$ is assumed. Under certain conditions, such as for an emissivity of 0.7 and a packed bed with solid fraction above 0.55, results are nearly identical. In contrast, for an emissivity of 1 and a solid fraction of 0.64, the ZBS and BB models overestimate F_E by 24% compared to the current study. While trends are generally similar, at low solid fractions the current study shows a much higher F_E than the

ZBS or BB models predict. (Note: The ZBS and BB models are identical for an emissivity of 1, so these lines overlap exactly in the figure.)

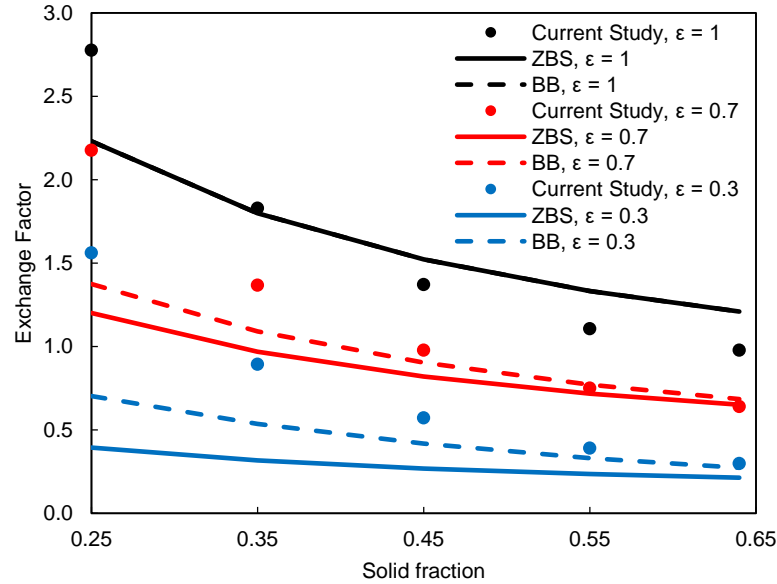


Figure 3.11. Comparison of Exchange Factors between present study and models by Zehner, Bauer, and Schlünder (ZBS), and Breitbach and Barthels (BB).

With a large disagreement in results found between the models under some conditions, ideally experiments would show which model is valid. However, experimental data is available only at the fully packed condition, as experiments with low solid fractions are very difficult to run; particles would have to be secured in a suspended state throughout the experiment while heat transfer data is collected. The method presented in this study aims to simulate such an experiment numerically by tracing each ray through a large group of randomly distributed particles, making it a close approximation to reality. In contrast, the ZBS and BB models use a single idealized unit cell based on two touching non-spherical particles to derive a relation that accounts for a lower fraction of particles in the domain. The method presented starts with relatively few assumptions and provides a close approximation to these hypothetical experiments, and therefore the results are expected to be valid and more physically realistic than the results of the ZBS or BB models, especially where particles have a solid fraction of less than 0.52.

3.3.8 Total Effective Thermal Conductivity

In addition to radiative transfer, most engineering applications require the full effective thermal conductivity including heat conduction through the fluid and solid phases as well. The model for k_{rad} given in this study can be combined with the models for the other modes of heat transfer by summing them to find the total effective thermal conductivity, which has been done to form Eq. (3.12). The first two terms represent heat that conducts from one particle to the next particle across the fluid gap, using the commonly cited Zehner and Schlünder model [30], and the third term is the radiation component from the current study. The Zehner and Schlünder model neglects the direct conduction between contacting particles, as this is typically much smaller than the heat conducted across the fluid gap. In this equation, k_{eff} is the effective thermal conductivity of the bed including all modes of heat transfer, λ_f and λ_p are the thermal conductivities of the fluid and particle phases respectively, α_s is the solid fraction, and B is a function of the solid fraction given in Eq. (3.13). F_E is the exchange factor found with Eq. (3.10), σ is the Stefan-Boltzmann constant, d_p is the particle diameter, and T is the temperature in Kelvin. Eq. (3.12) presents a convenient way to calculate the effective thermal conductivity for a randomly distributed particle bed, relying upon the Zehner and Schlünder model for solid and fluid conduction and the model presented in the current study for radiation. Because the unit cell used by Zehner and Schlünder is derived based upon two touching particles, Eq. (3.12) should be regarded as valid for $\alpha_s > 0.52$.

$$k_{eff} = \lambda_f(1 - \sqrt{\alpha_s}) + \lambda_f\sqrt{\alpha_s} \left[\frac{2}{1 - \frac{\lambda_f}{\lambda_p B}} \right] \left\{ \frac{\left(1 - \frac{\lambda_f}{\lambda_p}\right)^B}{\left(1 - \frac{\lambda_f}{\lambda_p B}\right)^2} \ln\left(\frac{\lambda_p}{B\lambda_f}\right) - \frac{B+1}{2} - \frac{B-1}{1 - \frac{\lambda_f}{\lambda_p B}} \right\} + F_E 4\sigma d_p T^3 \quad (3.12)$$

$$B = 1.25 \left(\frac{\alpha_s}{1 - \alpha_s} \right)^{10/9} \quad (3.13)$$

3.4 Conclusions for k_{rad}

Numerous modeling approaches in particle-based CSP involve the use of k_{eff} , so having a known and trusted model is essential, yet the k_{rad} values predicted by the leading previously published models do not match the results from this study under all emissivity and solid fraction combinations. The model in this study captures the complex phenomena involved, by modeling realistic “random” distributions of particles and taking into account radiation heat transfer that may include multiple diffuse reflections. Compared to the approaches based on an idealized unit cell or those based on the Radiative Transfer Equation, this is a much more physically realistic approach, making it likely that it is of higher accuracy. Moreover, unlike many other models, the method described is valid for nearly any solid fraction and emissivity combination.

Exchange Factors for 25 combinations of emissivity and solid fraction are presented, and a polynomial equation is given to find F_E for solid fractions from 0.25 to 0.64 and emissivities from 0.30 to 1. To find k_{rad} for a certain application, Eq. (3.10) can be used along with the particle diameter, the temperature, and F_E . Like many previous models, the Exchange Factors presented are only valid for particles that are sufficiently small and conductive that their temperature can be considered uniform. In future work, the model can be expanded to account for temperature gradients within particles.

CHAPTER 4

PARTICLE-SCALE RADIATION: THE DISTANCE BASED APPROXIMATION MODEL

Some of the content in this chapter has already been published by the author:

E.F. Johnson, İ. Tari, D. Baker, Radiative heat transfer in the discrete element method by distance based approximations, Powder Technology (2020). doi:10.1016/j.powtec.2020.11.050.

4.1 Introduction of the Distance Based Approximation Model

In this chapter, a new model is described to calculate particle-particle (PP) and particle-wall (PW) radiation, which is computationally efficient enough to embed in a dynamic DEM or CFD-DEM simulation and fixes several shortcomings of the existing models. To develop the model, a particle domain is generated using the DEM code LIGGGHTS, and the MCRT code is used to find the Radiation Distribution Factor (RDF) between PP and PW pairs. The RDF is plotted against distance for many PP and PW pairs, and a relationship is established, taking the form of an equation or table expressing the average RDF as a function of distance. With this curve established, it can be implemented in the DEM code, and the RDF can be approximated based on the distance between particles alone. The PP or PW heat transfer can then be immediately determined with a single equation. Thus, the MCRT simulation only has to be run initially to find the RDF-distance curves for a certain set of parameters, namely the solid fraction (SF), particle emissivity (ϵ_p), and wall emissivity (ϵ_w). In this chapter, the method to find these RDF-distance curves is described, and the RDF-distance curves are presented for various sets of parameters, which others can implement directly into their DEM codes. This approach, referred to herein as the Distance Based Approximation (DBA) model, is computationally efficient, simple to implement into any DEM code, and

sufficiently accurate for many engineering applications. Furthermore, it is applicable for both packed beds and diffuse flows such as fluidized beds or falling particles.

It offers several benefits compared to the previously proposed models. The DBA model does not suffer from the same radiosity errors as the Uniform Radiation Model [46] because all reflections are accurately simulated in the initial Monte Carlo model. Unlike the Black Model [46], the particle emissivity is taken into account in a physically realistic manner. In contrast to the SRM and the local environment temperature approaches, the DBA model accounts for radiative transfer to all nearby particles including those that are not direct neighbors, which is especially important for particles with a low solid fraction such as fluidized or falling particles. The DBA model has a very low computational cost, especially compared to the high cost of a direct Monte Carlo implementation [65] or subdividing particles with the Local Radiation Model [46].

The central premise of the DBA approach is that the RDF can be estimated instead of calculated explicitly, and any overestimation or underestimation of the RDF due to the random positions and shading of particles will balance out when large groups of particles are considered. This hypothesis is verified through several validation simulations, and results confirm that a sufficient accuracy for many engineering applications is achieved.

The key contributions of this research are the description of the DBA methodology and the RDF-distance curves for two particle emissivities, four wall emissivities, and a range of solid fractions. While results are only presented for the particle emissivities of sand and sintered bauxite due to their immediate relevance in the field of CSP, the method to develop and implement the tables is applicable for situations with other emissivities or solid fractions. Implementation of the DBA model alongside a DEM simulation is demonstrated for a heat exchanger with a dense granular flow, and numerous important implementation details are discussed. To the knowledge of the author, the DBA model is novel; no similar RDF-distance

tables have been published, and the implementation of those tables to calculate the radiative transfer in a domain of particles and walls has not been introduced in the literature or in commercial DEM software.

4.2 Methods

The DBA model is applicable under the same assumptions as the MCRT and particle-particle heat transfer model described in Section 3.1. Specifically, particles are assumed to be opaque, gray-diffuse emitting and reflecting, monodisperse spheres. Furthermore, each particle is assumed to have a uniform temperature, which is a valid assumption for $\Lambda > 10$ or for particles that are rotating fast enough that no temperature gradients can develop. Thus, the DBA model is well-suited for static beds of small metallic particles or for integration into dynamic DEM simulations.

4.2.1 PP Radiation: Generation of Particle Domains

A spherical group of 50,000 particles was generated using the DEM software LIGGGHTS following a procedure similar to that of Chapter 3. For packed beds, the procedure is simple: particles are allowed to settle at the bottom of the domain against a hard wall in the presence of gravity, and particles far from the bottom wall are analyzed to eliminate any effect of the wall on the packing structure. For non-packed beds (solid fraction of less than ~ 0.60), the following procedure is used. Many particles (roughly 100,000) are inserted into a cube-shaped domain, given a small initial velocity, and allowed to travel around the domain and collide with neighboring particles without gravity or other body forces. To eliminate any effects from walls on the distribution of particles, all edges of the domain are not modeled as hard walls but are instead given periodic boundary conditions, where any particle leaving one boundary of the domain reappears at the same place and with the same velocity on the opposite boundary. The PP coefficient of restitution

is set to 1 so the simulation can continue indefinitely, and by allowing the simulation to run for many time steps (typically 5×10^5 to 10^6), the particles become well-distributed around the domain, and any effects from the initial position or velocity of the injected particles are eliminated. Thus, a cubic domain of randomly distributed particles has been made, but for the radiation modeling to follow, only the 50,000 closest to the center are taken to be analyzed. The output is a “snapshot” of these particle positions, as shown in Figure 4.1. With this method, random distributions of particles can be created for any solid fraction (up to the limit of a packed bed) by changing the dimensions of the cubic domain while keeping the number of particles inserted constant.

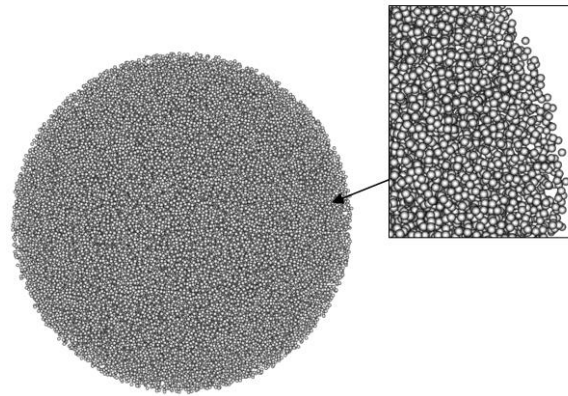


Figure 4.1. Group of 50,000 particles with a solid fraction of 0.45.

The solid fraction is defined as the sum of the volume of particles divided by the total volume of the “container” analyzed. In this work, this calculation includes the volume of partial spheres which are sliced by the spherical container volume. One simple method to calculate the solid fraction is to define a single region in the domain and calculate the total solid volume, however, the results with this method were found to vary over space and time more than desired. Instead, the solid fraction was found by choosing a random set of 500 particles and calculating the solid fraction in a spherical volume surrounding each of these particles. These 500 individual solid fractions were then averaged to find the overall solid fraction, leading to a much more consistent calculation of the solid fraction in the domain.

4.2.2 PP Radiation: Monte Carlo Ray Tracing

A randomly selected sample of 500 emitting particles were specified near the center of the domain, and the MCRT code was used to find the RDF from each of these emitting spheres to every other sphere in the domain. Each emitting sphere was far from the edges of the particle group to ensure that all photons were eventually absorbed by a particle and none were lost to the surroundings.

Results are shown in Figure 4.2 for all 500 emitting spheres, giving PP RDF as a function of the center-to-center distance between each particle pair, and a smoothing spline curve fit applied. There is a clear relationship between the distance and the PP RDF, though the data is somewhat scattered due to the random positions and shading of particles. It is noteworthy that the RDF prediction is relatively accurate for close particles at a distance of 2 to 3 radii, where the highest portion of the radiative transfer occurs, and there is more scatter between 3 and 5 radii. This is because when a pair of particles is close together (e.g. 2-3 radii) there is little room in between for other neighboring particles which would intercept radiation. In contrast, for particles further apart (e.g. 3-5 radii), there may be several neighboring particles in between the two particles of interest, so the degree of shading varies depending on the exact position of the particles in between, leading to the higher spread in the RDF data shown. However, while any specific pair of particles may have an RDF slightly higher or lower than the curve, the correct amount of heat transfer can still be calculated for a group of particles with reasonable accuracy due to the high number of particle-particle radiation interactions, as demonstrated in Section 4.3.

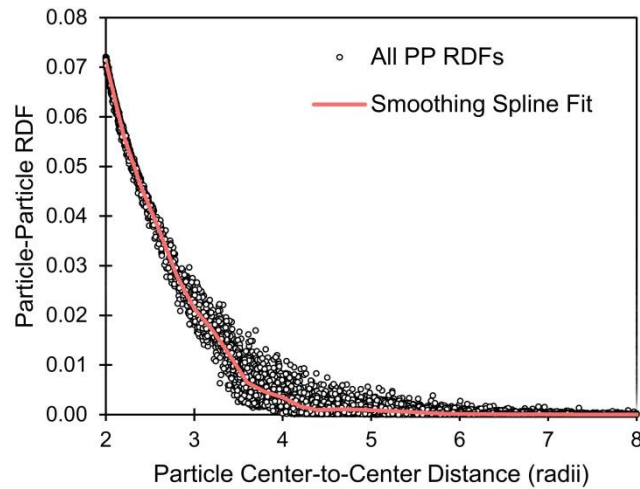


Figure 4.2. Particle-particle RDF at various distances between particles, for $\epsilon_p = 0.86$ and SF = 0.55, showing individual data points and a smoothing spline fit.

4.2.3 PP Radiation: RDF Tables

Within a DEM code the RDF between any two particles is approximated using a tabulated form of the smoothing spline curve, such as the one shown in Figure 4.2. Many attempts were made to fit the data to an equation such as polynomial, exponential, power function, and the fit suggested by Liu et al. [66], however, each of these failed to follow the RDF data to an adequate degree. Even a small deviation from the spline curve can lead to a model which fails in terms of heat transfer in the validation steps. Therefore, to maximize accuracy, the RDF at discrete PP distances is tabulated instead of given as an equation of a curve. The tables, found in Appendix A, give RDF as a function of distance, which is normalized by the particle radius so it is applicable for particles of any size. At short PP distances, a spacing of 0.2 radii is used to capture the high curvature, and at greater PP distances the spacing is increased to minimize the table length. Within a DEM simulation, the RDF for a pair of particles is calculated by interpolating between the tabulated data based on the exact distance between the particles.

The previous steps were used to generate a single RDF-distance table which is only valid for a specific solid fraction and particle emissivity. Different particle domains were generated with DEM to achieve different solid fractions (0.25, 0.35, 0.45, 0.55, and 0.64), and the MCRT modeling was performed using two particle emissivities (0.65 and 0.86), resulting in an RDF-distance table for each combination of solid fraction and particle emissivity, which are presented in Appendix A. The first application of the DBA model is intended for particle-based CSP devices, so the tables are given specifically for the emissivities of silica sand and sintered bauxite in the range of 700 to 800 °C (taken to be 0.65 and 0.86 respectively), as these are the top candidates for heat storage materials in this industry [56][7][81]. Though tables for only two particle emissivities are given here, the method can be followed to generate tables for particles of any emissivity and solid fraction with the procedure outlined along with the DEM and Monte Carlo simulations.

4.2.4 PP Radiation: Calculating Heat Exchange in DEM

Within the DEM code, the rate of radiative heat exchange (q_{ij}) between any two spheres i and j is found using Eq. (3.1) (Section 3.1). All of these variables are typically known in a DEM simulation except D_{ij} . To find D_{ij} , values for the PP distance and the solid fraction must be calculated within the DEM code. Then, with the RDF tables, two linear interpolations are used (or more directly, a bilinear interpolation [82]) to calculate the actual RDF at the distance and solid fraction of interest.

In the typical “soft-sphere” DEM approach [53] the deformation of contacting spheres is modeled by allowing them to overlap slightly, making the center-to-center distance just less than 2 radii. Since real particles cannot overlap and the deformation of small, hard particles is very slight, any deformation will not measurably change the RDF for the conditions of interest. Therefore, in the DBA

model the center-to-center distance of any slightly overlapping pair of particles is taken to be exactly 2 radii when using the tables to calculate the RDF.

4.2.5 PW Radiation: Generation of Particle-Wall Domains

Particle-wall domains with bulk solid fractions of 0.25, 0.35, 0.45, 0.55 and 0.64 were created in LIGGGHTS using a procedure similar to the PP domains, for groups of 24,000 spheres. For the cases of packed beds with a bulk solid fraction of 0.55 and 0.64, particles were inserted into the domain and allowed to come to rest on top of the wall in the presence of gravity, as shown in Figure 4.3(a). To generate domains with lower solid fractions, particles were inserted in between the top and bottom walls (Figure 4.3(b)) with some velocity, gravity was turned off, the coefficient of restitution was set to 1, and particles were allowed to collide and travel around the domain until a snapshot of the xyz particle locations was taken. In both cases, the vertical edges of the domain were given periodic boundary conditions, allowing particles to exert contact forces across the boundary and to leave one side of the domain and enter on the opposite side, eliminating any effects from side walls. The snapshot of particle locations was taken after a duration long enough such that particles were well-distributed throughout the domain, without any effect from the original position and velocity of the injected particles.

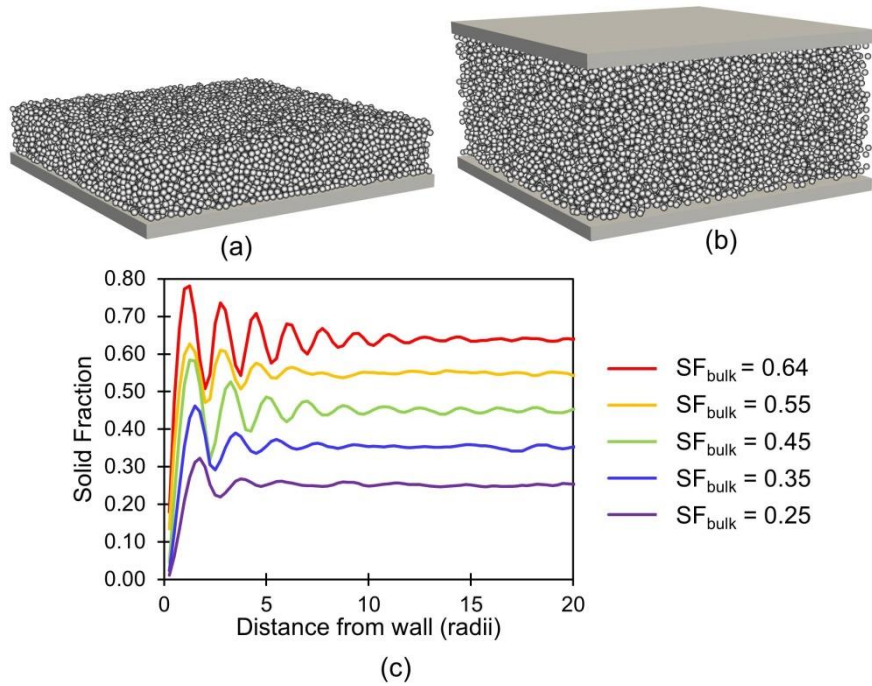


Figure 4.3. (a) Particle-wall domain with a $SF_{\text{bulk}} = 0.64$, (b) domain with $SF_{\text{bulk}} = 0.25$, and (c) local solid fraction at various distances from the wall, showing various bulk solid fractions.

The solid fraction is known to change near a wall due to the layering effect of particles contacting the wall [26]. For each PW domain, the local solid fraction at various distances from the wall was found by dividing the domain into layers parallel to the wall, with a thickness of 0.25 radii, and the volume of the sliced spheres within each layer was divided by the total volume of the layer. As shown in Figure 4.3(c), and consistent with results from previous research [26], for a packed bed the oscillations in solid fraction disappear at distances greater than ~ 12 radii from the wall, after which point the solid fraction is uniform and is considered the bulk solid fraction (SF_{bulk}). While the local solid fraction varies close to the wall, these packing conditions are referred to using the bulk solid fraction in the following analyses and in the tabulated PW RDF values.

4.2.6 PW Radiation: Monte Carlo Ray Tracing

Simulations were run with the MCRT code to find the RDF between particles and the wall for the five bulk solid fractions. During each simulation, photons were emitted from 4000 randomly-selected particles far from the sides of the domain to ensure negligible loss of photons to the surroundings. Sample PW RDF results for the case of a $\epsilon_p = 0.86$, $\epsilon_w = 0.60$, and $SF_{\text{bulk}} = 0.45$ are shown in Figure 4.4 along with a smoothing spline fit of the data. The layering of particles against the wall causes the concentration of particles at distances of one radius and three radii from the wall with few particles in between, which is consistent with the peaks in the solid fraction shown in Figure 4.3(c).

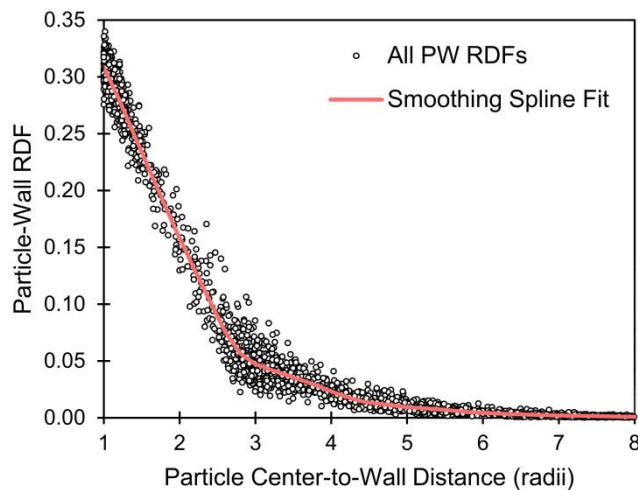


Figure 4.4. Particle-wall RDF at various distances, for a $\epsilon_p = 0.86$, $\epsilon_w = 0.80$, and $SF_{\text{bulk}} = 0.45$.

4.2.7 PW Radiation: RDF Tables

A set of PW RDF tables was generated and is given in Appendix B, with the wall emissivity being a third parameter affecting the PW RDF. The tables cover particle emissivities of 0.65 and 0.86, wall emissivities of 0.4, 0.6, 0.8, and 1.0, and bulk solid fractions of 0.25, 0.35, 0.45, 0.55, and 0.64. With the additional variable of the wall emissivity, the number of tables to cover all circumstances can become

high, but within any particular DEM simulation the wall and particle emissivities are typically constant, so only a single table with various bulk solid fractions and PW distances must be implemented.

4.2.8 PW Radiation: Calculating Heat Exchange in DEM

Radiative heat transfer from particle i to the wall is calculated with Eq. (4.1), where ε_p is the particle emissivity, A_p is the particle surface area, T is the absolute temperature, σ is the Stefan-Boltzmann constant, and D_{iw} is the RDF from particle i to the wall. Similar to the calculation of the PP RDF, D_{iw} requires a bilinear interpolation based on the PW distance and bulk solid fraction.

$$q_{iw} = \varepsilon_p A_p \sigma D_{iw} (T_i^4 - T_w^4) \quad (4.1)$$

4.3 Model Validation

The MCRT code has been validated to find RDFs to a high degree of accuracy for both PP and PW domains. Therefore, the DBA model was validated by comparing results in the simulations that follow, where the RDFs were found both with the highly accurate Monte Carlo code and by approximating RDFs using the tables in the appendices.

4.3.1 Validation of Particle-Particle DBA Model

According to the first law of thermodynamics all emitted photons must eventually be absorbed, so the sum of the RDFs from one particle to all particles (including the emitting particle) must be 1. While this is not enforced in the DBA model, if a valid PP RDF-distance curve is used, then the sum of all RDFs should, on average, be equal to 1. This fundamental property was tested for each of the ten proposed PP RDF curves. A *new* domain of particles was generated (i.e. a different snapshot of

particle positions was taken) for each of the solid fractions studied, and 100 particles were randomly selected near the center of the domain. The total RDF was calculated using the DBA model for each of these 100 particles, and the mean was found, leading to the results shown in Table 4.1. In all cases the mean total RDF is very close to 1, indicating that for any different set of particle positions having the solid fractions studied, this fundamental criterion is met by applying the proposed curves (in contrast, particles have a total view factor of only ~ 0.83 using the Short Range Model [46]). It should be noted that while the total PP RDF may be slightly more or less than 1, the first law of thermodynamics will not be violated in a DEM simulation because the same quantity of heat is removed from one particle and delivered to the second particle, keeping the total energy in the simulation unchanged.

Table 4.1. Mean of the total PP RDF over 100 particles, for the ten PP RDF cases studied.

Solid Fraction	$\epsilon_p = 0.65$	$\epsilon_p = 0.86$
0.64	0.9979	0.9990
0.55	1.0025	1.0032
0.45	1.0019	1.0023
0.35	1.0022	1.0025
0.25	1.0020	1.0024

The results in Table 4.1 show that the sum of the RDFs is very close to 1 using with the proposed PP RDF curves, however, it does not show that the RDFs are distributed correctly based on the distance from the emitting particle. An invalid PP RDF curve could, for example, overestimate the RDF for closely neighboring particles and underestimate the RDF for particles at a greater distance, and it is possible for the total RDF to still equal 1. To ensure the RDFs are correctly estimated based on distance, the cumulative RDF (i.e. the fraction of photons absorbed) is plotted as a function of distance from the emitting particle.

For each of the ten cases, a new particle domain was generated again, and the cumulative RDF curve was found and averaged over 100 randomly-selected particles using both the proposed PP RDF curves and the highly accurate RDFs found with the Monte Carlo model. Results are shown in Figure 4.5 for a particle emissivity of 0.65 and each of the solid fractions studied, and an extremely close

match is shown between the Monte Carlo (MC) and DBA results in each case. This comparison shows that by using the proposed RDF curves, the distribution of photons absorbed as a function of the distance from each particle can be accurately predicted for any domain of particles that has one of the solid fractions studied. Similarly close results were also found for an emissivity of 0.86, so all of the ten proposed RDF curves provide a valid estimate for the RDF as a function of distance from the emitting particle. In the figure, the RDF starts at a value above zero due to the photons reflected back onto and absorbed by the emitting particle, and the immediate rise at a distance of 2.0 is due to photons absorbed by particles in contact with the emitting particle.

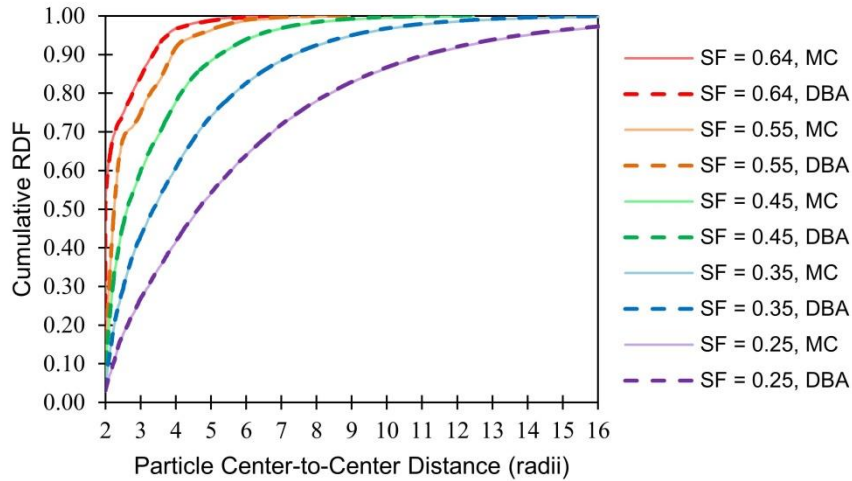


Figure 4.5. Mean cumulative RDF (fraction of photos absorbed) at various distances from the emitting particle, calculated with Monte Carlo and the DBA models, for $\epsilon_p = 0.65$ and various solid fractions.

Finally, each of the cases was validated using a heat transfer simulation, where the heat transfer rate between each particle and every other particle was calculated with Eq. (3.1). A spherical domain of 10,000 particles (Figure 4.6) of radius 0.01 m was generated for each of the five solid fractions, and a hot core with a radius of 0.07 m was designated where particles have a temperature of 1010 K, with all other particles having a temperature of 1000 K. The PP RDF values were found using both a full MCRT simulation and by using the tables to estimate the RDFs. The

total heat transfer rate leaving the hot core was then calculated to compare the two methods, and results are shown in Table 4.2 for each of the ten cases studied.

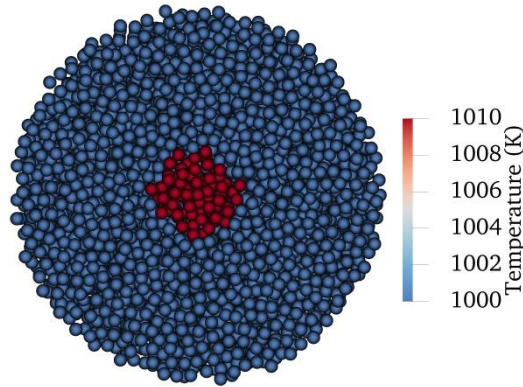


Figure 4.6. Cross section of the spherical domain used for validating the DBA model, with 10,000 particles and a solid fraction of 0.45.

Table 4.2. Total heat transfer from the hot core, comparing results from the DBA model with a full Monte Carlo ray tracing simulation.

SF	ϵ_p	# of particles in hot core	Total heat transfer from core (W)		
			Monte Carlo	DBA	Error
0.25	0.65	83	83.59	85.07	1.77%
0.25	0.86	83	107.68	111.00	3.09%
0.35	0.65	116	89.62	90.64	1.14%
0.35	0.86	116	116.78	118.84	1.76%
0.45	0.65	153	94.73	93.70	-1.09%
0.45	0.86	153	125.90	125.13	-0.61%
0.55	0.65	195	96.22	98.23	2.08%
0.55	0.86	195	131.05	134.03	2.27%
0.64	0.65	219	95.10	95.63	0.56%
0.64	0.86	219	131.99	133.00	0.76%

The lowest error is for the packed bed case of $SF = 0.64$, which is likely due to the dense and consistent packing compared to the lower solid fractions. The $SF = 0.25$ case shows the highest error, where the relatively larger space in between particles leads to more variation in particle positions and shading effects. Overall, the results predicted by the DBA model are shown to vary up to 3.09% when compared to the Monte Carlo simulation, which indicates the DBA model is accurate enough for many engineering applications. The number of particles in the heated core ranges from 83 to 219 particles depending on the solid fraction, but if a simulation is run with very few particles the accuracy is expected to decrease due to less radiation interactions included in the summation of the total heat transfer from the core.

However, since most DEM simulations are typically run with tens of thousands to hundreds of thousands of particles, this is not foreseen as a major constraint for the DBA model once it is implemented in a DEM code.

4.3.2 Validation of Particle-Wall DBA Model

To validate the PW portion of the DBA model, the domains studied consisted of 24,000 particles with a radius of 0.01 m, as shown in Figure 4.7. All particles were assigned a temperature of 1000 K, and the wall temperature was specified at 1010 K. The total heat transfer was calculated from the wall to a hemispherical-shaped group of 500 particles using Eq. (4.1). These particles are shown in red in Figure 4.7, where half of the domain is made semi-transparent to expose this region. The particle group is in the center of the domain to eliminate photons lost to the surroundings.

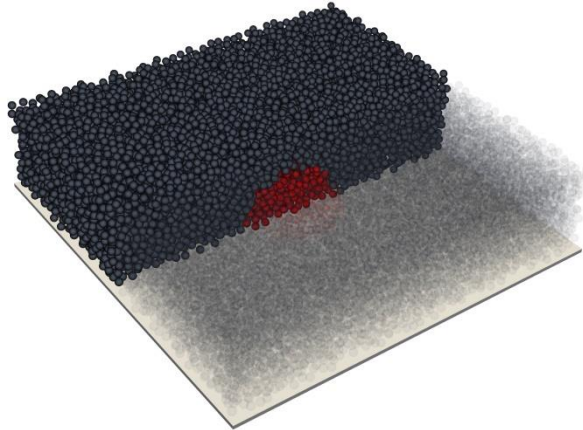


Figure 4.7. Particle-wall domain with a SF_{bulk} of 0.45. Half of the domain is semi-transparent to show the red particles included in the PW heat transfer calculation.

Total heat transfer from the wall to the red particle group was calculated, with PW RDF values found using both the Monte Carlo code and the DBA model. With two particle emissivities, four wall emissivities, and five bulk solid fractions, a total of 40 PW RDF-distance curves are given in Appendix B. A validation simulation was run for each of the 40 cases, and the total PW heat transfer is shown in Table 4.3. In all cases, the total heat transfer from the wall to the group of particles has a

difference of less than 2% between the two methods, indicating that each curve can predict the PW heat transfer to a sufficient accuracy for many engineering applications.

Table 4.3. Total heat transfer rate (W) from the wall to the red particles in the hemispherical volume, comparing Monte Carlo and DBA results for each PW RDF curve presented in Appendix B.

SF _{bulk}	ϵ_p	$\epsilon_w = 0.40$			$\epsilon_w = 0.60$			$\epsilon_w = 0.80$			$\epsilon_w = 1.00$		
		MC	DBA	Error	MC	DBA	Error	MC	DBA	Error	MC	DBA	Error
0.25	0.65	64.71	65.11	0.63%	93.25	93.88	0.67%	119.66	120.46	0.67%	144.36	145.19	0.57%
0.25	0.86	68.92	69.46	0.78%	101.99	102.74	0.73%	134.14	135.12	0.73%	165.50	166.58	0.65%
0.35	0.65	52.20	52.77	1.09%	74.97	75.75	1.04%	95.84	96.84	1.05%	115.03	116.23	1.05%
0.35	0.86	55.80	56.48	1.22%	82.48	83.31	1.01%	108.19	109.42	1.13%	133.32	134.74	1.07%
0.45	0.65	45.46	44.68	-1.72%	64.96	63.85	-1.71%	82.75	81.28	-1.77%	99.00	97.22	-1.80%
0.45	0.86	36.96	36.33	-1.71%	72.14	70.87	-1.76%	94.48	92.91	-1.67%	116.12	114.18	-1.67%
0.55	0.65	38.58	38.43	-0.39%	54.95	54.79	-0.30%	69.81	69.57	-0.34%	83.31	83.01	-0.36%
0.55	0.86	41.62	41.49	-0.32%	61.28	61.12	-0.26%	80.33	80.06	-0.34%	98.68	98.33	-0.36%
0.64	0.65	35.29	35.38	0.27%	50.11	50.15	0.08%	63.30	63.44	0.24%	75.32	75.41	0.12%
0.64	0.86	38.40	38.44	0.11%	56.53	56.56	0.05%	73.86	73.96	0.13%	90.55	90.74	0.20%

The results in this section demonstrate the validity of the DBA model for calculating PP and PW heat transfer in the relatively simple geometries of Figure 4.6 and Figure 4.7. More complex circumstances remain to be examined in detail, such as varying solid fractions, particles near the exposed edge of a domain, and PW heat transfer in corners or round geometry such as tubes. However, with the current scope being the introduction of the DBA model, the validation simulations show that the DBA model can be used to predict RDFs and heat transfer within groups of particles and from particles to flat walls with reasonable accuracy.

4.4 Results and Discussion

4.4.1 Particle-Particle Results and Discussion

Simulations were run to find the PP RDF values for each combination of two particle emissivities (0.65, 0.86) and five solid fractions (0.25, 0.35, 0.45, 0.55, 0.64), and the smoothing spline fitted data is tabulated in Appendix A. Each simulation domain consisted of 50,000 particles with a radius of 0.01 m, and during the Monte Carlo simulation 1×10^6 photons were emitted from 500 randomly

selected particles to build each table. The high number of emitting particles was used to find a very accurate average PP RDF-distance curve, with any local particle position or solid fraction variations balanced out.

The PP RDF tables are plotted for particle emissivities of 0.65 and 0.86 in Figure 4.8 (a) and (b), showing each solid fraction studied. In both cases, the lowest curve is for a solid fraction of 0.64 because it has the densest packing, which stops photons from penetrating far through the particle group. Several interesting phenomena can be seen in Figure 4.8(c), where particle emissivities of 0.65 and 0.86 are shown for the highest (0.64) and lowest (0.25) solid fractions. For both solid fractions, the curve for $\epsilon_p = 0.65$ is lower than for $\epsilon_p = 0.86$, a difference that is especially pronounced at close range and for touching particles. With a lower emissivity, and therefore a higher reflectivity, a higher number of rays reflect off neighboring particles and are absorbed by the original emitting particle. This reduces the rays absorbed by the neighboring particles and results in a lower RDF. Also shown in Figure 4.8(c), the RDF for touching particles (distance of 2 radii) is actually less for low solid fractions (red curves) than for packed beds (blue curves), for the same emissivity. While at first it may seem that two touching particles should have the same RDF regardless of the packing of the surrounding particles, the difference again is due to the reflections. For two touching particles with many close neighbors, rays emitted from one particle may reflect off other neighbors before being absorbed by the particle touching the emitting particle. For a sparsely packed group of particles, the emitting particle has fewer neighbors in close proximity, so the likelihood of a photon reflecting off a neighbor towards the touching particle is low. Due to the difference in reflectivities, this trend is visible in the case of $\epsilon_p = 0.65$, but it is hardly visible for $\epsilon_p = 0.86$.

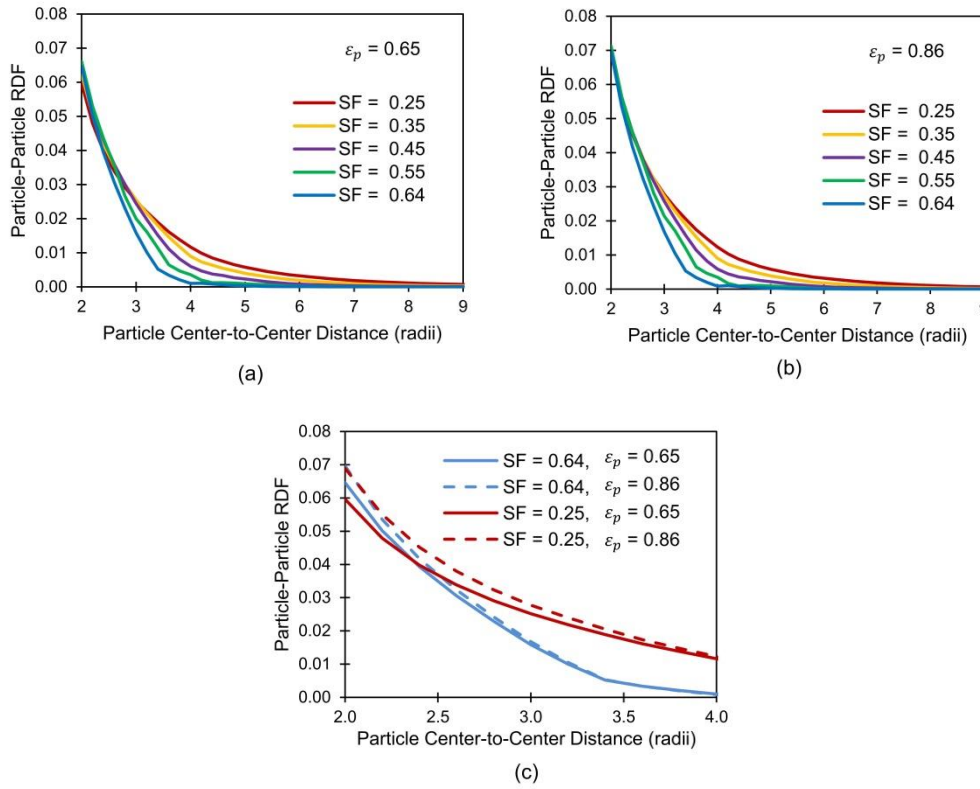


Figure 4.8. PP RDF as a function of distance for (a) $\epsilon_p = 0.65$, (b) $\epsilon_p = 0.86$, and (c) the extreme values of SF and ϵ_p .

Instead of presenting RDF-distance tables, expressing the RDF with an equation as function of distance would be more concise and easier to implement into a DEM code. However, no equation could be found to accurately represent the data in all cases because the mechanics of contacting particles often does not lead to a smooth curve. An example is shown in Figure 4.9(a) for SF = 0.64 and $\epsilon_p = 0.65$, where the data points make a distinct change in the curvature at ~ 3.25 and again at ~ 4 radii. The smoothing spline follows this change in curvature, whereas the curve fits of the form $y = a e^{-bx}$ and $y = a x^{-2} e^{-bx}$ (suggested by Liu et al. [66]) cannot follow these distinct changes in curvature. In the cumulative RDF graph in Figure 4.9(b) (similar to those shown in Section 4.3.1), the proposed equations do not match well with the MCRT results, and they each have a total PP RDF well above 1.00. In contrast, the cumulative RDF curve found by interpolating the points of the

smoothing spline matches the Monte Carlo results very closely, showing the higher accuracy of this method.

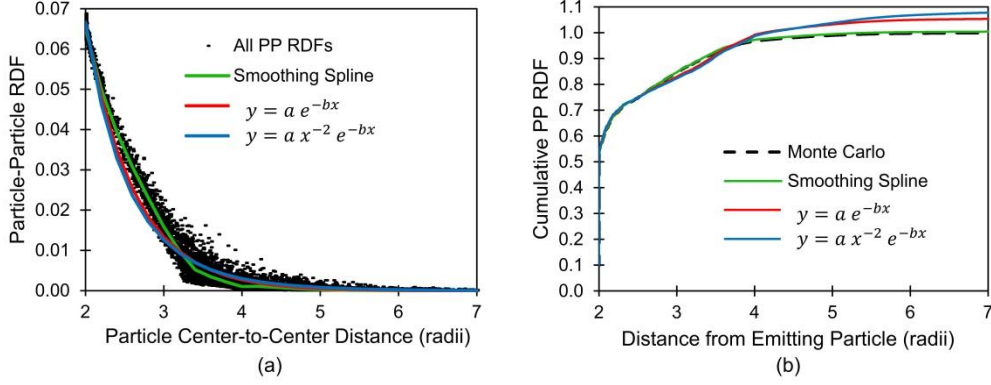


Figure 4.9. (a) Particle-particle RDF data and three proposed curves for SF = 0.64 and $\epsilon_p = 0.65$, and (b) Cumulative PP RDF at various distances from the emitting particle.

Another point of comparison is to the Short Range Model [46]. The total view factor, which is the same as the RDF for black particles, is calculated by the SRM as only 0.83 for a packed bed [46], which would lead to a large error in radiative transfer. Furthermore, the deviation of the total view factor from 1 only increases when particles are not tightly packed.

In a large DEM simulation, calculating the RDF between very distant particles is an unnecessary computational expense, since above a certain distance the RDF is negligible. To find the “cutoff” distance above which the PP radiative transfer can be omitted with negligible loss of accuracy, the cumulative PP RDF curve from the Monte Carlo simulation was analyzed to find the distance at which 99.9% of the photons had been absorbed. These distances are given in Table 4.4, and the tables in Appendix A are truncated to zero above these values as well.

Table 4.4. PP center-to-center cutoff distance based on 99.9% of photons absorbed.

Solid Fraction	PP Cutoff Distance (radii)	
	$\epsilon_p = 0.65$	$\epsilon_p = 0.86$
0.25	29.9	28.2
0.35	18.4	17.8
0.45	12.5	12.1
0.55	8.9	8.7
0.64	6.7	6.6

4.4.2 Particle-Wall Results and Discussion

PW RDF curves are found for each combination of two particle emissivities (0.65, 0.86), four wall emissivities (0.4, 0.6, 0.8, 1.0), and five bulk solid fractions (0.25, 0.35, 0.45, 0.55, 0.64), and tabulated results are found in Appendix B. Each domain consisted of 24,000 particles with a radius of 0.01 m, and during the Monte Carlo simulations 10^5 photons were emitted from 4000 particles. While there are 40 PW curves in total, several examples are shown in Figure 4.10. Results are plotted in Figure 4.10(a) for the case of $\epsilon_p = 0.65$, $\epsilon_w = 0.80$, and bulk solid fractions ranging from 0.25 to 0.64. The PW RDF is lowest for densely packed domains due to the many neighboring particles which intercept emitted rays, even for particles in contact with the wall (distance of 1 radius). The change in curvature around 3 radii is caused by the layering effect, as there are many particles with their centers in this region and very few with centers between 1 and 3 radii. Results are shown in Figure 4.10(b) for $\epsilon_p = 0.86$, $SF_{\text{bulk}} = 0.45$, and various wall emissivities, where low wall emissivities lead to low PW RDF values due to a higher portion of photons being reflected from the wall.

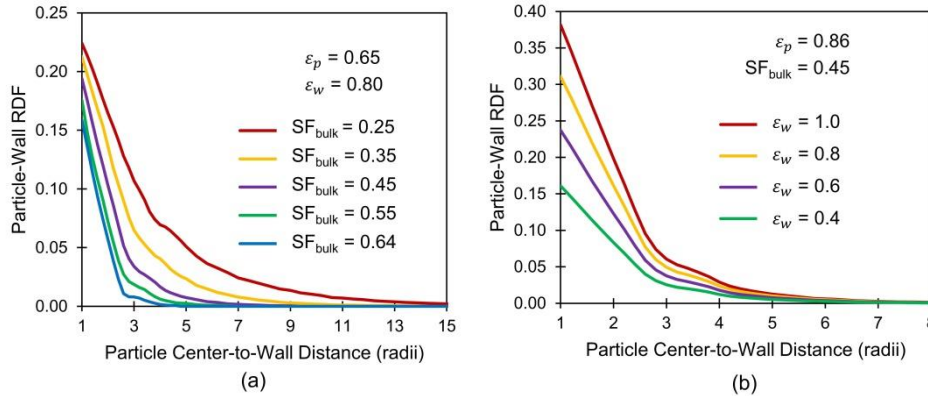


Figure 4.10. Particle-wall RDF for (a) $\epsilon_p = 0.65$, $\epsilon_w = 0.8$, and various bulk solid fractions, and (b) $\epsilon_p = 0.86$, $SF_{\text{bulk}} = 0.45$, and various wall emissivities.

Similar to the method applied to find the PP cutoff distance, cumulative PW RDF curves were constructed for each of the 40 cases using the Monte Carlo data, and the PW cutoff was determined as the point at which 99.9% of the total cumulative

PW RDF was reached. These values are given in Table 4.5 and the PW RDF tables are truncated above these values.

Table 4.5. PW cutoff distance based on 99.9% of photons absorbed.

Bulk Solid Fraction	$\epsilon_p = 0.65$ $\epsilon_w = 0.40$	$\epsilon_p = 0.65$ $\epsilon_w = 0.60$	$\epsilon_p = 0.65$ $\epsilon_w = 0.80$	$\epsilon_p = 0.65$ $\epsilon_w = 1.00$	$\epsilon_p = 0.86$ $\epsilon_w = 0.40$	$\epsilon_p = 0.86$ $\epsilon_w = 0.60$	$\epsilon_p = 0.86$ $\epsilon_w = 0.80$	$\epsilon_p = 0.86$ $\epsilon_w = 1.00$
0.25	22.2	22.2	22.2	22.2	21.7	21.7	21.7	21.7
0.35	14.1	14.1	14.1	14.1	13.7	13.7	13.7	13.7
0.45	9.2	9.2	9.2	9.2	8.9	8.9	8.9	8.9
0.55	6.8	6.8	6.8	6.9	6.6	6.6	6.6	6.6
0.64	4.7	4.7	4.8	4.8	4.6	4.6	4.6	4.6

The Monte Carlo code, and therefore the tables in Appendix B, gives the PW RDF values from one emitting particle to the entire wall. Therefore, when using the PW RDF values to calculate the heat transfer using Eq. (4.1), the entire wall must have a uniform temperature for the equation to be applied correctly. However, if a non-uniform temperature boundary condition is used by dividing the wall into surface mesh elements, as is common in CFD-DEM simulations, Eq. (4.1) can still be implemented by considering T_w to be the temperature of the closest wall element, and all heat transfer can be assumed to be to that element. Using Eq. (4.1) in this way is a valid approximation as long as temperature gradients along the wall are small over a length scale of several particle diameters, as the majority of PW heat transfer occurs close to the particle. This is true in almost all “unresolved” CFD-DEM simulations (when the particle size is smaller than the CFD mesh elements) [53] because the particle diameter must be several times smaller than the length of the element.

For highly reflective walls, the wall reflections can actually affect the RDF values between particle pairs. For example, in the extreme case of a wall with a reflectivity of 1, a pair of particles has a higher PP RDF if they are both touching the wall than they would in the center of a group of particles, due to the photons that are emitted from one particle which are reflected off the wall and then strike the second particle. However, this effect is relatively minor because it only affects particle pairs that are touching or nearly touching the wall. Furthermore, in many circumstances, such as the heat transfer simulation in Figure 4.11, the direction of

the heat flux is largely perpendicular to the wall, so two neighboring particles which are both touching the wall have very similar temperatures, and an error in the PP RDF due to wall reflections will contribute little to the error in actual heat transfer. Special near-wall PP RDF values could be investigated, but for the initial implementation of the DBA model this effect was neglected.

4.5 Modeling Radiation in a Dense Granular Flow

The initial implementation of the DBA model in a dynamic DEM simulation was performed for particles descending with gravity through a channel which is heated on one side, representing the conditions present in a particle heat exchanger or solar receiver with a dense granular flow [20][21][24]. The purpose is to demonstrate and discuss the DBA model implementation and to examine the radiative transfer in detail, so radiation was the only heat transfer mode considered. The channel, shown in Figure 4.11, has widths in the x and z directions of 10 mm, and the heated section is between $y = 20$ mm and $y = 40$ mm. The current implementation includes a DEM modeling step and a subsequent heat transfer modeling step, which are executed by separate codes.

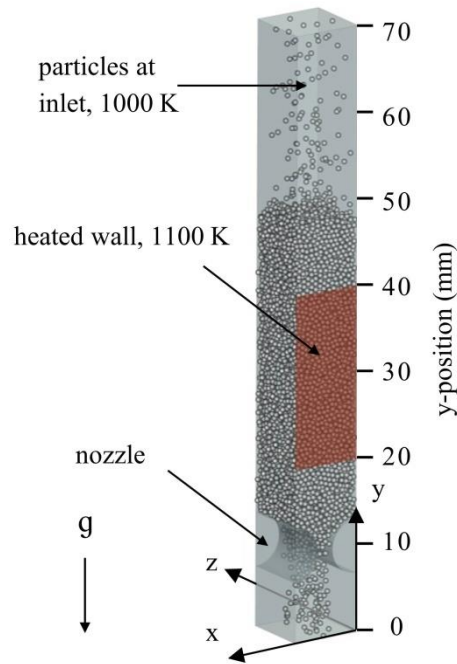


Figure 4.11. Simulation domain of a heated channel in dense granular flow.

First, LIGGGHTS was used to model the particle positions over time as they flow downward and drain through the nozzle. A group of 5000 particles with a radius of 500 μm was inserted into the domain, and after every 1000 DEM time steps the xyz positions of all particles were saved to a text file output. Boundaries on the z-planes at 0 and 10 mm were modeled as walls, while the boundaries on the x-planes at 0 and 10 mm were periodic, meaning particles could pass through one plane and reappear on the other. This was done to make the packing in the x-direction uniform by avoiding any layering effects, therefore making the simulation represent a channel of infinite length in the x-direction. The boundaries in the y-direction were also periodic, so as particles flowed out through the nozzle they reappeared with the same x-z position and velocity at the top of the domain. Thus, the total number of particles was always maintained at 5000, and the fill level at the top of the dense granular flow remained relatively constant over time at roughly $y = 48$ mm, above the heated section of the wall. Parameters used in the simulation are found in Table 4.6, with particle properties representing sintered bauxite [56][83][84]. However, the density and specific heat capacity values were

purposefully chosen to be less than the actual values. If the actual values are used, the outcome is a very thin thermal boundary layer, making the results less insightful when analyzed in detail and verified using the Monte Carlo simulation, which will be done in the following sections.

Table 4.6. Properties and boundary conditions used in the DEM and heat transfer simulations.

Parameter	Value
Number of Particles	5000
DEM Time Step	1×10^{-6} seconds
Radiation Time Step	1×10^{-3} seconds
Particle Radius	500 μm
Particle Material Density	1000 kg m^{-3}
Young's Modulus	$1 \times 10^9 \text{ N m}^{-2}$
Poisson's Ratio	0.30
Coefficient of sliding friction, PP	0.72
Coefficient of sliding friction, PW	0.30
Coefficient of rolling friction, PP	0.13
Coefficient of rolling friction, PW	0.50
Coefficient of restitution, PP	0.82
Coefficient of restitution, PW	0.44
DEM boundary type at $x = 0$ and $x = 10$ mm	periodic
DEM boundary type at $z = 0$ and $z = 10$ mm	wall
Specific heat capacity	100 $\text{J kg}^{-1} \text{K}^{-1}$
Particle emissivity	0.86
Wall emissivity, heated surface	0.60
Wall emissivity, all other walls	0
Particle temperature at inlet	1000 K
Initial particle temperatures	1000 K
Thermal boundary condition, heated surface	1100 K
Thermal boundary condition, all other walls	adiabatic

After the DEM modeling was complete, the radiative heat transfer was modeled using a separate code written in the Julia programming language [80]. In this code, the xyz position files from each DEM time step were read, and the net heat transfer rate to each i particle ($q_{i,net}$) was found with Eq. (4.2), which is simply the summation of Equations (3.1) and (4.1) over all other j particles, where $n_{particles}$ is the total number of particles in the simulation. PW heat transfer for each particle was only calculated with the heated section of the wall at $z = 0$ for $20 < y < 40$ mm, as all other boundaries are specified with $\varepsilon_w = 0$. As the goal is to analyze heat exchange in the dense granular flow, any PP heat transfer was neglected in the inlet region ($y > 50$ mm) and exit region ($y < 10$ mm). Particles exiting through the nozzle and reentering at the top were reset to 1000 K to keep the inlet temperature constant as the simulation progresses in time.

$$q_{i,net} = \varepsilon_p A_p \sigma D_{iw} (T_i^4 - T_w^4) + \sum_{j=1}^{n_particles} \varepsilon_p A_p \sigma D_{ij} (T_i^4 - T_j^4) \quad (4.2)$$

After calculating $q_{i,net}$ for each particle using Eq. (4.2), Eq. (4.3) was used to find the temperature ($T_{i,n}$) of each sphere i at the time step n based on the temperature at the previous time step ($T_{i,n-1}$), after a duration of one radiation time step (Δt_{rad}). The DEM time step size (Δt_{DEM}) must be extremely small due to limitations in the equations governing the collision mechanics [85], but changes in radiative transfer are more gradual and can therefore be recalculated much less frequently to save computation time, meaning the value of Δt_{rad} chosen can be many times that of Δt_{DEM} without loss of accuracy. The choice of Δt_{rad} will be examined in detail later in this section. Using Eq. (4.3), with m being the mass of one particle and C_p being the specific heat capacity of the particles, the temperature of each sphere i is found at time step n , and the heat transfer simulation can then proceed to the next time step.

$$T_{i,n} = T_{i,n-1} + \frac{q_{i,net} \Delta t_{rad}}{m C_p} \quad (4.3)$$

The RDFs D_{ij} and D_{iw} require interpolating within the tabulated data based on both the distance and the solid fraction. In general, for simulations where the bulk solid fraction is not uniform in space or time, the solid fraction must be calculated locally and at each radiation time step. However, in this simulation a simplification was made to use a single bulk solid fraction value because it was found to change minimally across all time steps and for all y-positions within the dense flow region of the domain. Therefore, the bulk solid fraction for the region adjacent to the heated wall ($20 < y < 40$ mm) was calculated to be 0.6278 at a time of 1.35 seconds, which is after a steady state is established, as will be shown later in this section. This bulk solid fraction value was used throughout the radiative transfer code for all time steps.

One important adjustment to the solid fraction was necessary to implement the PP RDF tables for particles near a wall. The PP RDF tables were developed assuming

a large group of particles with a nearly uniform solid fraction, but in the current simulation the local solid fraction varied due to layering effects against the wall (as shown in Figure 4.3(c) in Section 4.2.5). A separate near-wall region was implemented to account for this difference, taken to be between 0 and 5 radii in this simulation. The near-wall solid fraction in this region was calculated to be 0.5728, somewhat lower than the bulk value of 0.6278. In the heat transfer simulation, if both particles i and j were within 5 radii of the wall, then the near-wall solid fraction was used for determining the PP RDF from the tables, and if not, the bulk solid fraction was used. Accounting for the lower near-wall solid fraction in this way increases the accuracy of the current simulation in the near-wall region, but additional research is necessary to investigate if this approach can be generalized for various conditions, such as flow over more complex geometries, low solid fractions, and in different flow regimes. This type of adjustment is not necessary for the PW RDF tables because they were developed using domains of particles adjacent to a wall, so the varying solid fraction is already incorporated into the RDF-distance curve.

Several results relevant to the design or optimization of a particle heat exchanger are shown in Figure 4.12. The total heat transfer rate from the wall to the particles is likely the key metric for a heat exchanger, which is shown as a function of time in Figure 4.12(a). There is an initial transient phase with high heat transfer due to the initial particle temperatures of 1000 K coming in contact with the heated surface at 1100 K, and after a thermal boundary layer has developed, a steady state is achieved after roughly 1.35 seconds where heat transfer from the wall remains relatively constant at ~ 2.11 W. There is some variation even after reaching this steady state due to slight changes in the bulk particle velocity caused by frictional effects and bridging through the nozzle. Particle temperatures at 1.35 seconds are shown in Figure 4.12(b), where a thin thermal boundary layer forms and particle temperatures increase towards the lower edge of the heated surface. PW heat transfer for each particle is shown in Figure 4.12(c), where heat transfer is highest near the inlet and declines in the direction of flow.

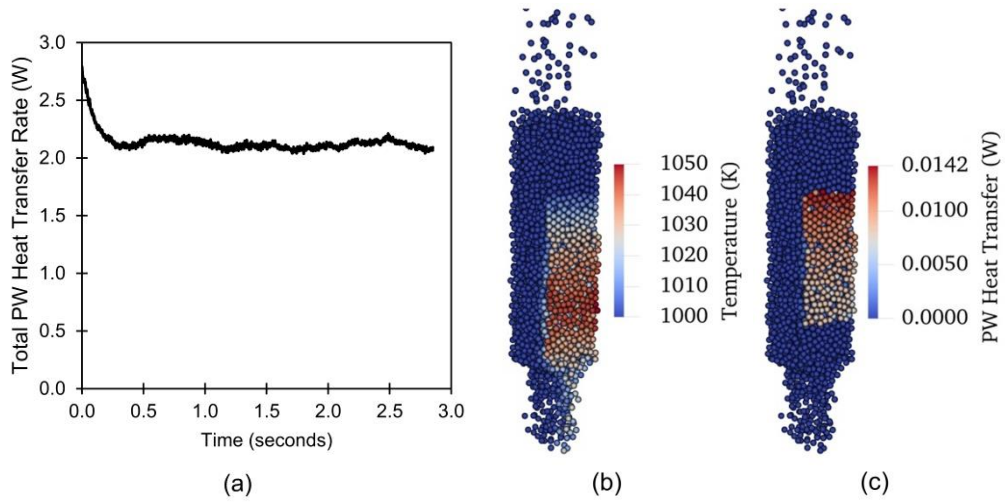


Figure 4.12. (a) Total PW heat transfer over time, (b) steady state particle temperatures, and (c) steady state PW heat transfer per particle.

To save computational time, the radiation time step size (Δt_{rad}) can be chosen to be many times larger than the value of Δt_{DEM} , and the accuracy of the simulation is not diminished as long as the chosen value of Δt_{rad} is small enough; a valid Δt_{rad} can be selected by running the radiation simulation with sequentially smaller values until the overall physical results cease to change. In this study, simulations were run with eight different Δt_{rad} values between 0.001 and 0.1 seconds (equivalent to 1000 and 100,000 DEM time steps), and results are compared in terms of the steady state heat transfer rate from the wall to the particles (over a time of 1.35 to 2.85 seconds) in Figure 4.13. In this case, using successively smaller Δt_{rad} values results in a lower heat transfer rate from the wall, but when Δt_{rad} is reduced from 0.002 to 0.001 the difference in heat transfer is only 0.00056 W or 0.026%, showing that further reducing Δt_{rad} would have very little impact on the results. An interesting observation is that even when Δt_{rad} is 0.02 seconds, equivalent to 20,000 DEM time steps, the heat transfer is only 0.59% different from the result found with a Δt_{rad} of 0.001 seconds, which may be an acceptable error in some simulations and could save significant computation time. In this simulation, a relatively high Δt_{rad} value is acceptable due to the dense granular flow regime modeled, which exhibits very little mixing and a very low relative velocity between PP and PW pairs, so the RDFs change minimally between sequential DEM time

steps, and therefore the estimated RDF values remain accurate for a relatively long time. In contrast, for simulations with a high relative velocity between particles such as fluidized beds, the RDF values change much more between each DEM time step, and the Δt_{rad} value required would be much lower. In the following results and analyses a Δt_{rad} value of 0.001 is used to maximize accuracy.

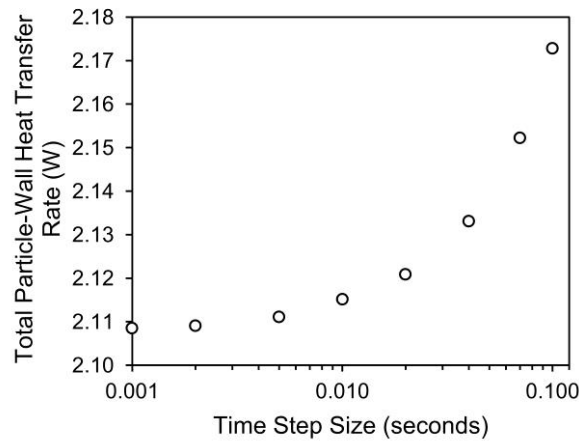


Figure 4.13. Steady state heat transfer rate from the wall, comparing results with various radiation time step sizes.

With 5000 particles and a simulation with hundreds of time steps, running a validation simulation using the Monte Carlo code to find the accurate RDF values at every time step is computationally unreasonable. However, a comparison can still be made by analyzing a single time step in detail using both a Monte Carlo simulation and the DBA model. The time step chosen to analyze is at 1.35 seconds, after a steady state has been established. For the xyz particle positions at this time step, the RDFs from each particle to every other particle and the wall were calculated with the Monte Carlo code and estimated with the DBA model. The net PP and PW heat transfer rate to each particle was then found using Eq. (4.2), and the mean PP and PW heat transfer per particle is plotted as a function of distance from the wall in Figure 4.14. The mean PP heat transfer is shown in Figure 4.14(a), where the particles against the wall (at a distance of 1 radius from the wall) have the highest temperature, and these particles transfer heat to the cooler particles on the interior of the domain, resulting in a large, negative PP heat transfer per

particle. The cooler interior particles receive this heat, resulting in the positive heat transfer per particle above 2 radii from the wall, which diminishes until a distance of 10 radii from the wall, after which almost no heat is transferred between particles. Similarly, the mean PW heat transfer is shown at various distances from the wall in Figure 4.14(b). As expected, the PW heat transfer is highest for particles in contact with the wall, and it quickly reduces with increasing PW distance. The chart shows that the PW heat transfer is negligible for distances greater than ~ 5.5 radii, which agrees with the PW cutoff distance range given in Table 4.5. Comparing the trends and values in Figure 4.14, a close match is shown between the DBA and Monte Carlo results for both PP and PW heat transfer. The overall PW heat transfer is calculated to be 2.025 W and 2.028 W with the Monte Carlo simulation and DBA models respectively, a difference of 0.14%, indicating the validity of the DBA model in the simulation.

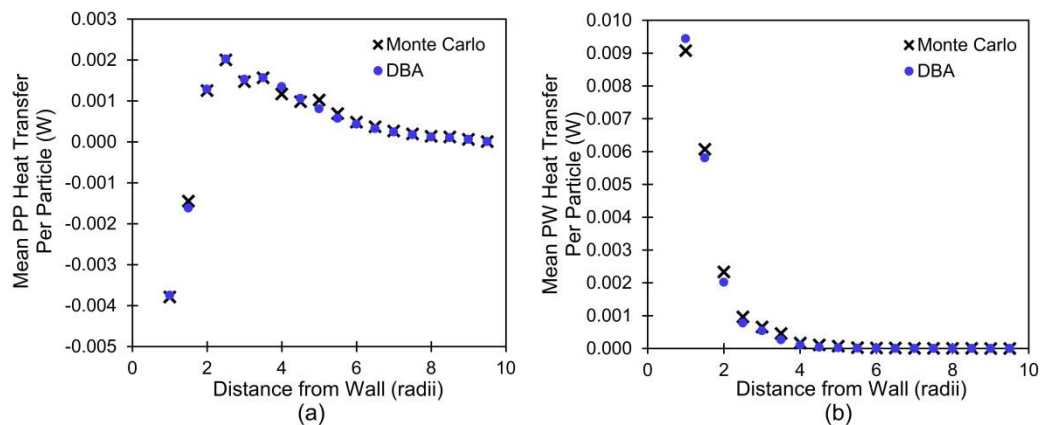


Figure 4.14. (a) Mean PP heat transfer per particle, and (b) mean PW heat transfer per particle, both as a function of distance from the wall.

4.6 Conclusions and Future Work for DBA Model

A method is presented to estimate the particle-particle and particle-wall radiative transfer by using a Distance Based Approximation (DBA) of the RDF between PP and PW pairs. Once the RDF-distance curve is established, the DBA model is both simple to implement and has a low computational cost in a DEM code, requiring

only two equations and an evaluation of the RDF with a lookup table. RDF tables are provided for solid fractions of 0.25, 0.35, 0.45, 0.55 and 0.64, particle emissivities of 0.65 and 0.86, and wall emissivities of 0.4, 0.6, 0.8 and 1.0, and these can be copied and directly implemented into DEM codes by other researchers. Several simulations have demonstrated the validity of both the DBA methodology and the actual curves provided, with errors typically less than ~2-3% in overall heat transfer between two groups of particles or between a group of particles and an adjacent wall.

An initial implementation of the DBA model in a dense granular flow shows it can accurately predict overall radiative transfer, by showing a high level of agreement with a full Monte Carlo solution for a time step analyzed in detail. It was demonstrated that a radiation time step in the range of 0.001 to 0.02 seconds (equivalent to 1000 to 20,000 DEM time steps) or less would be acceptable for the current simulation, but a lower radiation time step would likely be required in situations with higher particle velocities such as fluidized beds or falling particles.

The DBA model can potentially be used in many applications, but carefully analyzing the validity in more challenging situations is left for future work. For situations where the solid fraction varies in space and time such as in groups of fluidized or falling particles, the solid fraction must be recalculated locally and at each radiation time step. For modeling internal or external particle flow in contact with round tubes, the PW RDF tables provided are valid as long as the tube radius is much larger than the particle radius, though the degree of the size difference required has not yet been investigated. Particles in very thin channels, particles near two or more walls, and particles on the edge of the domain should be treated and verified with care, as these situations diverge from the original assumptions under which the RDF tables were developed. Additional suggested future work is to implement the DBA model directly into DEM software such as the open source code LIGGGHTS, commercial software, or the in-house codes developed by many research institutions.

CHAPTER 5

AN OPEN SOURCE CODE FOR DENSE PARTICLE HEAT TRANSFER

Throughout this research, codes were developed to model heat transfer in dense particulate flows. Initially, a rudimentary form of the DBA model [67] was implemented directly in LIGGGHTS, but due to the challenges of working within the confines of that code, the approach was adopted where particle mechanics are modeled with LIGGGHTS, and heat transfer is calculated afterwards using a separate code. This code, which has been refined and annotated for others to use, is referred to as the Dense Particle Heat Transfer (DPHT) code. More information as well as the code itself can be found on the GitHub repository found at <https://github.com/ef-johnson/Dense-Particle-Heat-Transfer>.

The combination of DEM and DPHT can be considered a “one-way” coupling, where information only flows from the DEM model to the DPHT model, and not in the other direction. The benefit is that after running the DEM simulation once to find the particle positions over time, multiple thermal simulations can be run to investigate the different thermal variables (e.g. temperature boundary conditions, particle thermal conductivity, etc.), without having to re-run the DEM simulation (which often takes the majority of the simulation time). The disadvantage of one-way coupling is that the mechanics cannot be modified based on thermal information, such as having temperature-dependent particle friction properties.

In the DPHT code, heat conduction models from literature are implemented, and several of them are modified to be more physically realistic. The DBA model is used for radiation, similar to the implementation shown in Section 4.5. While previous researchers have implemented similar codes for their own use, there is no open source code for heat transfer in dense granular flows that has been published and explained in detail for others to use and build upon.

5.1 Motivation

There are numerous industrial applications of dense granular flows with heat transfer, including many in CSP research. Modeling these processes at the particle level is still relatively new, and when models are described in literature, they are often performed with in-house codes. The current options for researchers or students are to develop their own code, which may take months or years, or to use an available DEM code such as LIGGGHTS.

While LIGGGHTS has some basic models for heat transfer, the features present are not nearly robust enough to simulate most industrial processes. Numerous heat transfer mechanisms are absent which are important in a dense flow, including particle-fluid-particle and particle-fluid-wall conduction, and PP and PW radiation. In addition, any mesh used as a boundary can only be given a single wall temperature, whereas it is much more useful to specify the wall temperature as a function or to assign various wall elements different temperatures. Within LIGGGHTS, the PP and PW conduction model for contacting particles has been implemented, but it appears to overestimate heat transfer by a factor of $\sqrt{\pi}$ (see Section 5.4.1). Additionally, heat transfer does not require recalculations nearly as frequently as the DEM simulation requires, which would save an enormous amount of computation time compared with executing heat transfer calculations at every DEM time step. Finally, for researchers interested in implementing their own model, modifying or adding to LIGGGHTS is cumbersome due to the many dependent functions and source files, and relatively little notation is provided in the C++ source code.

The aim of developing DPHT is to provide other researchers with a code that A) has all of the main heat transfer modes already implemented; B) has been validated under a basic set of circumstances; and C) is flexible enough so it can be easily adapted for similar work. Furthermore, to make it easier for others to adopt, the full workflow using all open source software is described here, starting from geometry generation and ending in heat transfer modeling with DPHT.

5.2 Applications and Assumptions

The DPHT code is valid for the special case of dense granular flows, as the interstitial fluid can be considered stationary with respect to the particles. Because the relative movement between the air and particles is negligible, no heat is transported away from the particles by convection. Heat transfer across the small fluid gap between particles is still modeled, but only as conduction through the stagnant fluid. This simplifies the model greatly because the fluid is not modeled explicitly as a separate phase, so only the particle phase must be modeled, and the more complex and computationally intense coupled CFD-DEM method is avoided. This approach has been taken previously by Qi and Wright [45] who studied a screw reactor and Chaudhuri et al. [86] who studied rotary calciners.

In addition, this approach neglects the heat absorbed by the fluid phase, which is almost always a valid assumption in CSP devices, as the heat capacity of the solid particles is much greater than the interstitial air. The assumptions of the radiation model follow those in Section 3.1, including uniform particle temperatures and geometric optics, with all spheres having gray, diffuse emissions and reflections.

The DPHT code could be directly useful for other CSP researchers who study devices with dense granular flows. For example:

- Watkins [21] studied dense granular flow through gravity-fed tubes as a solar receiver concept, but the “two-layer” model developed is not general; it is valid for only vertical tubes. If there were any mixing geometry or an orifice introduced, which are potential ways to significantly increase heat transfer, the two-layer model would not be valid.
- Albrecht and Ho [24] studied a particles-to-sCO₂ heat exchanger consisting of parallel plates with particles in a gravity-driven dense granular flow. An Eulerian approach was taken, and heat transfer equations were solved with effective properties. This approach works for the parallel plates geometry studied, but similar to work by Watkins described above, if the geometry is

varied by adding features to mix the flow, such a simple approach is invalid. Also, radiation was neglected.

- Baumann and Zunft [22][87] studied a “moving bed heat exchanger” for CSP where particles flow with gravity over a bank of horizontal tubes to heat the fluid (steam) flowing on the interior of the tubes. The authors point out discrepancies between the flow field in the experimental setup (taken with particle image velocimetry), and the Euler-Euler model. Particles form a stagnant region above (upstream of) each tube and an empty pocket below (downstream). This behavior is quite different from that of a fluid, so some disagreement between the experiment and model can be expected due to the continuum assumption inherent to Eulerian models.

Numerous other devices have been studied which could use DPHT either directly or with some additions or modifications, such as the CentRec receiver [16], the recently-proposed transparent tubular receiver [88], and the hexagonal tube receiver by NREL [17]. The DPHT code can also be used for other industrial processes, such as static powder beds used for laser sintering [71] and rotating kilns [89]. In contrast, DPHT is not applicable for particles falling through air or in fluidized beds.

5.3 Software Notes

DPHT is intended for use in Ubuntu (Linux) because it has been developed using tools such as LIGGGHTS and ParaView, which are most often run on Linux-based operating systems. DPHT is written in the Julia language because it is free to use, and it is nearly as simple as programming with Matlab (including many functions which are nearly identical). Simultaneously, it offers very fast computation speeds due to its “just-in-time” compilation scheme. Almost all other languages are either easy to program but slow (interpreted languages, e.g. Matlab, Python, Perl, Ruby), or more difficult to program but fast (compiled languages, e.g. C++, C, Fortran). Julia was built specifically to address the need for both speed and usability. Data

from benchmark tests [90] shows that Julia is comparable in speed to C, and it may be an order of magnitude faster than Matlab, depending on the nature of the code. Unlike Matlab, performing operations in vectors is not needed for speed, as *for* loops are generally faster than vector operations in Julia, making the programming more straightforward in many circumstances. The DPHT code takes advantage of parallel processing in Julia by using multi-threaded *for* loops for the bulk of the operations, leading to a large decrease in the run time over a serial code.

In addition to the DPHT code, a DEM code such as LIGGGHTS is needed to solve for the particle positions before DPHT can be run. As described in Section 5.7, several additional programs are needed for modeling, including a CAD drawing program (such as Onshape), surface meshing software (such as Gmsh or Ansys), and visualization software (ParaView), all of which can be obtained at no cost.

5.4 Heat Transfer Models

Each heat transfer mode is shown in Figure 5.1 and described in the following sections, which can be found in the code files *PP_ht.jl* and *PW_ht.jl*.

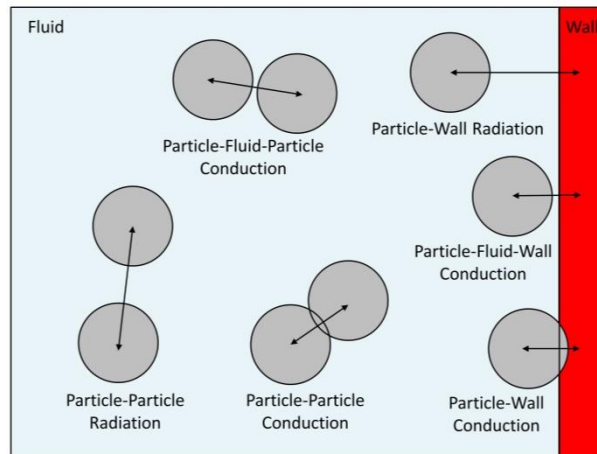


Figure 5.1. The six heat transfer modes included in DPHT.

The heat transfer modes are shown in more detail in Figure 5.2. The models for particle-fluid-particle (PFP) and particle-fluid-wall (PFW) heat transfer can be visualized with the sequence of red and purple arrows.

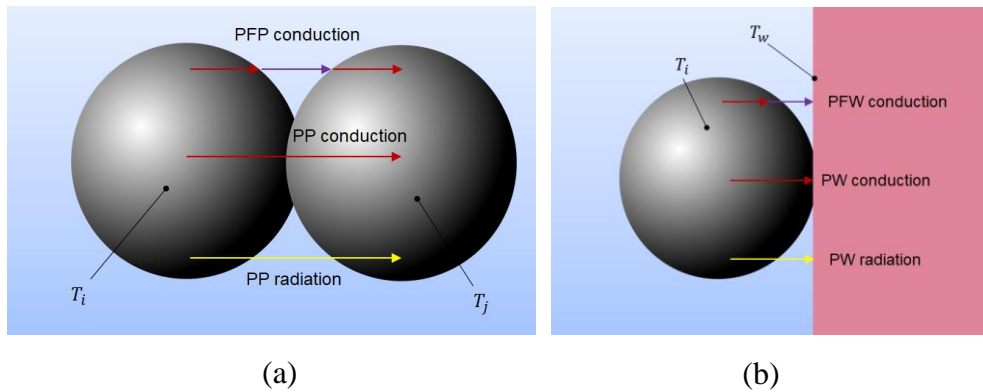


Figure 5.2. (a) The three particle-particle heat transfer modes, and (b) the three particle-wall heat transfer modes (blue = fluid, red = wall).

One note should be made about terminology: many of the studies referenced below, as well as the LIGGGHTS documentation, use the term *heat flux* to refer to the heat transfer rate between two particles (in units of Watts). Technically, this is not correct, since a heat flux must have units of power per area. To be clear, each of the heat transfer modes below solves for the heat transfer rate in Watts.

5.4.1 Particle-Particle Conduction

A model for conduction between two particles has been suggested by Batchelor and O'Brien [91] in 1976, given in Eq. (5.1). The thermal conductivity of the solid particle is k_s , and T_i and T_j are the temperatures of the two particles. In DEM models, two contacting spheres are allowed to overlap slightly, and r_c is the radius of contact of the overlapping lens, as shown in Figure 5.3. The degree of overlap is exaggerated in the figure for clarity, but it is very slight in an actual DEM simulation.

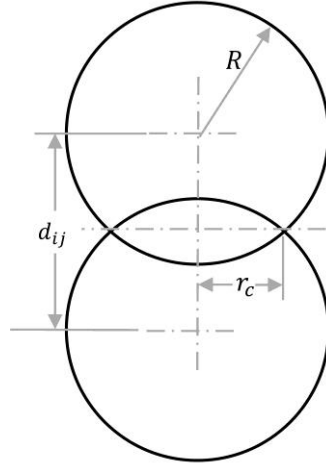


Figure 5.3. Geometry of two contacting spheres used to calculate PP conduction..

$$q_{cond} = 2k_s r_c (T_i - T_j) \quad (5.1)$$

This equation was originally derived for particles in static contact, though it has been used widely for dynamic calculations as well [86][92][93][94]. In the DPHT model, the PP distance is known, and the contact radius is found with Eq. (5.2), coming from the geometry of Figure 5.3.

$$r_c = \sqrt{R^2 - \left(\frac{d_{ij}}{2}\right)^2} \quad (5.2)$$

Since Eq. (5.1) was published by Batchelor and O'Brien, numerous researchers have modified it. In DEM modeling, typical practice is to use a Young's modulus several orders of magnitude lower than the actual material. This saves significant computation time by allowing for a larger DEM time step size, as this is limited by the Rayleigh and Hertz time step sizes, which are both functions of the Young's modulus. By reducing the Young's modulus, the particles become softer, leading to the undesired side effect of an increased overlap area between two colliding spheres in DEM, which in turn results in an overestimation of heat transfer when using Eq. (5.1). According to Zhou et al. [95] multiplying Eq. (5.1) by the factor c corrects this overestimation, where Y_{DEM} and Y_{real} are the DEM-modeled and true Young's moduli, respectively.

$$c = \left(\frac{Y_{DEM}}{Y_{real}} \right)^{1/5} \quad (5.3)$$

The equation implemented in the LIGGGHTS code is given in Eq. (5.4). The equation is similar, but not identical to, the Batchelor and O'Brien equation. The first term in parentheses represents an effective conductivity in case the particles have different thermal conductivities. If the two particles have the same thermal conductivity, this term becomes simply k_s and the equation is nearly identical to Eq. (5.1) by Batchelor and O'Brien.

$$q_{cond} = \left(\frac{2}{\frac{1}{k_i} + \frac{1}{k_j}} \right) 2\sqrt{A_c}(T_i - T_j) \quad (5.4)$$

The only difference between the LIGGGHTS version and the Batchelor and O'Brien version is the term $\sqrt{A_c}$, instead of r_c , where A_c is the contact area and r_c the contact radius. Though the makers of LIGGGHTS cite Chaudhuri et al. [89], that paper cites the original Batchelor and O'Brien equation, so the equations should all be the same. Substituting $A_c = \pi r_c^2$ into Eq. (5.4), it is clear that heat transfer is overpredicted by a factor of $\sqrt{\pi}$ or 1.77 in LIGGGHTS, compared to the cited paper. It appears to be a mistake in the LIGGGHTS implementation which may have implications for any researchers who have used or plan to use LIGGGHTS for heat transfer calculations.

5.4.2 Particle-Wall Conduction

The PW conduction model is essentially the same as the PP conduction model of Eq. (5.1), with several modifications. The contact radius r_c is found with Eq. (5.5), where R is the particle radius and d_{iw} is the particle-center to wall distance.

$$r_c = \sqrt{R^2 - d_{iw}^2} \quad (5.5)$$

The particle and wall thermal conductivities are combined to form an effective conductivity ($k_{p,w}$) from the particle conductivity (k_{si}) and wall conductivity (k_{sw}), following the method from Cheng et al. [94].

$$k_{p,w} = \frac{2}{\frac{1}{k_{si}} + \frac{1}{k_{sw}}} \quad (5.6)$$

The c factor is calculated with Eq. (5.7), which is interpreted from Zhou et al. [95] for the case where particles have different properties. The Poisson's ratios are ν_i and ν_j respectively, $Y_{i,DEM}$ and $Y_{j,DEM}$ are the Young's moduli used in the DEM simulation, and $Y_{i,real}$ and $Y_{j,real}$ are the Young's moduli of the actual materials. In this case, the particle j is taken to be the wall.

$$c = \left(\frac{\left(\frac{1 - \nu_i^2}{Y_{i,real}} \right) + \left(\frac{1 - \nu_j^2}{Y_{j,real}} \right)}{\left(\frac{1 - \nu_i^2}{Y_{i,DEM}} \right) + \left(\frac{1 - \nu_j^2}{Y_{j,DEM}} \right)} \right)^{1/5} \quad (5.7)$$

5.4.3 Particle-Fluid-Particle Conduction

The heat conducted across the stagnant fluid gap between two nearby particles is modeled with the particle-fluid-particle (PFP) conduction mode, for both contacting and non-contacting particles. In the DPHT code, this is often referred to as q_{conv} for ease of nomenclature, but technically the heat transfer is due to conduction instead of convection, as the fluid is stagnant.

The model implemented comes from Cheng et al. [94]. The derivation starts by building a ‘‘Voronoi’’ polyhedron around each particle, and a ‘‘double pyramid’’ is defined, where the base of each pyramid is the Voronoi polyhedron between the two spheres, and the pyramid edges are defined by connecting lines between each vertex of the Voronoi polyhedron and the center of the particle, forming the point of the pyramid. There is no analytical solution for such an arbitrary geometric pyramid, so a similar, simpler geometry is adopted consisting of two opposing cones, for which an analytical solution is possible. The cone bases lie on the center-

plane between the particles, the cone points are at the particle centers, and the volume of the cone is the same as the original double pyramid formed with the Voronoi polyhedron. A diagram showing the cone geometry is shown in Figure 5.4(a) for non-contacting particles and in Figure 5.4(b) for contacting particles, where orange lines designate the outline of the double cone.

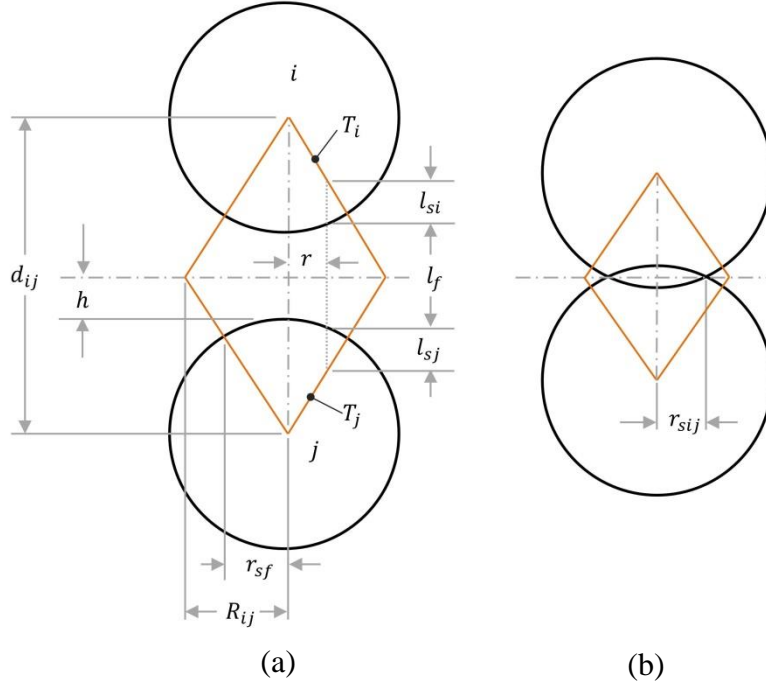


Figure 5.4. Dimensions relevant to Eq. (5.9) for calculating PFP conduction, showing (a) non-contacting and (b) contacting spheres. Outline of the double cone volume is shown in orange.

This treatment allows for an analytical calculation of heat transfer to particle i from particle j . The original form presented by Cheng et al. is shown for reference in Eq. (5.8). However, a mathematically identical form is shown in Equations (5.9)-(5.11), which is much more intuitive because, along with Figure 5.4, it reveals how the equation was derived.

$$q_{PFP,ij} = (T_j - T_i) \int_{r_{sij}}^{r_{sf}} \frac{2\pi r dr}{\left[\sqrt{R^2 - r^2} - \frac{r(R+h)}{R_{ij}} \right] \left(\frac{1}{k_{si}} + \frac{1}{k_{sj}} \right) + 2[(R+h) - \sqrt{R^2 - r^2}]/k_f} \quad (5.8)$$

In the geometry shown in Figure 5.4, the cone surfaces are considered isothermal at T_i and T_j . From Eq. (5.9), it is clear that the heat flux is assumed to be 1D and parallel to the vector between the particle centers. This equation uses resistances to heat conduction in a series configuration, where (referring Figure 5.4) at a certain radius r , heat first conducts through the solid in particle i a distance of l_{si} , then it conducts across the fluid gap a distance of l_f , and finally it conducts through particle j until it reaches the cone surface, after a distance of l_{sj} . In Eq. (5.9), k_{si} , k_{sj} , and k_f are the thermal conductivities of particle i , particle j , and the fluid, respectively. Because particles are assumed to be monodisperse in the current work, the distance traveled through the solid is the same for each sphere ($l_{si} = l_{sj}$). These distances are solved with Equations (5.10) and (5.11) for a certain radial location (r) in terms of the particle radius (R), the cone base radius (R_{ij}), and the distance from the center plane to the closest “tip” of the particle (h). This distance h is found with Eq. (5.14). The lower integration limit (r_{sij}) is taken as zero for non-contacting particles, or the contact radius (r_c) for overlapping particles. The upper integration limit (r_{sf}) represents the intersection of the cone and the sphere, calculated with Eq. (5.12).

$$q_{PP,ij} = (T_j - T_i) \int_{r_{sij}}^{r_{sf}} \frac{1}{\left(\frac{l_{si}}{k_{si}} + \frac{l_f}{k_f} + \frac{l_{sj}}{k_{sj}}\right)} 2\pi r \, dr \quad (5.9)$$

$$l_{si} = l_{sj} = \sqrt{R^2 - r^2} - \frac{r(R + h)}{R_{ij}} \quad (5.10)$$

$$l_f = 2 \left[(R + h) - \sqrt{R^2 - r^2} \right] \quad (5.11)$$

$$r_{sf} = \frac{R_{ij}R}{\sqrt{R_{ij}^2 + (R + h)^2}} \quad (5.12)$$

$$R_{ij} = \sqrt{\frac{3V_{ij}}{\pi d_{ij}}} \quad (5.13)$$

$$h = \frac{d_{ij} - 2R}{2} \quad (5.14)$$

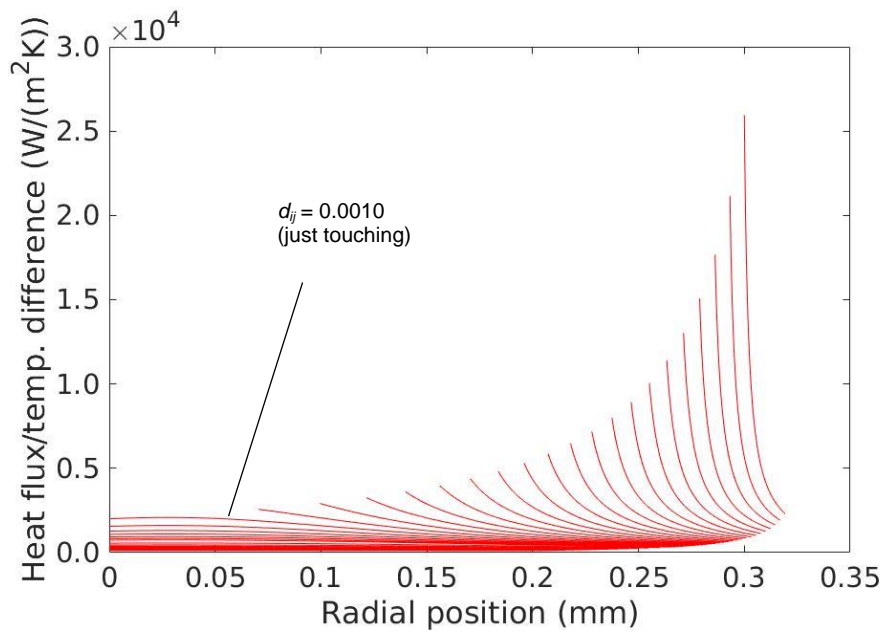
Unfortunately, in the original formulation of these equations, the cone base radius (R_{ij}) term must be calculated from the double pyramid volume (V_{ij}), which requires building the Voronoi polyhedra around all particles at each time step, a very computationally expensive process. To eliminate this requirement, Zhou et al. [93] interpreted the results from Yang et al. [96] to express the cone base radius as a function of only the particle radius and solid fraction (α_s). With this advancement, R_{ij} is much simpler to find using Eq. (5.15), and this eliminates the need to build the Voronoi polyhedra or use Eq. (5.13).

$$R_{ij} = 0.560R\alpha_s^{-1/3} \quad (5.15)$$

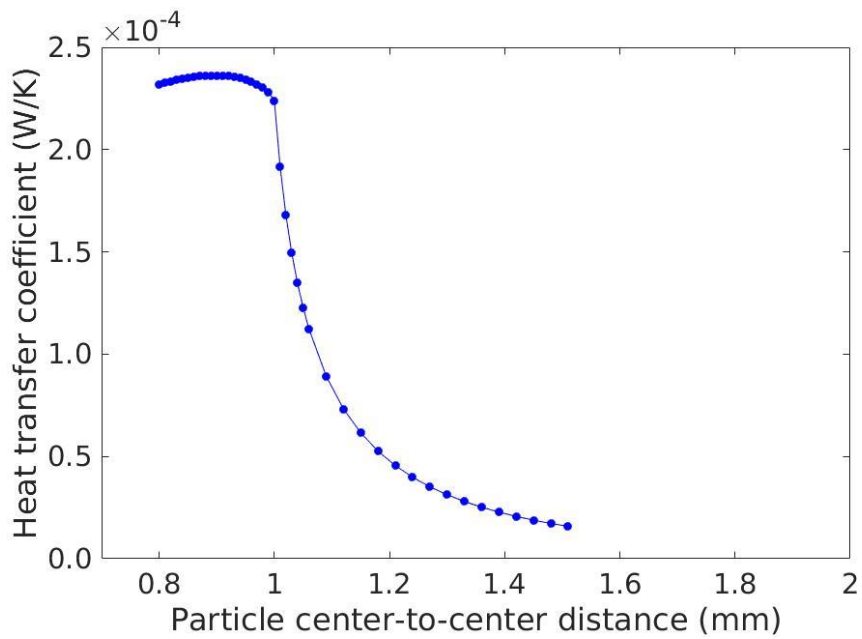
Instead of solving Eq. (5.9) within the main code at each time step, it is much more computationally efficient to use pre-calculated heat transfer coefficients as follows. Within the main function *go*, the function *PPF_conduction* is called once at the beginning of the simulation, which takes arguments of the solid fraction, the particle thermal conductivity, and the particle radius. This function computes the heat transfer coefficient (HTC) between two particles, where $q_{PPF,i} = HTC \times (T_j - T_i)$. This is done by numerically solving the integral in Eq. (5.9) using the trapezoid rule. These computations are repeated for many values of the particle distance (d_{ij}) and numerous temperatures, until a matrix of HTC values has been created, which is saved in the file *htc_values.txt*. Temperature must be included as a parameter because it affects the thermal conductivity of the fluid; the current implementation contains the values for air, which changes thermal conductivity by a factor of ~ 2.5 between room temperature and 750 °C. Within the code, the temperature for evaluating PFP conduction is chosen as the mean of the two particle temperatures. With the matrix of pre-calculated HTC values, the HTC for any two particles is found with a bilinear interpolation and multiplied by $(T_j - T_i)$ to find the PFP conduction in Watts. Thus, the computationally expensive

numerical integration must only be performed once, at the beginning of the simulation, making the calculation of heat transfer between particle pairs is very fast.

To verify the output of the function matches physical expectations, the quantity which will be integrated over $2\pi r dr$ (specifically, $\left[\frac{l_{si}}{k_{si}} + \frac{l_f}{k_f} + \frac{l_{sj}}{k_{sj}}\right]^{-1}$) is first plotted for numerous radial locations (r) in Figure 5.5(a). Each curve shows the heat flux at that radial location divided by the temperature difference between the two particles, and each curve represents a different particle pair separated by distance d_{ij} . When particles are overlapping, there is no PFP conduction at radial locations less than the contact radius, so the lines start at radial positions greater than zero in the figure. As expected, heat flux is highest at low radial locations, due to the ease of heat transfer through the thin fluid gap near the circle of contact.



(a)



(b)

Figure 5.5. PFP conduction as a function of distance, for $k_s=k_{sf}=2.0$, $k_f=0.0702$, $\alpha_s = 0.60$, and $R=0.0005$ m, showing (a) heat flux as a function of radial position, for various particle distances, and (b) heat transfer coefficient as a functions of particle distance (d_{ij}).

Next, the curves in Figure 5.5(a) are numerically integrated over $2\pi r dr$ with the trapezoid rule to calculate the integral in Eq. (5.9), thus solving for the HTC at each PP distance, with results shown in Figure 5.5(b). According to Zhou et al. [93], heat transfer becomes negligible for $\frac{h}{R} > 0.5$, or equivalently, $d_{ij} > 3R$. This recommendation is followed in the DPHT code with PFP conduction neglected for particles at a distance greater than 3 radii. The integration is repeated for a range of temperatures to account for varying fluid thermal conductivity with temperature, leading to the curves in Figure 5.6. These values are saved in *PFP_htc_values.txt* and used to look up the HTC as a function of distance and temperature using the function *bilin_interp.jl*.

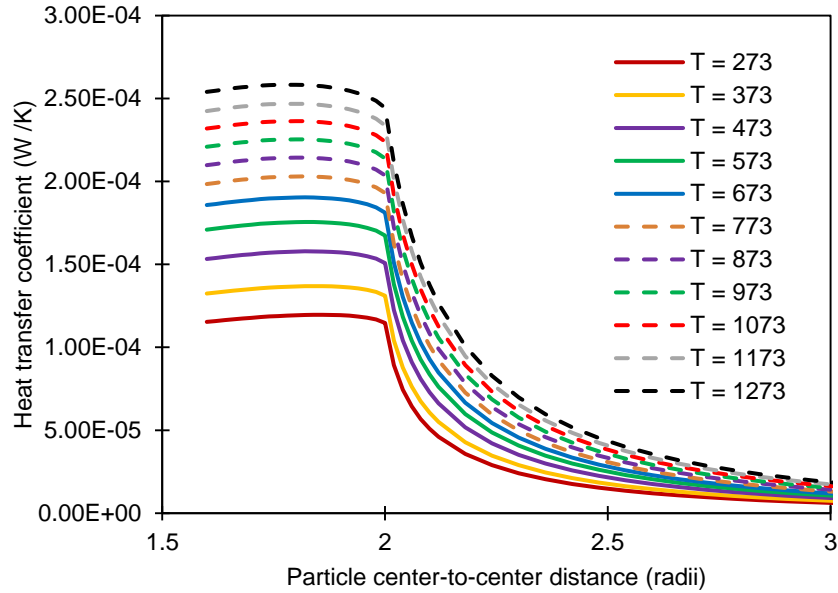


Figure 5.6. PFP heat transfer coefficient solved for various particle distances and temperatures (same parameters as Figure 5.5).

Similar to PP and PW conduction, because of the artificially low Young's modulus, the true distance between two contacting particles is less than it is in the DEM simulation. The relevant literature did not show a correction factor for PFP conduction, so one is derived here. The center-to-center distance between two particles within the DEM simulation ($d_{ij,DEM}$) is known, but to calculate the PFP conduction with the bilinear interpolation, the actual distance is desired ($d_{ij,real}$)

after taking into account the reduced Young's modulus. From the geometry of two overlapping spheres, Equations (5.16) and (5.17) relate the particle radius (R), the distance (d_{ij}), and contact radius of overlap (r_c) for both the real and DEM cases. Eq. (5.18) is another expression of the same c factor used previously (known from Eq. (5.3)) which relates the true and DEM-modeled contact radii.

$$R^2 = (d_{ij,DEM}/2)^2 + r_{c,DEM}^2 \quad (5.16)$$

$$R^2 = (d_{ij,real}/2)^2 + r_{c,real}^2 \quad (5.17)$$

$$c = \frac{r_{c,real}}{r_{c,DEM}} \quad (5.18)$$

Substituting and rearranging these three equations, the actual distance can be found in terms of the DEM-modeled distance, the radius, and c , to form Eq. (5.19). This corrected distance $d_{ij,real}$ can then be used in the bilinear interpolation of to find the HTC in PFP conduction. Using $d_{ij,real}$ instead of $d_{ij,DEM}$ has the effect of making contacting particles further away from each other, thus reducing PFP heat transfer. For non-contacting particles, this does not apply, and $d_{ij,real} = d_{ij,DEM}$.

$$d_{ij,real} = 2\sqrt{R^2 - c^2 [R^2 - (d_{ij,DEM}/2)^2]} \quad (5.19)$$

Initial tests were run to show the effect of this modification in terms of overall heat flow through the domain of particles found in Section 5.8. Results with the corrected and uncorrected d_{ij} differed by only a very small amount, showing this correction may not be needed in all cases. However, in this simulation the particles modeled were relatively hard, with a DEM Young's modulus of 10^8 . A larger difference is expected if softer particles are used in the DEM model, such as the minimum value allowable in LIGGGHTS (5×10^6 Pa) which is used by others [97]. Since the adjusted distance should be more physically realistic in all cases, it is used in the DPHT code in all modeling that follows.

5.4.4 Particle-Fluid-Wall Conduction

Qi and Wright [45] extended the PFP conduction model described above (originally from Cheng et al. [94]) to account for particle-fluid-wall (PFW) conduction. Their adaptation assumes that there is still a conduction resistance due to the wall. However, if the boundary condition is specified as T_w on the surface of the wall (as shown in Figure 5.7), there should be no heat transfer resistance due to the wall (i.e. heat does not have to conduct into the wall any distance to reach the specified T_w). Thus, there should only be two conduction resistances, as shown in Figure 5.7. This re-formulation of PFW conduction is given in Equations (5.20)-(5.22), and is thought to be more realistic. Note that now l_f is half of the value used in PFP conduction.

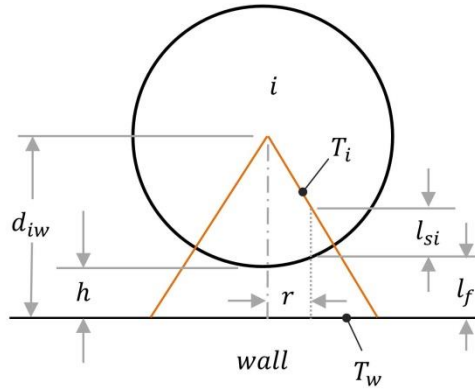


Figure 5.7. Particle-fluid-wall geometry.

$$q_{PFW,iw} = (T_w - T_i) \int_{r_{sij}}^{r_{sf}} \frac{1}{\left(\frac{l_{si}}{k_{si}} + \frac{l_f}{k_f}\right)} 2\pi r dr \quad (5.20)$$

$$l_{si} = \sqrt{R^2 - r^2} - \frac{r(R + h)}{R_{ij}} \quad (5.21)$$

$$l_f = (R + h) - \sqrt{R^2 - r^2} \quad (5.22)$$

When a particle overlaps the wall, we again must compensate for the artificially low Young's modulus for both the particles and the wall. Equations (5.23) to (5.25)

give the relations between particle radius (R), the particle-wall distance (d_{iw}), and contact radius (r_c) for both the DEM and real cases. The two cases are related through the factor c using Eq. (5.7). After substitutions, the real PW distance ($d_{iw,real}$) is found from the other known variables with Eq. (5.26).

$$R^2 = d_{iw,DEM}^2 + r_{c,DEM}^2 \quad (5.23)$$

$$R^2 = d_{iw,real}^2 + r_{c,real}^2 \quad (5.24)$$

$$c = \frac{r_{c,real}}{r_{c,DEM}} \quad (5.25)$$

$$d_{iw,real} = \sqrt{R^2 - c^2[R^2 - d_{iw,DEM}^2]} \quad (5.26)$$

Similar to in the PFP conduction case, this adjustment makes the particle center further away from the wall, reducing PFW heat transfer. This adjustment is only used for particles touching the wall.

Similar to PFP conduction, at the beginning of the DPHT simulation, the PW HTC is found for many temperatures and PW distances and saved in *PFW_htc_values.txt*. During the simulation, the bilinear interpolation is used to look up the correct HTC based on the PW distance and the temperature, where the temperature used is the mean of the particle and the nearest wall element. Example PW HTC curves are shown in Figure 5.8.

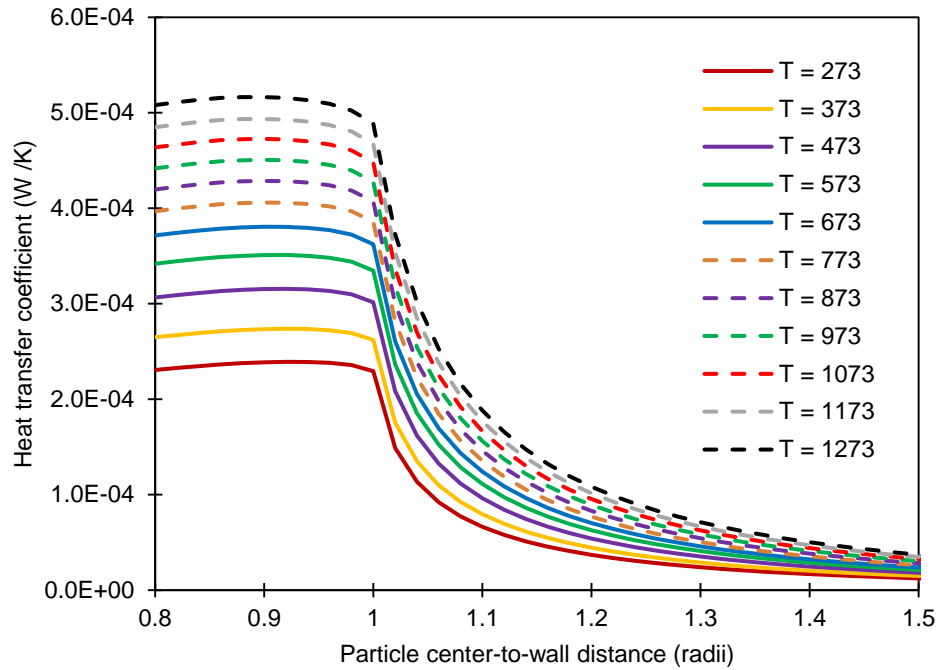


Figure 5.8. Particle-wall HTC values found for $k_s=2.0$, $\alpha_s = 0.60$, $R=0.0005$.

5.4.5 Particle-Particle and Particle-Wall Radiation

The Distance Based Approximation (DBA) model developed in Chapter 4 is implemented for both PP and PW radiation. The RDF tables are interpolated with the function *bilin_interp* using the PP or PW distance and the solid fraction. In the current DPHT code, separate solid fractions for the near wall region and for the bulk region have been used, as discussed in Section 4.5. These solid fractions must be calculated externally before the simulation is run and specified with the variables *VIF_near_wall* and *VIF_bulk*. The RDF tables must have the format of the first column being the PP or PW distance (in units of radii) and the first row being the solid fractions. Currently, RDF tables are available for solid fractions of 0.25, 0.35, 0.45, 0.55, and 0.64, for particle emissivities of 0.65 and 0.86, and for wall emissivities of 0.4, 0.6, 0.8, and 1.0. If different conditions are desired, these tables must be generated by finding the RDF as a function of distance as described in Chapter 4 or interpolated between the known curves. With the RDF estimated,

the PP and PW radiative transfer can be found with Equations (5.27) and (5.28), where $q_{rad,ij}$ is the radiative transfer rate to particle i from particle j , $q_{rad,iw}$ is the radiative transfer rate to particle i from the wall, ε_p is the particle emissivity, A_p is the surface area of the particle, σ is the Stefan-Boltzmann constant, and T represents the temperatures, where T_w is the temperature of the closest wall element.

$$q_{rad,ij} = \varepsilon_p A_p \sigma D_{ij} (T_j^4 - T_i^4) \quad (5.27)$$

$$q_{rad,iw} = \varepsilon_p A_p \sigma D_{iw} (T_w^4 - T_i^4) \quad (5.28)$$

5.5 Boundary Conditions

Boundary conditions are specified in DPHT by assigning a temperature to each triangular wall element. Unlike in CFD, a heat flux boundary condition cannot be easily specified, as this would require distributing the specified heat transfer among the nearby particles, likely requiring iterations.

Before specifying the wall element temperatures, the walls must first be drawn and meshed, and the mesh information must be saved as three text files (*vertices.txt*, *centers.txt*, and *relations.txt*). This is demonstrated in Section 5.7.

At the beginning of the DPHT simulation the function *create_BC*s is run. The temperature of each element is assigned, which can be specified as a function of the centroid coordinates. With the three vertex locations of each wall element defined in *vertices.txt*, the equation of a plane is found for each wall element. The coefficients of each element's plane equation are saved in the file *bdry_data.txt* and will be used later to find the perpendicular distance to nearby particles. With this information, a matrix is built which has all of the wall element centroid locations, temperatures, and coefficients defining the plane of the element. An arbitrary geometry of wall elements is shown in Figure 5.9, and more details on the coding are given in Section 5.6.1.

The simulation iterates through each particle to calculate the PP heat transfer to nearby particles and PW heat transfer to the nearest wall element. While iterating through each particle, the closest wall element is identified by finding the minimum distance between the particle and the centroid of each wall element. In Figure 5.9, the closest centroid belongs to the element shown in red. The plane equation for the closest element (which has been pre-computed and saved in *bdry_data.txt*) is then used to calculate the perpendicular distance between the wall element and the particle center, shown as d_{iw} in the figure. A correct calculation of this distance is critical, as it is used in all three PW heat transfer models.

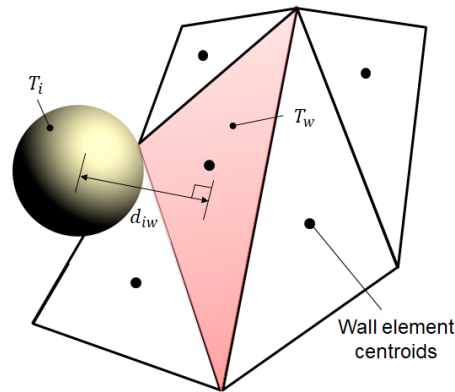


Figure 5.9. Particle and wall element geometry used for applying boundary conditions.

5.6 File Structure

Within the main DPHT folder, there are numerous folders and files, with the structure shown in Figure 5.10, and each is discussed below.

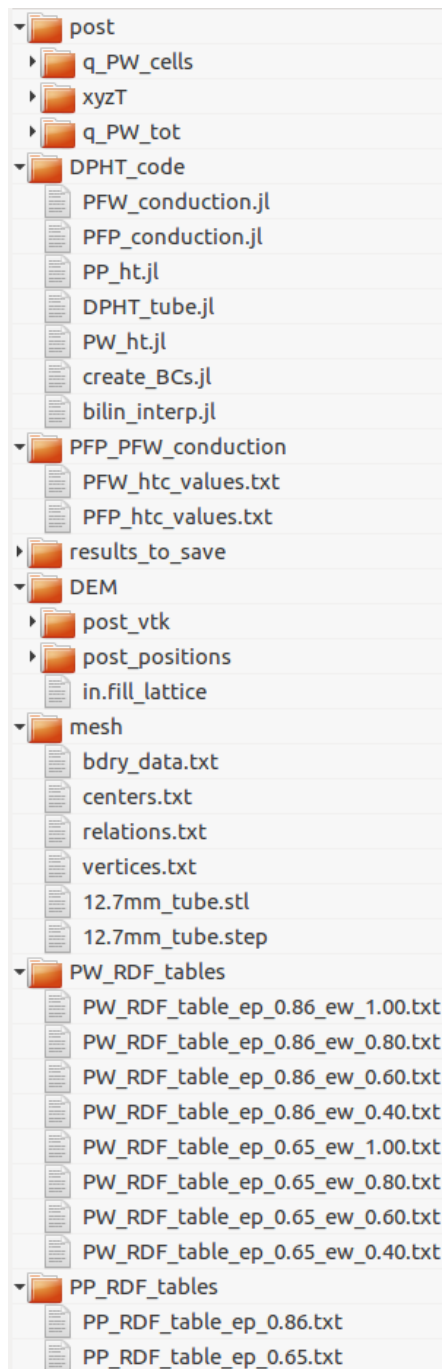


Figure 5.10. DPHT file structure.

5.6.1 DPHT_code

This folder contains all of the Julia functions required to run DPHT. The details of each file are described below:

- a. The file *DPH_tube.jl* contains the main function, which is simply called *go*. Several actions are taken at the start of the run. First, the user can select if the boundary condition file and the PFP and PFW conduction HTC matrices should be rebuilt or not, which is controlled by setting the booleans *rebuild_BC*s and *rebuild_PFP_cond* to true or false. The DEM time step size is set, which should match the *timestep* variable in the LIGGGHTS input file (in this case the file *in.fill_lattice*). The variable *LTS_stamp_delta* specifies the number of LIGGGHTS time steps in between each heat transfer calculation by DPHT, and the LIGGGHTS time steps to start and end are also specified. The number of threads for parallel processing is read in from an environment variable, which can be set by pasting the command `export JULIA_NUM_THREADS=4` (where 4 is the number of processors specified) into the `~.bashrc` file, or by typing this command directly into the terminal window before starting Julia. Next, various physical parameters and properties are set, such as the particle radius and particle thermal conductivity. Next, data is read in from several text files, including the RDF tables, PFP conduction HTC tables, and the boundary conditions corresponding to each wall element.

The next portion of the code executes at each time step, as specified by the variables *LTS_stamp_start*, *LTS_stamp_delta*, and *LTS_stamp_end*. At the current time step, the xyz position file and the temperature (in Kelvin) from the previously solved time step are read and stored in the vectors *xPos*, *yPos*, *zPos*, and *T*. The row number of these vectors can be thought of as the ID value for each particle, as the IDs remain unchanged throughout the simulation (this is because the command “*dump_modify dmpPos sort id*” is given in the LIGGGHTS input file, which orders the output file according to the particle ID). The functions *PP_ht* and *PW_ht* are called, where the actual heat transfer calculations are performed. These are included as functions, instead of keeping the functions in *go*, because the multi-threaded *for* loops work faster in their own functions. The outputs of these

functions are the vectors q_{PP} and q_{PW} , which contain the net heat transfer rate to each particle, in Watts. The function PW_{ht} also modifies the vectors q_{cond_wall} , q_{conv_wall} , and q_{rad_wall} which contain the heat transfer rates from each heat transfer mode to each wall element. Finally, the new temperature (T_{next}) of each particle is calculated based on heat transfer rates q_{PP} , q_{PW} , the thermal time step, and the heat capacity of the particle. Several output files are saved to the *post* folder, including the position and temperature of each particle at each time step, saved in the *xyzT* file. In addition to being a useful output to visualize particle temperatures over time (with a visualization program such as ParaView), the *xyzT* file is also used to save the temperature information for use in the next time step.

- b. The *PP_ht.jl* file contains the function *PP_ht*, where the PP heat transfer models are located. One key optimization step is found at the beginning of this function. The heat transfer must be evaluated from one particle to every other particle in the domain, though many are zero due to being far apart. In the code, this means calculating the heat transfer from each i particle to each other j particle, so if using a simple nested *for* loop, this would mean $n_{particles} \times n_{particles}$ heat transfer computations, where $n_{particles}$ is the number of particles in the simulation. However, the heat transferred from i to j is the same in magnitude but opposite in sign as from j to i , so iterating from 1 to $n_{particles}$ over both i and j is duplicative, and iterating j from 1 to i would suffice. For the specific case of $i = j$, this represents heat transfer from a particle to itself, which is clearly zero. Therefore, as implemented, the code iterates over all i particles (from 1 to $n_{particles}$), but it only iterates over j particles from 1 to $(i - 1)$. After calculating the heat transfer from i to j , this value is added to the total for the i particle and subtracted from the total of the j particle, which is stored in the q_{PP} vector. By switching to this iteration scheme, only half of the heat transfer calculations must be made, but multithreading in Julia presents one problem with this approach.

When using the threaded *for* loop with the *@threads* command, the iterators (*i* values) are split up by processors, with the first chunk given to the first processor, the second chunk given to the second processor, and so on (e.g. if there are three processors and *i* ranges from 1 to 9, processor 1 executes on *i* values from 1 to 3, processor 2 executes on *i* from 4 to 6, and processor 3 executes on *i* from 7 to 9). Unfortunately, with the *for* loop scheme described above, the iterations are extremely unbalanced in computation time; high *i* values must iterate through many *j* values, whereas low *i* values must iterate through fewer, so the lower numbered processors finish first and must wait for the higher numbered processors to finish, leading to a less than optimal run time. To fix this, a vector (*interleaved_ids*) is built which alternatively counts up and down (e.g. for *n_particles* = 100, *interleaved_ids* is: [1, 100, 2, 99, 3, 98... 49, 51, 50]). Then, the multi-threaded *for* loop is initiated with a variable *k*, but the actual *i* values for each processor to evaluate are found from the *interleaved_ids* vector. The outcome is that each processor gets an equal distribution of short jobs (low *i* values) and long jobs (high *i* values), and all should finish at roughly the same time, meaning the process has been optimized.

- c. The file *PW_ht.jl* contains the function *PW_ht*. Here, PW heat transfer is calculated between each *i* particle and each wall element. To find the PW distance, which is needed for the PW heat transfer models, the closest wall element center is identified, named *wall_id_closest*. The equation of the plane formed by each wall element in the form of $ax + by + cz + d = 0$, has already been pre-calculated at the beginning of the function *go* in the function *create_BC*s, and the coefficients *a* to *d* are stored in the matrix found in *mesh/bdry_data.txt*. The perpendicular distance from the particle-center to the plane of the nearest wall element is then calculated using these coefficients [98]. The temperature of the nearest wall element is found in the vector *T_wall*, and the heat transfer to the wall is then computed.

- d. The file *bilin_interp.jl* contains the function *bilin_interp*, which does the bilinear interpolations required in several places.
- e. The file *create_BC.jl* contains the function *create_BC*. It is called optionally at the beginning of *go*. It reads in three sets of data which define the surface mesh: the *vertices.txt* file contains the xyz locations of the vertices of the mesh, the *centers.txt* file contains the xyz locations of the centroid of each wall element, *relations.txt* contains the three vertex IDs corresponding to each wall element ID. The coefficients *a*, *b*, *c*, and *d* defining the plane of each wall element are calculated and output to the file *bdry_data*. The function *create_BC* is also where the boundary conditions for each wall element are set, by iterating through the wall elements and setting the variables *Temp* and *BC_type*. The variables *xCell*, *yCell*, and *zCell* can be used to set the element temperatures in any desired way, such as uniform temperature for all elements, or a linear variation in one direction (e.g. $Temp = 273 + 100 \times yCell$). In addition to *Temp*, the *BC_type* must also be set for each element: type 1 is a fixed wall temperature boundary condition, whereas type 2 is adiabatic, meaning any heat transfer interaction between this wall element and the nearby particles is ignored. This is useful in a scenario where, for example, one would like to neglect any heat transfer to the walls at the inlet section of a heat exchanger. These values are added to the *bdry_data* matrix and saved in *mesh/bdry_data.txt*.
- f. The file *PFP_conduction.jl* contains the function *PFP_conduction*. It is optionally called at the beginning of *go*, and it builds the matrix of HTC values needed for the PFP conduction heat transfer mode. The first row contains the temperature, the first column contains the PP distance (in meters) and the HTC values fill the matrix.
- g. The file *PFW_conduction.jl* behaves the same as *PFP_conduction.jl*, except the first column contains the PW distance.

5.6.2 Mesh

The *mesh* folder contains the files that define the triangular surface mesh, including *vertices.txt*, *centers.txt*, and *relations.txt*. The STL mesh file must also be stored in the *mesh* folder, as LIGGGHTS searches for the mesh used in the DEM simulation. Once the function *create_BC*s has been run, the file *bdry_data.txt* is also stored here.

5.6.3 PFP_PFW_conduction

This folder contains the heat transfer coefficients needed for the PFP and PFW conduction heat transfer modes, which are output to the files *PFP_htc_values.txt* and *PFW_htc_values.txt* by the functions *PFP_conduction* and *PFW_conduction*.

5.6.4 Post

This folder contains the simulation outputs. The files in *post/xyzT* contain the *xyz* position and temperature of each particle, with one file exported at each time step. This is useful for visualization of the particles and their temperatures in ParaView. The file *post/q_PW_tot/q_PW_tot.txt* contains one line for each time step. The columns show the time step, the total PW heat transfer rate at that time step (in W), and the individual contributions from PW conduction, PFW conduction, and PW radiation modes. Last, the *post/q_PW_cells* folder contains a file for each time step, with the *xyz* position of the cell center, the total PW heat transfer rate (in W), and the contributions from each PW heat transfer mode.

5.6.5 PP_RDF_tables

This folder contains the RDF tables for PP radiation. Each file has the format where the first column is the particle center-to-center distances (in radii) and the

first row is the solid fraction. The naming convention is *PP_RDF_table_ep_[particle emissivity].txt*, which must be followed so the correct table is chosen in the function *go*. Only PP RDF files for emissivities of 0.65 and 0.86 are currently available.

5.6.6 PW_RDF_tables

This folder contains the RDF tables for PW radiation. The format of the tables is the same as the PP RDF tables, but the distance column represents particle-center to wall distance, in units of radii. The naming convention used is *PW_RDF_table_ep_[particle_emissivity]_ew_[wall_emissivity].txt*, which again must be correct so the proper table can be chosen based on the emissivity values specified in the particle properties section of *go*. Currently, RDF tables for wall emissivity values of 0.4, 0.6, 0.8, and 1.0 are available.

5.6.7 Results_to_save

This folder, originally empty, can be used for storing the outputs from past runs. By default, the *post* folder is deleted (along with all data inside it) at the beginning of each simulation. To save the data, copy any outputs to the *results_to_save* folder.

5.7 Example Simulation with DPHT: Flow Through a Heated Tube

The following example shows how to model the heat transfer in a dense granular flow using DPHT, which requires several steps, including geometry creation, mesh generation, mesh element data extraction, DEM modeling, DPHT modeling, and post-processing. The software used below is all freely available.

5.7.1 Geometry Creation

This can be done in various software, such as SolidWorks, Onshape, or in Ansys. Onshape is free to use for non-commercial uses, and it has the benefit of being run fully within a web browser, so it can be run on any operating system. For this example, Onshape is used, and the tube and nozzle shown in Figure 5.11 are generated as surfaces with no thickness. This surface is exported in STEP format.

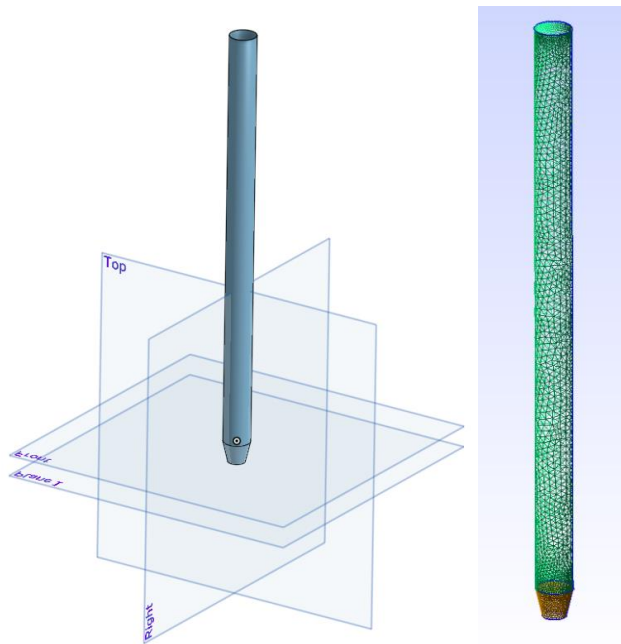


Figure 5.11. (a) Surface of tube with nozzle, drawn with Onshape, and (b) meshed surface using Gmsh.

5.7.2 Mesh Generation

Gmsh is used for this mesh generation (Figure 5.11 (b)), though there are many programs for mesh generation, including Ansys. The elements must be triangular for DPHT. In this instance, the dimensions have to be adjusted down using a factor of 0.001, which can be set using Tools > Options > Geometry > General > Global Model Scaling. The mesh can be adjusted by toggling between 2D and “refine by

splitting”, or by using many other more complex methods. The mesh is saved as file type STL.

5.7.3 Mesh Extraction

ParaView (version 5.8.0) is used to get the vertices, element centers, and relations into a usable file format for DPHT. It is also a time to check the mesh to ensure it is the expected size (in meters). After opening the STL file in ParaView, open a “spreadsheet view” to save the three necessary files:

- *vertices.txt*: as shown in Figure 5.12, make sure the STL file is selected, Attribute is set to Point Data, toggle the button with the “10” icon to ensure scientific notation is used, and Precision may be increased as needed. Use File>Export Scene to save the data as it is shown in the spreadsheet view, and name the file *vertices.txt*.

The screenshot shows the ParaView interface with the following settings: Showing: 12.7mm_tube.stl, Attribute: Point Data, Precision: 7. The table below is displayed in the spreadsheet view.

Point ID	Points	Points_Magnitude
0	0.00635 0.005 3.888253e-19	0.008082233
1	1 0.00635 0.0025 3.888253e-19	0.006824404
2	2 0.006260281 0.003115398 0.001063665	0.007073062
3	3 0.006260281 0.0006153... 0.001063665	0.00637975
4	4 0.00635 0 0	0.00635

Figure 5.12. ParaView settings for exporting the vertices.

- *relations.txt*: Switch Attribute to Cell Data, toggle the “{...}” icon to turn on the cell connectivity, and File>Export Scene, saving as *relations.txt*.

The screenshot shows the ParaView interface with the following settings: Showing: 12.7mm_tube.stl, Attribute: Cell Data, Precision: 7. The table below is displayed in the spreadsheet view.

Cell ID	Cell Type	Point Index 0	Point Index 1	Point Index 2	STLSolidLabeling
0	Triangle	0	1	2	0
1	Triangle	1	3	2	0
2	Triangle	1	4	3	0

Figure 5.13. ParaView settings for exporting the relations between cell IDs and vertices.

- *centers.txt*: Choose the “Cell Centers” filter, choose Point Data, and then File>Export Scene, saving as *centers.txt*.

Showing		CellCenters1		Attribute: Point Data		Precision: 7	
Point ID		Points		oints_Magnitud	STLSolidLabeling		
0	0	0.0063...	0.003538466	0.00035455...	0.007251899	0	
1	1	0.0062...	0.002076932	0.00070910...	0.006662052	0	
2	2	0.0063...	0.001038466	0.00035455...	0.006414648	0	

Figure 5.14. ParaView settings for exporting the cell centers.

5.7.4 DEM Modeling

The LIGGGHTS input file (*in.fill_lattice*) is found in the DEM folder. The STL mesh file created in Gmsh should be used in the *mesh/surface* command. The lattice filling method used in this file quickly inserts many particles into the domain. The simulation is periodic in the y-direction (vertical), so particles flowing out through the nozzle are re-inserted with the same x-z position and velocity, but at the top of the simulation domain. In this way, particles recirculate continuously from the bottom to the top, and the same number of particles is always present throughout the simulation. In the DPHT code the particle temperature will be reset to the inlet temperature each time the particle crosses the periodic boundary.

Open a terminal window within the DEM folder, and run LIGGGHTS with the command such as: `mpirun -np 3 ~/LIGGGHTS-PUBLIC/src/lmp_auto < in.fill_lattice`. Note: One change to LIGGGHTS can make working with the xyz position files easier. In the *src* folder, the source file *dump_custom.cpp* contains the function `void DumpCustom::header_item(bigint ndump)`. By commenting out all the lines of code contained in this function and recompiling LIGGGHTS (by issuing a “make auto” command in the *src* folder), the *dump/custom* command in the input file no longer include the ~9 lines of header information, making it easier to read and manipulate in Julia as well as other post-processing software such as Matlab or ParaView. In the function *go* of the DPHT code, particle positions are read using a *CSV.read* command where it is assumed this step has been done and there are no header lines in the xyz position file.

5.7.5 DPHT Modeling

To set up Julia to run DPHT for the first time, several steps are required. First, set the number of threads Julia will use for multithreading by adding a line such as “`JULIA_NUM_THREADS=20`” (where 20 is the number of threads you wish to specify) at the end of the hidden `.bashrc` file (found in the home folder). Second, it is easiest to open Julia using an alias, which can be done by adding another line in the `.bashrc` file such as “`alias julia='~/julia-1.5.2/bin/julia'`”. Then, Julia can be easily opened from any terminal by simply typing “`julia`”. Next, the DPHT code requires several downloadable packages, which can be installed by opening Julia, issuing the command “`using Pkg`” (to load the package management tool), and then using the following commands to add the necessary packages: “`Pkg.add(“CSV”)`”, “`Pkg.add(“DelimitedFiles”)`”, “`Pkg.add(“Formatting”)`”, “`Pkg.add(“Dierckx”)`”, and “`Pkg.add(“Printf”)`”.

After navigating to the `DPHT_code` folder and opening a terminal window, open Julia. Issue the command `include(“DPHT_tube.jl”)`, and then use the command `go()` to run the code. As shown in Figure 5.15, some information will be displayed including a report from the functions `PFP_conduction` and `create_BCs` at the beginning, and then at each time step the total PW heat transfer and execution times are given.

```

evanj@evanj-ThinkPad-Edge-E431:~/Documents/Particle_Modeling/heated_tube/DPHT_code
evanj@evanj-ThinkPad-Edge-E431:~/Documents/Particle_Modeling/heated_tube/DPHT_code$ julia
Documentation: https://docs.julialang.org
Type "?" for help, "j?" for Pkg help.
Version 1.5.2 (2020-09-23)
Official https://julialang.org/ release

julia> include("DPHT_tube.jl")
go (generic function with 1 method)

julia> go()
Thermal time step size: 0.004 sec
DEM time steps per thermal time step: 2000
Number of threads: 4
PP cutoff: 7
PW cutoff: 7

Executing PFP_conduction function.
Exporting disT, temp, and htc files to PFP_conduction folder.

Executing create_BC_array function.
Creating boundary conditions and exporting file to mesh folder.
5960 elements, and 3022 vertices

Number of wall elements: 5960
Number of particles: 22879
Time step: 1, DEM ts: 2000, q PW total: 57.766
  Loop timing: Total = 3.04, Init = 0.16, PP = 1.95, PW = 0.50, post = 0.44
Time step: 2, DEM ts: 4000, q PW total: 57.861
  Loop timing: Total = 2.83, Init = 0.57, PP = 1.60, PW = 0.57, post = 0.09
Time step: 3, DEM ts: 6000, q PW total: 57.690
  Loop timing: Total = 1.79, Init = 0.04, PP = 1.39, PW = 0.29, post = 0.07
Time step: 4, DEM ts: 8000, q PW total: 57.768
  Loop timing: Total = 1.82, Init = 0.04, PP = 1.42, PW = 0.29, post = 0.08
Time step: 5, DEM ts: 10000, q PW total: 57.717

```

Figure 5.15. Commands to run the DPHT code from the Julia terminal.

5.7.6 Post-Processing

After, or even during, the DPHT simulation, the results can be viewed with ParaView. Open the $xyzT$ data, deselect the “Have Headers” box in the “Properties” section, and change the “Field Delimiter Characters” to a space instead of a comma, as the output files from DPHT are space delimited. Choose the “Table to Points” filter, and in the Properties section, choose “X Column” as “Field 0”, “Y Column” as “Field 1”, and “Z Column” as “Field 2”. Change the “Representation” to “Point Gaussian” and change the “Gaussian Radius” to 0.0005 to match the particle diameter of 1 mm in the simulation. Change the coloring to be “Field 3”, and outputs can be seen such as Figure 5.16(a), which shows the view from the outside, and Figure 5.16(b) after it has been clipped at the $X=0$ plane to reveal a cross section.

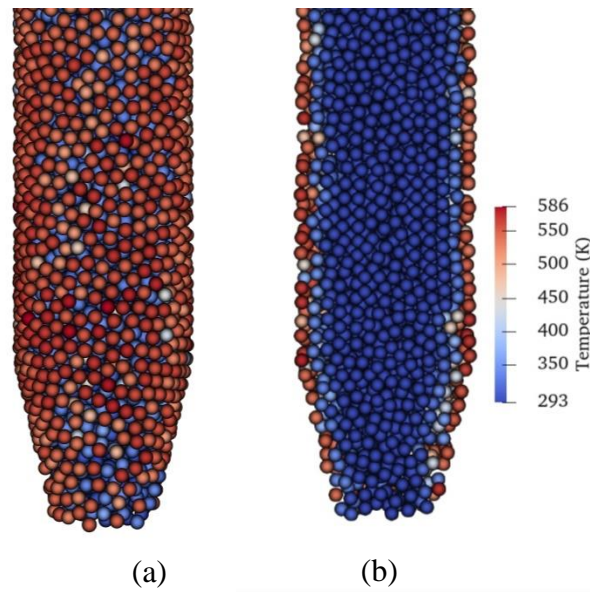


Figure 5.16. Particle temperatures at the outlet, showing (a) view from the outside, and (b) cross section view.

The overall PW heat transfer over time by each mode can be found in the output file *q_PW_tot.txt*, as shown in Figure 5.17. At the end of the simulation a steady state is nearly reached, and at this point the overall heat transfer to the particles is ~ 616 W, of which 2.8% is due to PW conduction, 80.9% is due to PFP conduction, and 16.4% is from PW radiation.

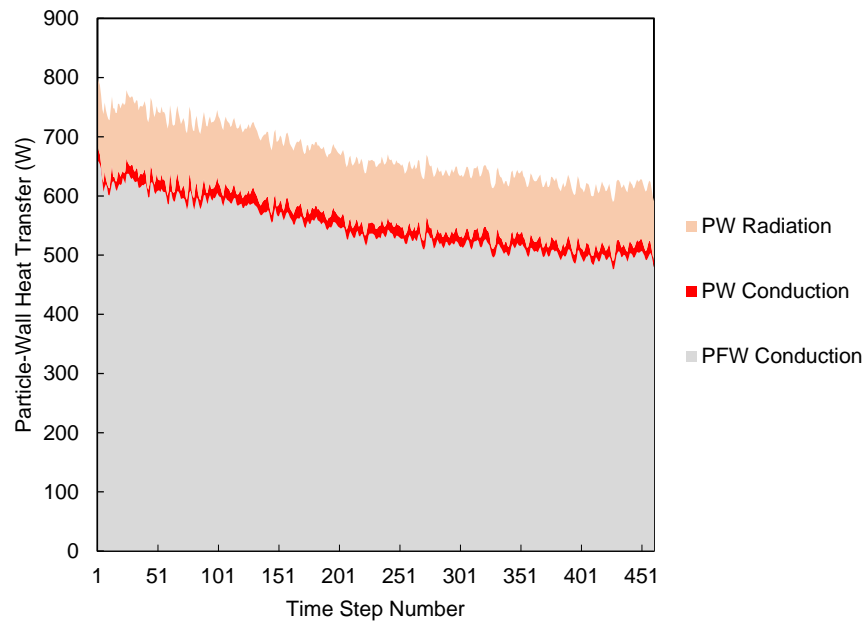


Figure 5.17. Total PW heat transfer over time, separated by heat transfer mode.

5.8 Comparison with ZBS Model

A simulation was run to compare the results of a DPHT simulation against the effective thermal conductivity (k_{eff}) predicted by the Zehner, Bauer, and Schlünder (ZBS) [31][32] model, which accounts for conduction through the fluid gap and via radiation. The simulation domain consisted of the rectangular prism shaped group of particles shown in Figure 5.18. The domain was created in LIGGGHTS by allowing particles to come to rest on top of a surface in the presence of gravity, and then the near-wall portions were removed to leave the particle group shown, so any influence from the walls on the packing structure was eliminated. The solid fraction was calculated to be 0.5924.

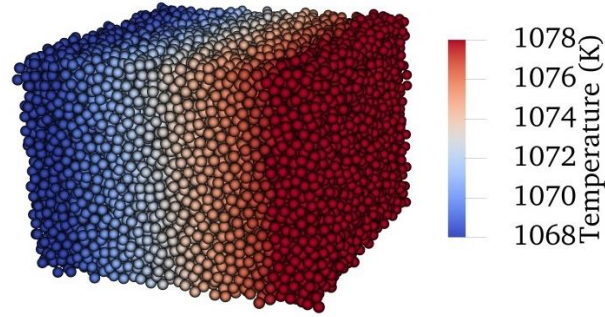


Figure 5.18. Simulation domain for finding k_{eff} from a DPHT simulation.

With the left and right sides of the region kept at 1068 K and 1078 K, the central particles were allowed to exchange heat until a steady state was reached. The linear temperature profile at steady state was plotted, and the slope of the line (i.e. the temperature gradient, $\frac{dT}{dx}$) was found, along with the total heat transfer from the hot to cold region (q) and cross sectional area (A_c). k_{eff} was then found with Eqn. (5.29). Because k_{eff} is temperature-dependent, using a large temperature difference between the hot and cold regions would cause k_{eff} to vary significantly from the hot to the cold region, and a non-linear temperature profile would result. Therefore, a small (10 K) temperature difference was used.

$$q = k_{eff} A_c \frac{dT}{dx} \quad (5.29)$$

This allows for the direct comparison to the continuum models of k_{eff} , such as the original ZS model [30] which only accounts for the heat conducted across the fluid gap between spherical particles, or the later ZBS model [31][32], which includes radiation. Results are shown in Figure 5.19, where the DPHT simulation results are compared to several models at four different temperatures. In the figure, the original ZS model [29] is used for the solid-fluid portion of k_{eff} , and the radiative portion is calculated with ZBS [31], Breitbach and Barthels (BB) [28], and the k_{rad} equation from Chapter 3.

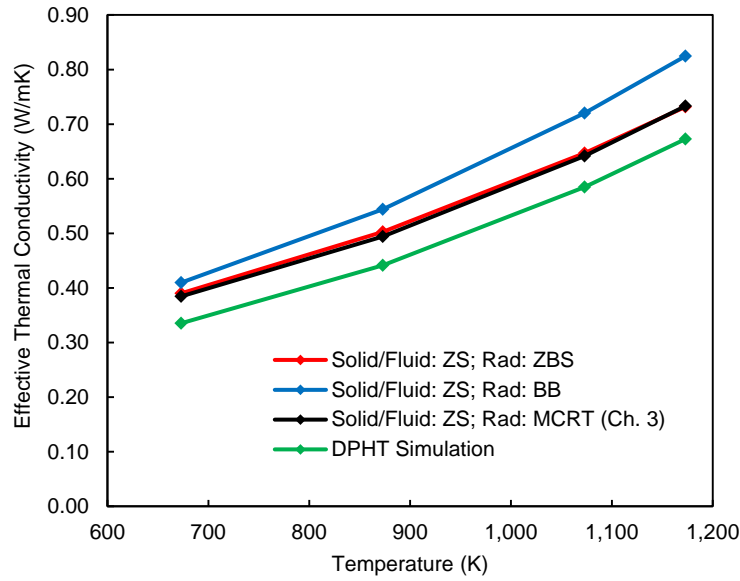


Figure 5.19. Results for k_{eff} calculated using the DPHT simulation, also showing the values predicted using the ZBS model for solid-fluid conduction [29] plus the radiative portion calculated with ZBS, Breitbach and Barthels [28], and the k_{rad} model from Chapter 3.

All the models show similar trends, with the DPHT simulation being the lowest among the tested models. To isolate the source of the discrepancy, k_{eff} is plotted in Figure 5.20 where radiation and direct contact PP conduction are neglected, providing a direct comparison between ZBS and the DPHT simulation where conduction across the fluid gap between particles is the only heat transfer mode. The comparison shows that the DPHT model still predicts less heat transfer than the ZBS model by 10-14%. This large of a disagreement may be too high to be acceptable for many analyses, but because this thesis focuses on radiation, the reason for the disagreement was not pursued in detail. It is likely due to the PFP conduction mode, where the complicated heat transfer problem of two spheres separated by a fluid gap is reduced to a geometry of two opposing isothermal cones. Though it is not possible to know which of the models is more correct, the ZBS model has been shown to be accurate over a range of parameters in various experiments. Therefore, when using the DPHT code for experimental validation in Section 7.2.1, the radius of the two-cone PFP conduction model is modified slightly so the k_{eff} found with the model matches the value predicted by ZBS.

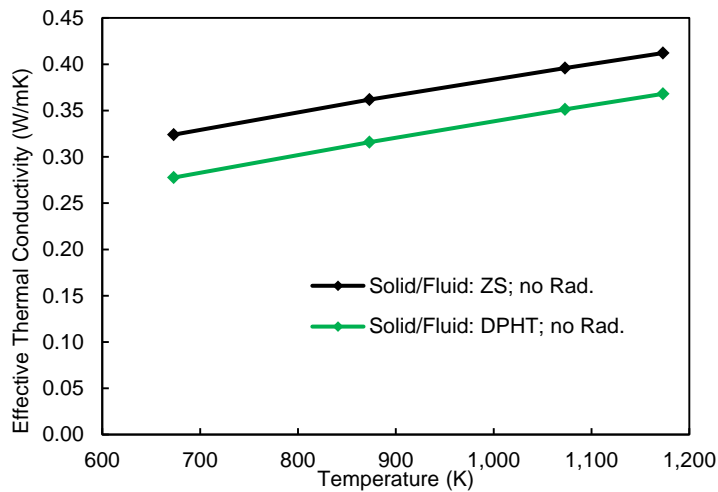


Figure 5.20. k_{eff} with radiation eliminated, comparing ZS and DPHT simulation results.

5.9 Solving Conjugate Heat Transfer Problems

For many actual devices, the boundary condition is known on the outside of the solid part, not on the boundary of the particle domain. For example, if cool particles flow downward through a thick-walled metal tube that is heated from the outside, the boundary condition is likely known on the *outside* surface of the tube. The interior surface of the tube forms the boundary of the particle/fluid domain, but the temperature there is typically unknown. The temperature of the interface changes based upon both the thermal properties of the tube and the characteristics of the particle/fluid domain. Such a problem is an example of conjugate heat transfer.

It is possible in some cases to incorporate the heat conduction through the solid directly into the model, but solvers in CFD often take a coupled approach. The fluid and solid domains are solved separately and then compared at the boundary. This allows for using the optimal solver in each domain, and meshes do not have to match at the boundary [99]. A similar approach adapted for a DEM+DPHT simulation is described in the following section. Then, an approach using the overall heat transfer coefficient is detailed in Section 5.9.2.

5.9.1 Matching the Interface of the Two Domains

This method requires starting with an estimate of the temperature distribution at the interface. This is used as a boundary condition in a DEM+DPHT simulation of the particle/fluid domain. Then, conduction heat transfer is simulated in the solid domain, which can be done with many CFD codes. The known boundary condition is used on the outside, and the assumed boundary condition is used at the interface boundary. After both simulations are at a steady state, they are compared in terms of heat transfer along the interface. If the heat transfer matches at each location on the boundary (within some desired accuracy), then the temperature estimate is correct. If not, a better estimate for the interface temperature must be made, and both the particle/fluid and solid domains must be re-modeled until a match is found. Commercial CFD software can solve similar problems consisting of a solid and fluid domain, and the iterative process is automated. With the recently developed DPHT code, these iterations would have to be performed manually or by developing the code further.

This type of iteration may become quite burdensome given the already high computational cost of DEM+DPHT modeling. However, often times the DPHT part of the simulation requires only a small amount of time compared to the DEM portion, and the DEM part would not have to be re-run in these iterations. No conjugate heat transfer simulations were run in this research, but the methodology was studied and considered, and the DPHT code could be used for this in the future. While computationally intense, this method can eventually lead to a solution with high accuracy with enough iterations.

5.9.2 Overall Heat Transfer Coefficient

Another approach is to find the overall heat transfer coefficient from the wall to the particle/fluid mixture for a representative sub-section of the domain, and then this is used in a simplified heat transfer model of the entire domain. This can

dramatically reduce the computational time, especially for large domains with millions of particles. However, the accuracy is likely not as high as the two-domain approach described in the previous section.

The overall heat transfer coefficient approach is used in Chapter 8 to model an entire solar receiver. In this case, a flat metal plate with a thickness of 4 mm forms the solar receiver surface. The boundary condition is known on the outside of the metal plate, which is a combination of incident heat flux and losses from reflection, convection, and emission. The temperature on the interior surface (facing the particle/fluid mixture) is unknown, making a straightforward DEM+DPHT simulation not possible. Furthermore, due to the large size, modeling the receiver would require ~450 million particles and would take perhaps years of computation time.

In the method used, the DPHT simulation was run using an estimate for the temperature boundary condition at the interface between the particle/fluid and solid domains. After reaching a steady state, the overall heat transfer coefficient from the wall to the particle/fluid mixture was calculated, which encompasses all of the complex effects due to the six particle-scale heat transfer models as well as the mixing characteristics and particle mechanics. In this case the heat transfer coefficient was found as a function of distance from the inlet, as it varies significantly in the flow direction. With the heat transfer coefficient known, a simple 1D heat transfer model can be used, where the heat flux to the particle/fluid mixture at each location is calculated by multiplying the heat transfer coefficient by the temperature difference between the wall and the particle mixture. More details on this model are given in Chapter 8.

One key for accurate results is to ensure that the temperature boundary condition used in the DPHT simulation is close to the interface temperature in the 1D simulation. The overall heat transfer coefficient is only valid under the exact conditions under which it was derived. For the case studied, the heat transfer

coefficient increases at higher temperatures due to radiative effects and the increased thermal conductivity of air.

5.10 Conclusions for DPHT

With the DBA radiation model developed, the goal was to implement it in a DEM-based heat transfer code for dense flows so it could be used to model CSP devices. However, no such software is publically available, so the entire modeling scheme had to be developed, resulting in the DPHT code. By assuming that the interstitial fluid is stagnant relative to the particles, heat transfer is only via conduction where particles touch, conduction across the thin fluid gap between particles, and radiation. Sub-models for both conduction modes were found in literature, though several modifications were made so they are more physically realistic than the originally published models.

In a DPHT simulation where only the PFP model was enabled, total heat transfer through a group of particles was found to be 10-14% less than the Zehner-Schlünder model predicts. This may reveal an underprediction by the PFP model, at least for the current case, pointing to the need for additional verification of the PFP model. In the experimental validation in Section 7.2.1, the PFP model will be tuned for the current conditions by increasing the radii of the two opposing cones, making the results match the more trusted ZS model.

The example simulation given in this chapter should provide enough detail that a newcomer to this type of modeling can understand, execute, and begin to modify the code to simulate a new device. Finally, several strategies are discussed to model more complicated boundary conditions.

CHAPTER 6

EXPERIMENTAL INVESTIGATION OF A DENSE GRANULAR FLOW AT HIGH TEMPERATURES

DEM and CFD-DEM are relatively new modeling methods which are still being developed by various research groups, and these models have been experimentally validated much less than other computational techniques such as CFD. To be accurate, these models require many parameters which must be either known or calibrated experimentally. As for the particle mechanics side of DEM, the properties (such as coefficient of restitution, Poisson's ratio, Young's modulus, PP and PW friction coefficients) can be experimentally calibrated using a series of lab tests, and they have been studied previously [84]. In contrast, the heat transfer side of DEM has been much less studied.

Given DEM heat transfer models are in need of validation but few relevant experiments in this research area exist, experimental results are pursued in this thesis. The specific aims are to:

- A. Provide the experimental results so particle-scale heat transfer models, including the DBA radiation model, can be validated under the high temperature conditions of CSP.
- B. Document practical lessons learned in the design and execution of experiments in dense granular flows at high temperatures for others in research or industry working on similar experiments or devices.
- C. Increase the technology readiness level (TRL) of the dense granular flow receiver [19][21] concept from TRL 3 (experimental proof of concept) to TRL 4 (technology validated in lab) by running experiments using highly concentrated light in a solar simulator facility.

The experimental work has been divided into the Experiment Design, Testing and Results, and Discussion of Practical Lessons Learned.

6.1 Experiment Design

6.1.1 Overall Setup

The experiment was designed to study a particle stream in a dense granular flow through a square tube, with concentrated light illuminating one face and all other faces insulated. This configuration is very similar to both a dense granular flow solar receiver and a parallel plate heat exchanger.

The overall experimental setup, shown in Figure 6.1, consists of a hopper which preheats the particles, a square tube “test section” through which the particles descend (which receives concentrated light on the front face), mixing devices on the inlet and exit of the test section, and a bin with a scale for measuring the mass flow rate. The setup is located in the solar simulator facility, which consists of three lamps each capable of producing 6 kW of light concentrated over a small area on the illuminated object. Figure 6.1(a) shows the lamps pointed towards the setup before it is outfitted with insulation, thermocouples, and mixing devices, and the front side of the lamps are shown in Figure 6.1(b). The main components are labeled in Figure 6.2, and a close-up of the test is shown in Figure 6.3. Finally, a diagram showing the different components and flow regimes is shown in Figure 6.4.

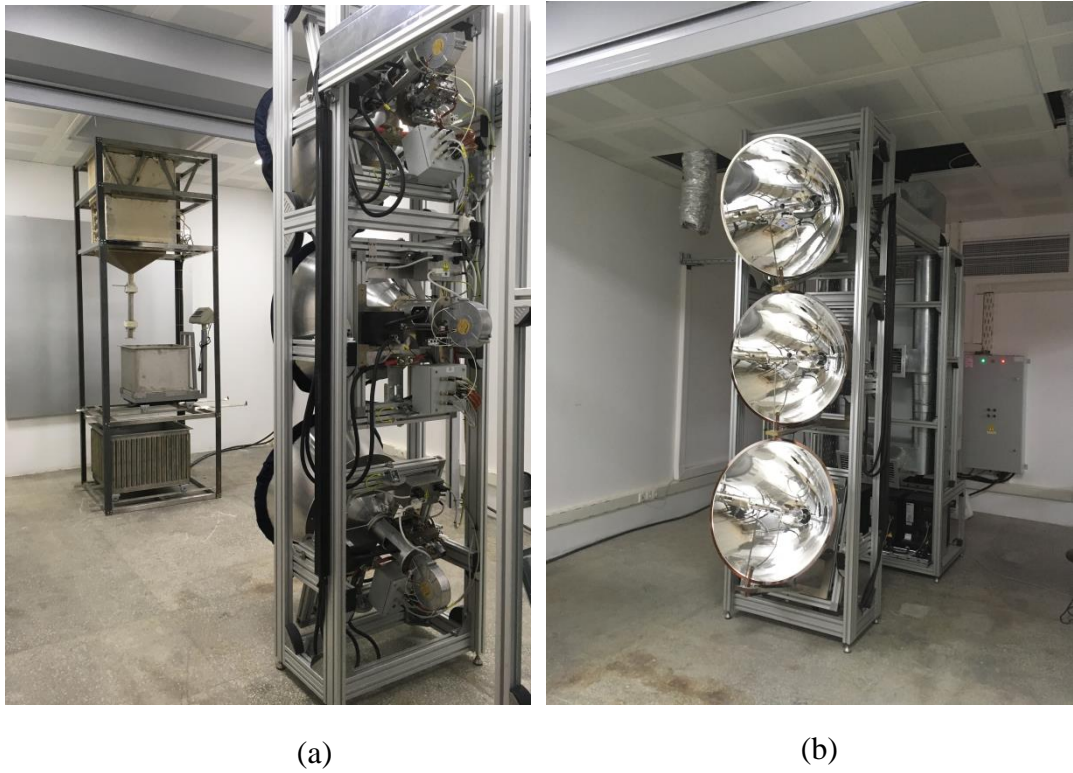


Figure 6.1. (a) Experimental setup in front of high flux solar simulator, and (b) front view of lamps.

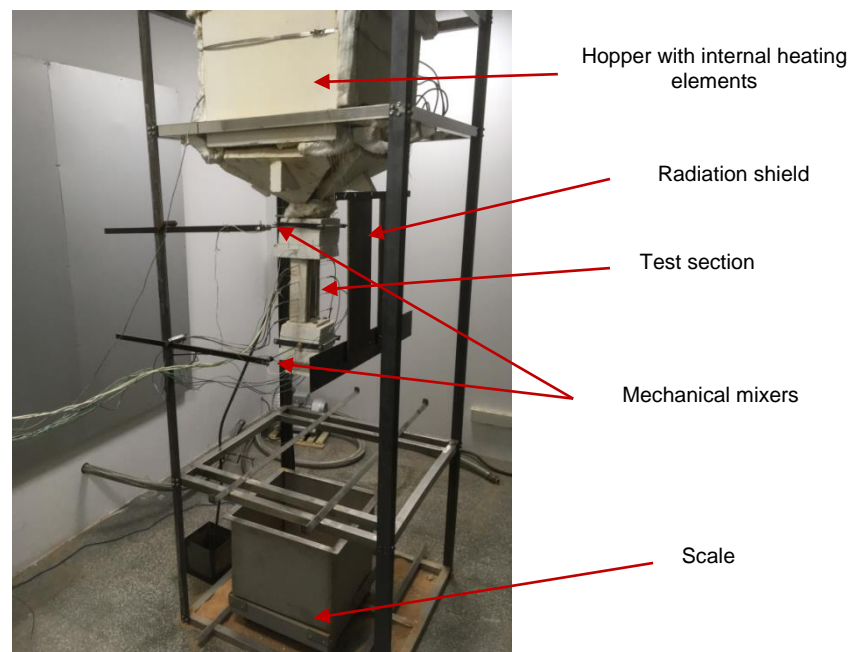


Figure 6.2. Main components of the experimental setup.

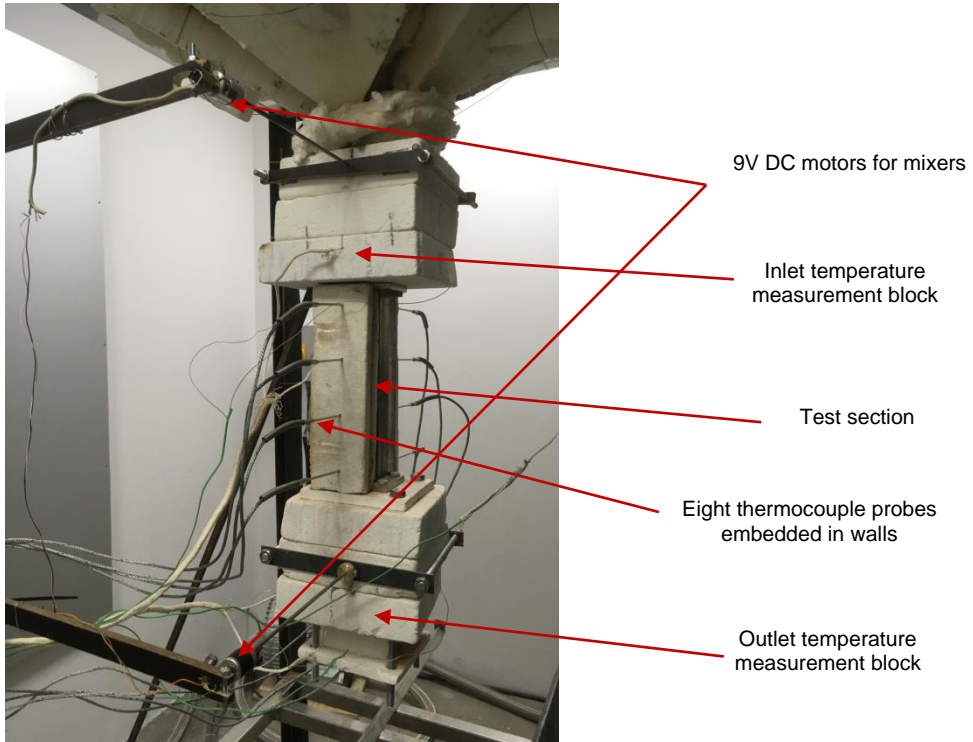


Figure 6.3. Close-up of measurement test section.

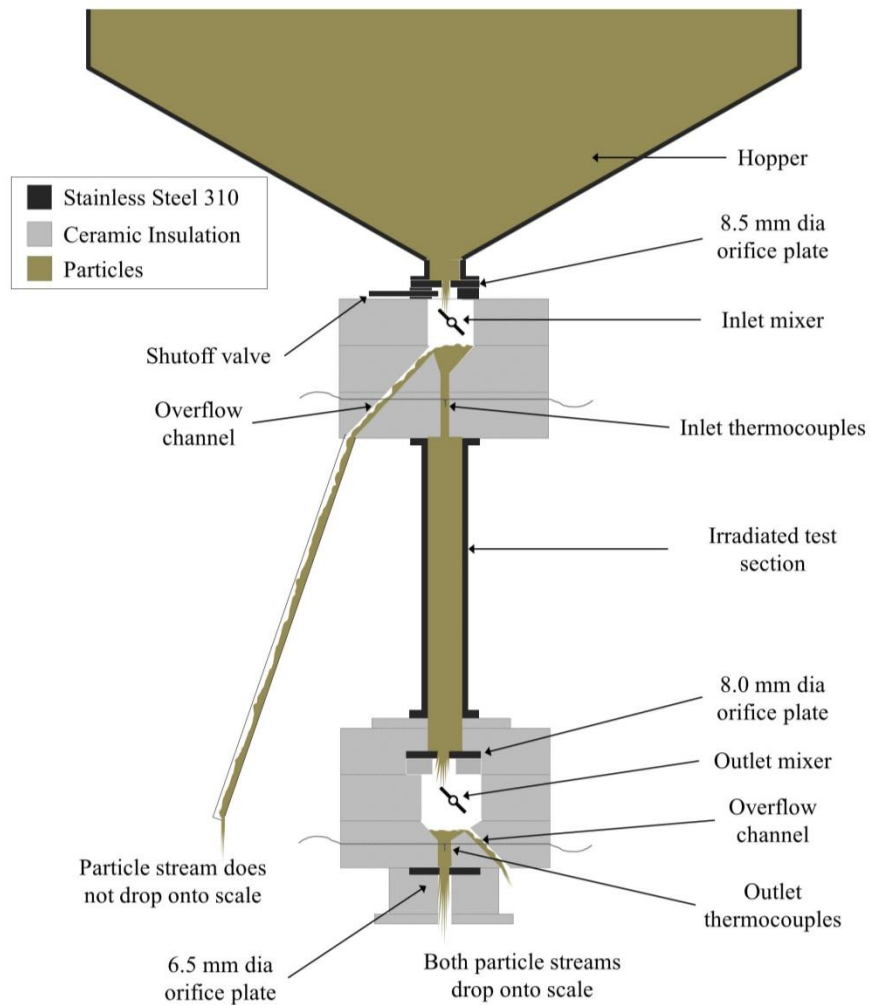


Figure 6.4. Diagram of the components and flow regimes in the setup.

6.1.2 Hopper

The hopper, along with all other metal components subject to high temperatures in this setup, is constructed from Stainless Steel 310, chosen for its strength at high temperatures. With only 18 kW of power available from the lamps, if particles were to enter the test section at room temperature, the outlet temperature would not reach the desired high temperatures of above 400 °C. Thus, particles are heated to a high temperature in the hopper, and then particles are heated a second time as they flow through the illuminated test section. This not only achieves the high

temperatures desired, but it mimics the conditions in a CSP solar receiver or particle heat exchanger where the inlet temperature is in the 500 to 600 °C temperature range. In this setup, particles are manually transported up to the hopper with a bucket before each test is run.

As shown in Figure 6.5 (insulation removed for photo), the preheaters were constructed of 24 Stainless Steel 310 tubes placed across the hopper. Only one side of each tube was welded in place, and the other side passes through a hole in the side of the hopper, allowing for thermal expansion of the tubes in the axial direction. Ceramic tubes were used for electrical insulation, and molybdenum wire coils were used for electrical resistance heating. The ends of these tubes can be seen in the figure, where the ceramic insulation tubes are white. They can output a combined power of up to 27.8 kW and were used to heat particles to over 750 °C.

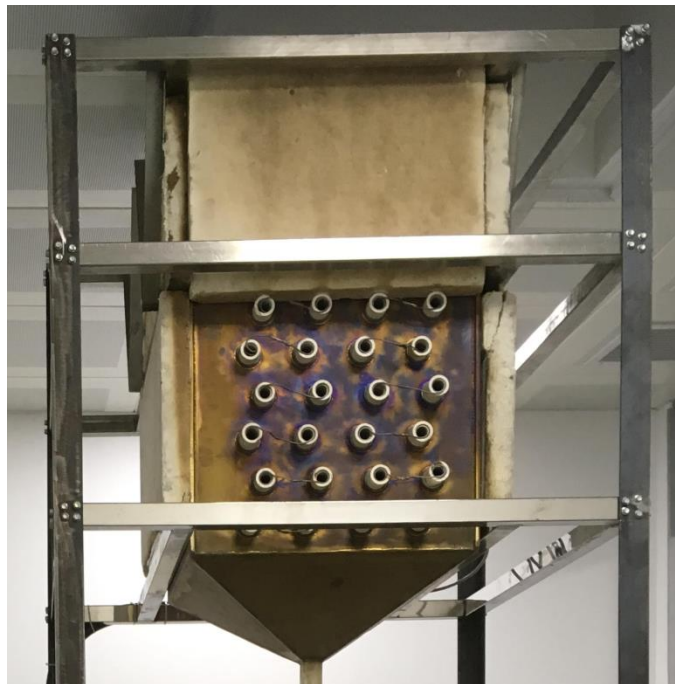


Figure 6.5. Hopper, with insulation removed to expose ends of the heating tubes.

6.1.3 Shutoff Valve

A shutoff valve (Figure 6.6) is located directly below the hopper, where particles flow through the square opening and flow is shut off by inserting the long plate shown on the left. The four holes are for bolts to hold it in place. It is located just below the hopper so flow can be shut off with particles stored in the hopper while work is performed on the test section and any components below it. During tests, the flat plate is removed completely so it does not conduct heat out of the setup, and insulation is placed over the opening. The valve offers the advantage of simplicity, with no moving parts having close tolerances that could jam with particles. It also works well at high temperatures and does not leak particles.



Figure 6.6. Shutoff valve used to stop the particle flow.

6.1.4 Test Section

The test section (the actual section portion used to characterize the heat transfer) consists of a square tube of Stainless Steel 310 with an interior cross section of 20 x 20 mm where particles flow, and a wall thickness of 8 mm. The length of the tube is 250 mm. The thick wall was chosen to allow for 3 mm diameter thermocouple probes to be inserted into the wall itself from the side. This was done by drilling four holes in the front (illuminated) side and four holes in the back (insulated) side of the test section. The holes are drilled deep enough such that the thermocouples are centered horizontally on the face (i.e. centered in the right-left direction in Figure 6.7(b), as shown by the red circles). The holes are sized to make a very tight fit with the thermocouple probes, ensuring good thermal contact. The test section

with holes drilled is shown from the side in Figure 6.7(a), before applying insulation. Thermocouple probes were inserted through insulation blocks, shown in Figure 6.7(b). Once installed, extra insulation was added to shield radiation from striking the thermocouple probes, as shown in Figure 6.7(c). Embedding the thermocouple probes in the wall was chosen as the most accurate method to measure the wall temperature, as a thermocouple placed on the inside of the wall would be affected by the temperature of the flowing particles and may also disturb the flow, and a thermocouple attached to the outside of the wall would likely melt under the high heat flux of the concentrated light. Measuring the front face temperature with an infrared camera was also considered, but this was not feasible because (without a detailed calibration) the camera cannot distinguish between radiation emitted from the test section and the radiation which is emitted from the lamps and reflected back to the camera.

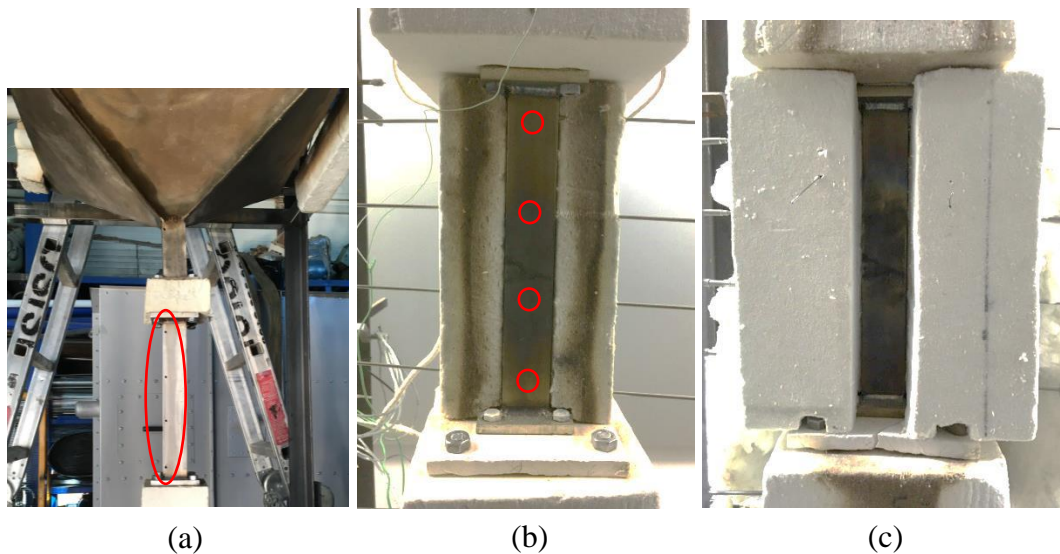


Figure 6.7. (a) Hopper and test section, with holes for thermocouple probes visible, circled in red, (b) front view of test section with thermocouples installed at locations circled in red, and (c) extra insulation installed in front test section.

6.1.5 Inlet and Outlet Measurement Blocks

The overall heat absorbed by the particle stream is calculated using the inlet and outlet temperatures of the test section. For this calculation to be valid, the particle stream at the inlet and outlet must be uniform in temperature, which is why the paddle wheel mixing devices are used, as described in the following section and discussed in more detail in Section 6.3.4. After mixing, the particle stream temperature is measured with several K-type thermocouples, with thermocouples placed specifically in the dense granular flow region, as opposed to in a dispersed flow (e.g. downstream from an orifice plate). This is done to avoid any effects of the air temperature, in case it is not perfectly mixed and identical to the particle temperature. The block where the inlet thermocouples are placed is shown in Figure 6.8, with the 14 mm diameter flow channel in the center, two thin grooves cut into the block where the thermocouples wires are placed, and four holes for mounting bolts. Each thermocouple is arranged such that it lies in a straight line, with the junction in the center of the flow channel and one wire exiting out opposing sides. This secures the thermocouple in place while allowing for manual adjustments of the location of the thermocouple junction in the flow channel. The two perpendicular grooves are used to allow for two thermocouples placed at different heights. Similar blocks are used to measure both the inlet and outlet temperatures.



Figure 6.8. Inlet temperature measurement block with grooves cut for thermocouples wires.

6.1.6 Orifice Plates, Overflow Channels, Mixing Devices

The test section and measurement sections must be in dense granular flows. In contrast, the high speed paddle-wheel mixing device developed in this research (more details given in Section 6.3.4) can only work in a dispersed flow regime; it cannot work in a packed state or a dense granular flow because there is too much friction to turn the paddle wheel and no space for particles to move and mix. In this setup, each mixing device is placed directly under an orifice plate, so particles pour directly onto the moving paddle wheel to ensure a high degree of mixing. A mixer (Figure 6.9 (a)) was constructed using a 4 mm diameter stainless steel shaft connected to a 9V motor, a rectangular paddle fixed to the end of the shaft, and a square block of ceramic insulation measuring 18 cm x 18 cm x 5 cm. A coupling was used to allow an easy connection and disconnection of the motor shaft while working on the setup. The paddle shaft wheel is located slightly off center, so the particle stream passing through the orifice (which is centered with respect to the rest of the setup) falls directly on the middle of one face of the paddle, therefore striking the particle stream with a high velocity.

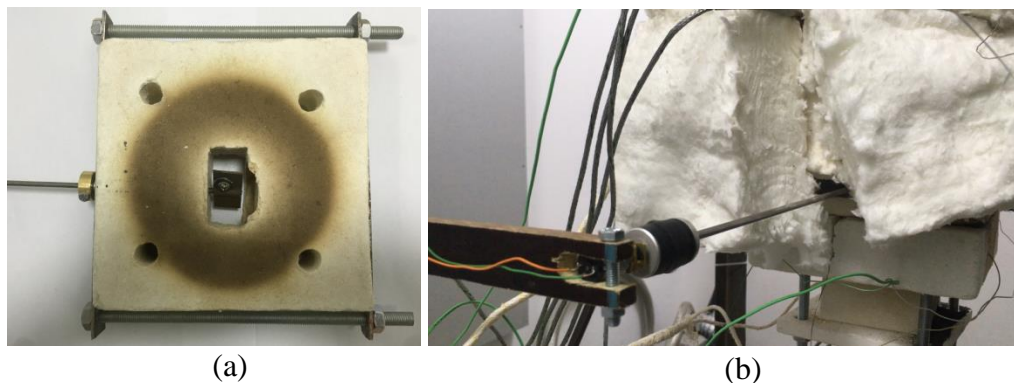


Figure 6.9. Paddle wheel mixing device showing (a) paddle wheel installed inside the insulation block, and (b) 9V DC motor mounted on the exterior, connected to stainless steel shaft.

The mixing device must work in a dispersed flow, but below this point a dense granular flow is needed again so the temperature can be measured in this flow regime to avoid any effects from the air. An overflow channel placed just below the paddle-wheel mixing device achieves this, by establishing a new fill height of the

dense flow; the dense granular flow cannot fill any higher than the overflow channel, as any particles at a higher level immediately descend through the overflow channel. This “trick” is done twice; once for each mixing device. For the top mixing device, the top orifice (8.5 mm diameter) is sized just larger than the orifice at the outlet of the test section (8.0 mm diameter), so there is always a slight excess flow of particles exiting through the overflow channel. These excess particles are routed out through a tube and not included in the mass flow rate calculation, which only includes particles flowing through the test section.

A similar configuration is used at the outlet as well, where a dense granular flow is needed after the outlet mixing device so that the thermocouple can be placed in a dense granular flow to eliminate any temperature effects from the air. Below the outlet mixer, a third orifice plate (with a 6.5 mm diameter orifice) is used to reestablish a dense granular flow, and a second overflow channel is used to release excess particles. In this case both streams are sent to the scale because both flow through the test section.

This scheme is extremely useful as it allows for establishing a dispersed flow and reestablishing a dense granular flow to meet the needs of different components. In the process, a small stream of excess particles must be rejected from the main stream, but by making the top orifice only slightly larger in size, the “lost” flow rate of these unused particles is minimal. To minimize any air intrusion from the outside, these overflow channels are sized such that the excess particle stream roughly fills the channel, so any air flow will be outward with the particles. The top overflow channel is shown in Figure 6.10, where particles are routed out through a tube to an external collection bin. The bottom overflow channel opens near the bottom, so particles drop straight into the weighing bin.

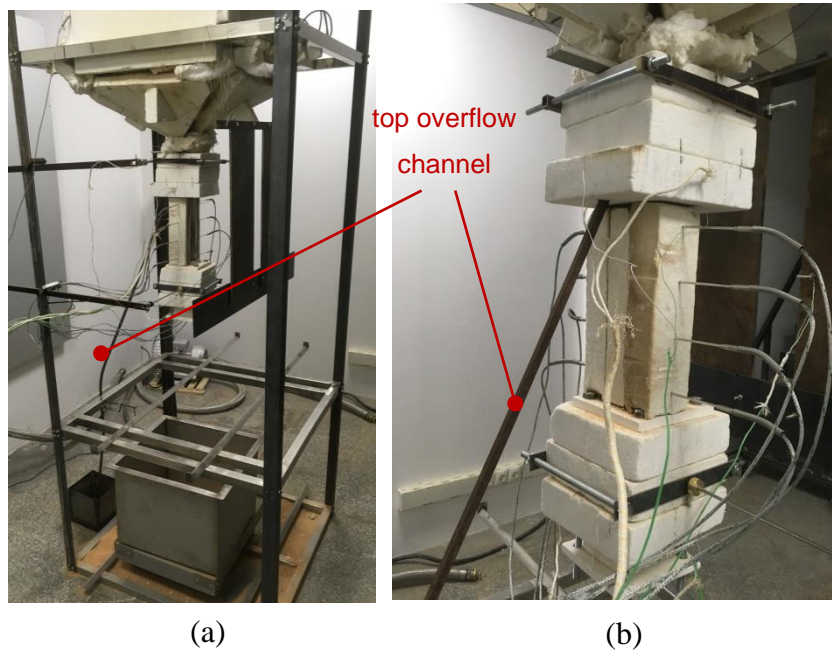


Figure 6.10. Top overflow channel shown (a) on full setup, and (b) close-up where it attaches to the insulation blocks.

6.1.7 Data Acquisition

For mass flow rate measurements a CAS brand DH-LED scale was used, with a maximum capacity of 300 kg and a sensitivity of 50 g, which is connected to a computer using a serial connection. The mass flow rate is calculated by fitting a straight line to the mass accumulation vs. time curve over the duration of each test. Temperature measurements from the thermocouples (all K-type) are recorded at an interval of 10 seconds, using a Keysight 34972A data acquisition system.

6.2 Testing and Results

6.2.1 Particle Materials Tested

Tests were run with both sand and sintered bauxite, chosen for their relevance as heat transfer materials in CSP. The sintered bauxite is Carbo HSP 40/70, which was chosen because many of its thermophysical properties have been previously

determined by others in the CSP field. The size distribution of both materials was analyzed with a Mastersizer 2000 laser diffraction analyzer. The Sauter mean diameter (also known as the surface weighted mean and abbreviated as d_{32}) for the Carbo HSP and sand is found to be 371.15 μm and 722.50 μm respectively. Following similar studies [97], the monodisperse spheres modeled with DEM and DPHT will use the Sauter mean diameter.

6.2.2 Procedure

The following sequence was used for each of the tests:

- a. All particles to be tested were filtered to ensure no debris would be introduced to the experiment.
- b. Particles were manually transported up to the hopper with a bucket, filling the hopper enough to cover all of the preheater tubes.
- c. Particles were preheated for 1-2 hours depending on the desired temperature.
- d. Particles were allowed to rest for at least one hour to reduce temperature gradients inside the hopper.
- e. The flow was started by opening the shutoff valve.
- f. Paddle wheel mixers were turned on.
- g. The flow was temporarily stopped by placing a block over the outlet for roughly 25 seconds, until particles start to pour out from the top overflow channel, indicating the dense fill level has reached that point. Because the flow rate through the top orifice (8.5 mm) is greater than the middle orifice (8 mm), with enough time the dense fill level would slowly rise from the middle orifice plate to the overflow channel, but temporarily blocking the exit quickly establishes the correct flow regimes.
- h. Each of the three lamps was turned on.
- i. Temperatures of the inlet, outlet, and walls of the test section were monitored until the system arrived at a steady state.

6.2.3 Results

Experiments were run under three conditions; (1) particles of silica sand preheated to 420 °C, (2) particles of sintered bauxite preheated to 620 °C, and (3) particles of sintered bauxite starting at room temperature. The data from each of these experiments are given below, where the thermocouples on the front (illuminated) and back (insulated) walls are referred to with numbers from 1 to 4, with 1 being the top thermocouple and 4 being the bottom thermocouple.

6.2.3.1 Test 1: Sand Preheated to 420 °C

In this test, sand was preheated to 420 °C, and the mixers were started at around a time of 200 seconds in Figure 6.11 below. The three lamps were turned on and adjusted, causing several inflections in the wall temperatures before temperatures stabilize, and the lamps were switched off at 1070 seconds. Due to heat loss from the hopper, the inlet temperature slowly decreased throughout the test, and therefore the other temperatures slowly declined as well. However, the difference between the temperatures is constant, so the condition can be considered quasi-static, and each time step can be considered a steady state for the purposes of validating with DEM. The temperatures at the steady state condition are taken as the average temperature between 1000 and 1070 seconds, which are reported in the summary of results in Table 6.1.

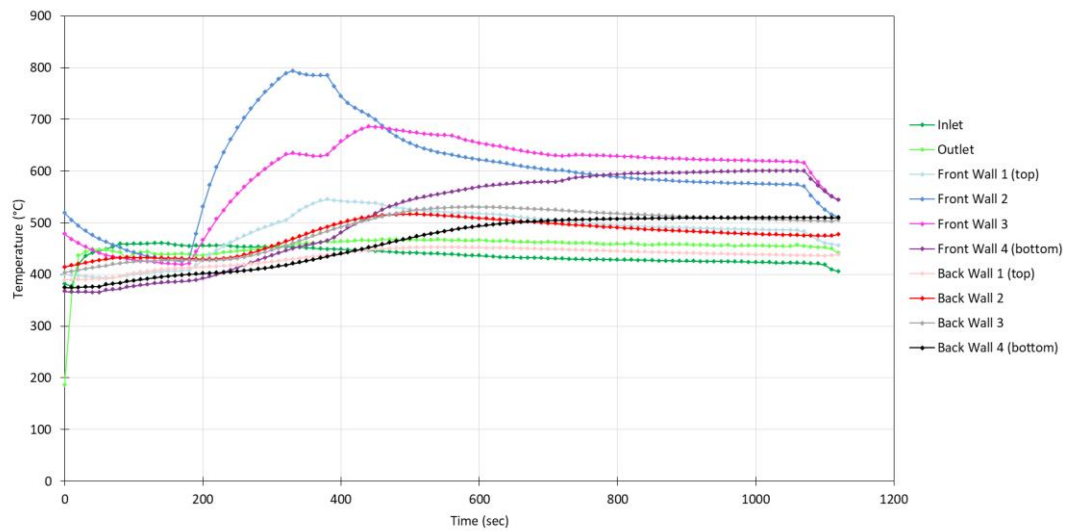


Figure 6.11. Temperature data from Test 1.

The mass accumulated in the weighing bin was measured over time at an interval of 10 s, with a nearly linear relationship shown in Figure 6.12 and therefore a very constant flow rate in the range of 500 to 1000 seconds. With linear curve fit, a flow rate of 0.0112 kg s^{-1} is found.

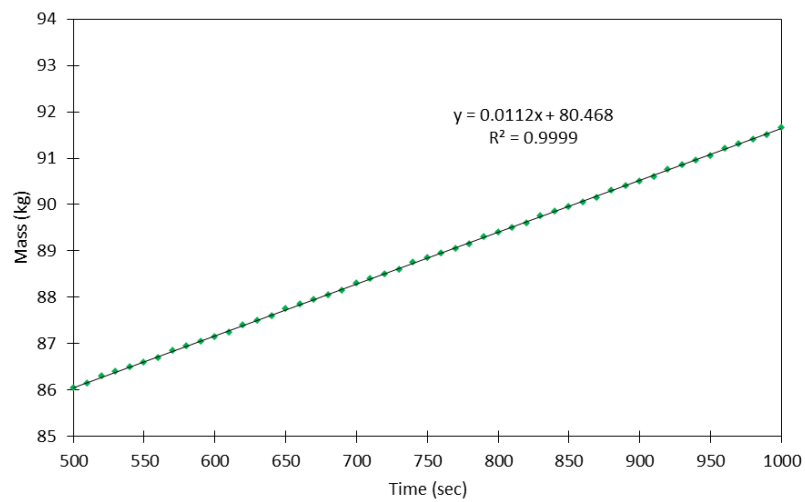


Figure 6.12. Mass of particles accumulated over time during Test 1.

6.2.3.2 Test 2: Sintered Bauxite Preheated to 620 °C

In Test 2, the sintered bauxite was heated to around 750 °C when the photos in Figure 6.13 were taken. In Figure 6.13(a), the mixer was not running, and the right half of the particle exit stream glows red, while it is black (not glowing) on the left side. The illuminated front face of the test section corresponds to the right side of this picture, so it matches expectations that the illuminated side of the particle stream is at a much higher temperature than the insulated side. This visually shows the extreme temperature gradient caused by the high heat flux from the illuminated surface. In Figure 6.13(b) the mixer has been turned on, and the temperature gradient can no longer be seen, and only a faint glow was visible. Note: the smaller particle stream on the right side of the main exit stream is from the lower overflow channel.

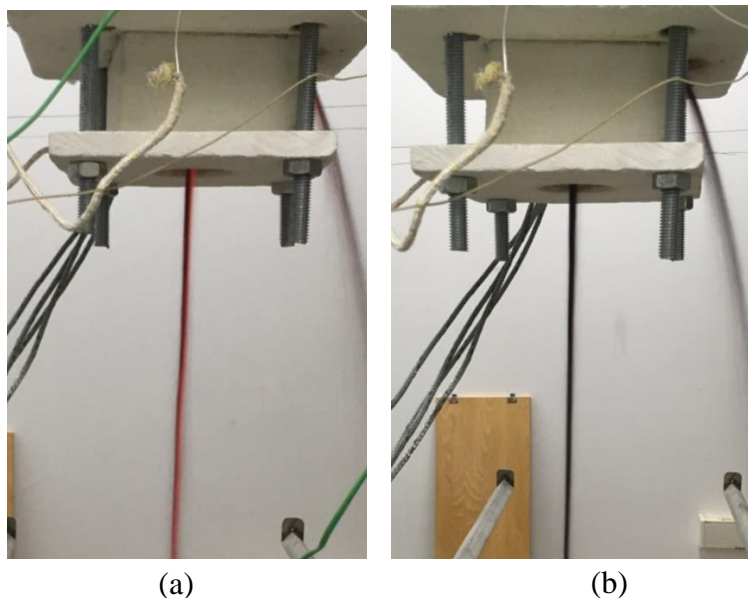
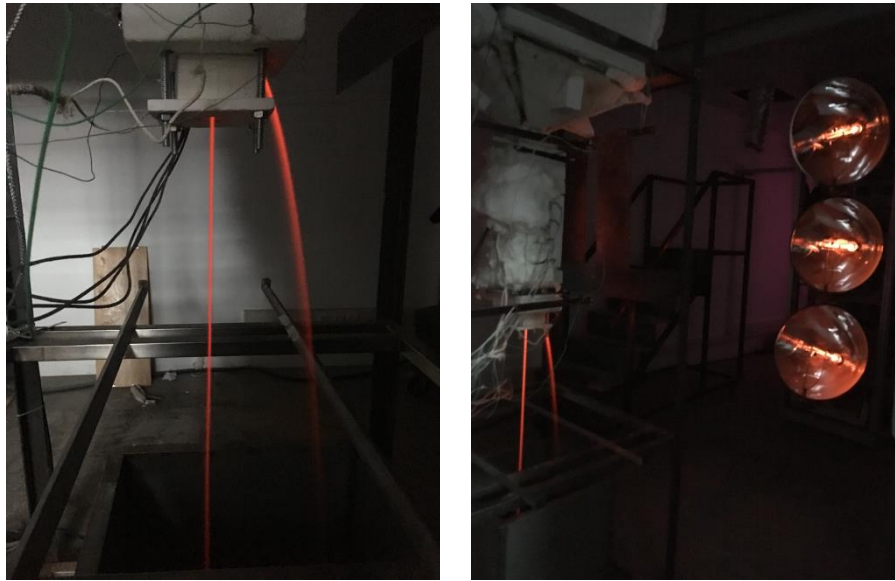


Figure 6.13. Sintered bauxite particles can be seen glowing at the exit, where (a) a gradient can be seen before while mixer is off, and (b) the gradient is eliminated once mixer is turned on.

With the room lights and lamps turned off, the particle stream glows red, as shown in Figure 6.14(a), and in (b) the lamps have been recently turned off but are still radiating a small amount of light as they cool.



(a) (b)
Figure 6.14. Stream of sintered bauxite radiating visible red light at ~ 750 °C.

As shown in Figure 6.15, temperatures fluctuate at the beginning of the test before becoming relatively constant after a time of 1200 seconds. The inlet temperature shows a significant dip between the times of 700 and 1000 seconds, likely due to the stream being drawn from a relatively colder place in the hopper. The dip can be seen to temporarily decrease all the other temperatures as well. The inlet temperature stabilizes again at around 1100 seconds, though it does drop again slightly at 1400 seconds. The most stable conditions are beyond this point, so the steady state mean temperatures are taken as the time steps between 1630 to 1760 seconds.

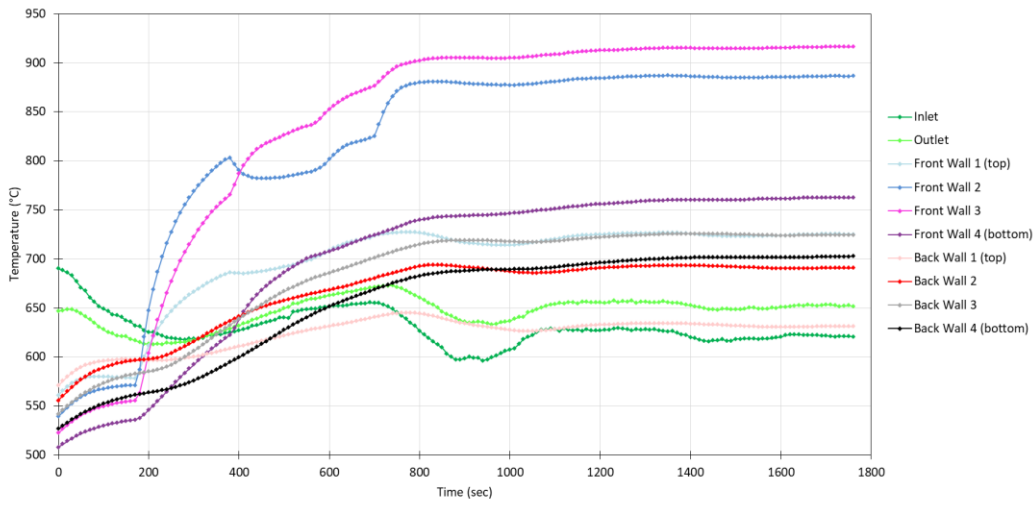


Figure 6.15. Temperature data from Test 2.

The mass accumulated by the weighing bin was measured over time, and plotted for the range of 1000 to 1800 seconds in Figure 6.16, showing, a mass flow rate of 0.0206 kg s^{-1} .

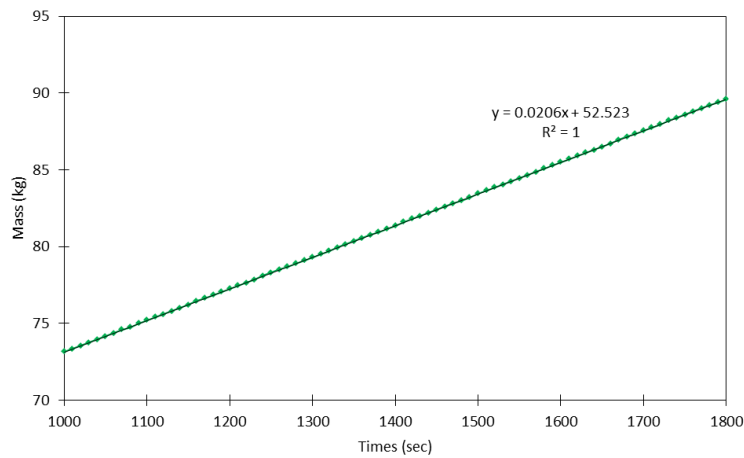


Figure 6.16. Mass of particles accumulated over time during Test 2.

6.2.3.3 Test 3: Sintered bauxite with no preheating

In this test the sintered bauxite particles were not preheated, though a small amount of heat remained in the hopper from tests on the previous days, making the inlet

temperature roughly 46 °C. As shown in Figure 6.17, most of the temperature readings appear to reach steady state values, though some of the thermocouples in the back wall still show a slight increase in temperature even at the end of the test, meaning they may not have quite reached a steady state. Without running the experiment longer, the values reported in Table 6.1 are taken to be the mean temperature, between 1170 and 1270 seconds.

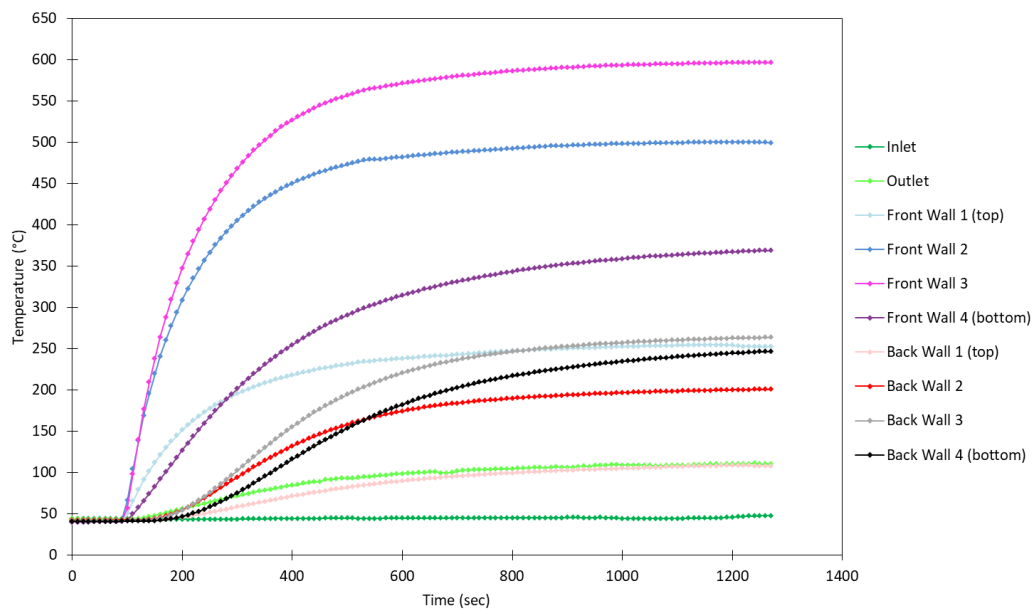


Figure 6.17. Temperature data from Test 3.

The mass of particles over time is plotted in Figure 6.18, and a mass flow rate of 0.0202 kg s⁻¹ is found.

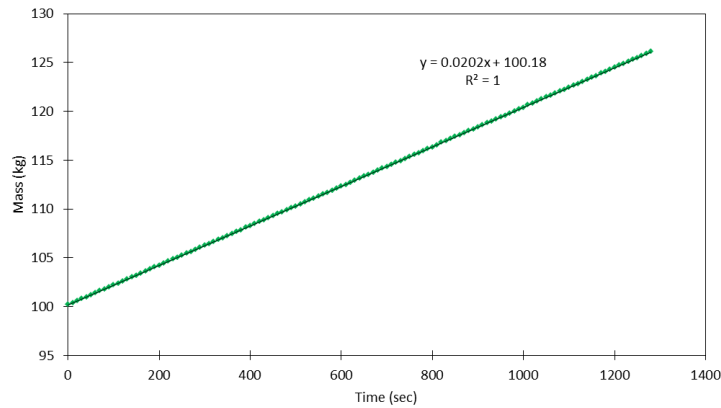


Figure 6.18. Mass of particles accumulated over time during Test 3.

6.2.4 Summary and Discussion

A summary of the steady state temperatures and flow rates from each of the three tests is shown in Table 6.1. This is one of the central outputs of this experimental research, as these data can be used to compare against results predicted by DEM modeling. Ideally, measurements should be taken under steady state conditions, and the inlet and outlet particle streams must be completely uniform in temperature. Many efforts were made to be as close to these ideal conditions as possible, but several shortcomings are discussed below.

Table 6.1 Steady state temperature conditions from each test.

Parameter	Units	Test 1	Test 2	Test 3
Material	-	Sand	Carbo HSP	Carbo HSP
Mass Flow Rate	kg s ⁻¹	0.0112	0.0206	0.0202
Inlet	°C	422.7	621.7	46.5
Outlet	°C	455.1	652.5	110.2
Front Wall 1 (top)	°C	485.7	725.1	253.2
Front Wall 2	°C	574.0	886.2	500.0
Front Wall 3	°C	618.7	916.3	596.3
Front Wall 4 (bottom)	°C	600.6	762.5	367.7
Back Wall 1 (top)	°C	437.7	631.0	108.1
Back Wall 2	°C	476.8	690.7	200.1
Back Wall 3	°C	505.7	724.4	262.8
Back Wall 4 (bottom)	°C	509.8	702.2	245.0

In the inlet and outlet test sections, two to three thermocouples were immersed in the flow to measure the temperature simultaneously. Of these, the high temperature

caused numerous outages, especially with the thinnest of the thermocouple wires used. Efforts were made to ensure the thermocouple wire was centered in the tubular shaped flow channel, but in some cases a thermocouple may have been off center. Thus, the inlet and outlet temperature data presented in Table 6.1 are the best available results taken from the collected data.

Testing was done to check the temperature uniformity of the particle stream by manually moving the thermocouple junction back and forth across the flow channel. With the paddle wheel mixers running, no temperature gradient due to the illuminated front wall could be found. However, the temperature measurement in the center of the stream appeared to be several degrees higher than the temperature next to the wall, which may indicate some heat loss through the insulation. Heat loss was minimized by constructing the channels from insulation blocks, with a minimum of 8.5 cm of insulation around the flow channel, plus more insulation blankets wrapping around the whole setup. Furthermore, the vertical distance that the particles must descend between the actual outlet of the test section and the thermocouples was kept to a minimum, only ~8 cm, so the residence time during which the particles could lose heat is very low. These measures were taken to ensure very little heat is lost before the temperature is measured, but still a small amount of deviation was noticed between the center of the flow and the edges. If there is indeed a significant radial temperature profile, quantifying it is complicated by the fact that the inlet temperature to the test section can also fluctuate in the range of several degrees over several minutes, due to the hopper output temperature being not quite constant. The experimental setup was not constructed to accurately investigate such a temperature profile, so studying this phenomenon is left for future experiments.

Thermocouples embedded in the walls of the test section are 3 mm in diameter, and the walls are 8 mm thick. The holes where the thermocouples are embedded are sized extremely close to the diameter of the thermocouple probes themselves; installing them was done by hand, but it required holding the probe with pliers while pushing with a high degree of manual force. Thus, the thermal contact

between the wall and the probe is thought to be extremely good, and the thermocouple readings should be an accurate representation of the wall temperature.

For each test, a time period was selected as the best representation of a steady state condition. In Test 2, the inlet temperature varied at several points throughout the test, though a fairly good approximation to a steady state was achieved near the end. This is likely due to an inherent deficiency in the hopper design, as will be discussed in Section 6.3.3. In Test 3, the test was stopped when the inlet and outlet temperatures reached steady values, but some of the wall temperatures were still slowly climbing and would in reality reach a steady state at a slightly higher value. Still, the last data points provide a relatively accurate approximation of steady state temperatures.

6.3 Discussion of Practical Lessons Learned

The setup shown is the result of an original design which evolved to the present state after numerous experimental trials and improvements. Through this process many practical insights were learned in the laboratory which can be used by other researchers in this field who are designing similar experimental setups or industrial systems.

6.3.1 Particle Filtration

Care should be taken to not introduce any foreign debris into the particles, such as small pieces of ceramic insulation that fall into the weighing bin. Several experimental runs were interrupted by a clogged flow from a small piece of insulation being stuck in an orifice plate. Thereafter, between each heated test run, the particles were filtered through a mesh of roughly 3.5 mm to strain out any small pieces of insulation or debris. It adds significant manual effort and time, but it is necessary to ensure the system runs smoothly. In the current setup the filtration is

performed outside of the system, but in future work a filter may be added in the flow just below the shutoff valve to ensure no foreign particles enter the test section.

6.3.2 Minimizing Heat Loss

At temperatures nearing 1000 °C, every component must be designed around minimizing heat loss. The inlet and outlet flow sections are made out of insulation blocks to minimize heat loss, and the test section is also insulated with tightly fitting insulation blocks on three sides. Steel bolts are used to connect the test section to the hopper and to connect the outlet mixing section to the test section, but in both cases these are isolated using hard insulation sheets to ensure there was no metal-to-metal thermal bridge between the test section and the other sections. Finally, the whole setup is insulated once more with several 5 mm thick insulation blankets, as shown in Figure 6.19, though the insulation integrity is reduced due to the penetration of the thermocouple wires. At these temperatures a significant amount of heat loss is essentially unavoidable, however, this does not limit the accuracy of the data; as long as the inlet, outlet, and wall temperatures are known, this can provide data to compare with DEM modeling.



Figure 6.19. Test section, well-insulated on three sides with ceramic insulation.

A high temperature rise from inlet to outlet is desired in order to minimize any inaccuracy in the inlet or outlet temperature measurements. However, if the lamps are off, the outlet temperature is actually much less than the inlet temperature due to the high heat loss to the surroundings, even with the extreme efforts taken to insulate the setup. Therefore, it takes a large portion of the incident energy from the lamps to simply compensate for the losses and bring the outlet temperature above the inlet temperature. The problem is exacerbated at high temperatures; the temperature rise from inlet to outlet is ~ 110 °C in Test 3 (starting at room temperature), whereas the temperature rise in Test 2 (starting at 621.7 °C) is only ~ 30 °C. The temperature on the outside of the insulation (measured with an infrared thermometer) is low, roughly 55 °C, so it can be concluded that the heat loss is predominantly from the exposed front side, and adding additional insulation would not significantly reduce the heat loss.

The temperature rise could be increased in the future in several ways. The surface of the test section is left uncoated with a dull reflective finish, so a large portion of

the incident radiation is reflected. High temperature black paint could be applied to increase radiation absorption, such as Pyromark paint with an absorptivity of ~0.96 [100], as done on actual solar receivers. Heat losses from the front face are also exacerbated by the ventilation system in the solar simulator facility, which has a strong air intake just above the setup, creating an updraft to suck up any smoke or material off-gassing. This air current likely promotes high convective losses from the front of the test section, which could be minimized by creating a cavity or hood around the setup, similar to actual solar receivers.

6.3.3 Heated Hopper Design

The hopper was successfully used to heat particles up to as high as 750 °C, but the main drawback is that the temperature of the particle stream leaving the hopper varies slightly with time, due to particles being drawn from hotter or colder regions of the hopper. During preheating, the molybdenum coils output a very high heat flux, which heats the particles directly around the tubes to a very high temperature but leaves the particles in between the tubes relatively colder. To minimize this effect, after preheating for several hours, the heating elements are turned off and the particles in the hopper are left to rest, but because the particle bed has a relatively low thermal conductivity, it takes a long time to reduce or eliminate the temperature variation in the hopper. Meanwhile, heat is lost out the sides of the hopper. The hopper is well insulated, but because it weighs several hundred kilograms, it is attached directly to the steel frame, making a thermal bridge to the outside air. With this construction, waiting long enough for the internal particle temperatures to fully equilibrate (which may take 24 hours or more) was not possible, as the heat loss to the surroundings is high enough that the overall temperature drops too quickly to maintain the desired temperature of ~600 to 700 °C. To help reduce the temperature gradients inside the hopper more quickly, 16 steel rods were bent into a “U” shape and inserted from the top, which hang over

the preheater tubes (Figure 6.20), which appeared to reduce, but not eliminate, this problem.

The hopper design could be improved by eliminating the thermal bridge between the hopper and the frame, increasing the insulation thickness, and adding many more conductive rods to promote equilibration of temperature. However, in practice it is hard to entirely eliminate these temperature gradients and to ensure a perfectly constant particle temperature supplied to the test section using such a hopper. A flow-through type design was also considered, where particles start in an unheated hopper, and the particle stream descends through a preheating section to raise the temperature by ~ 700 °C as the particles flow through. Such a design could create a constant temperature particle stream and would also eliminate time spent on preheating and waiting for the temperature in the hopper to equilibrate. The heated hopper design was chosen for its simplicity and because a flow-through style heater may take significant vertical length to raise the temperature more than 700 °C, but the overall vertical height of the current setup is limited by the ceiling of the facility to ~ 3.5 m. Originally, it was also thought that a flow-through heater would have the disadvantage of high temperature gradients across the particle stream, as some portions of the stream would be close to the heated walls of the device, while other particles would be further away from the walls. However, the paddle wheel mixing device developed during this research can effectively mix the particle stream completely, so it is no longer a problem if the particle stream leaving the preheater has large temperature gradients. Given these points, a flow-through style heater may be a better choice to achieve a constant output temperature for similar setups or for modifying this setup in the future.



Figure 6.20. Top view of the hopper, where U-shaped steel rods are placed over the heating tubes to promote conduction inside the hopper and reduce temperature gradients.

6.3.4 Mixing the Particle Stream

In the original design, the particle stream at the outlet of the test section was to be mixed by a *passive* mixing device, which would blend the stream by routing the flow around corners, orifices, or other obstacles. Also, in the original design, the inlet to the test section was assumed to be relatively uniform in temperature and only minor mixing would be required. After testing, it was evident that the particle stream at both the inlet and the outlet need a very high degree of mixing to accurately measure the bulk temperature of the particle stream.

Several of the passive mixing device prototypes are shown in Figure 6.21, where each is carved out of an insulation block 40 cm in length, and a similar sized un-carved piece of insulation would be clamped on to the piece shown in order to close the channel. In Figure 6.21(a), particles enter at the top and “zig-zag” down the flow channel, cascading over each protrusion until they fall into the bay created by the metal plate near the end. The metal plate has a 6 mm hole near the bottom, which established a downward moving dense granular flow in this compartment for measuring the temperature with a thermocouple, while excess particles spill over

the top and fall directly towards the exit. Another design, in Figure 6.21(b), uses two similar bays for measuring the particle temperature, along with a dispersed flow through a field of many small screws which enhances random collisions and therefore mixing. A third design is shown in Figure 6.21(c) where the mixing section is clamped against a piece of Plexiglas to show the flow pattern. This design has five bays, each with a 6 mm orifice to create a downward moving dense granular flow where thermocouples were installed.

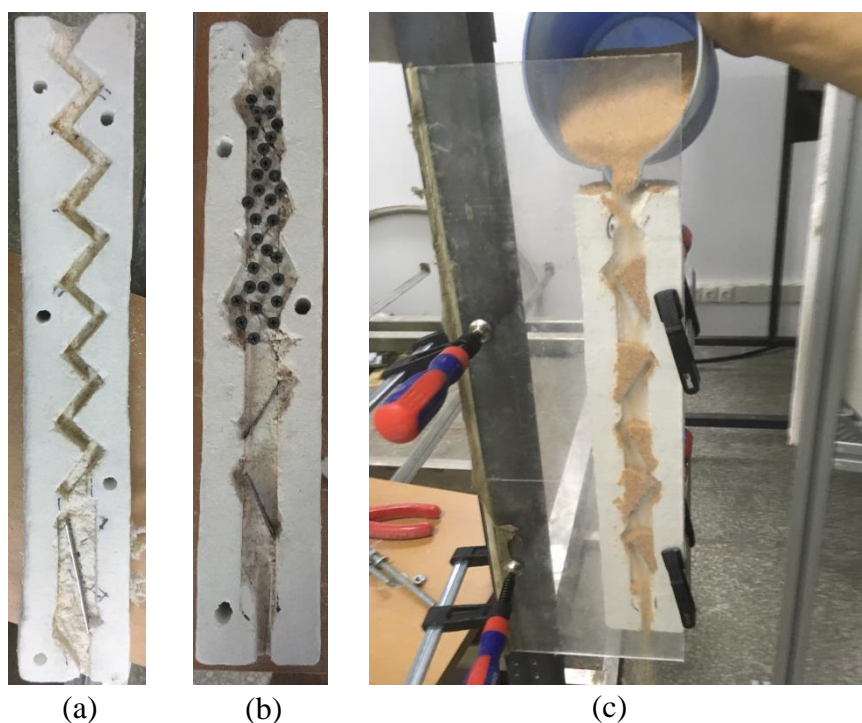


Figure 6.21. Three prototype passive mixing devices, none of which were found to completely mix the particle stream.

While the setup is running with the lamps turned on, the outlet stream has a very large temperature gradient, with particles near the illuminated front face being much higher in temperature than particles in the back. The designs shown in Figure 6.21 were tested by placing five to ten thermocouples in multiple locations, with some placed in the bays with a dense granular flow and some in the dispersed flow. If the particle stream is well mixed, readings from thermocouples near the end of the mixing section should become uniform as all the particles and the air should be

essentially equal in temperature at that point. However, this was generally not observed. For example, in the design of Figure 6.21(c), one test (no preheating and only one lamp on) showed steady state temperatures in the five bays from top to bottom of 45.9, 48.5, 41.6, 44.4, and 40.5 °C, which indicates particles are *not* well mixed. Of these three designs tested, the dispersed flow design in Figure 6.21(b) seemed to achieve the most mixing, though after many tests, it was clear that full mixing of the stream to completely destroy this temperature gradient was not possible with these passive designs, and much more aggressive mechanical mixing would be required.

Similarly, the temperature of particle stream at the inlet of the test section (that is, at the outlet of the hopper) was measured in three locations, each with the same axial (vertical) location but at different radial positions in the flow channel. In an initial test, with no mixer after the hopper, the temperature was found to vary by over 100 °C between these two thermocouples, even though the two thermocouples were less than 1 cm apart, apparently because one portion of the stream is drawn from a hot region of the hopper and another portion of the stream is drawn from a cold region. This clearly shows that the particle stream leaving the hopper must be mixed aggressively so an accurate bulk temperature measurement can be found.

The mechanical paddle wheel mixer described in Section 6.1.6 was designed to fix these problems and achieve a very high degree of mixing. Particles descend through the orifice plate above the mixer, dropping onto the center of the *upward* moving half of the paddle wheel, as shown in Figure 6.22. This ensures that the upward stroke of the paddle wheel collides with the downward motion of the particles, resulting in a high speed collision which sends particles in random directions with high velocity. Testing showed that if the stream collides with the downward moving half of the paddle, particles simply move along with the paddle, resulting in few collisions and little mixing. Even a particle stream centered on the paddle is not desired, as the half of the stream striking the upward moving part of the paddle is well mixed but the other half of the stream is not. The mixer behavior was observed outside of the setup and recorded with a slow motion camera,

revealing a particle flow which is extremely chaotic, with many high-velocity collisions and an extremely high degree of mixing. Several frames from the video footage are shown in Figure 6.23, where the stream is poured on the upward moving side of the paddle, and even from these still photographs the high degree of random collisions can be seen. Mixing was validated quantitatively as well by placing multiple thermocouples in the flow channel and comparing the readings, and unlike the passive mixing devices, the paddle wheel mixer eliminated any noticeable temperature gradient present in the incoming particle stream.

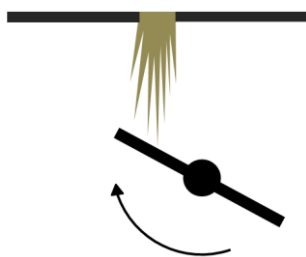


Figure 6.22. Paddle wheel mixing device used to achieve a uniform stream temperature.

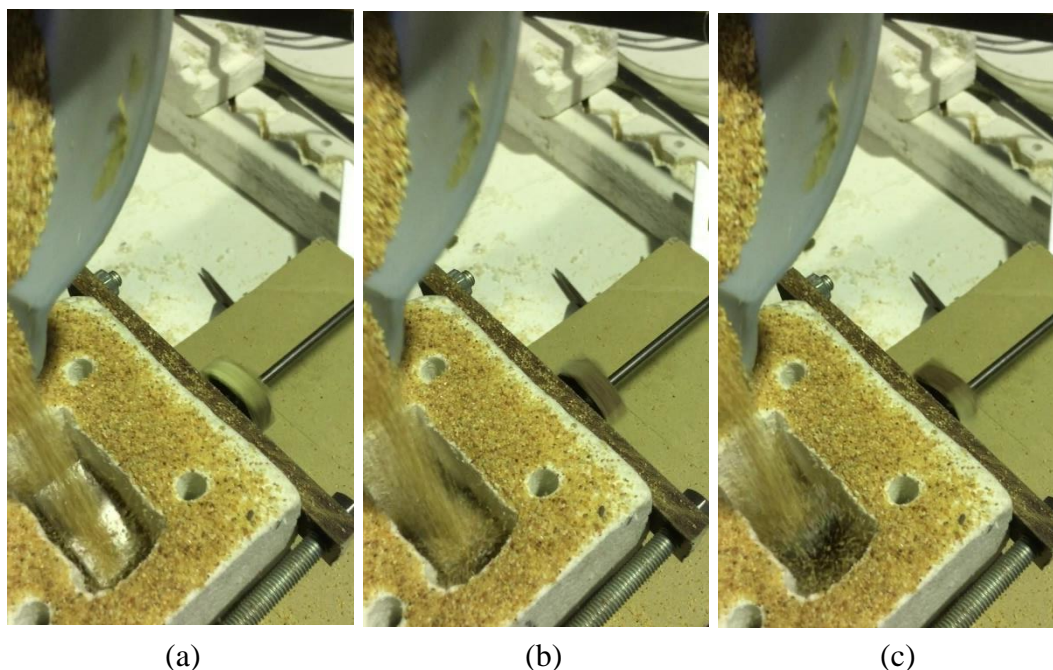


Figure 6.23. Three frames of video showing the high-speed and chaotic particle flow imparted by the paddle wheel, leading to a high degree of mixing.

6.4 Conclusions for Experimental Investigation

More experiments such the one described in this chapter are needed for validation of DEM based heat transfer models, but achieving trusted results at these high temperatures is extremely challenging. Through this process, several key concepts for obtaining trusted results were identified and addressed. To completely mix the particle stream, it was found that a high speed paddle-wheel type mixing device is needed, and the passive mixing devices originally designed were not adequate. To actually implement such a paddle-wheel device, the key development is to use a second orifice plate and an overflow channel to create a vacant pocket where the mixer can spin freely and mix particles at high velocity. With this combination of mixer, orifice plate, and overflow channel, various experimental setups could be devised for similar studies. The hopper type preheater was found to give a non-constant temperature output, and for future work a flow-through type heater is recommended. Future tests should aim for a much higher temperature rise, which would minimize the impact of any error in the bulk particle temperature measurements at the inlet and exit.

Data sets from three tests are presented, covering both sand and sintered bauxite at high, medium, and low temperatures. Given the many experimental challenges in obtaining these measurements, an uncertainty analysis was not performed, as the inaccuracy due to measurement errors is assumed to be larger than the contribution from the thermocouples and scale. Still, the three tests presented are the best results obtained during the experiment, so the data sets can be compared against DEM-based heat transfer models such as DPHT. This is the subject of Chapter 7.

CHAPTER 7

COMPARISON OF EXPERIMENTAL AND DPHT MODEL RESULTS

In this section, a comparison is made between the experimental results and the DEM+DPHT simulation, with the goal being to validate the methods, models, and assumptions described in the previous chapters. Comparisons are performed with data from the “Test 2” and “Test 3” experiments because the mechanical and thermal properties for sintered bauxite are available in literature, whereas properties are not known with high accuracy for the sand used in the experiment.

7.1 DEM Simulation

A DEM simulation was run in LIGGGHTS where the particles descend through the square tube and orifice plate shown in Figure 7.1. The surface shown has zero wall thickness and is made to replicate the dimensions of the inner surface of the square tube (test section). The lower and upper boundaries are periodic, so particles leaving the bottom are reinserted at the top. A total of 3.2 million particles were inserted, creating a dense flow where the fill level is above what will be the heated section. Files with the xyz particle positions were output every 2000 DEM time steps. A total of 48 seconds of real time were simulated, which took 20 days of run time, using 54 processors on a HP Z840 workstation with a clock speed of 2.8 GHz. DEM parameters are shown in Table 7.1.



Figure 7.1. Square tube test section and orifice plate used in modeling the experimental setup.

Table 7.1. DEM parameters used in simulation of experimental setup.

Parameter	Value
Number of Particles	3.2×10^6
DEM Time Step	1×10^{-5} s
Particle Radius	185.6 μm
Particle Material Density	3560 kg m^{-3}
Young's Modulus, P	$5 \times 10^6 \text{ N m}^{-2}$
Young's Modulus, W	$5 \times 10^6 \text{ N m}^{-2}$
Poisson's Ratio, P	0.30
Poisson's Ratio, W	0.30
Coefficient of sliding friction, PP	0.72
Coefficient of sliding friction, PW	0.30
Coefficient of rolling friction, PP	0.13
Coefficient of rolling friction, PW	0.50
Coefficient of restitution, PP	0.82
Coefficient of restitution, PW	0.44

Initial tests were run with an 8 mm orifice at the outlet (matching the experiment), but in post-processing the mass flow rate in the simulation was found to be lower than the experimental value of 0.0206 kg s^{-1} . The simulation orifice at the outlet was increased in size to 9 mm, making the mass flow rate much closer to the experimental value. It is not known why this difference is found, but it is likely attributable to the particle properties used in the simulation. The properties were taken from Grobbel [97], who did a detailed calibration with the same Carbo particles, though the particle size was slightly larger (30/60 mesh size used by Grobbel, instead of 40/70 used here). A higher mass flow rate could have been achieved by changing the DEM parameters (e.g. by reducing particle friction coefficients), but there are numerous parameters which must be calibrated simultaneously with several experiments, so blindly changing a single value to

match the current experiment may influence the mechanics in undesired or non-physically realistic ways. Therefore, to proceed, the orifice diameter was increased until the average mass flow rate was close to the experimental value of 0.0206 kg s^{-1} . The total mass passing a horizontal plane over time is shown in Figure 7.2, leading to the linear curve fit shown and an average mass flow rate of $0.020277 \text{ kg s}^{-1}$, close to the experimental value. To more exactly align the conditions in the simulation and experiment, the DEM time step is modified ($\Delta T_{DEM,mod}$) when proceeding with the heat transfer simulation using Eq. (7.1). This results in a modified time step of $9.84338 \times 10^{-6} \text{ s}$, which ensures that the mass flow rate in the thermal simulation exactly matches that of the experiment. Effectively, this increases the velocity of all of the particles a small amount, which is a reasonable way to increase the flow rate slightly. Alternatively, the orifice plate could have been adjusted iteratively until the simulation matched the experimental mass flow rate, but iterating many times is not feasible due to the high computation time of the simulations.

$$\Delta T_{DEM,mod} = \Delta T_{DEM} \left[\frac{\dot{m}_{DEM}}{\dot{m}_{exp}} \right] \quad (7.1)$$

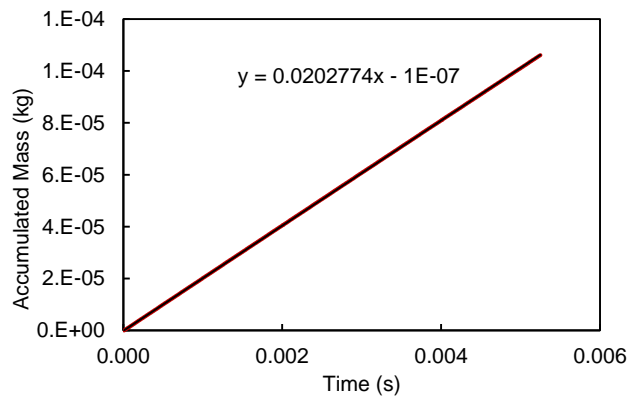


Figure 7.2. Mass accumulation over time, and equation for mass flow rate.

7.2 DPHT Simulation

Since the mass flow rates in Test 2 and Test 3 are nearly identical, the same DEM simulation was used to run both DPHT simulations. Section 7.2 describes how the heat transfer simulation was run using DPHT for Test 2, the high-temperature experiment. The same procedure was followed for Test 3, the lower temperature experiment. Details for Test 3 are not shown but results are presented.

7.2.1 Modified PFP Heat Transfer Model

As described in Section 5.8, the particle-scale model for PFP heat transfer by Cheng et al. [94] underpredicts the overall heat transfer through a packed bed compared to the k_{eff} model of Zehner and Schlünder (ZS) [30] by around 10-15%. Both the particle-scale PFP model and the continuum ZS model account for only the heat transferred through the fluid gap between particles, so this is a direct comparison. While it is not possible to know for certain which is more correct, the validity of the ZS model has been shown under many conditions with experimental data, while the PFP model from Cheng et al. has been implemented in several research studies but with less experimental validation. The PFP model takes the complicated heat transfer problem of two spheres with non-isothermal surfaces and reduces it down to a two-cone configuration with isothermal surfaces, so it may not lead to accurate results under all conditions, such as different particle radii, temperatures, thermal conductivities, and solid fractions. The cone radius was originally found by drawing Voronoi polyhedra around each sphere, but later the cone radius was found as a function of the solid fraction by Zhou et al. [93].

To make the results of the PFP model match more closely with the ZS model under the conditions relevant to the experiment of this thesis, the equation for the cone radius by Zhou et al. was multiplied by the correction factor f_c to form Eq. (7.2). The k_{eff} for the domain shown in Figure 7.3 was found using different values of f_c , until a match was found with the ZS model. In these simulations, the thermal

conductivity and the radius of the spheres were those of the sintered bauxite particles ($2.0 \text{ W m}^{-1} \text{ K}^{-1}$ and 0.1856 mm). The evaluation of k_{eff} was carried out at 873 K , leading to a f_c value of 1.28 .

$$R_{ij} = 0.560R\alpha_s^{-1/3} f_c \quad (7.2)$$

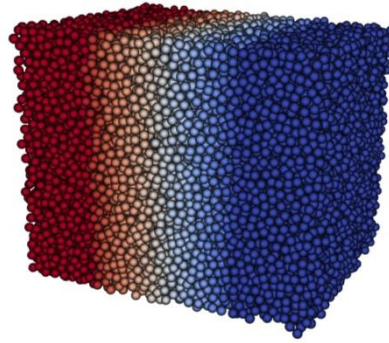


Figure 7.3. Particle group used for evaluation of k_{eff} , leading to a correction factor value of 1.28 in Eq. (7.2).

As shown in Figure 7.4, the k_{eff} found with the simulation using the original PFP model by Cheng et al. [94] was much lower than the value predicted by the ZS model. After applying the correction factor of 1.28 to the cone radius, a much closer match was found. The match is nearly perfect at 878 K because f_c was determined at that point, but a close match is also seen at the other temperatures. This f_c value is expected to increase accuracy for the current conditions, but it is probably not widely transferrable to other applications because it is tailored to the conditions of this experiment. In the DPHT simulation, an f_c value of 1.28 was applied in both the PFP and PFW conduction models.

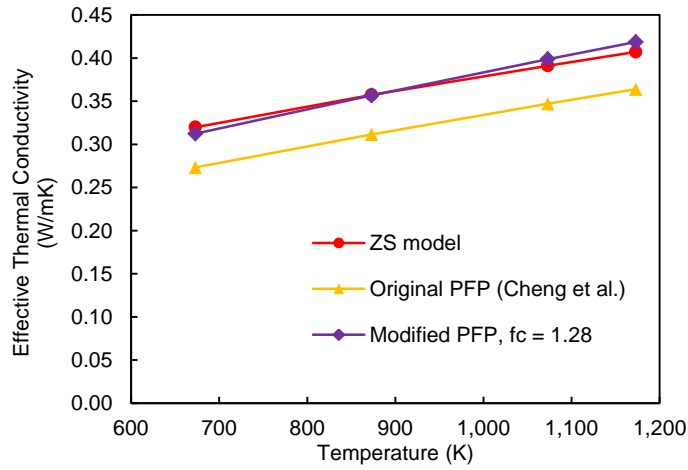


Figure 7.4. K_{eff} at several temperatures, showing the ZS model, the original PFP model, and the PFP model modified with a correction factor of 1.28 in Eq. (7.2).

7.2.2 Thermal Properties

The thermal simulation was run with the DPHT code using the parameters shown in Table 7.2.

Table 7.2. Thermal parameters used in simulation of experimental setup.

Parameter	Value
Thermal conductivity, P	$2.0 \text{ W m}^{-1} \text{ K}^{-1}$
Thermal conductivity, W	$16.6 \text{ W m}^{-1} \text{ K}^{-1}$
Emissivity, P	0.86
Emissivity, W	0.60
Particle temperature at inlet	621.7 °C
Initial particle temperature	621.7 °C
Young's Modulus, DEM, P	$5 \times 10^6 \text{ N m}^{-2}$
Young's Modulus DEM, W	$5 \times 10^6 \text{ N m}^{-2}$
Young's Modulus, real, P	$52 \times 10^9 \text{ N m}^{-2}$
Young's Modulus, real, W (stainless steel)	$180 \times 10^9 \text{ N m}^{-2}$
Solid Fraction, bulk	0.5791
Solid Fraction, near wall	0.5284
Specific heat capacity, P	$0.74857 \cdot T[\text{K}] + 560.768 \text{ J kg}^{-1} \text{ K}^{-1}$

Siegel et al. [56] presented specific heat capacity values for Carbo HSP particles, which were found experimentally as a function of temperature. Data points in the temperature range of interest were given a linear fit as shown in Figure 7.5, and the corresponding equation gives specific heat as a function of temperature, where units are in Kelvin.

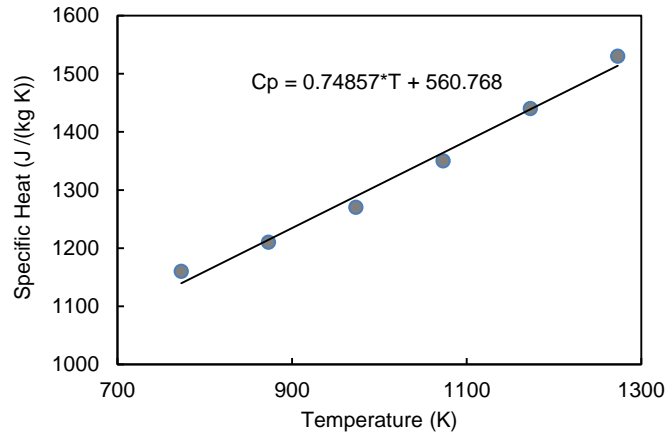


Figure 7.5. Specific heat as a function of temperature.

7.2.3 Thermal Boundary Conditions

With wall temperatures known only at eight locations, boundary conditions must be estimated for the entire surface. To do this, the square tube was “unfolded” to make a flat surface for which a temperature map can be found with curve fitting. However, the thermocouple probes measure the temperature at the *center* of the 8 mm thick wall, whereas the thermal boundary condition is desired at the interior surface, with a slightly lower temperature. This presents a challenge; the temperature at the interior surface could be found with Fourier’s law of conduction, Eq. (7.3), but this would require knowing the heat flux through the wall at each location, which is not known at the beginning of the simulation.

$$q'' = -k \frac{\Delta T}{\Delta x} \quad (7.3)$$

This problem was solved by estimating the heat flux at each location using the experimental data. First, the total heat transfer in the experiment was estimated using the inlet and outlet temperatures, mass flow rate, and an assumed constant specific heat of $1200 \text{ J kg}^{-1} \text{ K}^{-1}$, resulting in 761 W. Next, the temperatures on the sides of the square tube (still in the center of the wall) were estimated by linearly interpolating between the front and back measurements at the same height,

resulting in temperature values at a total of 16 locations. Figure 7.6 shows the measurement locations on the square tube as well as on the unfolded surface. The surface of the tube was broken up into 16 rectangular panels, with one temperature measurement for each panel. The key is to estimate how the total heat transfer (761 W) is distributed among the different panels.

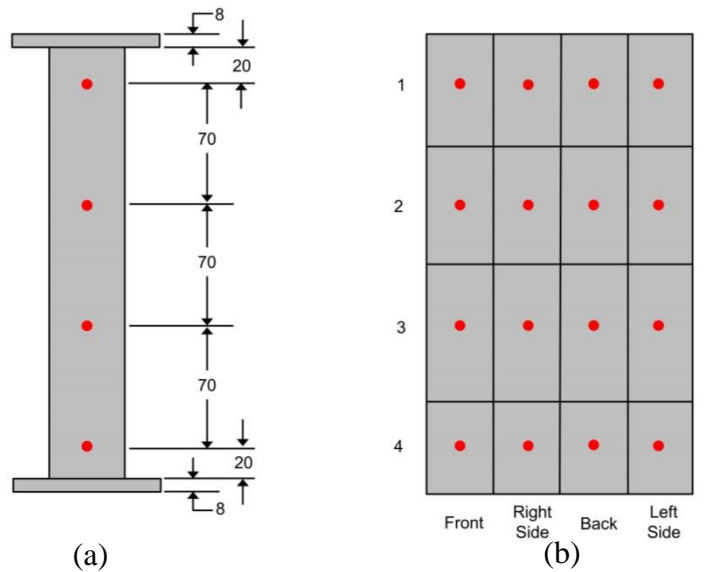


Figure 7.6. Temperature locations shown in red (a) on the front of the square tube, and (b) on all surfaces of the unfolded surface, subdivided into 16 panels.

To make this estimation, the heat transfer through each panel was assumed to be A) uniform, and B) proportional to the difference between the wall temperature and the inlet particle temperature. These should be reasonable approximations for a small temperature range, where variation in the T^4 radiative effects and any variation in thermal properties are minimal. Under this assumption, the temperature excess with respect to the inlet temperature (621.7 °C) was found at each of the 16 temperature locations, and this was divided by the total temperature excess from all temperature locations combined (2129.6 °C). The total of 761 W was then divided among the panels based on this proportion. The heat flux was then calculated for each panel, as not all panels have the same area due to the location of the drilled holes for the thermocouple probes. The temperature on the interior surface of the square tube was then found for each of the locations using Eq. (7.3), where the temperature at the center of the wall and the heat flux (q'') are known, the distance

from the center to the surface (Δx) is 4 mm, and the thermal conductivity (k) is $16.6 \text{ W m}^{-1} \text{ K}^{-1}$ for stainless steel. As shown in Table 7.3, the surface temperatures are reduced slightly ($\sim 6 \text{ }^\circ\text{C}$) on the back side, and up to $18 \text{ }^\circ\text{C}$ on the front side where the highest temperatures and heat flux are found. However, in all cases this is a fairly modest temperature adjustment, roughly 6% at each point, in comparison to the temperature difference between the wall and the particles, so the accuracy of this estimation was acceptable.

Table 7.3. Measured temperatures in center of wall, and calculated temperatures at interior surface.

Thermocouple Location	Measured temperature, center of wall ($^\circ\text{C}$)	Adjusted temperature, interior surface ($^\circ\text{C}$)
Front Wall 1 (top)	725.1	718.0
Front Wall 2	886.2	869.9
Front Wall 3	916.3	898.2
Front Wall 4 (bottom)	762.5	752.9
Back Wall 1 (top)	631.0	630.4
Back Wall 2	690.7	686.5
Back Wall 3	724.4	718.1
Back Wall 4 (bottom)	702.2	696.7

With the surface temperature at each of the original eight temperature locations calculated, a polynomial surface fit was found. This resulted in the temperature map shown in Figure 7.7, representing the right half of the square tube. A linear fit in the x -direction was used, as a higher order fit is not possible with only two points. A 3rd order fit in the y -direction was selected because it is the lowest order that conformed well to the known data points. In the figure, the vertical black lines represent the corners of the square tube, and white circles represent measurement locations. The left half of the receiver is the same but symmetrical around the center line ($x=0$).

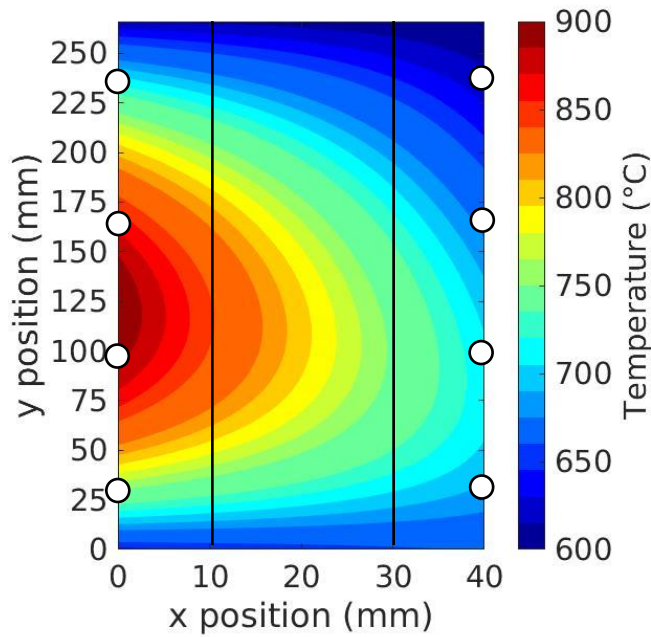


Figure 7.7. Temperature map of right half of square tube test section, found from polynomial surface fitting of eight known temperature locations.

The equation for this surface fit is given in Eq. (7.4), which is applied as a boundary condition in the DPHT code. In this equation, T is the temperature in K, and the xy coordinates relate to Figure 7.7, with units of meters.

$$T = 913.4 + 533.1x + 4664y - 7.80e4xy - 2.28e4y^2 + 2.80e5xy^2 + 1.91e4y^3 \quad (7.4)$$

This boundary condition is then “folded” around the 3D geometry of the square tube, and the result is shown in Figure 7.8.

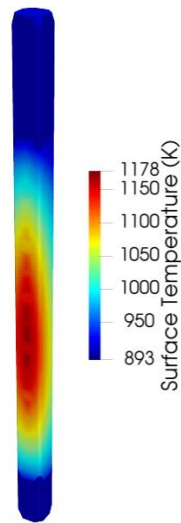


Figure 7.8. Temperature boundary condition applied to inner surface of square tube.

7.3 Results and Discussion

7.3.1 Test 2 Results

Results from the thermal simulation of Test 2 are shown in Figure 7.9, where the total heat transfer over time is separated by the three PW heat transfer modes. A steady state is established after roughly 10 seconds.

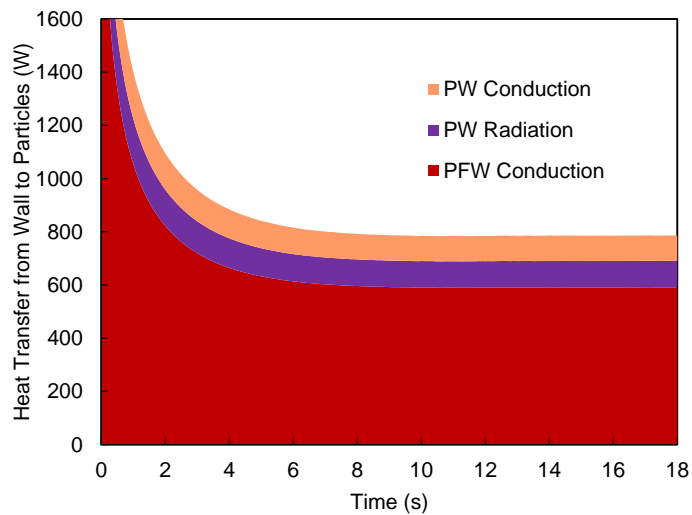


Figure 7.9. Total heat transfer from wall to particles over time, showing all three PW heat transfer modes.

The steady state values for heat transfer from each mode are shown in Table 7.4, along with the total heat transfer of 786.4 W. Under these conditions, the bulk of the heat transfer is through PFW conduction, while PW conduction and PW radiation mode each account for ~12% of the total. Both of these heat transfer modes are neglected in some research, but doing so would reduce the overall PW heat transfer by roughly 25%, showing such an assumption is invalid under these conditions.

Table 7.4. Steady state heat transfer rate from wall to particles, Test 2.

Heat Transfer Mode	Heat Transfer (W)	Proportion of Total (%)
PFW Conduction	591.6	75.2
PW Conduction	95.2	12.1
PW Radiation	99.5	12.7
Total	786.4	100

The chief criterion for comparing the simulation and experiment is the overall heat transfer rate to the particles at steady state. To find this quantity for the experiment, the inlet and outlet temperatures were averaged to find 910.25 K, corresponding to a specific heat of 1242.15 J kg⁻¹ K⁻¹ with the equation shown in Figure 7.5. With a mass flow rate of 0.0206 kg s⁻¹ and a temperature rise of 30.8 K, the total heat transfer rate is found to be 788.1 W. This value is extremely close to the simulation result of 786.4 W, lending validity to the many methods and assumptions used to achieve these results.

The steady state particle temperatures are shown in Figure 7.10. All particles are shown in Figure 7.10(a), a section view is shown in Figure 7.10(b), and a close-up section view near the outlet is shown in Figure 7.10(c). As expected, the particle temperatures increase most near the parts of the wall with highest temperature. As seen in the close-up section view, the interior particles heat up very little, leaving them essentially at the inlet temperature, while the near-wall particles are several hundred degrees higher in temperature.

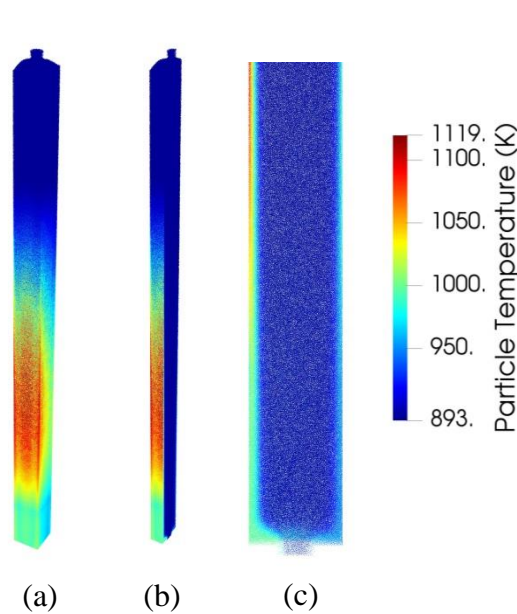


Figure 7.10. Steady state particle temperatures, showing (a) entire particle stream, and (b) section view to show interior particles, and (c) close-up section view to show particles near the outlet.

The steady state heat flux at the boundary is shown in Figure 7.11. As expected, the heat flux peaks at the front and center, where the incident radiation is the highest. An interesting and perhaps unexpected result is the *negative* heat flux shown at the lower portion of the tube, meaning heat is transferred from the particles to the wall. If the particle temperatures in Figure 7.10(a) are compared to the wall temperatures in Figure 7.8 this is logical; the hottest (red) particles are heated to ~ 1119 K before descending further to the part of the wall which is cooler at around 1000 K (shown in light blue), so heat is transferred from the particles to the wall.

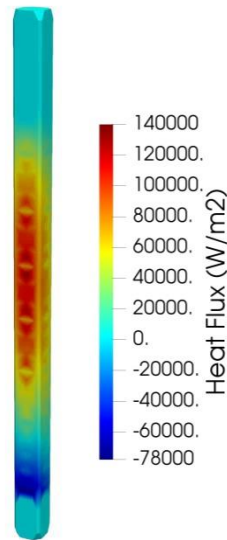


Figure 7.11. Heat flux of test section at steady state.

7.3.2 Test 3 Results

Steady state heat transfer rates from the wall to the particles, for Test 3, are shown in Table 7.5. Unlike at the higher temperatures of Test 2, radiation plays an almost negligible role, contributing only 3.2% to the overall PW heat transfer. This shows the need for the heated hopper in the experiments, as starting tests at room temperature largely misses any contributions from radiation, making it a less useful test for validation of all the implemented heat transfer models. The overall heat transfer to the particles was predicted to be 1167.2 W by the DPHT simulation.

Table 7.5. Steady state heat transfer rate from wall to particles, Test 3.

Heat Transfer Mode	Heat Transfer (W)	Proportion of Total (%)
PFW Conduction	938.9	80.4
PW Conduction	191.2	16.4
PW Radiation	37.1	3.2
Total	1167.2	100

The overall heat gain in the experiment was found from the temperature rise (63.7 K), a mass flow rate of 0.0202 kg s^{-1} , and an average specific heat of $825.7 \text{ J kg}^{-1} \text{ K}^{-1}$. The specific heat was found with a method similar to that shown in Figure 7.5, but the fit was found for the lower temperature range for Test 3. This yielded a total

heat transfer rate for the experiment of 1062.5 W, roughly 9% less than the value predicted by the DPHT simulation.

7.3.3 Uncertainty and Repeatability

There results show a close match between the simulation and the experiment for Test 2, and a difference of 9% for Test 3. Under the conditions of Test 3, radiation plays a very small part in the overall heat transfer, which points towards either experimental uncertainty/error, or a deficiency in the PFP conduction model as the root cause of the discrepancy. Nevertheless, the results from the two tests give some indication as to the accuracy that can be expected. Clearly, more comparisons with experiments must be run before the six heat transfer models in DPHT can be considered truly validated for high accuracy simulations.

An uncertainty analysis was run for the total heat gain in the experiment, which was found using Eq. (7.5). The mass flow rate was found with a linear curve fit using many (roughly 130) measurements of the mass on the scale over time, so the uncertainty in the mass flow rate is not considered in this analysis. In addition, the uncertainty in the specific heat is not considered, as it was taken from previously published data, and no uncertainty information is known. Thus, only the uncertainties in the thermocouple measurements were considered. For best accuracy, “Special Limit of Error” (SLE) K-type thermocouples were generally used for the inlet and outlet temperature measurements, as they offer higher accuracy than typical thermocouples. The stated accuracy is ± 1.1 °C or 0.004%, whichever is greater. Normal K-type thermocouples have an accuracy of ± 2.2 °C or 0.0075%, whichever is greater. During Test 2, the SLE thermocouple broke, so the reading was taken with a backup thermocouple, which was a normal K-type.

$$q = \dot{m} C_p (T_{outlet} - T_{inlet}) \quad (7.5)$$

For Test 2, an uncertainty of $\pm 17.3\%$ was found. The relatively high uncertainty is due both to the high temperature, and due to the normal K-type thermocouple used at the inlet. Thus, even though a very close match was found between the simulation and experimental results, the closeness of the match may not be repeatable, as the uncertainty in the experiment is quite high.

In Test 3, a low uncertainty of only 2.3% was found due to the low temperatures and SLE thermocouples used. Thus, the 9% difference between simulation and experimental results cannot simply be attributed to experimental uncertainty; there must be an error either in the measurement or in the model.

The comparisons shown represent a culmination of work to develop both new modeling and experimental techniques, so there are potential sources of error in both areas. In the model, perhaps the largest source of potential error is in the PFP and PFW conduction models because they account for the largest portion of heat transfer overall. The direct conduction and radiation models each have a lesser impact on the overall results. The DBA radiation model is expected to have a high accuracy given the rigorous numerical validations conducted under very similar conditions in Chapter 4.

The properties used in these models may also have a large effect on the results. The thermal conductivity of air is a main factor in the PFP conduction model, and for this reason it was found as a function of temperature instead of assuming a constant value. In contrast, the thermal conductivity of sintered bauxite was taken as a constant value of $2.0 \text{ W m}^{-2} \text{ K}^{-1}$, as no temperature dependent properties were available. However, the solid conductivity has a relatively minor impact on the overall heat transfer because in the PFP model, which is the leading mode of heat transfer, by far the largest resistance to heat transfer is due to the air gap between particles. Thus, any error in the solid thermal conductivity value likely contributes relatively little to the overall error. An error in the particle specific heat would be a large contributor to the overall error due to its direct effect on the temperature rise of the particles. The values used to find specific heat as a function of temperature

were taken from an experimental data set used widely by researchers in this field, so they are thought to be accurate. The emissivity of the stainless steel wall has a strong effect on the PW radiative transfer in the DBA model; 0.60 was chosen, though there is a wide variety of values found in literature but few at high temperatures, and the value strongly depends on the surface treatment. Radiation accounts for 12.7% of the total heat transfer from the wall in Test 2, so any inaccuracy in the wall emissivity could lead to several percent error overall.

In the experiment, perhaps the largest source of potential error is from the inlet and outlet temperature values measured, since the particle streams may not be perfectly uniform both spatially (across the stream) and in time, as noted in Section 6.2.4. Given the temperature rise (30.8 °C in Test 2, and 63.7 °C in Test 3), a small experimental error in the inlet or outlet temperature readings would lead to a large error in the computed overall heat gain. In future experiments, a much higher temperature rise is desired to minimize this effect.

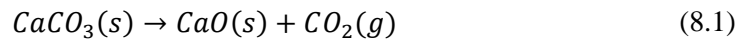
7.4 Conclusions for Comparison of Experimental and DPHT Model Results

When comparing the experimental and DPHT simulation results in terms of overall heat transfer, an extremely close match was found for Test 2 (high temperature), while a difference of ~9% was found for Test 3 (low temperature). This level of agreement indicates that, at a minimum, the model can predict with relative accuracy the behavior of a real system. With only these two tests for comparison, it is not clear how repeatable this is. There may be multiple errors in the model which have the effect of cancelling each other out under certain circumstances, leading to the close agreement shown in Test 2. This has to be addressed in future work, with more experimental studies performed until a repeatable pattern of high accuracy results can confirm the validity of the model.

CHAPTER 8

A SOLAR RECEIVER FOR PREHEATING LIME PARTICLES

Cement production is responsible for 5-7% of the annual CO₂ emissions globally [101], making it an industry which is critical to decarbonize in the coming decades to address climate change. Calcination of limestone is the key step in cement production, where limestone, predominantly CaCO₃, is converted to CaO and CO₂ through an endothermic reaction in the temperature range of 900 to 1500 °C. Carbon dioxide is released due to both the chemical reaction, shown in Eq. (8.1), as well as in the burning of fossil fuels to reach the high temperatures of the reaction.



Supplying heat from CSP may provide a solution to calcinate limestone without fossil fuels [102]. It can also be applied to other high-temperature and energy-intensive industrial processes such as metallurgy, waste incineration, and metals recycling [3]. In this research, a solar receiver is envisioned for preheating lime particles from ambient temperatures to roughly 700 °C, which would save a large portion of CO₂ in the heating step before calcination occurs. At temperatures above 700 °C the calcination reaction begins, where heating and off-gassing of the reaction products must be tightly controlled, so this initial receiver design is focused on preheating the particles only. Furthermore, by designing a receiver to preheat particles, the modeling method and results may be transferrable to other industrial heating processes which require a similar heating of granular material to high temperatures.

8.1 Receiver Design

The receiver designed uses a dense granular flow of particles which descend due to gravity in between parallel plates. One of these plates forms the heated surface of the receiver, shown in red in Figure 8.1, and the other plate is insulated. The overall dimensions of this receiver follow the designs of cavity receivers which circulate molten salt as a heat transfer fluid for electricity generation [103]. The receiver surface is 12 m wide by 6 m high, with a 5 m deep cavity (or hood), and a 2.5 m lip. The entire receiver and cavity is tilted towards the front at 12.5°. The cavity is critical, as it substantially reduces emissive and convective losses from the hot receiver surface, leading to a much higher efficiency than an “open” receiver without the cavity. Lime particles of diameter 1 mm descend between the parallel plates, which are spaced at a distance of 8 mm, as shown in the close-up in Figure 8.1. A thin channel is desired for the best heat transfer, but reducing it further may cause blockages in the flow due to clogging and bridging at the outlet. These dimensions all play a role in the final efficiency and heat gain of the receiver, and they can be adjusted to optimize the design in future work.

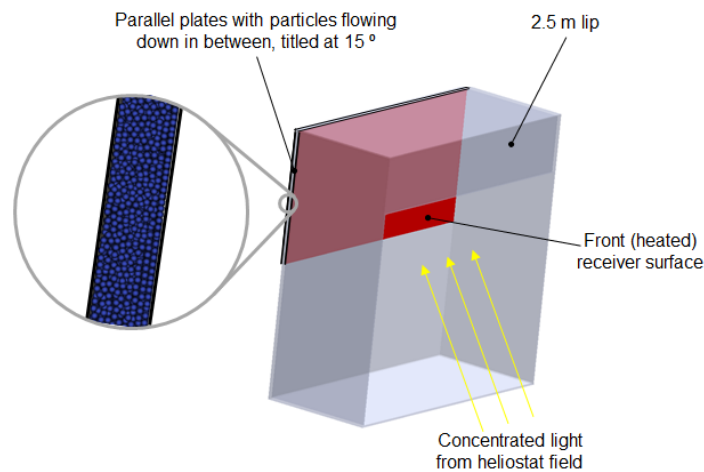


Figure 8.1. Receiver design and 1-mm diameter particles descending between parallel plates.

8.2 Modeling Methods

Simulating the entire receiver was done by integrating three different modeling components. The following sections detail these different models:

- 1) Ray tracing of the heliostat field, tower, and cavity to find the incident radiative flux on the receiver surface.
- 2) Particle-scale heat transfer modeling of a portion of the particle-air domain using the DPHT code.
- 3) Modeling the overall heat flows in the receiver using outputs from (1) and (2).

8.2.1 Ray Tracing of the CSP System

A collaborating researcher, Diogo Canavarro, at The University of Évora [104], performed ray tracing for the proposed receiver using the software Tonitruh [105], and results are publically available [106]. Given the receiver dimensions and cavity proposed in Figure 8.1, a heliostat field was designed to supply a radiative flux with a peak of 200 kW m^{-2} , or a concentration of the sun's rays by roughly 200 times. This guideline was used because preliminary modeling showed that this flux intensity would not melt the receiver surface. In designing such a receiver, the efficiency generally increases with higher light concentration, as absorbing the same amount of energy in a smaller surface area will lead to lower emissive and convective losses from the receiver surface. However, if the heat flux is too high, the receiver surface will exceed the working temperature range of the metal surface, or even melt. Thus, to maximize efficiency, the central goal is to increase the concentration while staying within the working temperature range of the material of the receiver surface.

To further concentrate the incident radiation towards the receiver surface, a secondary reflector (often termed a “compound parabolic concentrator”) is attached to the front of the receiver. This redirects radiation from a larger area towards the

receiver surface, reducing any light lost around the periphery of the receiver. The secondary reflector is shown in relation to the cavity receiver in Figure 8.2, where the cavity walls are shown in transparent gray, and the receiver surface is shown in red.

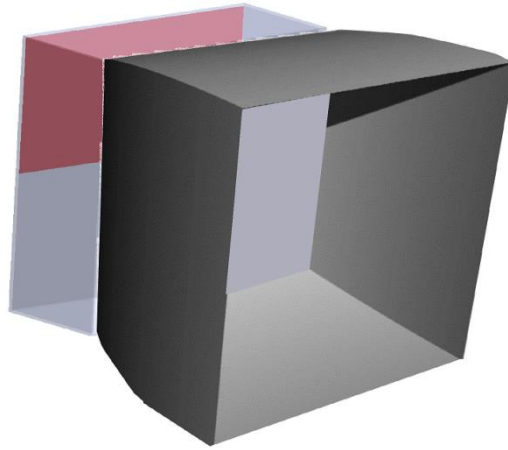


Figure 8.2. Secondary reflector used to further concentrate rays onto the receiver surface (image of secondary reflector supplied by Canavarro [106]).

The designed field layout is shown in Figure 8.3, along with the receiver, which is located at a height of 100 m above the ground. This ray tracing produces the flux map of the radiation incident to the receiver surface, as shown in Figure 8.4.

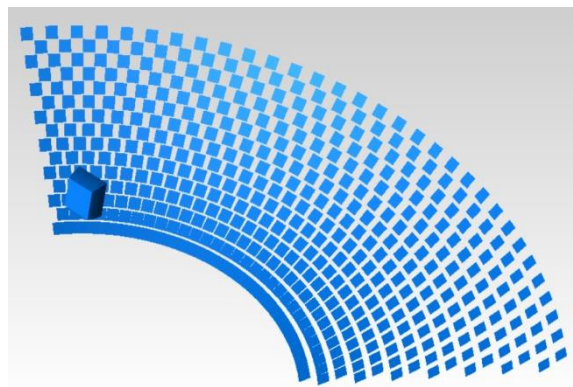


Figure 8.3. Configuration of heliostat field and solar receiver (supplied by Canavarro [106]).

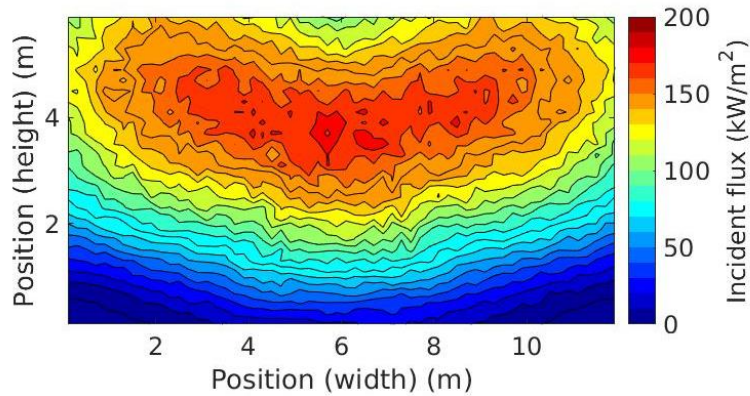


Figure 8.4. Incident radiative flux on the receiver surface.

8.2.2 Particle-Scale Heat Transfer Modeling with DPHT

Modeling the entire receiver with DPHT was not feasible due to the very large number of particles, which would number in the hundreds of millions. Therefore, the overall heat transfer coefficient method was followed, as described in Section 5.9.2. First, a DPHT simulation was used to find the overall heat transfer coefficient from the wall to the particles under the relevant conditions. This lumps all of the detailed and complex heat transfer effects of the particle-air mixture into a single parameter, which simplifies the next modeling step, the heat transfer model of the entire receiver. Thus, the DPHT simulation acts as a bridge between the complex heat transfer phenomena at the particle scale and the large dimensions of an actual receiver. This is conceptually similar to using experimental work, where the heat transfer coefficient might be found under the relevant conditions and then used afterwards for modeling an actual device.

The geometry modeled is a set of parallel plates separated by 8 mm and also 8 mm in width, as shown in Figure 8.5. Because the simulation domain must be long enough to establish a thermally fully developed flow, the plates are 6 m in length, with a static fill level of roughly 4.8 m, containing 329,376 particles. At the outlet, a diamond shaped obstruction (Figure 8.5(a)) is added to ensure the flow above it stays in a packed state (instead of in free-fall), but the constriction is very slight to

maintain a high flow rate. By setting the DEM boundary condition in the y-direction (vertical) to be periodic, particles exiting through the nozzle reappear at the top of the domain, making the number of particles constant throughout the simulation. When particles transit this periodic boundary, their temperatures are reset to the inlet temperature of 300 K in DPHT. A uniform temperature boundary condition of 1173 K is given to one plate, and an adiabatic boundary condition is given to the other. Simulation parameters are given in Table 8.1.

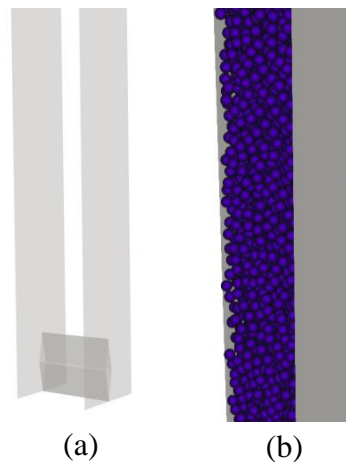


Figure 8.5. (a) Parallel plates with diamond-shaped obstruction, and (b) particles in between the 8-mm by 8-mm parallel plate strip studied.

Table 8.1 Properties used in DEM and DPHT modeling.

Property	Value	Units
Radius, P	0.0005	m
Density, P [VDI, p612]	2200	kg m ⁻³
Young's modulus, DEM, P	1e8	Pa
Young's modulus, DEM, W	1e8	Pa
Young's modulus, real, P	5.20e10	Pa
Young's modulus, real, W	1.80e11	Pa
Poisson's ratio, P	0.25	-
Poisson's ratio, W	0.30	-
Coeff. of restitution, PP	0.44	-
Coeff. of restitution, PW	0.825	-
Coeff of friction, PP	0.40	-
Coeff of friction, PW	0.30	-
Coeff of rolling friction, PP	0.40	-
Coeff of rolling friction, PW	0.50	-
Thermal conductivity, P	2.0	W m ⁻² K ⁻¹
Thermal conductivity, W	16.6	W m ⁻² K ⁻¹
Emissivity, P	0.86	-
Emissivity, W	0.60	-

The LIGGGHTS and DPHT codes are each run, for a total of 7 million DEM time steps and 3500 thermal time steps. The LIGGGHTS and DPHT runs took roughly 6 days and 1 day, respectively, using 50 processors on a Hewlett-Packard Z840 Workstation. The DPHT code has been refined and optimized for performance, and for the current simulation it takes ~24 seconds per thermal time step for the domain of 329,376 particles.

The three components of PW heat transfer are shown in Figure 8.6, which shows a steady state has been reached after ~60 seconds. At steady state, the heat transfer from the wall to the particles is separated by each mode and shown in Figure 8.6. Similar to examples in the previous chapters, direct PW conduction contributes the least to the overall heat transfer, and PFW conduction contributes the most.

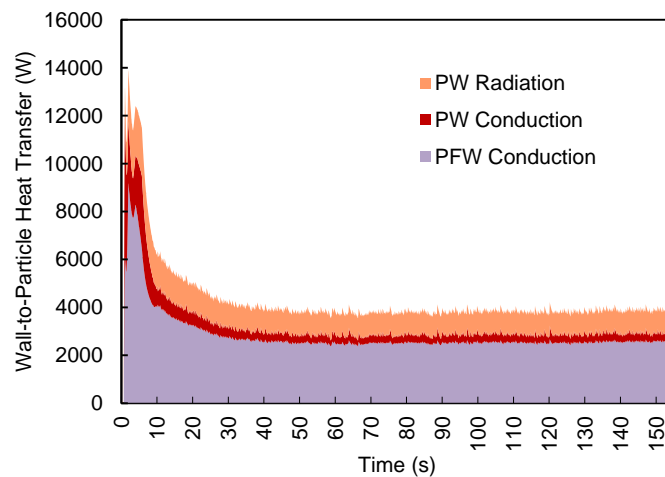


Figure 8.6. Overall heat transfer from wall to particles, separated by heat transfer mode.

The steady state particle temperatures at the outlet are shown in Figure 8.7, which indicates particles near the heated wall reach ~1124 K, while particles near the insulated wall are substantially cooler, down to 740 K. This temperature difference of nearly 400 degrees over a distance of only 8 mm is due to the low effective thermal conductivity and very little mixing in this geometry. The particles form a layer on the hot wall, which is enhanced by the fact that the parallel plates are tilted downward at 12.5 °C to match the receiver tilt. This is accomplished in LIGGGHTS by turning the gravity vector at a 12.5 degree angle. This actually

increases the PW heat transfer slightly, as noted by Natarajan and Hunt [69], because the gravity vector in the direction of the wall increases the solid fraction along the wall.

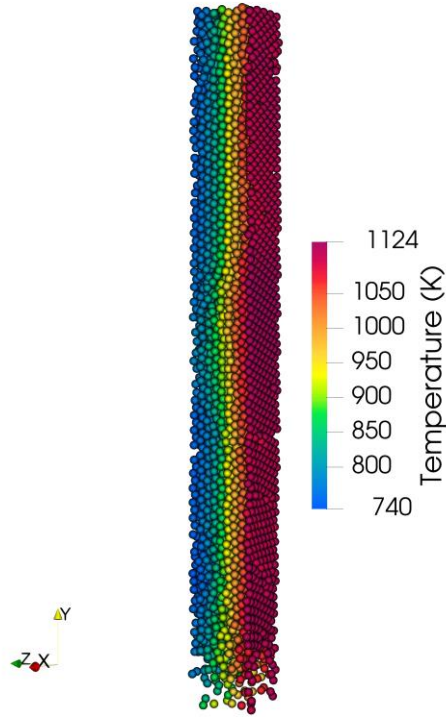


Figure 8.7. Particles at the outlet, colored by temperature.

For post-processing, the domain is subdivided into many different sections in the y -direction. The mean particle temperature in each section is plotted in Figure 8.8(a) as a function of the distance from the heated inlet, and the heat transfer coefficient is shown in Figure 8.8(b). Both plots show the averaged values over 100 time steps, after a steady state has been established. The heat transfer coefficient (h) in each section is found with Eq. (8.2), where T_{bulk} is the mean particle temperature in the section, and q_{PW} for the section is known from the DPHT outputs. The mass flow rate is analyzed over the same time period, with an average mass flow rate of 0.0056 kg s^{-1} found.

$$q_{PW} = hA_{section}(T_{wall} - T_{bulk}) \quad (8.2)$$

Similar to heat transfer in pipe flow, the heat transfer coefficient is highest near the inlet and decreases until it reaches a thermally developed state, in this case taken to be at a distance 1.5 m. The heat transfer coefficient is approximated with a fourth-order polynomial curve for the entrance region and a constant value in the fully developed region, and shown in Figure 8.8(b) and in Equations (8.3) and (8.4). After the particles were inserted, they reduced down due to compaction and established a fill level of ~4.8 m, so the x axis in this figure only extends to this distance. Nevertheless, the heat transfer coefficient value is expected to remain relatively unchanged between 4.8 m and the outlet at 6 m.

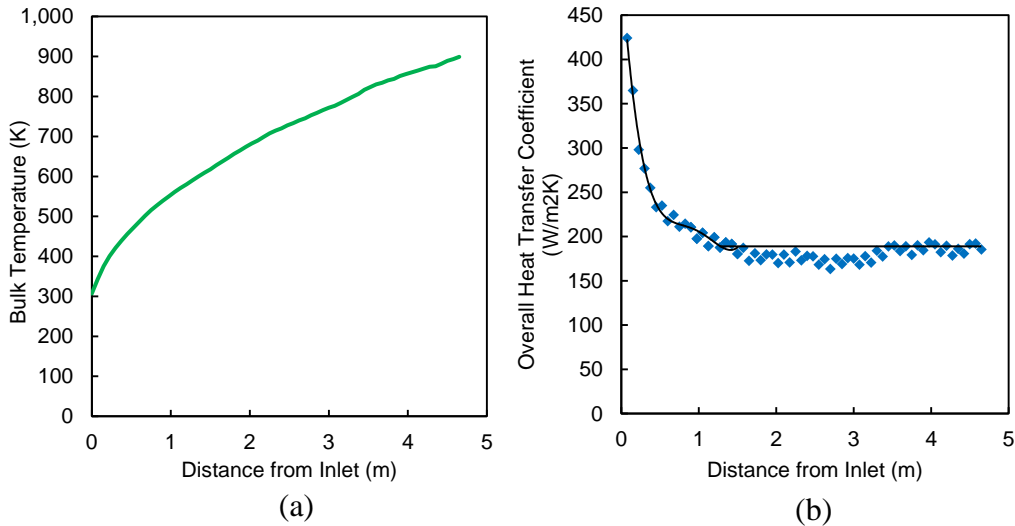


Figure 8.8. Outputs from DPHT simulation analyzed to show (a) bulk temperature, and (b) overall heat transfer coefficient, both as a function of distance from the inlet.

$$h = 353.65x^4 - 1388x^3 + 1965x^2 - 1228.7x + 503.53 \quad (x < 1.5) \quad (8.3)$$

$$h = 185.2 \quad (x \geq 1.5) \quad (8.4)$$

The heat transfer coefficient is the output of the DPHT simulation which will be used in the overall receiver heat transfer model. It is important to note that this heat transfer coefficient is found for a very specific set of conditions, and it depends on the particle properties, the mass flow rate, and the temperature range. The heat transfer coefficient would change based on the wall temperature modeled. A wall

temperature of 1173 K was chosen, as the wall temperature of the receiver when in operation is expected to be roughly this value. To pursue a more accurate model, the DPHT model could be run for multiple wall temperatures and particle inlet temperatures, so a heat transfer coefficient could be even more tailored to the conditions.

The proposed parallel plate geometry is clearly not an optimal design; as shown in Figure 8.7, the flow exhibits very little mixing, leading to the hottest particles remaining in constant contact with the wall, while the interior particles receive much less heat. If some geometry were placed in the flow to enhance mixing, such as orifice plates, ridges, or diagonal plates, this could bring cold particles towards the hot surface and enhance the heat transfer coefficient and the overall efficiency of the receiver.

8.2.3 Overall Receiver Heat Transfer Model

To model the overall receiver, the 12 m by 6 m surface is subdivided into 1800 square elements, each 20 cm x 20 cm. Each element is assumed to have a uniform temperature across its surface, and no heat is conducted to the neighboring elements. A set of seven heat transfer equations is solved simultaneously for each element, which is given in Equations (8.5) to (8.11). Figure 8.9 shows the geometry of a single wall element and the adjoining particle-air cell, along with the heat inflows and outflows. The key that enables the use of this simplified 1D model is that the overall heat transfer coefficient from the wall to the particles has already been found with the detailed DEM+DPHT simulation.

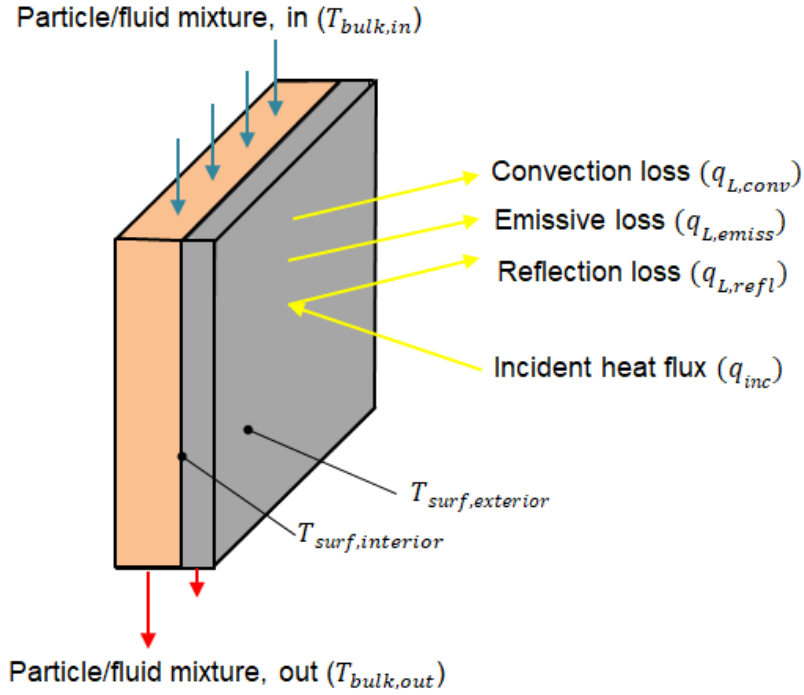


Figure 8.9. One element of the metal receiver surface and the adjoining cell containing the particle-air mixture.

$$q_{abs} = q_{inc} - q_{L,refl} - q_{L,conv} - q_{L,emiss} \quad (8.5)$$

$$q_{abs} = h_{particles}A \frac{T_{bulk,out} - T_{bulk,in}}{\ln\left(\frac{T_{surf,interior} - T_{bulk,in}}{T_{surf,interior} - T_{bulk,out}}\right)} \quad (8.6)$$

$$q_{abs} = \dot{m}C_p(T_{bulk,out} - T_{bulk,in}) \quad (8.7)$$

$$q_{abs} = k_{metal}A(T_{surf,exterior} - T_{surf,interior}) \quad (8.8)$$

$$q_{L,conv} = h_{ext}A(T_{surf,exterior} - T_{amb})B_{conv} \quad (8.9)$$

$$q_{L,refl} = \rho q_{inc}F_{el-ap} \quad (8.10)$$

$$q_{L,emiss} = \sigma A \epsilon F_{el-ap}(T_{surf,exterior}^4 - T_{amb}^4) \quad (8.11)$$

Equation (8.5) is an energy balance of the plane where the incident radiation initially strikes the metal receiver surface. The incident radiation striking that element (q_{inc}) with area A is found according to the flux map supplied by the ray tracing simulation described in Section 8.2.1. The heat passing into the metal

receiver wall, and eventually to the particle-air mixture, is q_{abs} , and losses due to reflection, convection, and emission are denoted as $q_{L,refl}$, $q_{L,conv}$, and $q_{L,emiss}$. Equation (8.6) solves for the absorbed energy by the particle-air stream in the volume directly behind the surface element. It uses the heat transfer coefficient ($h_{particles}$) from Equations (8.3) and (8.4), which were found with the DPHT heat transfer simulation. The temperature of the surface ($T_{surf,interior}$) and the temperature of the particle-air mixture are related with the log mean temperature difference. Equation (8.7) relates the heat gain to the temperature rise in the particle-air mixture, where \dot{m} is the mass flow rate, C_p is the specific heat of the particles, and the bulk temperatures are $T_{bulk,out}$ and $T_{bulk,in}$. Equation (8.8) calculates heat conduction across the metal receiver wall, by relating the exposed surface temperature ($T_{surf,exterior}$) to the internal surface facing the particles-air cell ($T_{surf,interior}$). Equation (8.9) is for the convective loss, where h_{ext} is the convection coefficient to the outside, which is taken to be $6 \text{ W m}^{-2} \text{ K}^{-1}$ [107]. The ambient temperature (T_{amb}) is taken as 300 K. The variable B_{conv} is either 0 or 1 according to the work of Clausing [107], where it is assumed that convection loss is negligible anywhere above the level of the lip due to a stagnant zone in the upper part of the receiver. Reflection loss is calculated with Eq. (8.10), which uses the reflectivity (ρ) and the diffuse view factor from the surface element to the aperture (F_{el-ap}). The calculation of emissive loss in Eq. (8.11) uses the same diffuse view factor, and the emissivity (ϵ) of Pyromark paint common to solar receivers. An emissivity value of 0.87 was used in this model, though values reported in literature vary to a small degree [14][100].

For each surface element, this set of equations was solved simultaneously using a non-linear solver. The top row of surface elements was solved first, as the inlet temperature ($T_{bulk,in}$) must be specified, which was set to 300 K. When solving the next row down, the bulk inlet temperature is taken as the bulk outlet temperature ($T_{bulk,out}$) of the element directly above.

The interior walls of the cavity (the bottom, top, and side walls) are not explicitly modeled with these equations. Due to convective and radiative transfer they will reach equilibrium somewhere between the receiver surface temperature and the ambient temperature. Studies that focus only on the heat transfer in cavity receivers [103] actually model these surfaces as adiabatic panels, but doing so requires solving Equations (8.5)-(8.11) over all surface elements simultaneously, due to the radiative interactions between surface elements. This would lead to a set of hundreds of non-linear equations to be solved simultaneously, a problem that cannot be readily solved by most non-linear solvers.

To reduce the complexity while still providing a valid estimate of the overall heat gain and receiver efficiency, the following approach is used. The solution is first found by solving Equations (8.5)-(8.11) for each element of the receiver surface. This underestimates the loss, since it includes no emissive or convective losses from the internal walls of the receiver cavity. The losses are calculated from the bottom, top, and side walls of the receiver by assuming the temperature of these surfaces is the mean of the solved receiver surface and ambient temperatures. For convective loss, the guidelines from Clausing [107] are followed again, where convection from the walls anywhere above the receiver lip is negligible. For the emissive losses, the diffuse view factors are calculated from each wall to the aperture. Therefore, while the original model is run without a detailed analysis of the interior cavity surfaces, these “extra” loss calculations are performed afterwards to compensate, providing an improved estimate of the receiver efficiency.

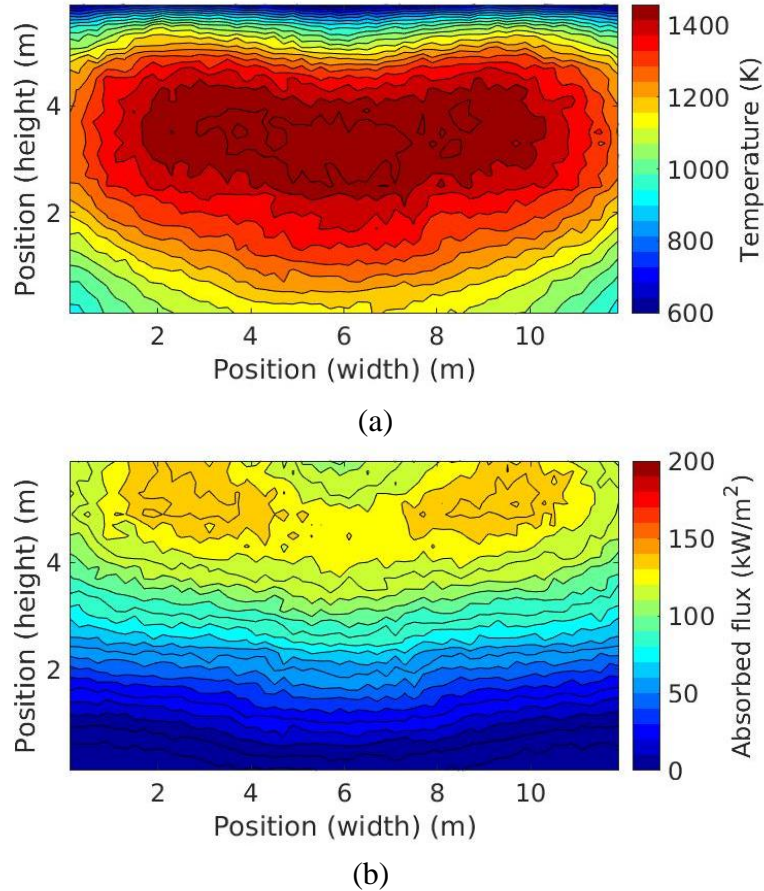


Figure 8.10. Receiver surface showing (a) external surface temperature, and (b) absorbed heat flux.

When solved by the original simulation (before extra cavity losses are subtracted), the outer temperature of the receiver surface ($T_{surf,exterior}$) is shown in Figure 8.10(a), and the absorbed heat flux is shown in Figure 8.10(b). Of the total 7.94 MW of radiation incident to the receiver, 5.65 MW were found to absorb before the “extra” cavity losses are subtracted. After the cavity losses are calculated, the total energy absorbed is reduced to 4.80 MW, representing a thermal efficiency of 60.5%. This neglects any “spillage” losses from light missing the receiver entirely. The average outlet temperature of the original simulation is 1092 K, but after reducing the temperature based on the extra cavity losses, the bulk outlet temperature is estimated to be 973 K, or 700 °C. This matches the output temperature originally designed, which was achieved by adjusting the mass flow rate through the receiver until an outlet temperature of 700 °C was found. The mass

flow rate in the 8 mm x 8 mm section studied with DPHT was 0.0056 kg s^{-1} , compared to a value of 0.0042 kg s^{-1} used in the final receiver simulation. The overall heat transfer coefficient is not expected to vary a high amount due to the lowered flow rate, but for best accuracy the DEM+DPHT simulations could be run again at a lower flow rate. However, such iterations may weeks of computation time, so the accuracy achieved with the current method is deemed high enough for this initial investigation. The maximum temperature reached on the surface of the receiver was $1228 \text{ }^\circ\text{C}$, which may be acceptable for Ni-based superalloys (e.g. Inconel), but this would exceed the temperature limit of stainless steels.

8.3 Conclusions for Solar Receiver Model

A dense granular flow receiver was modeled in this chapter, and the overall heat transfer coefficient provided a bridge between the detailed particle-scale model and the large-scale model of an entire solar receiver.

The receiver studied uses particles flowing downward through parallel plates. The receiver chosen, with a thermal efficiency of 60.5% under the conditions modeled, represents a base-case scenario for similar receivers. Adding either fins or some type of orifice plates to mix the particles would reduce the surface temperature and increase the overall thermal efficiency.

CHAPTER 9

CONCLUSIONS AND RECOMMENDED FUTURE WORK

As noted in the introduction, specific conclusions are included in each chapter. Therefore, this chapter contains only broad conclusions that span multiple chapters.

The goal of this work has been to improve the ability to model heat exchange devices for CSP systems, and several related areas were studied in pursuit of that goal. This research has added to the knowledge of the field in several ways, including the major contributions of an open source Monte Carlo code to calculate radiative transfer in groups of thousands of particles and an improved method to find the effective thermal conductivity due to radiation (k_{rad}). The effective thermal conductivity of packed beds has been studied by researchers in many fields, and the Monte Carlo code as well as the k_{rad} model can be used by researchers far beyond the field of CSP. The Monte Carlo method is widely regarded as an accurate and reliable way to simulate radiation in particles, so a model for k_{rad} that is built directly upon Monte Carlo simulation results should also yield a high accuracy.

Modeling particle flows with DEM provides detailed results for researchers in many fields, and in recent years industry has begun to adopt it. Within the field of CSP, DEM could be used to model many proposed heat exchange devices. Unfortunately, the commercial and open source software options for performing the DEM simulations with heat transfer are lacking in numerous aspects, so researchers have often turned to other, often less rigorous modeling methods instead. For simple geometries continuum models often suffice, but for more complex designs (e.g. particles flowing over a bank of tubes, or through an orifice) continuum models diverge from reality, as the bulk of particles does not flow as a fluid flows. This calls for a DEM approach. The modeling method developed to address this gap includes an initial DEM modeling step and a subsequent heat

transfer modeling step with DPHT. This is applicable for dense granular flows, an important flow regime used in many CSP heat exchange devices. The DPHT model is described in detail in this thesis and is posted as an open source code, with the hope that others can use it and improve it as new sub-models are developed. The DPHT code is currently only for uniform-sized spheres, but in future work the sub-models could be expanded to work for multi-sized spheres to reflect more realistic particle beds.

The Distance Based Approximation model was developed to estimate radiative transfer between particles and particle-wall pairs in DEM-based simulations. The method has been shown to accurately predict bulk heat transfer in large groups of particles by comparing results from the DBA model against detailed ray tracing calculations. Though there are several previous models in literature, these have numerous problems, ranging from the particle emissivity not being correctly incorporated, to the view factors not summing to 1, to simply adding an unreasonable computational burden. The DBA model does not have these shortcomings, and it is extremely easy to implement in a code, requiring only an equation and a lookup table. The DBA model was implemented in DPHT, but it has been described with sufficient detail for others to implement it into their own codes as well.

With little experimental work reported in literature under the conditions relevant to CSP, experiments were conducted to provide the data needed to start validating models such as DPHT. Numerous practical findings were made throughout the process, with a key development being the method to mix and measure the bulk temperature of the particle stream. The mechanical paddle-wheel mixer was determined to mix the particle stream to a high degree, and an air pocket where the paddle-wheel could spin at high speed was created by adding a secondary orifice plate and an overflow channel. This same method can be used by others needing to measure the bulk temperature in particle flows. Three successful experimental runs are described, covering two particle materials and temperature ranges up to ~650 °C. The geometry studied was a square tube heated on one face with a high flux

solar simulator. In the future, experiments should include more complex geometries for mixing particles to increase the overall heat transfer, both because that is the eventual goal and also because it would provide a more robust test case for the DPHT code.

With experimental results obtained and the DPHT model developed, a comparison was made between the two. An excellent match was found in terms of the overall heat gain at the high temperature range, with a difference of only 0.2% between the simulation and the experiment. In the lower temperature range, a difference of ~9% was found. This indicates the DPHT code calculates heat transfer that is in the right range, though with only these two points of comparison it is not clear if results are repeatable and if similarly accurate results would be found under different conditions. Future work should include further validation simulations until repeatability is shown under various circumstances, with special attention needed in the PFP and PFW conduction models. Having a DEM-based code that is easy to use, flexible, and validated to give reliable results would be a large step forward in the field of CSP, and it would lead to greater adoption of DEM-based models for heat transfer in numerous fields.

One of the original goals was to model a solar receiver with a DEM code. After developing the DBA model for radiation, developing the DPHT code to incorporate the other modes of heat transfer, and producing promising initial validation results, a solar receiver was modeled in Chapter 8. A dense granular flow receiver was modeled with DEM+DPHT, where a thin strip of the receiver was used to characterize the heat transfer in terms of a heat transfer coefficient. Results were then used in an overall heat transfer model of the receiver, which accounted for incident concentrated light from a heliostat field and heat losses from the receiver surface. This serves as an example of how the heat transfer between particles at the micron scale can be linked to an actual device at the length scale of several meters.

For particle-based CSP to play a role in addressing climate change, modeling tools are needed to evaluate and design the heat exchange devices that will be required.

Models must be both accurate and simple enough that researchers, students, and industry professionals can readily use them. With the developments in this thesis, DEM-based heat transfer modeling has been improved in several meaningful ways, allowing for the development of better particle-based CSP devices by researchers in the future.

REFERENCES

- [1] Z. Ma, M. Mehos, G. Glatzmaier, B.B. Sakadjian, Development of a Concentrating Solar Power System Using Fluidized-bed Technology for Thermal Energy Conversion and Solid Particles for Thermal Energy Storage, *Energy Procedia*. 69 (2015) 1349–1359. doi:10.1016/j.egypro.2015.03.136.
- [2] S.J. Antony, W. Hoyle, Y. Ding, *Granular Materials; Fundamentals and Applications*, 2004. doi:10.1017/CBO9781107415324.004.
- [3] E. Alonso, A. Gallo, M.I. Roldán, C.A. Pérez-rábago, E. Fuentealba, Use of rotary kilns for solar thermal applications : Review of developed studies and analysis of their potential, *Sol. Energy*. 144 (2017) 90–104. doi:10.1016/j.solener.2017.01.004.
- [4] E. O’Shaughnessy, J.R. Cruce, K. Xu, Too much of a good thing? Global trends in the curtailment of solar PV, *Sol. Energy*. 208 (2020) 1068–1077. doi:10.1016/j.solener.2020.08.075.
- [5] O. of E.E. and R.E. US Department of Energy, NOOR III | Concentrating Solar Power Projects, (2020). <https://solarpaces.nrel.gov/noor-iii> (accessed November 24, 2020).
- [6] C.A. Schoeneberger, C.A. McMillan, P. Kurup, S. Akar, R. Margolis, E. Masanet, Solar for industrial process heat: A review of technologies, analysis approaches, and potential applications in the United States, *Energy*. 206 (2020) 118083. doi:10.1016/j.energy.2020.118083.
- [7] N. Siegel, M. Gross, C. Ho, T. Phan, J. Yuan, Physical Properties of Solid Particle Thermal Energy Storage Media for Concentrating Solar Power Applications, *Energy Procedia*. 49 (2014) 1015–1023. doi:10.1016/j.egypro.2014.03.109.
- [8] H. Al-Ansary, A. El-Leathy, S. Jeter, E. Djajadiwinata, S. Alaqel, M. Golob, C. Nguyen, R. Saad, T. Shafiq, S. Danish, S. Abdel-Khalik, Z. Al-Suhaibani,

- N. Abu-Shikhah, M.I. Haq, A. Al-Balawi, F. Al-Harhi, On-sun experiments on a particle heating receiver with red sand as the working medium, *AIP Conf. Proc.* 2033 (2018) 1–8. doi:10.1063/1.5067038.
- [9] G. Flamant, D. Hernandez, C. Bonet, J.P. Traverse, Experimental aspects of the thermochemical conversion of solar energy; Decarbonation of CaCO₃, *Sol. Energy.* 24 (1980) 385–395. doi:10.1016/0038-092X(80)90301-1.
- [10] J. Hruby, R. Steeper, G. Evans, C. Crowe, An Experimental and Numerical Study of Flow and Convective Heat Transfer in a Freely Falling Curtain of Particles, *J. Fluids Eng.* 110 (1988) 172. doi:10.1115/1.3243531.
- [11] C.K. Ho, A new generation of solid particle and other high-performance receiver designs for concentrating solar thermal (CST) central tower systems, *Adv. Conc. Sol. Therm. Res. Technol.* (2017) 107–128. doi:10.1016/B978-0-08-100516-3.00006-X.
- [12] J. Christian, C. Ho, System Design of a 1 MW North-facing, Solid Particle Receiver, *Energy Procedia.* 69 (2015) 340–349. doi:10.1016/j.egypro.2015.03.038.
- [13] C.K. Ho, J.M. Christian, J. Yellowhair, N. Siegel, S. Jeter, M. Golob, S.I. Abdel-Khalik, C. Nguyen, H. Al-Ansary, On-sun testing of an advanced falling particle receiver system, *AIP Conf. Proc.* 1734 (2016). doi:10.1063/1.4949074.
- [14] C. Ho, J. Christian, D. Gill, A. Moya, S. Jeter, S. Abdel-Khalik, D. Sadowski, N. Siegel, H. Al-Ansary, L. Amsbeck, B. Gobereit, R. Buck, Technology Advancements for Next Generation Falling Particle Receivers, *Energy Procedia.* 49 (2014) 398–407. doi:10.1016/j.egypro.2014.03.043.
- [15] W. Wu, D. Trebing, L. Amsbeck, R. Buck, R. Pitz-Paal, Prototype Testing of a Centrifugal Particle Receiver for High-Temperature Concentrating Solar Applications, *J. Sol. Energy Eng.* 137 (2015) 041011–041011. doi:10.1115/1.4030657.

- [16] S. Hicdurmaz, E. Johnson, J. Grobbel, L. Amsbeck, R. Buck, B. Hoffschmidt, Numerical Heat Transfer Modelling of a Centrifugal Solar Particle Receiver, (n.d.).
- [17] A.B. Morris, Z. Ma, S. Pannala, C.M. Hrenya, Simulations of heat transfer to solid particles flowing through an array of heated tubes, *Sol. Energy*. 130 (2016) 101–115. doi:10.1016/j.solener.2016.01.033.
- [18] I.P. Lopez, H. Benoit, D. Gauthier, J.L. Sans, E. Guillot, G. Mazza, G. Flamant, On-sun first operation of a 150 kWth pilot solar receiver using dense particle suspension as heat transfer fluid, *AIP Conf. Proc.* 137 (2016) 463–476. doi:10.1063/1.4949080.
- [19] E. Johnson, D. Baker, I. Tari, Proposal of a Novel Gravity-Fed , Particle-Filled Solar Receiver, *AIP Conf. Proc.* 1850 (2017). doi:10.1063/1.4984371.
- [20] E. Johnson, Conceptual Design and Heat Transfer Investigation of a Dense Granular Flow Solar Receiver, Middle East Technical University, 2017.
- [21] M.F. Watkins, A Heat Transfer Analysis of Vertical Dense Granular Flows, North Carolina State University, 2018.
- [22] P. Bartsch, T. Baumann, S. Zunft, Granular Flow Field in Moving Bed Heat Exchangers: A Continuous Model Approach, *Energy Procedia*. 99 (2016) 72–79. doi:10.1016/j.egypro.2016.10.099.
- [23] S. Hicdurmaz, I. Tari, Numerical Investigaton of Bubbling Fluidized Bed to e Used as Thermal Energy Storage Integrated to High-Temperature Concentrated Solar Power, *Multiph. Sci. Technol.* 30 (2018).
- [24] K.J. Albrecht, C.K. Ho, Heat Transfer Models of Moving Packed-Bed Particle-to-sCO₂ Heat Exchangers, *J. Sol. Energy Eng. Trans. ASME*. 141 (2019) 1–10. doi:10.1115/1.4041546.
- [25] W. Van Antwerpen, P.G. Rousseau, C.G. Du Toit, Multi-sphere Unit Cell model to calculate the effective thermal conductivity in packed pebble beds of mono-sized spheres, *Nucl. Eng. Des.* 247 (2012) 183–201.

doi:10.1016/j.nucengdes.2012.03.012.

- [26] W. Van Antwerpen, C.G. Du Toit, P.G. Rousseau, A review of correlations to model the packing structure and effective thermal conductivity in packed beds of mono-sized spherical particles, *Nucl. Eng. Des.* 240 (2010) 1803–1818. doi:10.1016/j.nucengdes.2010.03.009.
- [27] X. Wang, J. Zheng, H. Chen, A prediction model for the effective thermal conductivity of mono-sized pebble beds, *Fusion Eng. Des.* 103 (2016) 136–151. doi:10.1016/j.fusengdes.2015.12.051.
- [28] G. Breitbach, H. Barthels, The Radiant Heat Transfer in the High Temperature Reactor Core after Failure of the Afterheat Removal Systems, *Nucl. Technol.* 49 (1980) 392–399. doi:10.13182/nt80-a17687.
- [29] P. Zehner, E.U. Schlünder, Einfluß der Wärmestrahlung und des Druckes auf den Wärmetransport in nicht durchströmten Schüttungen, *Chemie Ing. Tech.* 44 (1972) 1303–1308. doi:10.1002/cite.330442305.
- [30] P. Zehner, E.U. Schlünder, Wärmeleitfähigkeit von Schüttungen bei mässigen Temperaturen, *Chemie Ing. Tech.* 42 (1970) 933–941.
- [31] R. Bauer, E.U. Schlünder, Effective radial thermal conductivity of packings in gas flow. Part II thermal conductivity of the packing fraction without gas flow, *Int. Chem. Eng.* 18 (1978) 189–204.
- [32] E. Tsotsas, D6.3 Thermal Conductivity of Packed Beds. In: *VDI Heat Atlas*, 2nd ed., Springer, Berlin, Heidelberg, 2010. doi:10.1007/978-3-540-77877-6.
- [33] C.T. Hsu, P. Cheng, K.W. Wong, Modified Zehner-Schlünder models for stagnant thermal conductivity of porous media, *Int. J. Heat Mass Transf.* 37 (1994) 2751–2759. doi:10.1016/0017-9310(94)90392-1.
- [34] Y.S. Yang, J.R. Howell, D.E. Klein, Radiative Heat Transfer Through a Randomly Packed Bed of Spheres by the Monte Carlo Method, *J. Heat Transfer.* 105 (1983) 325. doi:10.1115/1.3245582.

- [35] J.C. Chen, S.W. Churchill, Radiant heat transfer in packed beds, *AIChE J.* 9 (1963) 35–41. doi:10.1002/aic.690090108.
- [36] D. Bouvard, C. Argento, A ray tracing method for evaluating the radiative heat transfer in porous media, 39 (1996) 3175–3180.
- [37] M. Kaviany, *Principles of Heat Transfer in Porous Media*, 1999.
- [38] B.P. Singh, M. Kaviany, Effect of solid conductivity on radiative heat transfer in packed beds, *Int. J. Heat Mass Transf.* 37 (1994) 2579–2583. doi:10.1016/0017-9310(94)90295-X.
- [39] M. De Beer, C.G. Du Toit, P.G. Rousseau, A methodology to investigate the contribution of conduction and radiation heat transfer to the effective thermal conductivity of packed graphite pebble beds, including the wall effect, *Nucl. Eng. Des.* 314 (2017) 67–81. doi:10.1016/j.nucengdes.2017.01.010.
- [40] P.G. Rousseau, C.G. Du Toit, W. Van Antwerpen, H.J. Van Antwerpen, Separate effects tests to determine the effective thermal conductivity in the PBMR HTTU test facility, *Nucl. Eng. Des.* 271 (2014) 444–458. doi:10.1016/j.nucengdes.2013.12.015.
- [41] K. Robold, *Wärmetransport im inneren und in der Randzone von Kugeischüttungen*, 1982.
- [42] G. Kasperek, D. Vortmeyer, Wärmestrahlung in Schüttungen aus Kugeln mit vernachlässigbarem Wärmeleitwiderstand, *Wärme- Und Stoffübertragung.* 9 (1976) 117–128. doi:10.1007/BF01589465.
- [43] A.J. Slavin, F.A. Londry, J. Harrison, A new model for the effective thermal conductivity of packed beds of solid spheroids: alumina in helium between 100 and 500°C, *Int. J. Heat Mass Transf.* 43 (2000) 2059–2073. doi:10.1016/s0017-9310(00)00208-8.
- [44] E.F. Johnson, İ. Tarı, D. Baker, Radiative heat transfer in the discrete element method by distance based approximations of radiation distribution

- factors, *Powder Technol.* (2020). doi:10.1016/j.powtec.2020.11.050.
- [45] F. Qi, M.M. Wright, Particle scale modeling of heat transfer in granular flows in a double screw reactor, *Powder Technol.* 335 (2018) 18–34. doi:10.1016/j.powtec.2018.04.068.
- [46] H. Wu, N. Gui, X. Yang, J. Tu, S. Jiang, Analysis and evaluations of four models of thermal radiation for densely packed granular systems, *Chem. Eng. Sci.* 211 (2020) 115309. doi:10.1016/j.ces.2019.115309.
- [47] M.L. Pitso, Characterisation of long range radiation heat transfer in packed pebble beds, North-West University, 2011. http://dspace.nwu.ac.za/bitstream/handle/10394/8435/Pitso_ML.pdf;sequence=1.
- [48] J.R. Mahan, *The Monte Carlo Ray-Trace Method in Radiation Heat Transfer and Applied Optics*, Wiley-ASME Press, 2019. doi:10.1002/9781119518471.
- [49] J.R. Howell, *The Monte Carlo Method in Radiative Heat Transfer*, *Mech. Eng. J. Heat Transf.* 120 (1998) 547–560.
- [50] B.K. Liu, J.M. Zhao, L.H. Liu, Radiative heat transfer in densely packed spherical particle system by Monte Carlo method, *Int. Heat Transf. Conf. 2018-Augus* (2018) 8439–8446. doi:10.1615/ihtc16.rti.024195.
- [51] C. Goniva, C. Kloss, A. Hager, S. Pirker, An open source CFD-DEM perspective, *Proc. OpenFOAM Work.* (2010) 1–10. ftp://ftp.heanet.ie/disk1/sourceforge/o/op/openfoam-extend/OpenFOAM_Workshops/OFW5_2010_Gothenburg/Papers/ChristopherGonivaPaperOFWS5.pdf.
- [52] C. Brennen, *Fundamentals of Multiphase Flow*, Cambridge University Press, 2002.
- [53] C. Kloss, C. Goniva, A. Hager, S. Amberger, S. Pirker, Models , algorithms and validation for opensource DEM and CFD-DEM, *Prog. Comput. Fluid*

- Dyn. 12 (2012) 140–152. doi:10.1504/PCFD.2012.047457.
- [54] H.R. Norouzi, R. Zarghami, R. Sotudeh-gharebagh, N. Mostoufi, Coupled CFD - DEM Modeling Coupled CFD - DEM Modeling and Application to Multiphase Flows, n.d.
- [55] J. Marti, A. Haselbacher, A. Steinfeld, A numerical investigation of gas-particle suspensions as heat transfer media for high-temperature concentrated solar power, *Int. J. Heat Mass Transf.* 90 (2015) 1056–1070. doi:10.1016/j.ijheatmasstransfer.2015.07.033.
- [56] N.P. Siegel, M.D. Gross, R. Coury, The Development of Direct Absorption and Storage Media for Falling Particle Solar Central Receivers, 137 (2018) 1–7. doi:10.1115/1.4030069.
- [57] H. Wu, N. Gui, X. Yang, J. Tu, S. Jiang, Numerical simulation of heat transfer in packed pebble beds: CFD-DEM coupled with particle thermal radiation, *Int. J. Heat Mass Transf.* 110 (2017) 393–405. doi:10.1016/j.ijheatmasstransfer.2017.03.035.
- [58] B. Krause, B. Liedmann, J. Wiese, P. Bucher, S. Wirtz, H. Piringer, V. Scherer, 3D-DEM-CFD simulation of heat and mass transfer, gas combustion and calcination in an intermittent operating lime shaft kiln, *Int. J. Therm. Sci.* 117 (2017) 121–135. doi:10.1016/j.ijthermalsci.2017.03.017.
- [59] H. Komossa, S. Wirtz, V. Scherer, F. Herz, E. Specht, Heat transfer in indirect heated rotary drums filled with monodisperse spheres: Comparison of experiments with DEM simulations, *Powder Technol.* 286 (2015) 722–731. doi:10.1016/j.powtec.2015.07.022.
- [60] G.J. Cheng, A.B. Yu, Particle scale evaluation of the effective thermal conductivity from the structure of a packed bed: Radiation heat transfer, *Ind. Eng. Chem. Res.* 52 (2013) 12202–12211. doi:10.1021/ie3033137.
- [61] H. Wu, N. Gui, X. Yang, J. Tu, S. Jiang, Effect of scale on the modeling of radiation heat transfer in packed pebble beds, *Int. J. Heat Mass Transf.* 101

- (2016) 562–569. doi:10.1016/j.ijheatmasstransfer.2016.05.090.
- [62] L. Chen, C. Wang, M. Moscardini, M. Kamlah, S. Liu, A DEM-based heat transfer model for the evaluation of effective thermal conductivity of packed beds filled with stagnant fluid: Thermal contact theory and numerical simulation, *Int. J. Heat Mass Transf.* 132 (2019) 331–346. doi:10.1016/j.ijheatmasstransfer.2018.12.005.
- [63] G. Ruiz, N. Ripoll, N. Fedorova, A. Zbogar-Rasic, V. Jovicic, A. Delgado, M. Toledo, Experimental and numerical analysis of the heat transfer in a packed bed exposed to the high thermal radiation flux, *Int. J. Heat Mass Transf.* 136 (2019) 383–392. doi:10.1016/j.ijheatmasstransfer.2019.03.009.
- [64] W.J. Yang, Z.Y. Zhou, A.B. Yu, Particle scale studies of heat transfer in a moving bed, *Powder Technol.* 281 (2015) 99–111. doi:10.1016/j.powtec.2015.04.071.
- [65] S. Amberger, S. Pirker, C. Kloss, Thermal Radiation Modeling Using Ray Tracing in LIGGGHTS, in: DEM6 Conf., 2013.
- [66] B. Liu, J. Zhao, L. Liu, Continuum approach based on radiation distribution function for radiative heat transfer in densely packed particulate system, (2019) 1–37. <http://arxiv.org/abs/1910.06905>.
- [67] E. Johnson, D. Baker, I. Tari, Development of view factor correlations for modeling thermal radiation in solid particle solar receivers using CFD-DEM, in: AIP Conf. Proc., 2019. doi:10.1063/1.5117540.
- [68] A. Malinouski, O. Rabinovich, Evaluation of particle-scale radiative heat transfer in polydisperse beds, in: CFDEM Conf., Linz, Austria, 2017.
- [69] V.V.R. Natarajan, M.L. Hunt, Heat Transfer in Vertical Granular Flows, *Exp. Heat Transf.* 10 (1997) 89–107. doi:10.1080/08916159708946536.
- [70] W.N. Sullivan, *Heat Transfer to Flowing Granular Media*, California Institute of Technology, 1973.

- [71] A. V. Gusarov, Radiative transfer, absorption, and reflection by metal powder beds in laser powder-bed processing, *J. Quant. Spectrosc. Radiat. Transf.* 257 (2020) 107366. doi:10.1016/j.jqsrt.2020.107366.
- [72] T.L. Bergman, A.S. Lavine, F.P. Incropera, D.P. DeWitt, *Introduction to Heat Transfer*, 6th ed., John Wiley & Sons, 2011.
- [73] R. Siegel, J.R. Howell, *Thermal Radiation Heat Transfer*, NASA, 1971.
- [74] J.R. Howell, R. Siegel, *Thermal Radiation Heat Transfer*, NASA, 1969.
- [75] S. Tanaka, Exact view-factor analysis for radiation from a sphere to another sphere linked with a coaxial cylinder, *Rev. Fac. Marit. Sci. Kobe Univ.* (2008) 85–92. <http://www.lib.kobe-u.ac.jp/repository/thesis/d1/D1002621.pdf>.
- [76] Y.T. Feng, K. Han, An accurate evaluation of geometric view factors for modelling radiative heat transfer in randomly packed beds of equally sized spheres, *Int. J. Heat Mass Transf.* 55 (2012) 6374–6383. doi:10.1016/j.ijheatmasstransfer.2012.06.025.
- [77] H. Wu, N. Gui, X. Yang, J. Tu, S. Jiang, Numerical simulation of heat transfer in packed pebble beds: CFD-DEM coupled with particle thermal radiation, *Int. J. Heat Mass Transf.* 110 (2017) 393–405. doi:10.1016/j.ijheatmasstransfer.2017.03.035.
- [78] B.P. Singh, M. Kaviany, Independent theory versus direct simulation of radiation heat transfer in packed beds, *Int. J. Heat Mass Transf.* 34 (1991) 2869–2882. doi:10.1016/0017-9310(91)90247-C.
- [79] C.L. Tien, *Thermal Radiation in Packed and Fluidized Beds*, *J. Heat Transfer*. 110 (1988) 1230. doi:10.1115/1.3250623.
- [80] J. Bezanson, A. Edelman, S. Karpinski, V.B. Shah, Julia: A fresh approach to numerical computing, *SIAM Rev.* 59 (2017) 65–98. doi:10.1137/141000671.

- [81] M. Diago, A.C. Iniesta, A. Soum-Glaude, N. Calvet, Characterization of desert sand to be used as a high-temperature thermal energy storage medium in particle solar receiver technology, *Appl. Energy*. 216 (2018) 402–413. doi:10.1016/j.apenergy.2018.02.106.
- [82] W.H. Press, S.A. Teukolsky, W.T. Vetterling, B.P. Flannery, *Numerical Recipes in C: The Art of Scientific Computing*, 3rd ed., Cambridge University Press, Cambridge, UK, 2007.
- [83] K. Kim, N. Siegel, G. Kolb, V. Rangaswamy, S.F. Moujaes, A study of solid particle flow characterization in solar particle receiver, *Sol. Energy*. 83 (2009) 1784–1793. doi:10.1016/j.solener.2009.06.011.
- [84] J. Grobbel, S. Brendelberger, M. Henninger, C. Sattler, R. Pitz-Paal, Calibration of parameters for DEM simulations of solar particle receivers by bulk experiments and surrogate functions, *Powder Technol.* 364 (2020) 831–844. doi:10.1016/j.powtec.2019.11.028.
- [85] C. Kloss, C. Goniva, G. Aichinger, S. Pirker, *Comprehensive DEM-DPM-CFD Simulations-Model Synthesis, Experimental Validation and Scalability*, Seventh Int. Conf. CFD Miner. Process Ind. (2009) 1–7. http://www.cfd.com.au/cfd_conf09/PDFs/090KLO.pdf.
- [86] B. Chaudhuri, F.J. Muzzio, M.S. Tomassone, Experimentally validated computations of heat transfer in granular materials in rotary calciners, *Powder Technol.* 198 (2010) 6–15. doi:10.1016/j.powtec.2009.09.024.
- [87] T. Baumann, S. Zunft, Development and Performance Assessment of a Moving Bed Heat Exchanger for Solar Central Receiver Power Plants, *Energy Procedia*. 69 (2015) 748–757. doi:10.1016/j.egypro.2015.03.085.
- [88] S. Niederwestberg, F. Schneider, C. Boura, U. Herrmann, Introduction to a Direct Irradiated Transparent Tube Particle Receiver, in: (Currently under Rev., 2020).
- [89] B. Chaudhuri, F.J. Muzzio, M.S. Tomassone, Modeling of heat transfer in

- granular flow in rotating vessels, *Chem. Eng. Sci.* 61 (2006) 6348–6360.
doi:10.1016/j.ces.2006.05.034.
- [90] Julia Micro-Benchmarks, (2020). <https://julialang.org/benchmarks/>
(accessed November 29, 2020).
- [91] G.K. Batchelor, R.W. O’Brien, Thermal or Electrical Conduction Through a Granular Material, *Proc R Soc London Ser A.* 355 (1977) 313–333.
doi:10.1098/rspa.1977.0100.
- [92] T. Oschmann, M. Schiemann, H. Kruggel-Emden, Development and verification of a resolved 3D inner particle heat transfer model for the Discrete Element Method (DEM), *Powder Technol.* 291 (2016) 392–407.
doi:10.1016/j.powtec.2015.12.008.
- [93] Z.Y. Zhou, A.B. Yu, P. Zulli, Particle Scale Study of Heat Transfer in Packed and Bubbling Fluidized Beds, *AIChE J.* 55 (2009) 868–884.
doi:10.1002/aic.
- [94] G.J. Cheng, A.B. Yu, P. Zulli, Evaluation of effective thermal conductivity from the structure of a packed bed, *Chem. Eng. Sci.* 54 (1999) 4199–4209.
doi:10.1016/S0009-2509(99)00125-6.
- [95] Z.Y. Zhou, A.B. Yu, P. Zulli, A new computational method for studying heat transfer in fluid bed reactors, *Powder Technol.* 197 (2010) 102–110.
doi:10.1016/j.powtec.2009.09.002.
- [96] R.Y. Yang, R.P. Zou, A.B. Yu, Voronoi tessellation of the packing of fine uniform spheres, *Phys. Rev. E - Stat. Physics, Plasmas, Fluids, Relat. Interdiscip. Top.* 65 (2002) 8. doi:10.1103/PhysRevE.65.041302.
- [97] J. Grobbel, Modeling Solar Particle Receivers with the Discrete Element Method, (2019).
- [98] E.W. Weisstein, Point-Plane Distance, (n.d.).
<https://mathworld.wolfram.com/Point-PlaneDistance.html> (accessed December 11, 2020).

- [99] L.C. Yau, *Conjugate Heat Transfer with the Multiphysics Coupling Library preCICE*, Technische Universitat Munchen, 2016.
- [100] M. López-Herraiz, A.B. Fernández, N. Martinez, M. Gallas, Effect of the optical properties of the coating of a concentrated solar power central receiver on its thermal efficiency, *Sol. Energy Mater. Sol. Cells.* 159 (2017) 66–72. doi:10.1016/j.solmat.2016.08.031.
- [101] E. Benhelal, G. Zahedi, E. Shamsaei, A. Bahadori, Global strategies and potentials to curb CO₂ emissions in cement industry, *J. Clean. Prod.* 51 (2013) 142–161. doi:10.1016/j.jclepro.2012.10.049.
- [102] T. Esence, E. Guillot, M. Tessonnaud, J.L. Sans, G. Flamant, Solar calcination at pilot scale in a continuous flow multistage horizontal fluidized bed, *Sol. Energy.* 207 (2020) 367–378. doi:10.1016/j.solener.2020.06.098.
- [103] P. Schöttl, G. Bern, D.W. van Rooyen, J.A. Fernández Pretel, T. Fluri, P. Nitz, Optimization of Solar Tower molten salt cavity receivers for maximum yield based on annual performance assessment, *Sol. Energy.* 199 (2020) 278–294. doi:10.1016/j.solener.2020.02.007.
- [104] D. Canavarro, J. Chaves, M. Collares-Pereira, New dual asymmetric CEC linear Fresnel concentrator for evacuated tubular receivers, in: *AIP Conf. Proc.*, 2017. doi:10.1063/1.4984397.
- [105] M.J. Blanco, J.M. Amieva, A. Mancilla, The tonatiuh software development project: AN open source approach to the simulation of solar concentrating systems, *Am. Soc. Mech. Eng. Comput. Inf. Eng. Div. CED.* 10 (2005) 157–164. doi:10.1115/IMECE2005-81859.
- [106] INSHIP DELIVERABLE 4.4, (n.d.). <http://www.inship.eu/deliverables.php> (accessed January 6, 2021).

- [107] A.M. Clausing, Convective Losses From Cavity Solar Receivers - Comparisons Between Analytical Predictions and Experimental Results., J. Sol. Energy Eng. Trans. ASME. 105 (1983) 29–33. doi:10.1115/1.3266342.

APPENDICES

A. Particle-Particle RDF Tables

Table A. Particle-particle RDF at various center-to-center distances, for $\epsilon_p = 0.65$ and 0.86 , and solid fractions of $0.25, 0.35, 0.45, 0.55,$ and 0.64 .

Distance (radii)	$\epsilon_p = 0.65$					$\epsilon_p = 0.86$				
	0.25	0.35	0.45	0.55	0.64	0.25	0.35	0.45	0.55	0.64
2.0	5.9648E-2	6.2474E-2	6.4735E-2	6.6076E-2	6.4606E-2	6.8927E-2	7.0160E-2	7.0970E-2	7.1238E-2	6.9641E-2
2.2	4.7897E-2	5.0344E-2	5.2083E-2	5.2931E-2	5.0158E-2	5.5013E-2	5.5901E-2	5.6380E-2	5.6331E-2	5.3533E-2
2.4	3.9789E-2	4.1856E-2	4.3041E-2	4.3481E-2	3.9354E-2	4.5201E-2	4.5913E-2	4.6042E-2	4.5814E-2	4.1730E-2
2.6	3.3854E-2	3.5363E-2	3.5840E-2	3.5481E-2	3.0555E-2	3.7956E-2	3.8331E-2	3.8025E-2	3.7267E-2	3.2344E-2
2.8	2.9062E-2	3.0067E-2	2.9904E-2	2.6513E-2	2.2903E-2	3.2338E-2	3.2321E-2	3.1534E-2	2.8125E-2	2.4196E-2
3.0	2.5198E-2	2.5529E-2	2.4453E-2	2.0015E-2	1.5843E-2	2.7762E-2	2.7265E-2	2.5717E-2	2.1370E-2	1.6743E-2
3.2	2.1915E-2	2.1576E-2	1.9645E-2	1.6067E-2	1.0061E-2	2.3979E-2	2.2903E-2	2.0601E-2	1.7166E-2	1.0540E-2
3.4	1.8891E-2	1.7936E-2	1.5113E-2	1.1366E-2	5.2250E-3	2.0533E-2	1.8941E-2	1.5753E-2	1.1924E-2	5.3138E-3
3.6	1.6129E-2	1.4600E-2	1.1083E-2	6.4577E-3	3.3830E-3	1.7399E-2	1.5264E-2	1.1396E-2	6.4791E-3	3.3448E-3
3.8	1.3816E-2	1.1707E-2	8.1696E-3	4.6578E-3	2.0798E-3	1.4771E-2	1.2080E-2	8.2259E-3	4.5877E-3	1.9698E-3
4.0	1.1636E-2	8.9337E-3	6.0044E-3	3.5683E-3	1.0051E-3	1.2282E-2	9.0278E-3	5.8775E-3	3.4518E-3	8.7552E-4
4.2	9.8468E-3	7.3030E-3	4.6600E-3	1.9322E-3	1.0476E-3	1.0282E-2	7.2489E-3	4.4503E-3	1.6681E-3	9.8179E-4
4.4	8.4606E-3	6.3324E-3	3.7760E-3	1.1816E-3	8.0026E-4	8.7580E-3	6.2506E-3	3.5748E-3	8.9625E-4	7.5712E-4
4.6	7.4786E-3	5.3876E-3	3.2824E-3	1.2132E-3	5.9882E-4	7.6698E-3	5.2572E-3	3.1055E-3	1.0592E-3	5.7076E-4
4.8	6.5021E-3	4.6876E-3	2.6610E-3	1.0849E-3	4.0616E-4	6.6111E-3	4.5667E-3	2.4987E-3	1.0487E-3	3.8731E-4
5.0	5.7356E-3	3.9691E-3	2.2920E-3	9.0910E-4	2.8432E-4	5.7881E-3	3.8353E-3	2.1765E-3	8.9368E-4	2.6972E-4
5.4	4.4995E-3	2.9725E-3	1.5063E-3	5.9693E-4	1.2178E-4	4.4834E-3	2.8480E-3	1.4110E-3	5.8799E-4	1.0961E-4
5.8	3.5797E-3	2.1475E-3	9.6895E-4	2.3504E-4	6.1086E-5	3.5222E-3	2.0235E-3	8.8790E-4	1.9564E-4	5.4136E-5
6.2	2.8999E-3	1.6569E-3	6.4512E-4	1.4960E-4	3.5927E-5	2.8376E-3	1.5563E-3	5.7508E-4	1.2283E-4	3.4894E-5
6.6	2.3261E-3	1.1886E-3	4.5699E-4	9.1014E-5	1.8705E-5	2.2431E-3	1.0892E-3	4.0798E-4	7.9711E-5	1.9997E-5
7.0	1.8745E-3	9.3542E-4	3.2362E-4	6.4764E-5	1.0969E-5	1.7853E-3	8.5755E-4	2.8839E-4	5.9783E-5	1.3190E-5
7.4	1.5235E-3	7.0323E-4	2.1988E-4	4.1793E-5	0.0	1.4393E-3	6.3656E-4	1.9246E-4	3.8822E-5	0.0
7.8	1.2564E-3	5.4257E-4	1.4966E-4	2.1862E-5	0.0	1.1789E-3	4.8487E-4	1.2877E-4	1.9580E-5	0.0
8.2	1.0223E-3	4.0782E-4	1.0852E-4	1.5259E-5	0.0	9.5046E-4	3.5959E-4	9.3396E-5	1.4860E-5	0.0
8.6	8.4470E-4	3.1355E-4	7.6371E-5	9.3283E-6	0.0	7.7777E-4	2.7465E-4	6.5820E-5	1.0459E-5	0.0
9.0	7.0175E-4	2.4964E-4	5.2881E-5	7.7623E-6	0.0	6.3875E-4	2.1809E-4	4.5487E-5	8.7663E-6	0.0
9.4	5.8807E-4	1.9845E-4	3.8785E-5	0.0	0.0	5.3335E-4	1.7292E-4	3.3995E-5	0.0	0.0
9.8	4.9488E-4	1.5217E-4	2.7558E-5	0.0	0.0	4.4692E-4	1.3131E-4	2.4637E-5	0.0	0.0
10.2	4.0727E-4	1.1911E-4	2.0244E-5	0.0	0.0	3.6279E-4	1.0219E-4	1.9162E-5	0.0	0.0
10.6	3.4034E-4	9.2135E-5	1.4268E-5	0.0	0.0	3.0099E-4	7.8245E-5	1.4025E-5	0.0	0.0
11.0	2.9145E-4	7.3511E-5	1.0215E-5	0.0	0.0	2.5674E-4	6.2131E-5	1.0788E-5	0.0	0.0
11.4	2.4757E-4	5.8778E-5	8.1796E-6	0.0	0.0	2.1742E-4	4.9817E-5	9.3684E-6	0.0	0.0
11.8	2.0680E-4	4.6697E-5	6.5213E-6	0.0	0.0	1.8025E-4	3.9494E-5	7.9478E-6	0.0	0.0
12.2	1.7088E-4	3.6652E-5	5.2818E-6	0.0	0.0	1.4726E-4	3.1200E-5	6.9363E-6	0.0	0.0
12.6	1.4753E-4	2.8899E-5	4.2857E-6	0.0	0.0	1.2631E-4	2.4862E-5	0.0	0.0	0.0
13.0	1.2740E-4	2.3567E-5	0.0	0.0	0.0	1.0905E-4	2.1067E-5	0.0	0.0	0.0
13.4	1.0933E-4	1.8458E-5	0.0	0.0	0.0	9.3663E-5	1.6886E-5	0.0	0.0	0.0
13.8	9.2009E-5	1.5066E-5	0.0	0.0	0.0	7.7938E-5	1.4556E-5	0.0	0.0	0.0
14.2	7.7104E-5	1.2016E-5	0.0	0.0	0.0	6.4710E-5	1.1786E-5	0.0	0.0	0.0
14.6	6.6746E-5	9.8062E-6	0.0	0.0	0.0	5.5806E-5	1.0180E-5	0.0	0.0	0.0
15.0	5.8855E-5	8.4398E-6	0.0	0.0	0.0	4.9283E-5	9.3326E-6	0.0	0.0	0.0
16.0	3.9422E-5	5.3513E-6	0.0	0.0	0.0	3.3041E-5	6.5248E-6	0.0	0.0	0.0
17.0	2.7131E-5	3.8105E-6	0.0	0.0	0.0	2.2890E-5	5.0481E-6	0.0	0.0	0.0
18.0	1.8940E-5	3.0957E-6	0.0	0.0	0.0	1.6703E-5	4.4253E-6	0.0	0.0	0.0
19.0	1.3345E-5	2.3721E-6	0.0	0.0	0.0	1.2463E-5	0.0	0.0	0.0	0.0

20.0	9.5900E-6	0.0	0.0	0.0	0.0	9.7688E-6	0.0	0.0	0.0	0.0
21.0	7.2078E-6	0.0	0.0	0.0	0.0	7.8921E-6	0.0	0.0	0.0	0.0
22.0	5.3667E-6	0.0	0.0	0.0	0.0	6.2811E-6	0.0	0.0	0.0	0.0
23.0	4.2484E-6	0.0	0.0	0.0	0.0	5.3729E-6	0.0	0.0	0.0	0.0
24.0	3.4265E-6	0.0	0.0	0.0	0.0	4.5571E-6	0.0	0.0	0.0	0.0
25.0	2.9827E-6	0.0	0.0	0.0	0.0	4.2433E-6	0.0	0.0	0.0	0.0
26.0	2.5433E-6	0.0	0.0	0.0	0.0	3.7209E-6	0.0	0.0	0.0	0.0
27.0	2.2955E-6	0.0	0.0	0.0	0.0	3.3674E-6	0.0	0.0	0.0	0.0
28.0	2.1426E-6	0.0	0.0	0.0	0.0	3.1938E-6	0.0	0.0	0.0	0.0
29.0	1.9656E-6	0.0	0.0	0.0	0.0	3.0204E-6	0.0	0.0	0.0	0.0
30.0	1.7255E-6	0.0	0.0	0.0	0.0	0.0	0.0	0.0	0.0	0.0

B. Particle-Wall RDF Tables

Table B1. Particle-wall RDF at various particle center-to-wall distances, for $\epsilon_p = 0.65$, $\epsilon_w = 0.4$ and 0.6, and bulk solid fractions of 0.25, 0.35, 0.45, 0.55, and 0.64.

Distance (radii)	$\epsilon_p = 0.65, \epsilon_w = 0.4$					$\epsilon_p = 0.65, \epsilon_w = 0.6$				
	0.25	0.35	0.45	0.55	0.64	0.25	0.35	0.45	0.55	0.64
1.0	2.2417E-1	2.1267E-1	1.9396E-1	1.7567E-1	1.5871E-1	3.2158E-1	3.0387E-1	2.7678E-1	2.5012E-1	2.2481E-1
1.2	2.1357E-1	1.9733E-1	1.7554E-1	1.4853E-1	1.3619E-1	3.0709E-1	2.8273E-1	2.5046E-1	2.1129E-1	1.9364E-1
1.4	2.0220E-1	1.8236E-1	1.5631E-1	1.2690E-1	1.1429E-1	2.9122E-1	2.6144E-1	2.2375E-1	1.8050E-1	1.6301E-1
1.6	1.9001E-1	1.6793E-1	1.3765E-1	1.0821E-1	9.3588E-2	2.7383E-1	2.4135E-1	1.9723E-1	1.5429E-1	1.3361E-1
1.8	1.7668E-1	1.5372E-1	1.2049E-1	9.1001E-2	7.4453E-2	2.5490E-1	2.2102E-1	1.7263E-1	1.3029E-1	1.0627E-1
2.0	1.6449E-1	1.3625E-1	1.0295E-1	7.2008E-2	5.6784E-2	2.3756E-1	1.9569E-1	1.4745E-1	1.0333E-1	8.1042E-2
2.2	1.5307E-1	1.1764E-1	8.6265E-2	5.4756E-2	3.8950E-2	2.2085E-1	1.6911E-1	1.2314E-1	7.8481E-2	5.5636E-2
2.4	1.4129E-1	1.0368E-1	6.8619E-2	3.8924E-2	2.2999E-2	2.0405E-1	1.4896E-1	9.7917E-2	5.5656E-2	3.2787E-2
2.6	1.2794E-1	9.0049E-2	5.1641E-2	2.7301E-2	1.0688E-2	1.8491E-1	1.2946E-1	7.4153E-2	3.9179E-2	1.5194E-2
2.8	1.1794E-1	7.5649E-2	4.0595E-2	2.1067E-2	8.0888E-3	1.7021E-1	1.0884E-1	5.8427E-2	3.0181E-2	1.1582E-2
3.0	1.0694E-1	6.4803E-2	3.3881E-2	1.8543E-2	7.9484E-3	1.5420E-1	9.3284E-2	4.8550E-2	2.6606E-2	1.1337E-2
3.2	9.8977E-2	5.8155E-2	2.9577E-2	1.6031E-2	6.9887E-3	1.4289E-1	8.3904E-2	4.2221E-2	2.3144E-2	9.9634E-3
3.4	9.0808E-2	5.2815E-2	2.6936E-2	1.4372E-2	5.0752E-3	1.3134E-1	7.6122E-2	3.8561E-2	2.0799E-2	7.2526E-3
3.6	8.0463E-2	4.7872E-2	2.3963E-2	1.1059E-2	3.7683E-3	1.1640E-1	6.8894E-2	3.4242E-2	1.5877E-2	5.3907E-3
3.8	7.3815E-2	4.3094E-2	2.0620E-2	8.1950E-3	2.6505E-3	1.0644E-1	6.2188E-2	2.9635E-2	1.1673E-2	3.7970E-3
4.0	6.9430E-2	4.0536E-2	1.6594E-2	6.0444E-3	1.4976E-3	1.0016E-1	5.8516E-2	2.3870E-2	8.6595E-3	2.1391E-3
4.2	6.7613E-2	3.6366E-2	1.3555E-2	4.8187E-3	1.0460E-3	9.7701E-2	5.2341E-2	1.9377E-2	6.9247E-3	1.4952E-3
4.4	6.4247E-2	3.1613E-2	1.1545E-2	3.9136E-3	7.6399E-4	9.2758E-2	4.5298E-2	1.6477E-2	5.6263E-3	1.1210E-3
4.6	6.0056E-2	2.8209E-2	9.8947E-3	3.0007E-3	6.5636E-4	8.6825E-2	4.0563E-2	1.4142E-2	4.3029E-3	9.8431E-4
4.8	5.5771E-2	2.5385E-2	8.5348E-3	2.6620E-3	0.0	8.0788E-2	3.6650E-2	1.2253E-2	3.8123E-3	0.0
5.0	5.1026E-2	2.3564E-2	7.3468E-3	2.4193E-3	0.0	7.3703E-2	3.4062E-2	1.0547E-2	3.4475E-3	0.0
5.4	4.2659E-2	1.7818E-2	5.6914E-3	1.4133E-3	0.0	6.1689E-2	2.5635E-2	8.1619E-3	1.9902E-3	0.0
5.8	3.6444E-2	1.4906E-2	3.9832E-3	9.1745E-4	0.0	5.2697E-2	2.1444E-2	5.7636E-3	1.3181E-3	0.0
6.2	3.2606E-2	1.1852E-2	3.2523E-3	6.9073E-4	0.0	4.6969E-2	1.6947E-2	4.7022E-3	9.7941E-4	0.0
6.6	2.8517E-2	9.7582E-3	2.1235E-3	4.1384E-4	0.0	4.1321E-2	1.4157E-2	3.0700E-3	5.7473E-4	0.0
7.0	2.4149E-2	7.8113E-3	1.6216E-3	0.0	0.0	3.4949E-2	1.1158E-2	2.3618E-3	0.0	0.0
7.4	2.1909E-2	6.5990E-3	1.3182E-3	0.0	0.0	3.1758E-2	9.5122E-3	1.8645E-3	0.0	0.0
7.8	1.9476E-2	5.3345E-3	9.7363E-4	0.0	0.0	2.8128E-2	7.6137E-3	1.3621E-3	0.0	0.0
8.2	1.7097E-2	4.4308E-3	6.2535E-4	0.0	0.0	2.4683E-2	6.4523E-3	8.8199E-4	0.0	0.0
8.6	1.4751E-2	3.4017E-3	5.0335E-4	0.0	0.0	2.1326E-2	4.9811E-3	7.1637E-4	0.0	0.0
9.0	1.3477E-2	2.8354E-3	4.0343E-4	0.0	0.0	1.9457E-2	4.1383E-3	5.5986E-4	0.0	0.0
9.4	1.1451E-2	2.4802E-3	0.0	0.0	0.0	1.6515E-2	3.5406E-3	0.0	0.0	0.0
9.8	1.0391E-2	1.9645E-3	0.0	0.0	0.0	1.4962E-2	2.8261E-3	0.0	0.0	0.0
10.2	9.1511E-3	1.6394E-3	0.0	0.0	0.0	1.3285E-2	2.3712E-3	0.0	0.0	0.0
10.6	7.4557E-3	1.2914E-3	0.0	0.0	0.0	1.0830E-2	1.8406E-3	0.0	0.0	0.0
11.0	6.9788E-3	1.0191E-3	0.0	0.0	0.0	1.0242E-2	1.4957E-3	0.0	0.0	0.0
11.4	6.2711E-3	9.7901E-4	0.0	0.0	0.0	9.1237E-3	1.4299E-3	0.0	0.0	0.0
11.8	5.6095E-3	7.8197E-4	0.0	0.0	0.0	8.0287E-3	1.1318E-3	0.0	0.0	0.0
12.2	4.7413E-3	6.6092E-4	0.0	0.0	0.0	6.8434E-3	9.2881E-4	0.0	0.0	0.0
12.6	4.2546E-3	4.7828E-4	0.0	0.0	0.0	6.2286E-3	6.9601E-4	0.0	0.0	0.0
13.0	3.8149E-3	4.3633E-4	0.0	0.0	0.0	5.4676E-3	6.2421E-4	0.0	0.0	0.0
13.4	3.3267E-3	3.6126E-4	0.0	0.0	0.0	4.7976E-3	5.4559E-4	0.0	0.0	0.0
13.8	3.0184E-3	3.0261E-4	0.0	0.0	0.0	4.3400E-3	4.5009E-4	0.0	0.0	0.0
14.2	2.5551E-3	0.0	0.0	0.0	0.0	3.7163E-3	0.0	0.0	0.0	0.0
14.6	2.3201E-3	0.0	0.0	0.0	0.0	3.3511E-3	0.0	0.0	0.0	0.0
15.0	2.1186E-3	0.0	0.0	0.0	0.0	3.0433E-3	0.0	0.0	0.0	0.0
15.4	1.9917E-3	0.0	0.0	0.0	0.0	2.8603E-3	0.0	0.0	0.0	0.0
15.8	1.6944E-3	0.0	0.0	0.0	0.0	2.4621E-3	0.0	0.0	0.0	0.0

16.2	1.4750E-3	0.0	0.0	0.0	0.0	2.1801E-3	0.0	0.0	0.0	0.0
16.6	1.2370E-3	0.0	0.0	0.0	0.0	1.8112E-3	0.0	0.0	0.0	0.0
17.0	1.1584E-3	0.0	0.0	0.0	0.0	1.6765E-3	0.0	0.0	0.0	0.0
17.4	1.0361E-3	0.0	0.0	0.0	0.0	1.4884E-3	0.0	0.0	0.0	0.0
17.8	9.4419E-4	0.0	0.0	0.0	0.0	1.4117E-3	0.0	0.0	0.0	0.0
18.2	8.9235E-4	0.0	0.0	0.0	0.0	1.2882E-3	0.0	0.0	0.0	0.0
18.6	7.0752E-4	0.0	0.0	0.0	0.0	1.0129E-3	0.0	0.0	0.0	0.0
19.0	6.5728E-4	0.0	0.0	0.0	0.0	9.4971E-4	0.0	0.0	0.0	0.0
19.4	5.8784E-4	0.0	0.0	0.0	0.0	8.1932E-4	0.0	0.0	0.0	0.0
19.8	5.0871E-4	0.0	0.0	0.0	0.0	7.2663E-4	0.0	0.0	0.0	0.0
20.2	4.9343E-4	0.0	0.0	0.0	0.0	7.3143E-4	0.0	0.0	0.0	0.0
20.6	4.2924E-4	0.0	0.0	0.0	0.0	6.1457E-4	0.0	0.0	0.0	0.0
21.0	4.1687E-4	0.0	0.0	0.0	0.0	5.9133E-4	0.0	0.0	0.0	0.0
21.4	3.5807E-4	0.0	0.0	0.0	0.0	4.9505E-4	0.0	0.0	0.0	0.0
21.8	3.3874E-4	0.0	0.0	0.0	0.0	4.9459E-4	0.0	0.0	0.0	0.0
22.2	2.8176E-4	0.0	0.0	0.0	0.0	4.1359E-4	0.0	0.0	0.0	0.0

Table B2. Particle-wall RDF at various center-to-wall distances, for $\epsilon_p = 0.65$, $\epsilon_w = 0.8$ and 1.0 , and bulk solid fractions of 0.25 , 0.35 , 0.45 , 0.55 , and 0.64 .

Distance (radii)	$\epsilon_p = 0.65, \epsilon_w = 0.8$					$\epsilon_p = 0.65, \epsilon_w = 1.0$				
	0.25	0.35	0.45	0.55	0.64	0.25	0.35	0.45	0.55	0.64
1.0	4.1057E-1	3.8722E-1	3.5131E-1	3.1709E-1	2.8413E-1	4.9287E-1	4.6273E-1	4.1914E-1	3.7762E-1	3.3754E-1
1.2	3.9308E-1	3.6071E-1	3.1882E-1	2.6803E-1	2.4443E-1	4.7247E-1	4.3229E-1	3.8106E-1	3.2031E-1	2.9098E-1
1.4	3.7333E-1	3.3408E-1	2.8505E-1	2.2930E-1	2.0581E-1	4.4942E-1	4.0096E-1	3.4077E-1	2.7491E-1	2.4547E-1
1.6	3.5117E-1	3.0837E-1	2.5111E-1	1.9622E-1	1.6917E-1	4.2335E-1	3.7084E-1	3.0073E-1	2.3561E-1	2.0200E-1
1.8	3.2674E-1	2.8269E-1	2.1940E-1	1.6591E-1	1.3512E-1	3.9405E-1	3.3997E-1	2.6353E-1	1.9912E-1	1.6152E-1
2.0	3.0477E-1	2.5096E-1	1.8768E-1	1.3185E-1	1.0335E-1	3.6755E-1	3.0177E-1	2.2570E-1	1.5784E-1	1.2375E-1
2.2	2.8402E-1	2.1694E-1	1.5774E-1	1.0041E-1	7.0990E-2	3.4247E-1	2.6112E-1	1.8930E-1	1.2019E-1	8.4972E-2
2.4	2.6237E-1	1.9072E-1	1.2549E-1	7.1301E-2	4.1868E-2	3.1670E-1	2.2985E-1	1.5047E-1	8.5508E-2	4.9994E-2
2.6	2.3772E-1	1.6558E-1	9.4701E-2	4.9961E-2	1.9488E-2	2.8717E-1	1.9944E-1	1.1369E-1	6.0073E-2	2.3169E-2
2.8	2.1891E-1	1.3951E-1	7.4587E-2	3.8600E-2	1.4666E-2	2.6421E-1	1.6772E-1	8.9460E-2	4.6422E-2	1.7628E-2
3.0	1.9817E-1	1.1960E-1	6.2009E-2	3.3923E-2	1.4456E-2	2.3912E-1	1.4359E-1	7.4498E-2	4.0903E-2	1.7315E-2
3.2	1.8367E-1	1.0741E-1	5.4090E-2	2.9429E-2	1.2725E-2	2.2179E-1	1.2908E-1	6.4924E-2	3.5449E-2	1.5199E-2
3.4	1.6903E-1	9.7383E-2	4.9392E-2	2.6558E-2	9.1901E-3	2.0407E-1	1.1740E-1	5.9299E-2	3.1903E-2	1.1032E-2
3.6	1.4954E-1	8.8157E-2	4.3978E-2	2.0479E-2	6.8413E-3	1.8048E-1	1.0629E-1	5.2756E-2	2.4582E-2	8.1795E-3
3.8	1.3682E-1	7.9564E-2	3.7884E-2	1.5074E-2	4.8731E-3	1.6514E-1	9.5726E-2	4.5562E-2	1.8197E-2	5.7966E-3
4.0	1.2879E-1	7.4890E-2	3.0450E-2	1.1123E-2	2.7215E-3	1.5531E-1	8.9929E-2	3.6592E-2	1.3393E-2	3.2963E-3
4.2	1.2538E-1	6.7141E-2	2.4846E-2	8.8451E-3	1.8916E-3	1.5122E-1	8.0596E-2	2.9787E-2	1.0614E-2	2.2972E-3
4.4	1.1908E-1	5.8301E-2	2.1122E-2	7.1324E-3	1.3994E-3	1.4407E-1	7.0056E-2	2.5536E-2	8.5848E-3	1.6771E-3
4.6	1.1159E-1	5.2105E-2	1.8219E-2	5.5069E-3	1.2392E-3	1.3502E-1	6.2642E-2	2.1929E-2	6.6356E-3	1.4782E-3
4.8	1.0373E-1	4.7032E-2	1.5703E-2	4.8422E-3	0.0	1.2531E-1	5.6469E-2	1.8870E-2	5.8922E-3	0.0
5.0	9.4795E-2	4.3648E-2	1.3454E-2	4.4142E-3	0.0	1.1444E-1	5.2427E-2	1.6269E-2	5.3140E-3	0.0
5.4	7.9212E-2	3.2891E-2	1.0366E-2	2.5298E-3	0.0	9.5927E-2	3.9707E-2	1.2468E-2	3.0543E-3	0.0
5.8	6.7895E-2	2.7581E-2	7.2873E-3	1.7016E-3	0.0	8.1940E-2	3.3166E-2	8.7691E-3	2.0531E-3	0.0
6.2	6.0298E-2	2.1884E-2	5.9887E-3	1.2600E-3	0.0	7.2925E-2	2.6228E-2	7.2305E-3	1.5216E-3	0.0
6.6	5.3264E-2	1.8133E-2	3.8537E-3	7.4399E-4	0.0	6.4225E-2	2.1782E-2	4.6597E-3	8.9942E-4	0.0
7.0	4.5121E-2	1.4350E-2	3.0042E-3	0.0	0.0	5.4324E-2	1.7200E-2	3.6043E-3	0.0	0.0
7.4	4.0785E-2	1.2249E-2	2.4569E-3	0.0	0.0	4.9060E-2	1.4641E-2	2.8942E-3	0.0	0.0
7.8	3.6291E-2	9.7825E-3	1.7564E-3	0.0	0.0	4.3785E-2	1.1812E-2	2.1071E-3	0.0	0.0
8.2	3.1810E-2	8.2308E-3	1.1569E-3	0.0	0.0	3.8483E-2	9.9863E-3	1.3734E-3	0.0	0.0
8.6	2.7459E-2	6.3686E-3	9.1441E-4	0.0	0.0	3.3238E-2	7.6235E-3	1.0908E-3	0.0	0.0
9.0	2.5109E-2	5.3340E-3	7.1638E-4	0.0	0.0	3.0371E-2	6.3710E-3	8.6769E-4	0.0	0.0
9.4	2.1292E-2	4.5559E-3	0.0	0.0	0.0	2.5622E-2	5.4621E-3	0.0	0.0	0.0
9.8	1.9188E-2	3.6789E-3	0.0	0.0	0.0	2.3213E-2	4.3343E-3	0.0	0.0	0.0
10.2	1.7036E-2	3.0485E-3	0.0	0.0	0.0	2.0606E-2	3.6790E-3	0.0	0.0	0.0

10.6	1.3905E-2	2.3624E-3	0.0	0.0	0.0	1.6826E-2	2.8552E-3	0.0	0.0	0.0
11.0	1.3075E-2	1.8918E-3	0.0	0.0	0.0	1.5697E-2	2.3029E-3	0.0	0.0	0.0
11.4	1.1771E-2	1.8536E-3	0.0	0.0	0.0	1.4090E-2	2.2265E-3	0.0	0.0	0.0
11.8	1.0272E-2	1.4593E-3	0.0	0.0	0.0	1.2569E-2	1.7495E-3	0.0	0.0	0.0
12.2	8.8016E-3	1.2043E-3	0.0	0.0	0.0	1.0660E-2	1.4553E-3	0.0	0.0	0.0
12.6	7.9383E-3	8.8823E-4	0.0	0.0	0.0	9.6574E-3	1.1043E-3	0.0	0.0	0.0
13.0	7.0230E-3	8.0851E-4	0.0	0.0	0.0	8.5017E-3	9.6594E-4	0.0	0.0	0.0
13.4	6.1577E-3	6.8999E-4	0.0	0.0	0.0	7.4978E-3	8.6088E-4	0.0	0.0	0.0
13.8	5.6144E-3	5.6393E-4	0.0	0.0	0.0	6.7782E-3	6.8072E-4	0.0	0.0	0.0
14.2	4.6954E-3	0.0	0.0	0.0	0.0	5.7467E-3	0.0	0.0	0.0	0.0
14.6	4.3315E-3	0.0	0.0	0.0	0.0	5.2421E-3	0.0	0.0	0.0	0.0
15.0	3.9215E-3	0.0	0.0	0.0	0.0	4.7655E-3	0.0	0.0	0.0	0.0
15.4	3.7233E-3	0.0	0.0	0.0	0.0	4.4966E-3	0.0	0.0	0.0	0.0
15.8	3.1620E-3	0.0	0.0	0.0	0.0	3.8251E-3	0.0	0.0	0.0	0.0
16.2	2.7298E-3	0.0	0.0	0.0	0.0	3.3397E-3	0.0	0.0	0.0	0.0
16.6	2.3145E-3	0.0	0.0	0.0	0.0	2.8329E-3	0.0	0.0	0.0	0.0
17.0	2.1337E-3	0.0	0.0	0.0	0.0	2.5776E-3	0.0	0.0	0.0	0.0
17.4	1.9389E-3	0.0	0.0	0.0	0.0	2.2840E-3	0.0	0.0	0.0	0.0
17.8	1.7971E-3	0.0	0.0	0.0	0.0	2.1987E-3	0.0	0.0	0.0	0.0
18.2	1.6668E-3	0.0	0.0	0.0	0.0	2.0045E-3	0.0	0.0	0.0	0.0
18.6	1.3027E-3	0.0	0.0	0.0	0.0	1.5792E-3	0.0	0.0	0.0	0.0
19.0	1.2554E-3	0.0	0.0	0.0	0.0	1.5035E-3	0.0	0.0	0.0	0.0
19.4	1.0828E-3	0.0	0.0	0.0	0.0	1.3380E-3	0.0	0.0	0.0	0.0
19.8	9.5382E-4	0.0	0.0	0.0	0.0	1.1127E-3	0.0	0.0	0.0	0.0
20.2	9.2287E-4	0.0	0.0	0.0	0.0	1.1116E-3	0.0	0.0	0.0	0.0
20.6	7.9606E-4	0.0	0.0	0.0	0.0	9.4957E-4	0.0	0.0	0.0	0.0
21.0	7.5978E-4	0.0	0.0	0.0	0.0	9.4345E-4	0.0	0.0	0.0	0.0
21.4	6.7251E-4	0.0	0.0	0.0	0.0	7.8938E-4	0.0	0.0	0.0	0.0
21.8	6.3575E-4	0.0	0.0	0.0	0.0	7.4414E-4	0.0	0.0	0.0	0.0
22.2	5.1895E-4	0.0	0.0	0.0	0.0	0.0	0.0	0.0	0.0	0.0

Table B3. Particle-wall RDF at various center-to-wall distances, for $\epsilon_p = 0.86$, $\epsilon_w = 0.4$ and 0.6 , and bulk solid fractions of 0.25 , 0.35 , 0.45 , 0.55 , and 0.64 .

Distance (radii)	$\epsilon_p = 0.86, \epsilon_w = 0.4$					$\epsilon_p = 0.86, \epsilon_w = 0.6$				
	0.25	0.35	0.45	0.55	0.64	0.25	0.35	0.45	0.55	0.64
1.0	1.8843E-1	1.7781E-1	1.6101E-1	1.4528E-1	1.3118E-1	2.7784E-1	2.6170E-1	2.3722E-1	2.1398E-1	1.9296E-1
1.2	1.7969E-1	1.6467E-1	1.4564E-1	1.2263E-1	1.1213E-1	2.6533E-1	2.4273E-1	2.1485E-1	1.8011E-1	1.6548E-1
1.4	1.6993E-1	1.5174E-1	1.2947E-1	1.0431E-1	9.3600E-2	2.5115E-1	2.2397E-1	1.9079E-1	1.5324E-1	1.3856E-1
1.6	1.5903E-1	1.3946E-1	1.1337E-1	8.8419E-2	7.6078E-2	2.3540E-1	2.0583E-1	1.6692E-1	1.3024E-1	1.1286E-1
1.8	1.4704E-1	1.2696E-1	9.8420E-2	7.3802E-2	6.0037E-2	2.1799E-1	1.8703E-1	1.4505E-1	1.0901E-1	8.9065E-2
2.0	1.3627E-1	1.1129E-1	8.3249E-2	5.7744E-2	4.5539E-2	2.0177E-1	1.6441E-1	1.2288E-1	8.5295E-2	6.7287E-2
2.2	1.2604E-1	9.5312E-2	6.8917E-2	4.3341E-2	3.1051E-2	1.8634E-1	1.4089E-1	1.0173E-1	6.4030E-2	4.5630E-2
2.4	1.1564E-1	8.3339E-2	5.4010E-2	3.0337E-2	1.7954E-2	1.7086E-1	1.2291E-1	7.9656E-2	4.4762E-2	2.6420E-2
2.6	1.0368E-1	7.1659E-2	3.9931E-2	2.0915E-2	8.0347E-3	1.5354E-1	1.0556E-1	5.8970E-2	3.0716E-2	1.1836E-2
2.8	9.4634E-2	5.9164E-2	3.0984E-2	1.5860E-2	5.9851E-3	1.4013E-1	8.7426E-2	4.5715E-2	2.3342E-2	8.8303E-3
3.0	8.5017E-2	4.9949E-2	2.5413E-2	1.3861E-2	5.9636E-3	1.2556E-1	7.3842E-2	3.7525E-2	2.0649E-2	8.8122E-3
3.2	7.8336E-2	4.4741E-2	2.2046E-2	1.2103E-2	5.2964E-3	1.1582E-1	6.5950E-2	3.2649E-2	1.7988E-2	7.7921E-3
3.4	7.1494E-2	4.0434E-2	2.0137E-2	1.0937E-2	3.8168E-3	1.0604E-1	5.9724E-2	2.9742E-2	1.6179E-2	5.5771E-3
3.6	6.2641E-2	3.6451E-2	1.7911E-2	8.3106E-3	2.7971E-3	9.2712E-2	5.3908E-2	2.6317E-2	1.2267E-2	4.0913E-3
3.8	5.6967E-2	3.2653E-2	1.5348E-2	6.0201E-3	1.9439E-3	8.4139E-2	4.8280E-2	2.2562E-2	8.9184E-3	2.8740E-3
4.0	5.3388E-2	3.0763E-2	1.2215E-2	4.4273E-3	1.0624E-3	7.8931E-2	4.5264E-2	1.7942E-2	6.5003E-3	1.5867E-3
4.2	5.2054E-2	2.7452E-2	9.8469E-3	3.4989E-3	7.4653E-4	7.7209E-2	4.0378E-2	1.4409E-2	5.1833E-3	1.1115E-3

4.4	4.9460E-2	2.3497E-2	8.3210E-3	2.8110E-3	5.4555E-4	7.3277E-2	3.4744E-2	1.2220E-2	4.1394E-3	8.0948E-4
4.6	4.6103E-2	2.0905E-2	7.1581E-3	2.1493E-3	0.0	6.8387E-2	3.1005E-2	1.0573E-2	3.1694E-3	0.0
4.8	4.2624E-2	1.8792E-2	6.1244E-3	1.8958E-3	0.0	6.3420E-2	2.7861E-2	9.0436E-3	2.8090E-3	0.0
5.0	3.8678E-2	1.7440E-2	5.2071E-3	1.7557E-3	0.0	5.7553E-2	2.5837E-2	7.6892E-3	2.5522E-3	0.0
5.4	3.2031E-2	1.2886E-2	4.0125E-3	9.7357E-4	0.0	4.7461E-2	1.9054E-2	5.8968E-3	1.4649E-3	0.0
5.8	2.7137E-2	1.0787E-2	2.8138E-3	6.5123E-4	0.0	4.0039E-2	1.5856E-2	4.1173E-3	9.5783E-4	0.0
6.2	2.4072E-2	8.4312E-3	2.2605E-3	4.7303E-4	0.0	3.5486E-2	1.2515E-2	3.3559E-3	7.1441E-4	0.0
6.6	2.0965E-2	6.9572E-3	1.4536E-3	0.0	0.0	3.1117E-2	1.0267E-2	2.1507E-3	0.0	0.0
7.0	1.7532E-2	5.3943E-3	1.1065E-3	0.0	0.0	2.6044E-2	8.0355E-3	1.6142E-3	0.0	0.0
7.4	1.5824E-2	4.6450E-3	9.1184E-4	0.0	0.0	2.3424E-2	6.8246E-3	1.3402E-3	0.0	0.0
7.8	1.4069E-2	3.6901E-3	6.5221E-4	0.0	0.0	2.0753E-2	5.4352E-3	9.6853E-4	0.0	0.0
8.2	1.2221E-2	3.1425E-3	3.9139E-4	0.0	0.0	1.8177E-2	4.6334E-3	6.0726E-4	0.0	0.0
8.6	1.0542E-2	2.3188E-3	3.3764E-4	0.0	0.0	1.5601E-2	3.4454E-3	5.1714E-4	0.0	0.0
9.0	9.5561E-3	1.9618E-3	0.0	0.0	0.0	1.4233E-2	2.8649E-3	0.0	0.0	0.0
9.4	8.1038E-3	1.6834E-3	0.0	0.0	0.0	1.1949E-2	2.4899E-3	0.0	0.0	0.0
9.8	7.3343E-3	1.3360E-3	0.0	0.0	0.0	1.0775E-2	1.9774E-3	0.0	0.0	0.0
10.2	6.4326E-3	1.1044E-3	0.0	0.0	0.0	9.4440E-3	1.6422E-3	0.0	0.0	0.0
10.6	5.1633E-3	8.8002E-4	0.0	0.0	0.0	7.7083E-3	1.2904E-3	0.0	0.0	0.0
11.0	4.9044E-3	6.5830E-4	0.0	0.0	0.0	7.2388E-3	9.7972E-4	0.0	0.0	0.0
11.4	4.3400E-3	6.8708E-4	0.0	0.0	0.0	6.4487E-3	9.8881E-4	0.0	0.0	0.0
11.8	3.8758E-3	5.1790E-4	0.0	0.0	0.0	5.7226E-3	7.6476E-4	0.0	0.0	0.0
12.2	3.2265E-3	4.1899E-4	0.0	0.0	0.0	4.7232E-3	6.3256E-4	0.0	0.0	0.0
12.6	2.9066E-3	3.1655E-4	0.0	0.0	0.0	4.3673E-3	4.6095E-4	0.0	0.0	0.0
13.0	2.5422E-3	2.8303E-4	0.0	0.0	0.0	3.7624E-3	4.1044E-4	0.0	0.0	0.0
13.4	2.2149E-3	2.4603E-4	0.0	0.0	0.0	3.3268E-3	3.6451E-4	0.0	0.0	0.0
13.8	2.0301E-3	0.0	0.0	0.0	0.0	3.0412E-3	0.0	0.0	0.0	0.0
14.2	1.7261E-3	0.0	0.0	0.0	0.0	2.5096E-3	0.0	0.0	0.0	0.0
14.6	1.5355E-3	0.0	0.0	0.0	0.0	2.2887E-3	0.0	0.0	0.0	0.0
15.0	1.4089E-3	0.0	0.0	0.0	0.0	2.1103E-3	0.0	0.0	0.0	0.0
15.4	1.3422E-3	0.0	0.0	0.0	0.0	1.9767E-3	0.0	0.0	0.0	0.0
15.8	1.1269E-3	0.0	0.0	0.0	0.0	1.6854E-3	0.0	0.0	0.0	0.0
16.2	9.8476E-4	0.0	0.0	0.0	0.0	1.4564E-3	0.0	0.0	0.0	0.0
16.6	8.4342E-4	0.0	0.0	0.0	0.0	1.1980E-3	0.0	0.0	0.0	0.0
17.0	7.6683E-4	0.0	0.0	0.0	0.0	1.1343E-3	0.0	0.0	0.0	0.0
17.4	6.7033E-4	0.0	0.0	0.0	0.0	1.0009E-3	0.0	0.0	0.0	0.0
17.8	6.5334E-4	0.0	0.0	0.0	0.0	9.4223E-4	0.0	0.0	0.0	0.0
18.2	5.8696E-4	0.0	0.0	0.0	0.0	8.5933E-4	0.0	0.0	0.0	0.0
18.6	4.5459E-4	0.0	0.0	0.0	0.0	6.7962E-4	0.0	0.0	0.0	0.0
19.0	4.3977E-4	0.0	0.0	0.0	0.0	6.3632E-4	0.0	0.0	0.0	0.0
19.4	3.7111E-4	0.0	0.0	0.0	0.0	5.3649E-4	0.0	0.0	0.0	0.0
19.8	3.1067E-4	0.0	0.0	0.0	0.0	4.8788E-4	0.0	0.0	0.0	0.0
20.2	3.3007E-4	0.0	0.0	0.0	0.0	4.7712E-4	0.0	0.0	0.0	0.0
20.6	2.7182E-4	0.0	0.0	0.0	0.0	3.8634E-4	0.0	0.0	0.0	0.0
21.0	2.7543E-4	0.0	0.0	0.0	0.0	3.9673E-4	0.0	0.0	0.0	0.0
21.4	2.3159E-4	0.0	0.0	0.0	0.0	3.4236E-4	0.0	0.0	0.0	0.0

Table B4. Particle-wall RDF at various center-to-wall distances, for $\epsilon_p = 0.86$, $\epsilon_w = 0.8$ and 1.0 , and bulk solid fractions of 0.25 , 0.35 , 0.45 , 0.55 , and 0.64 .

Distance (radii)	$\epsilon_p = 0.86, \epsilon_w = 0.8$					$\epsilon_p = 0.86, \epsilon_w = 1.0$				
	0.25	0.35	0.45	0.55	0.64	0.25	0.35	0.45	0.55	0.64
1.0	3.6482E-1	3.4311E-1	3.1094E-1	2.8013E-1	2.5223E-1	4.4912E-1	4.2175E-1	3.8176E-1	3.4387E-1	3.0941E-1
1.2	3.4867E-1	3.1855E-1	2.8143E-1	2.3595E-1	2.1562E-1	4.2949E-1	3.9217E-1	3.4564E-1	2.8956E-1	2.6525E-1
1.4	3.3023E-1	2.9391E-1	2.5002E-1	2.0083E-1	1.8019E-1	4.0683E-1	3.6207E-1	3.0747E-1	2.4655E-1	2.2219E-1
1.6	3.0914E-1	2.7025E-1	2.1886E-1	1.7073E-1	1.4690E-1	3.8117E-1	3.3315E-1	2.6957E-1	2.0991E-1	1.8125E-1
1.8	2.8607E-1	2.4586E-1	1.9017E-1	1.4304E-1	1.1629E-1	3.5282E-1	3.0321E-1	2.3423E-1	1.7595E-1	1.4342E-1
2.0	2.6539E-1	2.1599E-1	1.6122E-1	1.1209E-1	8.8167E-2	3.2722E-1	2.6661E-1	1.9830E-1	1.3790E-1	1.0867E-1
2.2	2.4541E-1	1.8533E-1	1.3356E-1	8.4203E-2	5.9968E-2	3.0241E-1	2.2819E-1	1.6413E-1	1.0354E-1	7.3753E-2
2.4	2.2488E-1	1.6186E-1	1.0467E-1	5.8759E-2	3.4759E-2	2.7718E-1	1.9874E-1	1.2870E-1	7.2275E-2	4.2671E-2
2.6	2.0223E-1	1.3895E-1	7.7311E-2	4.0306E-2	1.5539E-2	2.4918E-1	1.7077E-1	9.5454E-2	4.9665E-2	1.9100E-2
2.8	1.8477E-1	1.1478E-1	5.9865E-2	3.0712E-2	1.1626E-2	2.2765E-1	1.4154E-1	7.3928E-2	3.7786E-2	1.4242E-2
3.0	1.6564E-1	9.7127E-2	4.9324E-2	2.7039E-2	1.1524E-2	2.0427E-1	1.1986E-1	6.0642E-2	3.3293E-2	1.4218E-2
3.2	1.5258E-1	8.6909E-2	4.2797E-2	2.3516E-2	1.0147E-2	1.8844E-1	1.0705E-1	5.2744E-2	2.8973E-2	1.2571E-2
3.4	1.3942E-1	7.8533E-2	3.9051E-2	2.1146E-2	7.3430E-3	1.7206E-1	9.6612E-2	4.8084E-2	2.6080E-2	9.0095E-3
3.6	1.2208E-1	7.0615E-2	3.4635E-2	1.6102E-2	5.4206E-3	1.5044E-1	8.7172E-2	4.2527E-2	1.9898E-2	6.5771E-3
3.8	1.1107E-1	6.3279E-2	2.9612E-2	1.1676E-2	3.7735E-3	1.3681E-1	7.8180E-2	3.6467E-2	1.4493E-2	4.5893E-3
4.0	1.0406E-1	5.9692E-2	2.3672E-2	8.5098E-3	2.0535E-3	1.2842E-1	7.3503E-2	2.9035E-2	1.0501E-2	2.5376E-3
4.2	1.0161E-1	5.3207E-2	1.9142E-2	6.7173E-3	1.4485E-3	1.2531E-1	6.5593E-2	2.3455E-2	8.3222E-3	1.7864E-3
4.4	9.6479E-2	4.5743E-2	1.6225E-2	5.3904E-3	1.0612E-3	1.1900E-1	5.6313E-2	1.9905E-2	6.6816E-3	1.3115E-3
4.6	9.0141E-2	4.0747E-2	1.3879E-2	4.1545E-3	0.0	1.1107E-1	5.0027E-2	1.7098E-2	5.0836E-3	0.0
4.8	8.3293E-2	3.6591E-2	1.1854E-2	3.6969E-3	0.0	1.0271E-1	4.5083E-2	1.4643E-2	4.5113E-3	0.0
5.0	7.5572E-2	3.3915E-2	1.0129E-2	3.3858E-3	0.0	9.3098E-2	4.1831E-2	1.2459E-2	4.1231E-3	0.0
5.4	6.2268E-2	2.5210E-2	7.7128E-3	1.9143E-3	0.0	7.6901E-2	3.0929E-2	9.5066E-3	2.3672E-3	0.0
5.8	5.2677E-2	2.0941E-2	5.3825E-3	1.2727E-3	0.0	6.5361E-2	2.5701E-2	6.5965E-3	1.5357E-3	0.0
6.2	4.6820E-2	1.6508E-2	4.4636E-3	9.2125E-4	0.0	5.7840E-2	2.0279E-2	5.4671E-3	1.1221E-3	0.0
6.6	4.0835E-2	1.3487E-2	2.8511E-3	0.0	0.0	5.0458E-2	1.6677E-2	3.5193E-3	6.3980E-4	0.0
7.0	3.4181E-2	1.0547E-2	2.1404E-3	0.0	0.0	4.2330E-2	1.3107E-2	2.6601E-3	0.0	0.0
7.4	3.0981E-2	8.9904E-3	1.7594E-3	0.0	0.0	3.8212E-2	1.1127E-2	2.1573E-3	0.0	0.0
7.8	2.7335E-2	7.1661E-3	1.2662E-3	0.0	0.0	3.3875E-2	8.7938E-3	1.5477E-3	0.0	0.0
8.2	2.3770E-2	6.0447E-3	8.1037E-4	0.0	0.0	2.9380E-2	7.5061E-3	9.6927E-4	0.0	0.0
8.6	2.0500E-2	4.6009E-3	6.5476E-4	0.0	0.0	2.5410E-2	5.6141E-3	8.0150E-4	0.0	0.0
9.0	1.8697E-2	3.7983E-3	0.0	0.0	0.0	2.3055E-2	4.6585E-3	0.0	0.0	0.0
9.4	1.5892E-2	3.2659E-3	0.0	0.0	0.0	1.9514E-2	4.0364E-3	0.0	0.0	0.0
9.8	1.4233E-2	2.5753E-3	0.0	0.0	0.0	1.7615E-2	3.1805E-3	0.0	0.0	0.0
10.2	1.2548E-2	2.1485E-3	0.0	0.0	0.0	1.5564E-2	2.6670E-3	0.0	0.0	0.0
10.6	1.0096E-2	1.6527E-3	0.0	0.0	0.0	1.2493E-2	2.0419E-3	0.0	0.0	0.0
11.0	9.5407E-3	1.3071E-3	0.0	0.0	0.0	1.1682E-2	1.6306E-3	0.0	0.0	0.0
11.4	8.5348E-3	1.2976E-3	0.0	0.0	0.0	1.0497E-2	1.6054E-3	0.0	0.0	0.0
11.8	7.5291E-3	1.0029E-3	0.0	0.0	0.0	9.3219E-3	1.2791E-3	0.0	0.0	0.0
12.2	6.2484E-3	8.3033E-4	0.0	0.0	0.0	7.8054E-3	1.0066E-3	0.0	0.0	0.0
12.6	5.7433E-3	6.1281E-4	0.0	0.0	0.0	7.0719E-3	7.5825E-4	0.0	0.0	0.0
13.0	4.9909E-3	5.6862E-4	0.0	0.0	0.0	6.1742E-3	6.7798E-4	0.0	0.0	0.0
13.4	4.3378E-3	4.8134E-4	0.0	0.0	0.0	5.3786E-3	5.9859E-4	0.0	0.0	0.0
13.8	3.9886E-3	0.0	0.0	0.0	0.0	4.9715E-3	0.0	0.0	0.0	0.0
14.2	3.3167E-3	0.0	0.0	0.0	0.0	4.1117E-3	0.0	0.0	0.0	0.0
14.6	3.0149E-3	0.0	0.0	0.0	0.0	3.7269E-3	0.0	0.0	0.0	0.0
15.0	2.7487E-3	0.0	0.0	0.0	0.0	3.3715E-3	0.0	0.0	0.0	0.0
15.4	2.6232E-3	0.0	0.0	0.0	0.0	3.1809E-3	0.0	0.0	0.0	0.0
15.8	2.1970E-3	0.0	0.0	0.0	0.0	2.6985E-3	0.0	0.0	0.0	0.0
16.2	1.8907E-3	0.0	0.0	0.0	0.0	2.3541E-3	0.0	0.0	0.0	0.0
16.6	1.6097E-3	0.0	0.0	0.0	0.0	1.9697E-3	0.0	0.0	0.0	0.0
17.0	1.5055E-3	0.0	0.0	0.0	0.0	1.8607E-3	0.0	0.0	0.0	0.0

17.4	1.2891E-3	0.0	0.0	0.0	0.0	1.5939E-3	0.0	0.0	0.0	0.0
17.8	1.2128E-3	0.0	0.0	0.0	0.0	1.5539E-3	0.0	0.0	0.0	0.0
18.2	1.1451E-3	0.0	0.0	0.0	0.0	1.4124E-3	0.0	0.0	0.0	0.0
18.6	8.8705E-4	0.0	0.0	0.0	0.0	1.1134E-3	0.0	0.0	0.0	0.0
19.0	8.2700E-4	0.0	0.0	0.0	0.0	1.0295E-3	0.0	0.0	0.0	0.0
19.4	7.3170E-4	0.0	0.0	0.0	0.0	8.9618E-4	0.0	0.0	0.0	0.0
19.8	6.3366E-4	0.0	0.0	0.0	0.0	7.6251E-4	0.0	0.0	0.0	0.0
20.2	6.4708E-4	0.0	0.0	0.0	0.0	7.7417E-4	0.0	0.0	0.0	0.0
20.6	5.3813E-4	0.0	0.0	0.0	0.0	6.5023E-4	0.0	0.0	0.0	0.0
21.0	5.2513E-4	0.0	0.0	0.0	0.0	6.6582E-4	0.0	0.0	0.0	0.0
21.4	4.3954E-4	0.0	0.0	0.0	0.0	5.3931E-4	0.0	0.0	0.0	0.0

CURRICULUM VITAE

PERSONAL INFORMATION

Surname, Name: Johnson, Evan
Nationality: United States of America

EDUCATION

Degree	Institution	Year of Graduation
MS	METU	2017
BS	California Polytechnic State University, San Luis Obispo	2009
High School	Newport High School, Oregon, USA	2004

PUBLICATIONS

- [1] E.F. Johnson, İ. Tari, D. Baker, Radiative heat transfer in the discrete element method by distance based approximations, Powder Technol. (2020). doi:10.1016/j.powtec.2020.11.050.
- [2] S. Hicdurmaz, E. Johnson, J. Grobbel, L. Amsbeck, R. Buck, B. Hoffschmidt, Numerical Heat Transfer Modelling of a Centrifugal Solar Particle Receiver, (n.d.).
- [3] E. Johnson, İ. Tari, D. Baker, A Monte Carlo method to solve for radiative effective thermal conductivity for particle beds of various solid fractions and emissivities, J. Quant. Spectrosc. Radiat. Transf. 250 (2020). doi:https://doi.org/10.1016/j.jqsrt.2020.107014.
- [4] E. Johnson, D. Baker, I. Tari, Development of View Factor Correlations for Modeling Thermal Radiation in Solid Particle Solar Receivers Using CFD-DEM, AIP Conf. Proc. (2018).
- [5] N. Bonyadi, E. Johnson, D. Baker, Technoeconomic and exergy analysis of a solar geothermal hybrid electric power plant using a novel combined cycle, Energy Convers. Manag. 156 (2018). doi:10.1016/j.enconman.2017.11.052.
- [6] E. Johnson, Conceptual Design and Heat Transfer Investigation of a Dense Granular Flow Solar Receiver, Middle East Technical University, 2017.

[7] E. Johnson, D. Baker, I. Tari, Proposal of a Novel Gravity-Fed , Particle-Filled Solar Receiver, AIP Conf. Proc. 1850 (2017). doi:10.1063/1.4984371.